DE-FG22-91PC91305
FINAL TECHNICAL REPORT

DOE/PC/91305--T2

FINAL TECHNICAL REPORT

CHARACTERIZATION OF POROSITY *VIA* SECONDARY REACTIONS

by

J. M. Calo (PI)
L. Zhang, P. J. Hall, and M. Antxustegi

BROWN UNIVERSITY
Division of Engineering, Box D
Providence, Rhode Island 02912-9104

September 1997

Prepared for: **U. S. Department of Energy**
Federal Energy Technology Center
P. O. Box 10940
Pittsburgh, PA 15236

DISCLAIMER

DE-FG22-91PC91305-FINAL

CHARACTERIZATION OF POROSITY *VIA* SECONDARY REACTIONS

J.M. Calo (Principal Investigator), L. Zhang, P.J. Hall, and M. Antxustegi

Division of Engineering
BROWN UNIVERSITY
Providence, Rhode Island 02912

Final Report
1 September 1991 - 30 November 1995

Prepared for:
U.S. DEPARTMENT OF ENERGY
Pittsburgh Energy Technology Center
Pittsburgh, Pennsylvania 15236

Disclaimer

Acknowledgement

The small angle neutron scattering data were obtained at the Intense Pulsed Neutron Source (IPNS), Small Angle Diffractometer (SAD) located at the Argonne National Laboratory, which is operated under United States Department of Energy contract number W-31-109-ENG-38.

SUMMARY

A new approach to the study of porosity and porosity development in coal chars during gasification was investigated. This approach involves the establishment of the relationships between the amount and type of surface complexes evolved during post-activation temperature programmed desorption (TPD), and the porosity, as measured by gas adsorption and small angle neutron scattering (SANS) techniques. With this new method, the total surface area and micropore volume can be determined by the interpretation of post-activation TPD spectra.

Oxygen gasification, and subsequent TPD were carried out for Wyodak and Pittsburgh #8 coal char, and phenol-formaldehyde resin char samples. The rate of conversion and the desorption features were investigated. The porosity characteristics of these chars were first obtained using the α_s-plot method from nitrogen isotherm data. These data showed that Wyodak coal char is microporous prior to activation in oxygen. Its porosity develops continuously with burn-off, and about half of the total surface area is due to the larger pores at 80% burn-off. The resin char is also a microporous material before activation in oxygen, but the rate of pore size development is slower with burn-off, such that at 72% burn-off, only 5% of the surface area is attributed to larger porosity. Pittsburgh #8 coal char is essentially a nonporous material prior to activation in oxygen, but as gasification proceeds, porosity is created and develops rapidly, such that at 80% burn-off, more than half the surface area (about 61%) is due to the larger porosity. The total surface areas of these char samples increase with degree of burn-off at low conversion, attains a maximum *ca.* 40% burn-off, and then decreases as gasification proceeds further. At the same time, the nonmicroporous surface area increases continuously with burn-off.

The total surface area and the total amount of CO evolved upon TPD were shown to be correlated. The micropore volume and the CO evolved, "corrected" for the expected contribution from carboxylic acid anhydride surface complexes are also correlated. In addition, the total CO_2 evolved upon TPD follows the surface area of the larger porosity (mesoporosity, or even macroporosity). From these results, it is concluded that the CO-evolving, oxygen surface complexes are formed over the entire surface area of the chars during gasification, but that the surface area in the larger porosity is primarily responsible for the formation of the CO_2-evolving complexes.

The favorable comparison of the random pore model theory with the nitrogen adsorption

isotherm data supports the feasibility of the application of this theory to chars which are initially microporous. In this case, it was shown that he total surface area during the entire burn-off history can be determined from the conversion rate *via* a master equation. The random pore model predicts that at low conversion, the mean micropore radius increases, and attains a peak value *ca.* 40% burn-off, and then decreases with burn-off thereafter. At the same time, the larger pores develop and some of the pore walls of the smaller porosity collapse as burn-off proceeds, causing surface area loss at high conversion.

The primary conclusion of this work is that it is possible to predict total surface area and micropore volume from TPD spectra. From the extended random pore model, additional information about the micropore surface area, the nonmicroporous surface area, and the mean micropore size development as a function of reaction time (or burn-off) can also be predicted. Therefore, combining the TPD technique and the extended random pore model provides a new method for the characterization of char porosity.

In addition to the desorption method and nitrogen adsorption data, the same chars were also characterized using small angle neutron scattering (SANS). In these experiments, conducted at the IPNS-SAD facility of the Argonne National Laboratory, scattering from dry char samples was used to obtain information about the total porosity present. When the samples were "contrast matched" with deuterated toluene, scattering from the "open" porosity was eliminated and information about "closed" porosity was obtained. The difference between the dry and contrast matched scattering curves provided information about the "open" or accessible porosity, *vs.* the "closed" or inaccessible porosity. For the phenolic resin char, it was shown that the porosity in the unactivated sample was primarily due to porosity which was closed to the external surface. Activation was shown to open up previously closed porosity. In contrast, unactivated Pittsburgh #8 coal char was shown to contain very little porosity. Subsequent activation continuously developed open porosity. Scattering experiments on the Wyodak coal char showed that in the initial stages of activation (up to ~30% burn-off), a steadily decreasing amount of closed porosity is evident. At higher burn-offs, all of the porosity becomes effectively open.

The results presented show that all three methods described the same qualitative behavior with respect to the nature of char porosity and its development upon activation. The thermal desorption method shows promise as a characterization technique, particularly since it is by far the most rapid and facile to perform. Consequently, the next stage in the development of this porosity characterization procedure is to develop calibration methods to place it on a firm quantitative basis.

TABLE OF CONTENTS

1.0. INTRODUCTION **1**

1.1. Overview. 1

1.2. The Current Project. 2

1.3. Porosity Characterization of Carbons and Chars. 3

1.3.1. Adsorption of Gases and Vapors. 3

1.3.2. Techniques for Micropore Characterization. 7

1.3.2-1. The Langmuir Equation. 7

1.3.2-2. The BET Equation. 8

1.3.2-3. The Dubinin-Radushkevich (DR) Equation. 9

1.3.2-4. Standard Isotherm Methods. 10

1.3.3. Pore Size Distributions. 12

1.3.3-1. Micropore Size Distributions. 12

1.3.3-2. Mesopore Size Distributions. 14

2.0. EXPERIMENTAL **19**

2.1. Char Samples. 19

2.1.1. General Sample Characteristics. 19

2.1.1-1. Phenol-Formaldehyde Resin. 19

2.1.2. Char Preparation. 20

2.1.3. Char Demineralization. 20

2.2. Char Characterization by Gas Adsorption Techniques. 21

2.2.1. Nitrogen Isotherms. 21

2.2.2. Pore Size Distributions. 22

2.3. Temperature Programmed Desorption-Mass Spectrometry/Thermogravimetric

Analysis (TPD-MS/TGA) System. 23

2.3.1. TPD-MS/TGA Apparatus. 23

2.3.2. Experimental Tests and Results. 24

2.3.2-1. Reactor Temperature Profile. 24

2.3.2-2. Heating Rate Program. 25

2.3.2-3. Effect of Reactor Pressure on TPD Results. 25

2.3.2-4. The Effect of Buoyancy on Mass Measurement. 26

2.4. Correction of High Temperature CO Evolution From TPD. 27

2.5. Experimental Procedures for TGA/TPD. 28

3.0. CHAR POROSITY CHARACTERIZATION AND DEVELOPMENT *VIA* TPD TECHNIQUES 50

3.1. Introduction. 50

3.2. Experimental. 50

3.3. Nitrogen Adsorption Isotherm Data. 51

3.3.1. Wyodak Coal Char. 51

3.3.2. Pittsburgh #8 Coal Char. 53

3.3.3. Resin Char. 53

3.4. Correlations With Temperature Programmed Desorption (TPD) Spectra. 54

3.5. The Random Pore Model. 58

3.5.1. Background and Theory. 59

3.5.2. Extension of the Random Pore Model. 62

3.5.3. Application of the Random Pore Model. 67

3.6. Correlation/Prediction of Porosity Development via TPD. 69

3.7. Summary and Conclusions. 70

4.0. POROSITY CHARACTERIZATION *VIA* SMALL ANGLE NEUTRON SCATTERING (SANS).116

4.1. Overview. 116

4.2. Porosity Development in Chars. 116

4.2.1. Background. 116

4.2.2. Experimental. 121

4.2.3. Results and Discussion. 122

4.2.3-1. Pittsburgh #8 Coal Char. 122

4.2.3-2. Phenol-Formaldehyde Resin Char (PRC). 125

4.2.3-3. Wyodak Coal Char. 128

4.3. Modeling Porosity From SANS Data. 131

4.3.1. Analysis Procedures. 132

4.3.2. Results and Discussion. 137

4.4. Summary and Conclusions. 139

REFERENCES 169

APPENDICES

Appendix A. Sample Calculation of Specific Surface Area, External Surface Area, and Micropore Volume for a Char Sample. 173

Appendix B. Roberts (1967) Method of Determining Mesopore Size Distributions. 181

Appendix C. Calculation of the CO_2 Mass Spectrometer "Cracking Factor" and Relative Sensitivities of CO and CO_2. 189

Appendix D. Random Pore Model Program. 194

Appendix E.1. Program SCATTER. 198

Appendix E.2. Program SYNTHESIZE. 213

LIST OF TABLES

Table 2.1. Elemental composition (wt %) of Wyodak and Pittsburgh #8 coal. 30

Table 2.2. Mineral matter composition of ash (%) for Wyodak and Pittsburgh #8 coal samples. 31

Table 2.3. Elemental composition of phenolic resin char as a function of pyrolysis temperature. 32

Table 2.4. Relative pressure, P/P° values, and corresponding N_2 (adsorbate) and He (carrier gas) flow rates. 33

Table 2.5. Third order polynomial coefficients for the voltage-temperature relationship for the type R thermocouple. 34

Table 3.1. Summary of experimental results for TPD of Wyodak coal char gasified in oxygen at 390°C and 10% burn-off. 73

Table 3.2. Summary of experimental results for Wyodak coal char. 74

Table 3.3. Summary of experimental results for Pittsburgh #8 coal char. 75

Table 3.4. Summary of experimental results for resin char. 76

Table 4.1. Phenolic resin char (PRC) mean micropore sizes and fractal dimensions. 140

Table 4.2. Phenolic resin char (PRC) Porod scattering invariants ($Q \times 10^3, \pm 0.1$) 140

Table 4.3. Wyodak coal char surface areas and Porod invariants (Q). 141

Table 4.4. Parameter values for bimodal Schulz FPPS model for unactivated PRC. 141

Table 4.5. Parameter values for bimodal Schulz FPPS model for PRC burned-off to 21%. 141

LIST OF FIGURES

Figure 1.1. The five types of adsorption isotherms, I to V, according to the classification scheme of Brunauer, Deming, Deming and Teller [1940], together with Type VI stepped isotherm. 16

Figure 1.2. Three different types of isotherms found most often for microporous chars (see text) [Rodriguez-Reinoso, 1986]. 17

Figure 1.3. Effect of microporosity on the isotherm and α_s-plot. (a) (A) is the isotherm of a non-porous adsorbent, and (B) is the same solid with additional microporosity. (b) An α_s-plot corresponding to the isotherms of (a). (schematic only) [see Gregg and Sing, 1982]. 18

Figure 2.1. Schematic of the gas flow circuit of the Quantasorb surface area analyzer. 35

Figure 2.2. Nitrogen uptake at 77 K on Wyodak coal char gasified in oxygen at 420°C to 30% burn-off. 36

Figure 2.3. Schematic of the TPD-MS/TGA apparatus. 37

Figure 2.4. Schematic of the TPD-MS/TGA reactor hangdown tube. 38

Figure 2.5. Temperature profile in the reactor hangdown tube. 39

Figure 2.6. Temperature programs at different heating rates. 40

Figure 2.7. 50K/min CO TPD spectra as a function of helium carrier gas pressure for resin char gasified in oxygen at 470°C to 10% burn-off. 41

Figure 2.8. 50K/min CO TPD spectra as a function of helium carrier gas pressure for natural Wyodak coal char gasified in oxygen at 380°C to 10% burn-off. 42

Figure 2.9. Comparison of 50K/min TPD spectra from natural Wyodak coal char and demineralized Wyodak coal char gasified in oxygen at 420°C to 30% burn-off, for a helium carrier gas pressure of 25 torr. 43

Figure 2.10. Mass signal for the empty sample bucket as a function of temperature at a heating rate of 50 K/min. 44

Figure 2.11. CO desorption spectra from Wyodak coal char and resin char gasified in 1 atm of oxygen to 15% burn-off. 45

Figure 2.12. 50K/min CO Evolution curve for "empty" contaminated quartz sample bucket. 46

Figure 2.13. "Corrected" 50K/min CO desorption spectra from Wyodak coal char and resin char gasified in 1 atm oxygen to 15% burn-off. 47

Figure 2.14 Typical TGA data for resin char in 1 atm of oxygen, gasified at 470°C to 15% burn-off. The data were corrected for buoyancy. 48

Figure 2.15. Typical raw data obtained during 50K/min TPD run at a reactor pressure of 25 torr for resin char gasified in oxygen at 470°C to 15% burn-off. The sample mass data were not corrected for buoyancy. 49

Figure 3.1. Nitrogen desorption isotherms for Wyodak coal char samples as a function of burn-off in oxygen at 420°C. 77

Figure 3.2. α_s-plots for Wyodak coal char samples constructed from the nitrogen desorption isotherm data presented in Figure 3.1. 78

Figure 3.3. Variation of total specific surface area with burn-off for Wyodak coal char, obtained from the α_s-plots presented in Figure 3.2. 79

Figure 3.4. Variation of micropore volume with burn-off for Wyodak coal char, obtained from the α_s-plots presented in Figure 3.2. 80

Figure 3.5. Variation of nonmicroporous surface area with burn-off for Wyodak coal char, obtained from the α_s-plots presented in Figure 3.2. 81

Figure 3.6. Mesopore size distributions for Wyodak coal char, as determined by the method of Roberts (1967) from the nitrogen desorption isotherm data presented in Figure 3.1. 82

Figure 3.7. Nitrogen desorption isotherms for Pittsburgh #8 coal char samples gasified in oxygen at 470°C. 83

Figure 3.8. α_s-plots for Pittsburgh #8 coal char samples constructed from the nitrogen desorption isotherm data presented in Figure 3.7. 84

Figure 3.9. Apparent specific surface area as a function of burn-off for Pittsburgh #8 coal char, obtained from the α_s-plots presented in Figure 3.8. 85

Figure 3.10. Micropore volume as a function of burn-off for Pittsburgh #8 coal char, obtained from the α_s-plots presented in Figure 3.8. 86

Figure 3.11. Apparent specific surface area as a function of burn-off for Pittsburgh #8 coal char, obtained from the α_s-plots presented in Figure 3.8. 87

Figure 3.12. Mesopore size distributions for Pittsburgh #8 coal char gasified in oxygen at 470°C, as determined by the method of Roberts (1967). 88

Figure 3.13. Nitrogen desorption isotherms for phenol-formaldehyde resin coal char gasified in oxygen at 470°C. 89

Figure 3.14. Total surface area as a function of burn-off for resin char gasified in oxygen at 470°C. 90

Figure 3.15. Micropore volume as a function of burn-off for resin char gasified in oxygen at 470°C. 91

Figure 3.16. Nonmicroporous surface area as a function of burn-off for resin char gasified in oxygen at 470°C. 92

Figure 3.17. 50K/min CO TPD spectra from Wyodak coal char as a function of burn-off in oxygen at 420°C. 93

Figure 3.18. 50K/min CO_2 TPD spectra from Wyodak coal char as a function of burn-off in oxygen at 420°C. 94

Figure 3.19. CO evolved and specific surface area as a function of burn-off for Wyodak coal char gasified in oxygen at 420°C. 95

Figure 3.20. Comparison of nonmicroporous surface area with total CO_2 evolved as a function of burn-off for Wyodak coal char gasified in oxygen at 420°C. 96

Figure 3.21. Comparison of total CO evolved with specific surface area for Pittsburgh #8 coal char gasified in oxygen at 470°C. 97

Figure 3.22. Comparison of CO evolution with specific surface area for resin char gasified in oxygen at 470°C. 98

Figure 3.23. Comparison of total CO_2 evolved with nonmicroporous surface area for Pittsburgh #8 coal char gasified in oxygen at 470°C. 99

Figure 3.24. Comparison of total CO_2 evolution with nonmicroporous surface area for resin char gasified in oxygen at 470°C. 100

Figure 3.25. Comparison of micropore volume with "corrected" CO evolved from Wyodak coal char gasified in oxygen at 420°C. 101

Figure 3.26. Comparison of micropore volume with "corrected" CO evolved from resin char gasified in oxygen at 470°C. 102

Figure 3.27. Comparison of micropore volume with "corrected" CO evolved from resin char gasified in oxygen at 470°C. 103

Figure 3.28. Comparison of random pore model predictions (Eq.[3.37]) with experimental gasification data for Wyodak coal char in oxygen at 420°C. 104

Figure 3.29. Comparison of random pore model predictions (Eq.[3.37]) with experimental gasification data for resin char in oxygen at 470°C. 105

Figure 3.30. Comparison of random pore model predictions with BET surface area for Wyodak coal char gasified in oxygen at 420°C. 106

Figure 3.31. Comparison of random pore model predictions with BET surface area for resin char gasified in oxygen at 470°C. 107

Figure 3.32. Mean micropore radius change as a function of burn-off. 108

Figure 3.33. Mean micropore radius as a function of burn-off. 109

Figure 3.34. Comparison of random pore model with experimental nonmicroporous surface area for gasification of Wyodak coal char in oxygen at 420°C. 110

Figure 3.35. Comparison of random pore model predictions with experimental nonmicroporous surface area for resin char gasified in oxygen at 470°C. 111

Figure 3.36. Total Specific area as a function of total CO evolution for resin char gasified in oxygen at 470°C. 112

Figure 3.37. Total Specific area as a function of total CO evolution for Wyodak coal char gasified in oxygen at 470°C. 113

Figure 3.38. Micropore volume as a function of "corrected" CO evolution for resin char gasified in oxygen at 470°C. 114

Figure 3.39. Micropore volume as a function of "corrected" CO evolution for Wyodak coal char gasified in oxygen at 420°C. 115

Figure 4.1. Nitrogen desorption isotherms for Pittsburgh #8 coal char samples as a function of burn-off in air at 400°C. The isotherm for the ungasified char (0% burn-off) is shown in the inset on an expanded scale. 142

Figure 4.2. Mesopore size distributions for Pittsburgh #8 coal char, as determined by the method of Roberts (1967) from the nitrogen desorption isotherm data presented in Figure 4.1. 143

Figure 4.3. Small angle neutron scattering from unactivated (0% burn-off) Pittsburgh #8 coal char: (a) dry; (b) contrast matched with deuterated toluene; and (c) difference between scattering curves (a) and (b). The straight line is the fractal fit at low q values with $D_s = 2.13$. The same curves are shown on a linear scale in the inset. 144

Figure 4.4. Guinier plot of the "dry" scattering intensity data presented in Figure 4.3 for the unactivated (i.e., 0% burn-off) Pittsburgh #8 coal char. 145

Figure 4.5. Small angle neutron scattering from Pittsburgh #8 coal char gasified to 0.8% weight loss in air at 400°C: (a) dry; (b) contrast matched with deuterated toluene; and (c) difference between scattering curves (a) and (b). A comparison of the scattering from the contrast matched ungasified and 0.8% gasified Pittsburgh #8 coal char samples is shown in the inset. 146

Figure 4.6. Small angle neutron scattering from Pittsburgh #8 coal char gasified to 0.8%, 4.5% and 13.5% weight loss in air at 400°C, dry. 147

Figure 4.7. Small angle neutron scattering from unactivated (0% burn-off) phenolic resin char (PRC): (a) dry; (b) contrast matched with deuterated toluene; and (c) difference between scattering curves (a) and (b). 148

Figure 4.8. Small angle neutron scattering from phenolic resin char (PRC) activated in air at 400°C to 21% burn-off:: (a) dry; (b) contrast matched with deuterated toluene; and (c) difference between scattering curves (a) and (b). 149

Figure 4.9. Comparison of the "dry" scattering curves for unactivated phenolic resin char and resin char activated to 21% burn-off from Figures 4.7 and 4.8. 150

Figure 4.10. A comparison of small angle neutron scattering from unactivated phenolic resin char and phenolic resin char activated in air to 21% burn-off, that have been contrast matched by mixing with deuterated toluene. The relative intensity ratios of the two curves (0%/21%) are also shown in the inset. 151

Figure 4.11. Comparison of the "difference" scattering curves for unactivated phenolic resin char and resin char activated to 21% burn-off from Figures 4.7 and 4.8. 152

Figure 4.12. Small angle neutron scattering from unactivated (0% burn-off) Wyodak coal char. 153

Figure 4.13. Small angle neutron scattering from Wyodak coal char activated to 9.2% burn-off in air at 400°C. 154

Figure 4.14. Small angle neutron scattering from Wyodak coal char activated to 32.7% burn-off in air at 400°C. 155

Figure 4.15. Small angle neutron scattering from Wyodak coal char activated to 58% burn-off in air at 400°C. 156

Figure 4.16. Small angle neutron scattering from Wyodak coal char activated to 68% burn-off in air at 400°C. 157

Figure 4.17. Small angle neutron scattering "difference" curves from Wyodak coal char as a function of burn-off in air at 400°C. 158

Figure 4.18. Comparison of nitrogen BET surface areas and Porod invariants for the difference and contrast matched SANS curves from Wyodak coal char as a function of burn-off. 159

Figure 4.19. Comparison of nitrogen BET surface areas and Porod invariants for the difference SANS curves from Wyodak coal char. 160

Figure 4.20. Schulz distribution functions for various values of b. $R_0 = 20$Å. 161

Figure 4.21. Correlation function, $\gamma(\rho)$, for the bimodal FPPS model with the following parameter set: $R_{0,1} = 10$Å; $R_{0,2} = 60$Å; $b_{1,2} = 20$; $\phi_s = 0.99999$; $\varepsilon_1 = 0.9091$. [Foster and Jensen, 1990]. 162

Figure 4.22. Scattering curve for the correlation function presented in Figure 4.20. The two distinct regions of the curve correspond to the two modes of the FPPS distribution. [Foster and Jensen, 1990]. 163

Figure 4.23. Contrast matched and difference scattering curves for unactivated PRC, and the corresponding bimodal FPPS Schulz model fits to the data. 164

Figure 4.24. Both modes of the bimodal FPPS Schulz distributions for the contrast matched unactivated PRC sample, presented on a logarithmic scale. 165

Figure 4.25. Distributions of scatterers for the contrast matched and difference scattering curves for the unactivated PRC sample. 166

Figure 4.26. Contrast matched and difference scattering curves for PRC burned-off to 21%, and the corresponding bimodal FPPS Schulz model fits to the data. 167

Figure 4.27. Distributions of scatterers for the contrast matched and difference scattering curves for the PRC sample burned-off to 21%. 168

Figure A.1. α_S-plot for nitrogen adsorption at 77K on olive stone carbon activated to 34% burn-off [Rodriguez-Reinoso *et al.*, 1987]. 179

Figure A.2. α_S-plot for Wyodak coal char gasified to 30% burn-off at 420°C in oxygen. 180

Figure B.1. Spreadsheet template for mesopore size distribution calculation for Pittsburgh #8 coal char samples burned-off to 15% in oxygen @ 470°C, according to the method of Roberts (Gregg and Sing, 1982). 182

Figure B.2. Nitrogen desorption isotherms for Pittsburgh #8 coal char samples as a function of burn-off in oxygen @ 470°C. 183

Figure B.3. Mesopore size distributions for Pittsburgh #8 coal char samples as a function of burn-off in oxygen @ 470°C, according to the method of Roberts (Gregg and Sing, 1982), using the data presented in Figure B.2. 183

Figure B.4. Nitrogen desorption isotherms for Wyodak coal char samples as a unction of burn-off in oxygen @ 420°C. 185

Figure B.5. Mesopore size distributions for Wyodak coal char samples as a function of burn-off in oxygen at 420°C, as determined by the method of Roberts (Gregg and Sing, 1982), using the nitrogen desorption isotherm data presented in Figure B.4. 186

Figure B.6. Nitrogen desorption isotherms for phenol-formaldehyde resin char samples as a function of burn-off in oxygen @ 420°C. 187

Figure B.7. Mesopore size distributions for phenol-formaldehyde resin char samples as a function of burn-off in oxygen, according to the method of Roberts (Gregg and Sing, 1982). 188

1.0. INTRODUCTION

1.1. Overview.

Porosity and porosity development in carbons and chars can control the accessibility of fluid species to their internal surface area. This potentially affects all interactions occurring within these materials. Accessibility to this surface area is governed by the pore structure morphology of the char; i.e., pore size distribution, tortuosity, intersections, shape, etc. The porosity morphology of coal chars varies over a considerable range and is determined by a large number of factors including the nature of the porosity of the precursor material prior to carbonization, the carbonization process, and extent and method of any subsequent activation or gasification.

A persistent problem in this area has been the availability of reliable and rapid techniques for characterizing the porosity of these materials, especially the microporosity. All the various methods that are currently available have significant drawbacks. For example, electron microscopy tends to be qualitative; small angle X-ray and small angle neutron scattering (SAXS/SAN) (Janosi and Stoeckli, 1979; Glatter and Kratky, 1982) can suffer from sensitivity to interpretive models, and the inability to distinguish porosity that communicates with the external surface from that which does not. High-resolution transmission electron-microscopy (HRTEM) (March *et al.*, 1982; Inners *et al.*, 1989) can provide information about pore size and shape, but such information may not be statistically representative, especially for microporosity, because of the necessarily localized nature of this technique. Mercury intrusion porosimetry (Day and Fletcher, 1988) is not suitable for micropore analysis, and the easily contaminated mercury tends to produce misleading results. Perhaps the most often used technique for porosity characterization of carbons involves physical adsorption of gases (e.g., Barrer and Bradley, 1991; Casquero-Ruiz, 1988; Seaton *et al.*, 1989; Ehrburger *et al.*, 1992; Floess *et al.*, 1992; Mittelmeijer-Hazeleger and Martin-Martinez, 1992; Laine and Yunes, 1992; Jagiello *et al.*, 1992; Agarwal *et al.*, 1990; Barton *et al.*, 1991). However, gas adsorption techniques can be quite labor-intensive and time consuming. Therefore, there is a continuing need for

new methods and approaches to supplement or even replace some of these techniques.

1.2. The Current Project.

The current project is directed at the development of a new approach to this very old problem. During the course of recent work applying temperature programmed desorption (TPD) to the determination of energetic distributions of oxygen complexes on the surfaces of oxidized coal chars (Calo *et al.*, 1989, 1991), we discovered that secondary interactions occurring within the char structure during TPD produce characteristic features in the resultant spectra that appear to be quite sensitive to char porosity. Consequently, it was proposed to develop these observations into a porosity characterization technique. This approach essentially involves the interpretation of post-activation temperature programmed desorption (TPD) spectra from oxidized chars. The results presented here show that there exist both qualitative and quantitative relationships among porosity development, rate of reaction, and post-reaction desorption features of oxygen surface complexes formed during the activation process.

The use of such a method to characterize coal char porosity is potentially attractive because the requisite data can be obtained in a single TPD experiment -- a very facile procedure. However, the unambiguous and quantitative interpretation of such data in terms of parameters that can be used to characterize coal char porosity still requires development and an improved understanding of the controlling phenomena. These issues define the primary focus of the work reported here.

The project also included the use of other techniques to characterize porosity in addition to the secondary interaction approach for the purposes of comparison, quantification, and validation. Essentially, two of the other more well established methods will be used in such a manner. Specifically, gas adsorption techniques in our own laboratory, and small angle scattering neutron scattering (SANS).

1.3. Porosity Characterization of Carbons and Chars.

1.3.1. Adsorption of Gases and Vapors.

The pore system of porous solids, including coal chars, can vary over a broad range. The individual pores may vary greatly both in size and shape within a given sample and between one sample and another. Based on the experience of adsorption chemistry, a convenient classification of pore sizes according to their average width, originally proposed by Dubinin (1960) and now officially adopted by the International Union of Pure and Applied Chemistry (1972), is summarized as follows:

Micropores: Pore width < 2 nm

Mesopores: 2 nm < Pore width < 50 nm

Macropores: Pore width > 50 nm

The micropore size range has been further subdivided into the very narrow pores, or *ultramicropores* (width < 0.5 nm), and *supermicropores* (1.0 nm < width < 2.0 nm). Micropores are considered as being about the size of adsorbate molecules and can accommodate one, two or perhaps three molecules. The mesoporosity is comprised of larger pores, and the macroporosity are transport pores to the interior of particles, and are considered as *external* surface.

When a porous solid, such as a coal char, is exposed in a closed volume to a gas or vapor at some pressure, it can adsorb the gas. Adsorption occurs due to intermolecular forces between the solid and the gas phase molecules. These forces are of two principal types: physical and chemical. Chemical adsorption, or chemisorption, involves a chemical interaction with attendant transfer of electrons between the adsorbent and the adsorbing species. The adsorbed species are bound to the surface by valence forces that are the same order of magnitude as those that hold atoms together in a molecule. Physical adsorption, or physisorption, on the other hand, arises from intermolecular forces involving permanent dipole, induced dipole, and quadrupole interactions. The forces responsible for physical adsorption, which is usually dominant at low temperature, always include dispersion forces,

which are attractive. In addition, there may be higher order electrostatic forces if either the solid or the gas is polar in nature.

The quantity of gas taken up by a solid is determined by its surface area and porosity, the temperature, T, and the pressure, P, of the gas, and the nature of both the gas and the solid. If n is the quantity of gas adsorbed expressed in moles per gram of solid, then:

$$n = f(P,T, \text{gas}, \text{solid}) \qquad [1.1]$$

For a given gas adsorbed on a particular solid maintained at a fixed temperature, Eq. [1.1] simplifies to:

$$n = f(P)_{T,\ \text{gas},\ \text{solid}} \qquad [1.2]$$

If the temperature is below the critical temperature of the gas, the alternative form :

$$n = f(P/P^{\circ})_{T,\text{gas},\text{solid}} \qquad [1.3]$$

is more useful, where P° is the saturation vapor pressure of the adsorbate.

Eqns.[1.2] and [1.3] are expressions of the adsorption isotherm; i.e., the relationship, at constant temperature, between the amount of gas adsorbed and the pressure, or relative pressure of the gas, respectively.

The isotherms which result from gas/vapor adsorption may be grouped into five classes (see Figure 1.1), as originally proposed by Brunauer, Deming, Deming and Teller (BDDT) (1940), and Brunauer, Emmett and Teller (BET) (1938). The stepped isotherm, designated as Type VI, although rare, was later added to this classification system due to a particular theoretical interest it inspired. Most of the adsorption isotherms encountered in practice fall into the six categories, but there are certainly other cases that are more difficult, if not impossible, to classify.

Adsorption in a microporous solid typically results in an isotherm of Type I. A type I isotherm is characterized by a plateau which is horizontal or nearly so above a certain value of relative pressure. It may also exhibit a "tail" as P/P° approaches unity. The physical adsorption of gases by nonporous solids in the vast majority cases gives rise to a Type II isotherm. The mesopore range of pore size is usually taken to be that range which yields a Type IV isotherm. In the low pressure region, a Type IV isotherm is qualitatively similar to the Type II isotherm. However at a certain point, it begins to deviate upwards until at higher pressures its slope decreases. Both Type II and Type IV isotherm are amenable to surface area determinations, provided no special complications occur. One standard technique used is nitrogen adsorption at its boiling point temperature of -196°C. Pore size distributions are routinely obtained from Type IV isotherms using Kelvin equation. The Kelvin equation is used to relate the equilibrium vapor pressure of adsorbate to the radius of a pore filled by the condensed adsorbate:

$$\ln (P/P^{\circ}) = - (2\gamma V_1/RT\, r_m) \cos \theta \qquad [1.4]$$

where r_m is the radius of curvature of the adsorbed film (pore radius minus thickness of the adsorbed film), γ and V_1 are the surface tension and molar volume of the liquid adsorbate, respectively, and θ is the wetting angle.

Type III and Type V isotherms are characteristic of weak gas-solid interactions, and they do not occur as frequently as the other types. Type III isotherms are usually exhibited by nonporous or macroporous solids, and the Type V isotherm by mesoporous or microporous solids. The weakness of the absorbent-adsorbate interaction causes the uptakes at low relative pressures to be small; however, once a molecule has become adsorbed at a primary site, the adsorbate-adsorbate force promote further adsorption in a cooperative process. Therefore these two isotherms are convex towards the relative pressure axis.

The micropores constitute the largest portion of the internal surface of an activated carbon, as

well as some coal chars. Consequently, most of the adsorption takes place within them. Their size prevents capillary condensation and they can be filled with the adsorbate at low relative pressures. Since activated carbons are not crystalline, their microporous structure cannot be studied by broad angle X-ray diffraction. Also transmission electron microscopy techniques alone do not seem to be satisfactory enough at the present stage of development. Consequently, the adsorption of gases arguably remains the best currently available method for the characterization of the porous structure of activated carbons.

In Figure. 1.2 are presented the three types of adsorption isotherms that are typically found in microporous carbons (Rodriguez-Reinoso, 1986). Isotherm (a) corresponds to a carbon that is exclusively microporous. Since only narrow micropores are present in this carbon, once they are filled with adsorbate, the amount taken up by the solid does not increase at higher relative pressure, thereby producing a well-defined plateau parallel to the relative pressure axis. Isotherm (b) corresponds to a carbon with a wider micropore size distribution. Carbons exhibiting isotherm (b) have narrow micropores which are responsible for the steep initial branch, and wider micropores which give a more rounded or gradual approach to the plateau.

If significant mesoporosity exists in addition to the micropores, a carbon can exhibit isotherm (c). A large and widely distributed microporosity is accompanied by a well-developed mesoporosity, so that the linear branch at higher relative pressures is no longer parallel to the relative pressure axis.

Because a number of conditions have to be met, the number of gases which are suitable adsorbates for porosity characterization is severely limited. For example, the adsorbate must be chemically inert towards the solid; and the saturation vapor pressure, P_0, at the working temperature must be large enough to allow accurate measurement of the relative pressure over a reasonably wide range. In practice, nitrogen, argon, krypton, xenon, n-butane, benzene, oxygen, carbon dioxide and the lower molecular weight alkanes have been widely used for surface area determination.

There have been many reports on studies of adsorption and corresponding pore structure determination in microporous carbons using various adsorbates. Among these, nitrogen is the most

common adsorbate used in the characterization of coal char. It is believed to belong to the class of gases that adsorb non-specifically on most solid surfaces [Barrer (1966), Kiselev (1965)] (i.e., without other than dispersion and repulsion forces involved). Bradley [1991], Casquero-Ruiz [1988], Seaton *et al.* [1989], Ehrburger *et al.* [1992], Floess *et al.* [1992], Mittelmeijer-Hazeleger and Martin-Martinez [1992] and Agarwal *et al.* [1990] were among a number of workers who used nitrogen to study pore structures in chars.

Another widely used adsorbate is carbon dioxide. For example, Medek [1976] reported the possibility of micropore analysis of coal and coke from carbon dioxide isotherms. Ehrburger *et al.*, [1992], Mittelmeijer-Hazeleger and Martin-Martinez [1992], Agarwal *et al.*, [1990], also used carbon dioxide to analyze carbon porosity. Argon [see Laine and Yunes (1992), Mittelmeijer-Hazeleger and Martin-Martinez (1992)], helium [Floess *et al.*, (1992)], xenon [Cochrane (1967)], methane [Jagiello *et al.* (1992), Agarwal *et al.* (1990)], ethane, ethylene, propane [see Agarwal *et al.* (1990)], n-butane [Mittelmeijer-Hazeleger and Martin-Martinez (1992)], water vapor [Barton *et al.* (1991)] have also been used to study the structure and physical properties, such as entropies and heats of adsorption, of carbons and chars.

1.3.2. Techniques for Micropore Characterization.

1.3.2-1. The Langmuir Equation. The Type I isotherm, which is typically exhibited by microporous solids, was typically assumed to follow the Langmuir equation (1918), which has the form of:

$$P/n = 1/(Bn_m) + P/n_m \qquad [1.5]$$

where B is an adsorption coefficient which depends on the specific adsorbate-adsorbent system. From this expression, a plot of P/n as a function of P should yield a straight line of slope $1/n_m$. If the surface area occupied by the adsorbed molecule, a_m, is known, the surface area can be determined from:

$$S = n_m a_m N_{av}, \qquad [1.6]$$

where S is specific surface area (i.e., the surface area per gram), a_m is the average area occupied by an adsorbate molecule in the completed monolayer, N_{av} is Avogadro's number, and n_m is the amount of adsorbate per gram of adsorbent.

In practice, however, the degree of conformity to the Langmuir equation varies considerably. In some cases, the calculated values of specific surface area are improbably high (Gregg and Sing, 1982). Part of the reason for the failure of the Langmuir equation is that it is based on the assumption that the heat of adsorption does not change with coverage; but, in some systems, the heat of adsorption varies with the amount adsorbed. More importantly, however, the Langmuir equation was originally derived to describe monolayer adsorption on an open surface; i.e., on a nonporous solid. But in very fine pores, such as micropores, the mechanism of adsorption is pore filling rather than surface coverage. Thus, the plateau of the Type I isotherm represents volumetric filling of the microporosity by the adsorbate in a process similar to, but not identical with capillary condensation, rather than a layer-by layer build-up of an adsorbate film on the pore walls.

1.3.2-2. The BET Equation. The best known, and perhaps the most used equation for the analysis of surface area is that of Brunauer, Emmett, and Teller (1938), derived for multilayer adsorption (i.e., the BET equation):

$$\frac{P}{n\,(P - P^\circ)} = \frac{1}{n_m C} + \frac{(C-1)P}{n_m\, C\, P^\circ}, \qquad [1.7]$$

where n_m is the specific amount of adsorbate per gram of adsorbent in a monolayer, n is the total amount of adsorbate per gram of adsorbent at the equilibrium pressure, and $C = P^\circ B$, is a constant. According to Eq.[1.7] a plot of $P/n(P^\circ - P)$ *vs.* P/P° should be a linear with a slope of $[(C-1)/n_m C]$,

and an intercept of $1/n_mC$, from which the values of n_m and C can be calculated.

The BET equation is often applied to the analysis of adsorption in microporous solids. However its use is subject to severe limitations. For some activated carbons, for example, the resultant values of surface area can be unrealistically high, as is also the case for the Langmuir equation. This is because the BET treatment is based on the same kinetic model as the Langmuir equation; it is essentially an extension of the Langmuir approach to multilayer adsorption. Consequently, the BET expression shares some of the same limitations as the Langmuir equation when applied to the analysis of adsorption in microporous solids.

1.3.2-3. The Dubinin-Radushkevich (DR) Equation. The concept of mono- or multilayer surface coverage is of questionable validity in micropores, since a mechanism of pore filling appears to be a better description of adsorption in micropores. Dubinin and Radushkevich [1947, 1965] put forward an equation for the estimation of the micropore volume for the low- and medium-pressure regions of adsorption isotherms. These workers adapted Polanyi's [1914] theory of adsorption in their treatment and, assuming a Gaussian pore size distribution, derived the following relation:

$$\ln V = \ln V_o - D \ln^2(P/P^\circ), \qquad [1.8]$$

where V is the amount of adsorbate taken up, expressed as a liquid volume ($V = n M/\rho_l$, where ρ_l is the density of the bulk liquid adsorbate), V_o is the total volume of micropores, and D is a constant dependent on the pore structure and temperature. From Eq. [1.8], the DR plot of ln V *versus* $\ln^2(P/P^\circ)$ should be linear with an intercept equal to the total micropore volume, $\ln V_o$. It should be emphasized that only the volume of micropores, and not the specific surface area, can be determined from the Dubinin-Radushkevich equation.

1.3.2-4. Standard Isotherm Methods. One particularly useful class of methods for characterizing microporosity is based on comparison of an experimental isotherm to a *standard isotherm.* For example, the α_s-plot method belongs to this class. These methods are based on the

observation that 77K nitrogen isotherms for a number of typical porous solids can be represented by a single curve (Shull, 1948). Similar findings have been reported by several other workers (Cranston and Inkley, 1957; Pierce, 1959). This led to the idea of a standard isotherm.

Perhaps the best known of the *standard isotherm* methods is the t-plot method of Lippens and de Boer (1964, 1965), which provides a simple and direct method of comparing the shape of the adsorption isotherm of a sample with that of a standard isotherm. A t-plot is a plot of the amount adsorbed on the porous adsorbent *vs.* t, the corresponding multilayer adsorbate thickness on the standard nonporous solid, where $t = (n/n_m)\, s$, in which s is the thickness of a single molecular layer and n_m is the amount of adsorbate per gram of adsorbent in the monolayer, which is determined from the BET equation.

The dependence of the t-plot method on the evaluation of n_m from the BET equation for the standard isotherm has been criticized (Dubinin, 1966, and Pierce, 1968). In order to avoid this problem, Sing (1970) proposed to replace n_m as the normalization factor by n_s, the amount adsorbed at some fixed relative pressure; in practice usually taken as $P/P^\circ = 0.4$. The reduced isotherm on the nonporous reference solid is, therefore, arrived at empirically, and not *via* the BET monolayer capacity. The normalized adsorption $n/n_{0.4}$ ($= \alpha_s$) obtained on a reference sample of solid, is then plotted against P/P° to obtain a standard α_s-curve. The α_s-curve can then be used to construct an α_s-plot from the isotherm of a test sample of the solid. In most cases, α_s-plots have the same form as t-plots. But unlike the situation with the t-plot method, they can be used on all types of adsorption isotherms, provided that the isotherm is linear at low relative pressures. On the other hand, if the area of the reference adsorbent is determined without resorting to the BET equation (by transmission electron microscopy, for example), the α_s-plot method becomes independent of the BET theory.

Although activated carbons are predominantly microporous, and, therefore should be characterized by micropore volume, some carbons may also possess important mesoporosity, and perhaps even macropore contributions to the total porosity. Therefore it is necessary to separate adsorption in micropores from that on the nonmicroporous surfaces in order to determine the

external surface area. The t- and α_s-plot methods can both be used for this purpose.

The concept of a standard isotherm implies that solid surfaces, when free of the complications of adsorption in pores, adsorb to equal extents of surface coverage at constant relative pressure. This means that the t- or α_s-plot will then be a straight line passing the origin with a slope equal to V_m/s (where s is the thickness of a monolayer), which is proportional to the surface area of the solid. If the specific surface area of the reference material is known, the specific surface area of the test sample can be calculated from the ratio of the two slopes of the α_s-plots for the reference and test samples. The use of t- and α_s-plot methods for characterization of microporous carbons is based on the assumption that the adsorption in the micropores is complete before it begins on the rest of surface, and that mesoporosity, in which capillary condensation occurs, exhibits an upward deviation in t- and α_s-plots following completion of micropore filling.

The effect of microporosity on the isotherm and t- (or α_s-) plot is indicated in Figure 1.3. The slope of the α_s-plot passing through the origin, provides a measure of the total surface area of the solid. If the surface area of the reference adsorbent (A_r) is known, the surface area of the sample (A_a) may be calculated from the ratio of the slopes of the initial linear portion of the α_s-plot from the sample and the reference: A_a = (sample slope/reference slope) x A_r. The intercept on the adsorption axis of the extrapolated linear branch is related to the micropore volume; when converted to a liquid volume, it may be taken as equal to the micropore volume itself. When mesopores exist (in addition to micropores), the plot will show an upward deviation at high relative pressures. The slope of the linear branch will then be proportional to the area of the mesopore walls together with the external surface area.

The α_s-plot method has been widely used by workers to analyze microporous carbons. Lecloux and Pirard (1979) reported on the importance of a standard isotherm in the analysis of isotherms for determination of the porous texture of various solids. More recently, Casquero-Ruiz *et al.* (1988), Ehrburger *et al.* (1992) and Mittelmeijer-Hazeleger (1992) have reported results for microporous carbons using the α_s-plot method. The use of a standard isotherm as a tool to

characterize porosity may be limited by the appropriate choice of a reference material. Gregg and Sing (1982) have suggested that the chemical nature of the sample and the reference should be the same. According to de Boer (1965), the t-curve is independent of the chemical nature. Rodriguez-Reinoso *et al.* (1987) have proposed a standard adsorption isotherm for the characterization of activated carbons.

In the current project, the α_s-plot method was used for porosity characterization. Nitrogen adsorption isotherms were analyzed by the α_s-plot method for determination of surface area and pore volume of char samples.

1.3.3. Pore Size Distributions.

1.3.3-1. Micropore Size Distributions. Distributions of pore sizes can also be determined from adsorption isotherms. For example, the DR equation (Eq. [1.8]) can be differentiated to produce a pore size distribution. However, for microporous materials with heterogeneous distributions or strongly activated carbons, such as may be encountered with some coal chars, the DR equation does not characterize the adsorption isotherm very well. A more generalized form of the DR equation, known as the Dubinin-Astakhov (DA) equation has been shown to provide improved fits to adsorption isotherms for such materials (Stoeckli, 1990):

$$\ln V = \ln V_o - [-RT \ \ln(P/P^\circ)/E]^n, \qquad [1.9]$$

where the exponent, n, which is equal to 2 in the DR equation, is a fit, non-integer value, typically between 1 and 2. The DA equation requires the parameters n and E (a characteristic energy) to be determined by fitting the nonlinear expression to adsorption isotherms in the low relative pressure, micropore region. These values are then used in the differentiated form of the DA equation to provide a pore size distribution.

Many pore size distribution methods are derived from the Kelvin equation which describes the process of capillary condensation. Some workers, however, have questioned the validity of the

capillary condensation approach in the close confines of micropores. For example, the Horvath-Kawazoe (HK) method (Horvath and Kawazoe, 1983) expresses the adsorption potential within slit-like micropores as a function of effective pore width, r, independent of the Kelvin equation. This potential can then used to provide the quantity RT $\ln(P/P^{\circ})$ to substitute in the DR equation, which can then be differentiated with respect to pore width to provide a pore size distribution. Being independent of the Kelvin equation, the HK method has been thought to be one of the more realistic methods for the determination of pore size distributions for materials with slit-shaped micropores. Recently, however, the validity of this approach has also come into question. Kruk *et al.* (1997) have shown that for nitrogen adsorption into slit-like pores at 77K, the HK method erroneously attributes monolayer formation on pore walls to the presence of non-existing 0.6 nm micropores. Therefore, the method would be expected to yield incorrect results (i.e., artificial peaks and improper pore volumes) for samples possessing significant amounts of micropores wider than about 0.9 nm. The authors concluded that the validity of the HK method is restricted to samples with narrow micropores (width < 0.9 nm). The authors also concluded that a density functional theory (DFT) approach (Evans *et al.,* 1986) is more valid for these types of materials.

The DFT approach accounts for the fact that adsorbed molecules tend to pack according to the strength of both surface forces and interactions with other molecules. That is, molecules adsorbed within small pores cannot pack as efficiently as those found within large pores. Consequently, their molar density varies as a function of pore size. In order to incorporate this expected variation, an experimental adsorption isotherm can be interpreted in terms of a Generalized Adsorption Isotherm (GAI), which describes the total isotherm as the sum of individual, single-pore isotherms, multiplied by their relative distribution over a range of pore sizes. The DFT method derives sets of these isotherms using the local mean-field molar density approximation. The pore size distribution is determined by solving the GAI equation numerically.

For the most part, the DFT method has been applied to microporous carbons *via* nitrogen adsorption at 77K (Seaton *et al.,* 1989; Russel and LeVan, 1994). Currently, this method seems to

be the most preferred for this application. However, the numerical solution of the GAI equation requires a relatively large number of data points. Therefore, it is most conveniently applied using adsorption isotherms generated with automated systems.

In the current work, adsorption isotherms were determined with a Quantachrome Quantasorb flow BET apparatus, which did not have the accuracy to determine large densities of points in the relative pressure region representative of the micropores (i.e., the "knee" of the Type I isotherm). Consequently, pore size distributions in the micropore size range could not be determined from the measured adsorption isotherms with the preceding methods.

1.3.3-2. Mesopore Size Distributions. Mesopore size distributions are typically made by assuming cylindrical pore geometry and applying the Kelvin equation:

$$r_K = -2\,\gamma\,V_m/[RT\,\ln(P/P^\circ)], \qquad [1.10]$$

where r_K is the Kelvin radius of the pore, γ the surface tension of nitrogen at its normal boiling point (8.85 ergs/cm^2) at 77K), and V_m is the molar volume of liquid nitrogen (34.7 cm^3/mol). The Kelvin radius, r_K, is the radius of the pore in which condensation occurs at a relative pressure P/P°. Prior to condensation, however, some adsorption has to take place on the pore walls, and thus r_K does not represent the true pore radius. Consequently, during desorption, an adsorbed layer remains on the pore walls when evaporation occurs, and the actual pore radius, r_p, is given by:

$$r_p = r_K + t, \qquad [1.11]$$

where t is the thickness of the adsorbed layer.

Various methods have been proposed for determining the adsorbed layer thickness, t (Gregg and Sing, 1982, p. 132 *et seq.*). In the current work, we have used a method proposed by Roberts (1967), as subsequently modified by Gregg and Sing (1982), since it does not explicitly depend on

pore length and surface area, as some of the other methods do. This approach belongs to the general class of methods which allow for film-thinning during the evaporation or desorption process, which Gregg and Sing (1982) contend is of first order importance. The latter authors allowed for a more even spacing of the groupings of pore sizes than those originally used by Roberts (1967). They used 13 groups of pore sizes ranging from 100Å down to 17Å.

Using this approach, the procedure for determining a pore size distribution from desorption isotherm data translates nicely into a spreadsheet calculation, as presented in Appendix B.

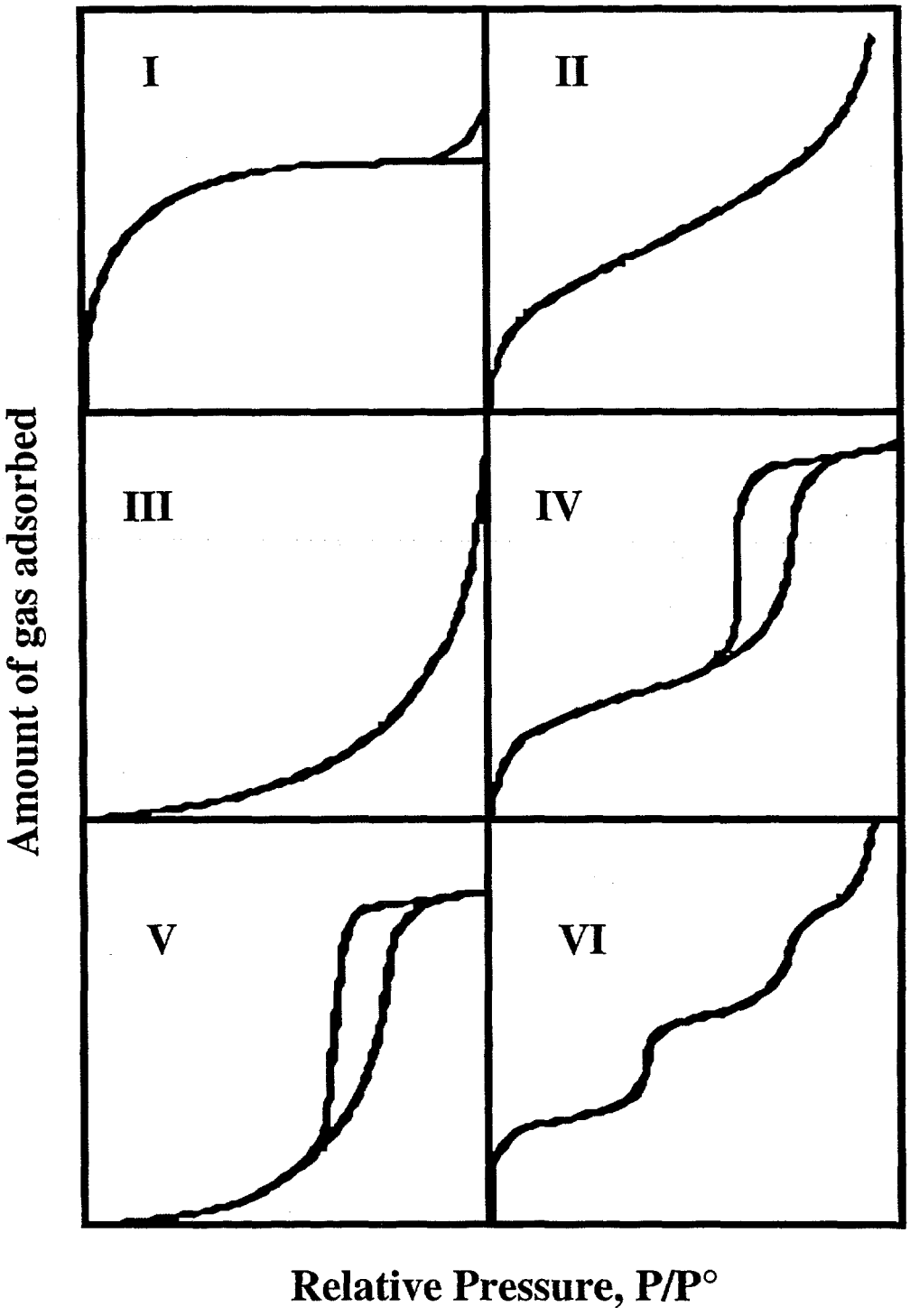

Figure 1.1. The five types of adsorption isotherms, I to V, according to the classification scheme of Brunauer, Deming, Deming and Teller [1940], together with Type VI stepped isotherm.

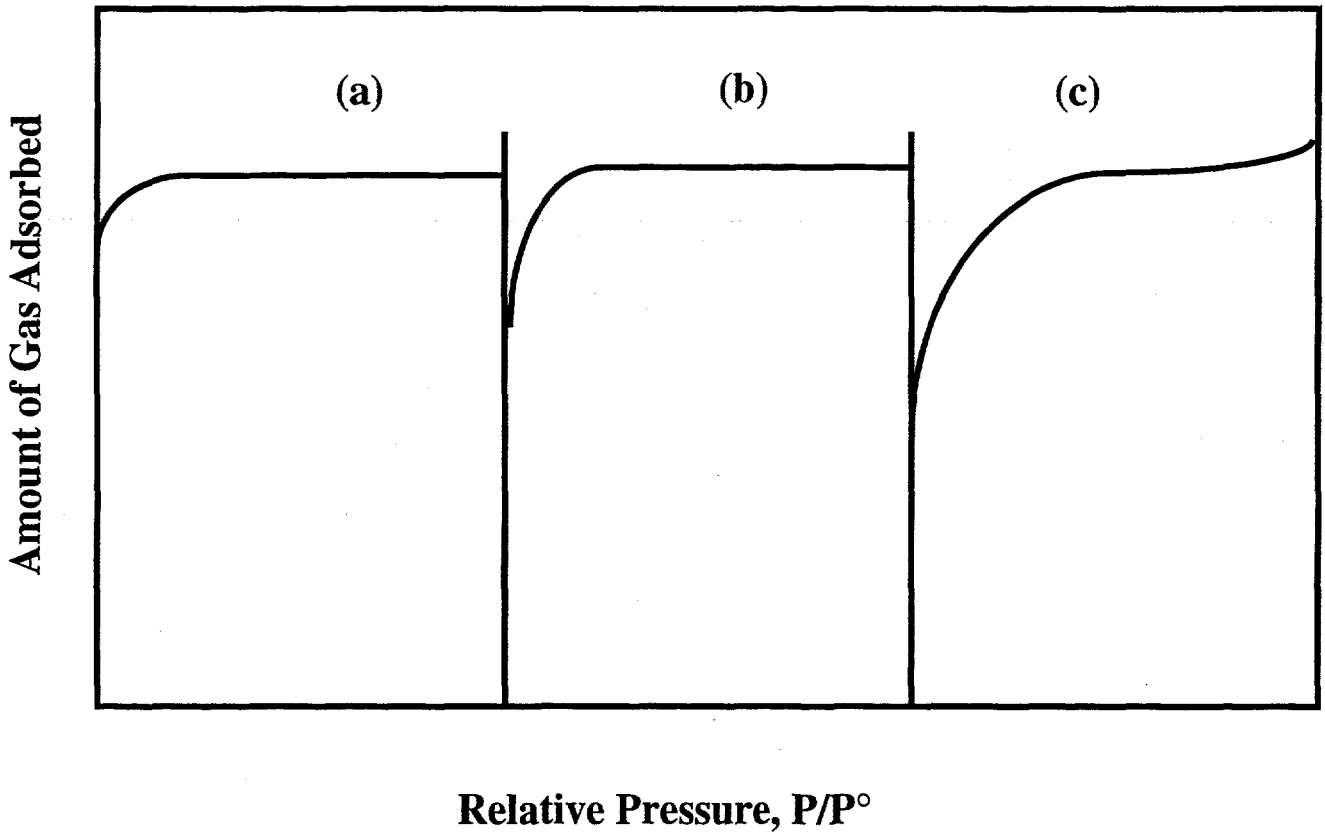

Figure 1.2. Three different types of isotherms found most often for microporous chars (see text) [Rodriguez-Reinoso, 1986].

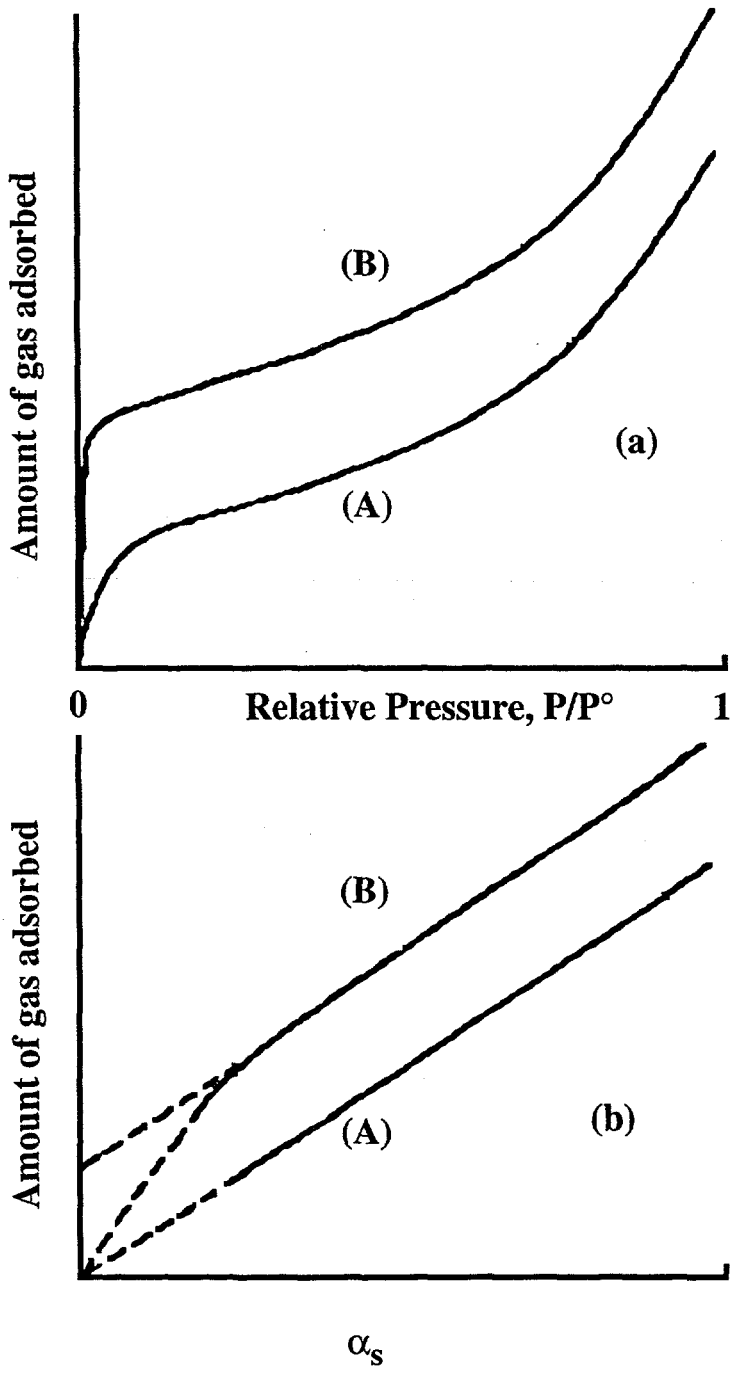

Figure 1.3. Effect of microporosity on the isotherm and α_s-plot. (a) (A) is the isotherm of a non-porous adsorbent, and (B) is the same solid with additional microporosity. (b) An α_s-plot corresponding to the isotherms of (a). (schematic only) [see Gregg and Sing, 1982].

2.0. EXPERIMENTAL

2.1. Char Samples.

2.1.1. General Sample Characteristics.

The precursors of the char samples used in the project were Wyodak subbituminous coal and Pittsburgh #8 bituminous coal, obtained from the Argonne Premium Coal Sample Bank (Vorres, 1993), and a phenol-formaldehyde resin synthesized in our laboratory. The latter was used as a prototype of a non-mineral matter-containing sample.

The Wyodak coal samples were collected about 6 miles northeast of St. Louis (St. Clair County) in December 1985. The sample consisted of a 6-inch core sample through the entire seam. Wyodak is a subbituminous coal, and its composition of Wyodak coal is presented in Table 2.1. The composition of the ash in Wyodak coal is presented in Table 2.2. As shown, Al_2O_3, SiO_2, CaO, and Fe_2O_3 are the principal impurities.

The Pittsburgh #8 coal samples were collected about 60 miles south and west of Pittsburgh in Greene County, Pennsylvania, in March 1986. Pittsburgh #8 is a high volatile bituminous coal, and its composition is presented in Table 2.1. The mean ash composition is presented in Table 2.2. As shown, Al_2O_3, SiO_2, and Fe_2O_3 are the principal impurities.

2.1.1-1. Phenol-Formaldehyde Resin. The overall synthesis process for phenol-formaldehyde resin can be represented as:

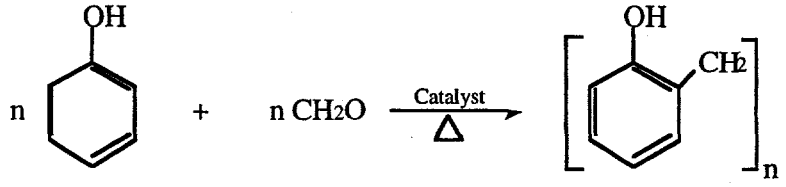

phenol formaldehyde resin

The following procedure was followed in performing the synthesis (Wojtowicz, 1987). 150g of phenol were mixed with 500 ml of 40% vol. solution of formaldehyde (40g of formaldehyde in 100 ml of solution) in a 1 liter flask, which corresponds to a formaldehyde/phenol molar ratio of

4.33. 50 drops of 30% NH_4OH were added as a catalyst. The flask was connected to a reflux condenser and heated in a hot water bath until the contents of the flask were milky in appearance (about 16 hour). In order to avoid oxidation during the condensation reactions, the flask was continuously flushed with argon. The flask was then cooled down (still under flowing argon). After about 24 hours, two phases were clearly discernible in the liquid. The upper phase (water + methanol + unreacted formaldehyde) was decanted, and the catalyst in the lower phase (resin) was neutralized by adding about 30 drops of glacial acetic acid. The resultant creamy, resinous material was thoroughly washed with distilled water and dissolved in acetone.

The curing procedure for the resultant phenol-formaldehyde resin involved: (a) 2 hours at 60°C in vacuo; (b) 12 hours at 120°C in vacuo; followed by (c) 2 hours at 30°C in helium. Steps (a) and (b) were carried out in a vacuum oven, whereas a tube furnace was used for the last step.

Resin char samples were prepared by pyrolyzing the cured resin at high temperature. The elemental composition of phenolic resin chars pyrolyzed at different temperature, as determined by Wojtowicz (1987), is presented in Table 2.3.

2.1.2. Char Preparation.

Carbonization (pyrolysis) was performed in a tube furnace (Lindberg Co., Inc.). The pyrolysis temperature and heating rate were controlled with a digital controller. A quartz tube, 3.2 cm ID. and 76 cm long, was located in the heating zone of the furnace. A ceramic boat containing 3-4 g of sample was placed at the center of the quartz tube. After purging with ultrahigh purity helium for at least one hour at a flow rate of about 50 ml/min, the furnace was heated to the desired pyrolysis temperature (850°C to 1000°C) at a heating rate of about 20°C/minute. Following the completion of the pyrolysis procedure, the sample was cooled down in flowing helium. The resultant chars were ground if necessary, and sieved to -16 to +100 mesh.

2.1.3. Char Demineralization.

Some of coal and char samples were demineralized using a method similar to that described by Morgan and Jenkins (1981). The general procedure is as follows.

The coal or char sample was treated with a mixed 5N HCl and 29N HF acid for two hours at 50-60°C in a covered teflon beaker. The cover was then removed to allow all the liquid to evaporate until the sample was nearly dry. About 5 ml of 12N HCl and 10 ml of distilled water were added to the sample and mixed well. The sample was then filtered in a vacuum filtration system. The sample was then rinsed several times with distilled water until the sample was pH neutral. The sample was then dried in a vacuum oven at 60-70°C.

For Wyodak coal samples, atomic absorption (AA) spectroscopy measurements (see Table 2.4), indicate that 81% of the calcium and 86% of the iron was removed using this procedure.

2.2. Char Characterization by Gas Adsorption Techniques.

2.2.1. Nitrogen Isotherms.

Multipoint adsorption isotherms were determined for the various char samples with a Quantasorb Surface Area Analyzer (Quantachrome Corp.). A schematic of the gas flow circuit for this instrument is presented in Figure 2.1. Nitrogen at 77K was used as the adsorbate, and helium as the carrier gas. In most cases, a total flow rate of 20 cm^3/min was adequate for the measurements. Table 2.4 presents the relative pressure, P/P°, values and the corresponding N_2 and He flow rates.

The experimental procedure was as follows:

(1) The sample is first outgassed at 150°C for 1 hour in the outgassing station.

(2) The nitrogen flow rate is set to the desired P/P° value and the sample U-tube is immersed in a liquid nitrogen-filled dewar.

(3) The sample is equilibrated at this flow rate for about 10 - 15 minutes. The "Ads/Des" switch is changed to "Des", and the liquid nitrogen dewar is removed and the sample U-tube is immersed in a beaker of room temperature water. When the desorption is complete, the integrator number is recorded.

(4) The desorption data are calibrated using the precision gas sampling syringes to withdraw gas samples from the "OUT" septum and inject them into the "IN" septum. The volume injected and

the corresponding integrator readings are recorded. The calibration value should agree with the sample desorption signal within ±15%. This will prevent any error due to nonlinear detector response. If the agreement is poor, the injection volume is changed until the criterion is satisfied.

(5) After finishing the calibration, the "Ads/Des" switch is changed to "Ads"; the sample cell is immersed in the liquid nitrogen dewar at the same P/P° value. The adsorption signal is recorded.

(6) In order to generate an isotherm, the P/P°is then changed to a lower value, and the preceding steps are repeated for each value of P/P°.

From these data, the isotherms can be constructed, and surface areas and pore volumes can be determined. As an example, Figure 2.2 is the desorption isotherm of a Wyodak char sample gasified in oxygen at 420°C to 30% burn-off.

2.2.2. Pore Size Distributions.

As indicated in Section 1.3.3-1, adsorption isotherms were determined with a Quantachrome Quantasorb flow BET apparatus, which did not have the accuracy to determine sufficiently high densities of points in the relative pressure region representative of the micropores (i.e., the "knee" of the Type I isotherm). Consequently, pore size distributions in the micropore size range could not be determined from the measured adsorption isotherms with the preceding methods.

Mesopore size distributions, however, were determined from nitrogen desorption isotherms for the various chars in the current study, using the method of Roberts (1967), as subsequently modified by Gregg and Sing (1982). In this method, the pore system in the mesopore size range is divided into 13 groups, in order to achieve a fairly uniform spacing in relative pressure, from mean pore radii of 100Å to 17Å. Allowance is made for the progressive thinning of the multilayer adsorbate in each pore as desorption proceeds. The calculation can be efficiently performed in a tabular format. Consequently a spreadsheet template was developed for this purpose. An example of the resultant template for a Pittsburgh #8 sample burned-off to 15% is presented as Appendix B.

2.3. Temperature Programmed Desorption-Mass Spectrometry/Thermogravimetric Analysis (TPD-MS/TGA) System.

2.3.1. TPD-MS/TGA Apparatus.

An experimental system was developed for the current work which was designed to operate both as a TGA and as a TPD apparatus. In this manner, samples could be prepared, oxidized, and thermally desorbed without ever exposing them to the ambient atmosphere.

A schematic of the TPD-MS/TGA apparatus is presented in Figure 2.3. This apparatus consists of five principal parts: (1) a gas flow/metering system which provides the oxidant gas and an inert carrier gas to convect away desorbed species from the vicinity of the char sample during TPD; (2) a Cahn D-200 digital recording microbalance; (3) a reactor where the sample is subjected to gasification and/or to the controlled heating program for desorption of surface species; and (4) a detector for evolved species during TPD; and (5) a computer and application software to control the operation of the entire system and to record the data.

A three-way ball valve, a flow meter, and an eight-port, zero dead volume rotary chromatography valve were connected to the gas flow/metering system. The three-way valve enables the selection of either inert carrier gas or reactant gas flow into the reactor. The flow meter and the rotary valve were installed in the inert carrier gas feed line. The former was used to control the flow of inert gas, and the latter was connected to a 0.5 cm^3 calibration sample loop used to calibrate the mass spectrometer. The carrier gas bypasses the sample loop except during the calibration procedure.

The digital recording microbalance, which is used to monitor the sample mass change, is enclosed in an aluminum cap. This cap was machined to minimize the dead volume inside the balance assembly, and to decrease the residence time of flowing gases. The reactor is a quartz hangdown tube connected to the balance assembly beneath the cap by an Ultratorr™ connector. Char samples are loaded in a quartz bucket and suspended inside the quartz hangdown tube from a Nichrome wire connected to the microbalance. The reactor is enclosed by a furnace constructed for this purpose. Power to the furnace is provided by a high current Variac autotransformer. The Kanthal alloy wire-wound furnace allows linear heating rates up to 200K/min to 1200°C.

The detection of desorbed species is by means of a quadrupole mass spectrometer (MS). Computer software was developed to automatically switch the mass spectrometer among four selected mass numbers during the course of a TPD experiment. For the current applications, normally masses m/e=18, 28, 32 and 44, corresponding to H_2O, CO, O_2, and CO_2, respectively, were monitored during the course of an experiment.

The electron energy and ion source voltages of the mass spectrometer were tuned in order to have sufficient sensitivity to detect low levels of CO and CO_2. Tests showed the existence of some cracking of CO_2 to CO^+ upon electron impact. The relative sensitivity of the mass spectrometer to CO and CO_2 and the CO_2 "cracking factor" were determined by injecting a calibration gas mixture of 48/52 mol % CO/CO_2 and pure CO_2 separately. The levels of the two peaks for each gas injected were recorded and the averaged background for each peak was subtracted from these values. The method used to calculate the relative sensitivities of CO and CO_2, the CO_2 "cracking factor," and a simple FORTRAN program to calculate these values from the known calibration data are presented in Appendix C. The MS signals during TPD were converted to an absolute basis from these calibration data.

A Macintosh IIcx microcomputer with a MacADIOS Jr. 625 interface was used to control the experimental system and record the data. All the control software was written in Microsoft QuickBASIC™. The data recorded were time, temperature, pressure, and electrometer signal from the mass spectrometer.

2.3.2. Experimental Tests and Results.

The following tests were performed on the apparatus in order to characterize its behavior.

2.3.2-1. Reactor Temperature Profile. As shown in the schematic of the TPD-MS/TGA reactor presented in Figure 2.4, the length of the furnace was about 22 cm, and the sample bucket was located in the center of the furnace, about 11 cm from the top. A thermocouple probe (Type R) was located immediately beneath the bucket. One major concern was whether the thermocouple reading accurately reflected the sample temperature. Consequently, the temperature profile in the

reactor tube was measured. As shown in Figure 2.5, the temperature difference between the final location of the thermocouple probe and the bucket was less than 0.5°C. Therefore, it was concluded that the thermocouple accurately measured the sample temperature.

2.3.2-2. Heating Rate Program. The sample temperature was measured using a Type R thermocouple. It is important to use accurate relationships in the application software to calculate corresponding temperatures from the digital voltage readings recorded using the microcomputer. The resultant expressions for the voltage-temperature relationships are listed in Table 2.5.

The power to the furnace is provided by means of a high current Variac autotransformer. The power input is controlled by the furnace control program *via* a solid state relay. One important objective of the control program was to achieve a linear ramp for temperature programmed desorption experiments. Since the temperature increase is not proportional to the applied power, to find the best relationship between the temperature variation and the power input was somewhat difficult, especially in the low temperature range (usually below 400°C), where temperature "overshoot" was more likely to occur. The key factor to achieving good linear behavior was power control of the Variac autotransformer. The power input to the furnace was determined as a function of the setting temperature and the difference between the actual measured temperature and the set point temperature. Many tests were performed, and different expressions for the relationship between the power input and temperature were used in order to achieve a linear temperature ramp at various heating rates. Figure 2.6 presents the temperature programs corresponding to a few different heating rates. These data show nearly perfect linear behavior above 400°C, where the bulk of the desorption behavior typically occurred.

2.3.2-3. Effect of Reactor Pressure on TPD Results. It was desirable to use a low carrier gas pressure in the reactor in order to maintain a high sensitivity for the CO and CO_2 product gases during TPD. The most important aspect of achieving this condition was keeping the system oxygen-free. Another concern was the effect of pressure on the TPD spectra. Since the pressure inside the reactor is a function of inert carrier gas flow rate, and upstream and downstream pressure,

it was essential to insure that these parameters were kept the same for each experiment in a series of runs if the total pressure had an effect the TPD spectra.

Wyodak coal char gasified in oxygen at 380°C to 10% burn-off and resin char gasified in oxygen at 470°C to 10% burn-off were tested at different reactor pressures. Figure 2.7 presents the TPD spectra at different helium carrier gas pressures from 25 torr to 100 torr for the resin char samples. As can be seen, the reactor pressure does not affect the TPD results for these samples.

Corresponding data are presented in Figure 2.8 for the gasified Wyodak coal char samples. As shown, these spectra exhibit two distinct maxima in the rate of production of CO. The lower temperature maximum does not change with the carrier gas pressure, but the higher temperature maximum appears to decrease with the carrier gas pressure. Figure 2.9 presents a comparison of TPD spectra between a natural Wyodak coal char sample and a demineralized Wyodak coal char sample. As shown, the first maximum in the CO production rate are the same for both samples. This suggests that the second maximum rate of CO production for the natural Wyodak coal char is apparently related to the mineral matter. Since apparently the reactor pressure can affect TPD results for samples containing mineral matter, it is important to keep the experimental conditions constant in each series of TPD runs.

Another concern was the effect of the carrier gas pressure on the temperature measurement. The experimental data (*cf.* Figures 2.7 and 2.8) show that the corresponding desorption peaks are located at the same temperature at a heating rate of 50K/min for the four different pressures. This result indicates that even at the lowest carrier gas pressure of 25 torr, the temperature measurement was not affected. This is due to the fact that the heating rates employed were sufficiently slow that the time response of the thermocouple probe was adequate. Therefore, the carrier gas pressure was standardized at 25 torr for all the current experiments. At the same time, helium was used as the standardized carrier gas since it was reported (Britten *et al.*, 1985) that the nature of the carrier gas can also affect TPD results.

2.3.2-4. The Effect of Buoyancy on Mass Measurement. As mentioned previously, the reactor for the TPD-MS/TGA apparatus was a quartz hangdown tube, and the char samples were

placed in a quartz bucket and suspended inside the this tube from a Nichrome hangdown wire connected to the microbalance. One important factor affecting the accuracy of the mass measurements is the effect of buoyancy during experiments. Precise quantitative prediction of the buoyancy effect inside the reactor is difficult, since it is a function of the velocity of the carrier gas, pressure, temperature, heating rate, heat transfer coefficient, the shape of the quartz bucket, the size of the reactor, etc. Therefore, in the current work, the buoyancy effect on mass measurement was determined experimentally.

Figure 2.10 presents the TGA mass output signal of the empty bucket for a heating rate of 50 K/min as a function of temperature. Since the balance was initially tared, the mass reading was due purely to the buoyancy effect during the heating process. This experimental result shows that the mass increase due to buoyancy becomes significant as the temperature increases. These values should be subtracted from the mass reading during a TPD run. In order to obtain the actual mass variation of a sample during a heating program, the data were corrected for this effect as part of the data analysis procedure following each experiment.

2.4. Correction of High Temperature CO Evolution From TPD.

50K/min CO TPD spectra are presented in Figure 2.11 for both Wyodak coal char and resin char samples gasified in one atmosphere of oxygen. As can be seen, the spectra are composed of one peak for resin char and two peaks for Wyodak coal char plus a high temperature "tail" which appears at temperatures greater than about 1000°C. This feature is significantly greater for Wyodak coal char than for resin char. This high temperature feature has been attributed to oxidation of the char samples with the quartz (SiO_2) sample bucket, amplified by the catalytic effect of the mineral matter in the Wyodak coal char. Evidence for this conclusion includes the fact that little or no CO evolution was observed at the same temperatures when the quartz sample bucket was new. However, once the bucket was exposed to char samples, the feature appeared immediately and thereafter it occurred even with the empty bucket in the absence of a sample due to residual contamination of the quartz with

char which diffuses into the quartz at high temperatures. Elimination of this feature proved to be quite difficult. Various attempts at cleaning the bucket and using a platinum lining met with only limited success.

The procedure that was finally developed to cope with this problem is as follows. Spectra from an empty, "char contaminated" quartz bucket were found to be quite reproducible upon repeated temperature cycling; an example of such a spectrum is presented in Figure 2.12. This feature was fit to a fifth order polynomial. It was then assumed that this feature becomes amplified in the presence of a sample (due to the considerably greater interfacial area between the sample and quartz bucket), but that its shape remains unaltered. Consequently, the polynomial fit was scaled by the signal values at 1200°C and it was then subtracted from the data. Figure 2.13 presents the data from Figure 2.11 corrected in this manner.

2.5. Experimental Procedures for TGA/TPD.

The following experimental procedure was used for a typical TGA/TPD experiment.

(1) The carbon sample was placed in the quartz sample bucket in the apparatus. The system was then purged using a repeated cycle of evacuation followed by backfilling with helium, a total of three times.

(2) The sample was then thermally cleaned by heating in ultrahigh purity helium to a temperature 50°C less than the sample pyrolysis temperature. The holding time for this temperature was 15 minutes or until no CO or CO_2 could be observed mass-spectrometrically evolving from the sample. The sample was then cooled to room temperature in helium.

(3) The system was then evacuated, and the oxidant gas (i.e., oxygen, CO_2 or other gas mixtures) was introduced into the system. The sample was then heated to the desired gasification or activation temperature, which was maintained until the desired burn-off was achieved.

(4) At the end of a gasification run, the system was immediately evacuated and backfilled with helium. After the oxidized sample was cooled to room temperature in helium, the helium carrier gas

flow rate was set.

(5) The mass spectrometer was calibrated prior to each TPD experiment, as discussed in Section 2.2.1.

(6) The sample was then heated at the desired heating rate to an ultimate temperature of 1200°C, and the evolution rates of CO and CO_2 (as well as H_2O and O_2) were measured with the mass spectrometer. The temperature, pressure and the analog signal from the mass spectrometer electrometer were digitized and recorded in a data file on the microcomputer.

Figure 2.14 presents a typical TGA time history for a resin char sample pyrolyzed in helium at 1000°C for 2 hours. An example of the raw TPD experimental data, along with the TGA trace is shown in Figure 2.15, for resin char gasified in oxygen at 470°C to 15% burn-off.

Table 2.1. Elemental composition (wt %) of Wyodak and Pittsburgh #8 coal samples.†

Element	Wyodak	Pittsburgh #8
C	75	83
H	5.4	5.3
O	18	9
S	0.6	2.2
Ash	5	9

†Vorres, 1993; C, H, O are on MAF basis; S and ash are on a dry basis.

Table 2.2. Mineral matter composition of ash (%) for Wyodak and Pittsburgh #8 coal samples.[†]

Element	Wyodak	Pittsburgh #8
Al	8.2	13.3
Ba	0.4	
Ca	10.8	1.9
Fe	7.1	13.6
K	0.7	1.7
Mg	2.2	0.8
Mn	0.3	-
Na	1.1	-
P	0.5	-
S	8.8	0.8
Si	10.8	15
Sr	0.3	-
Ti	0.7	0.7

[†]Vorres, 1993.

Table 2.3. Elemental composition of phenolic resin char as a function of pyrolysis temperature.†

T_{pyro}(°C)	wt%			
	N	C	H	O
1000	0.4	97.1	0.8	1.7
1111	0.2	97.9	0.7	1.2
1243	0.2	98.5	0.3	1.0
1400	0.1	98.8	0.3	0.8

†Wojtowicz, 1987.

Table 2.4. Relative pressure, P/P° values, and corresponding N_2 (adsorbate) and He (carrier gas) flow rates.†

P/P°	V_{He} (cm^3/min)	V_{N_2} (cm^3/min)
1.00	0.00	20.00
0.95	0.62	19.38
0.90	1.64	18.36
0.85	2.66	17.34
0.80	3.68	16.32
0.75	4.70	15.30
0.70	5.72	14.28
0.65	6.74	13.26
0.60	7.76	12.24
0.55	8.78	11.22
0.50	9.80	10.20
0.45	10.82	9.18
0.40	11.84	8.16
0.35	12.86	7.14
0.30	13.88	6.12
0.25	14.90	5.10
0.20	15.92	4.08
0.15	16.94	3.06
0.10	17.96	2.04
0.05	18.98	1.02

†Laboratory Manual, Chemical Engineering Laboratory, Division of Engineering, Brown University.

Table 2.5. Third order polynomial coefficients for the voltage-temperature relationship for the type R thermocouple:†

$$T = C_1 + C_2 \times (emf) + C_3 \times (emf)^2 + C_4 \times (emf)^3$$

Temperature Range (°C)	C_1	C_2	C_3	C_4
[0, 300]	1.2446	1.7168	-3.299×10^{-3}	5.674×10^{-6}
[300, 600]	34.151	1.2069	-4.609×10^{-4}	2.060×10^{-7}
[600, 1250]	48.722	1.1096	-2.461×10^{-4}	4.949×10^{-8}

†T is the temperature in °C; emf is the voltage, 100 x mV.

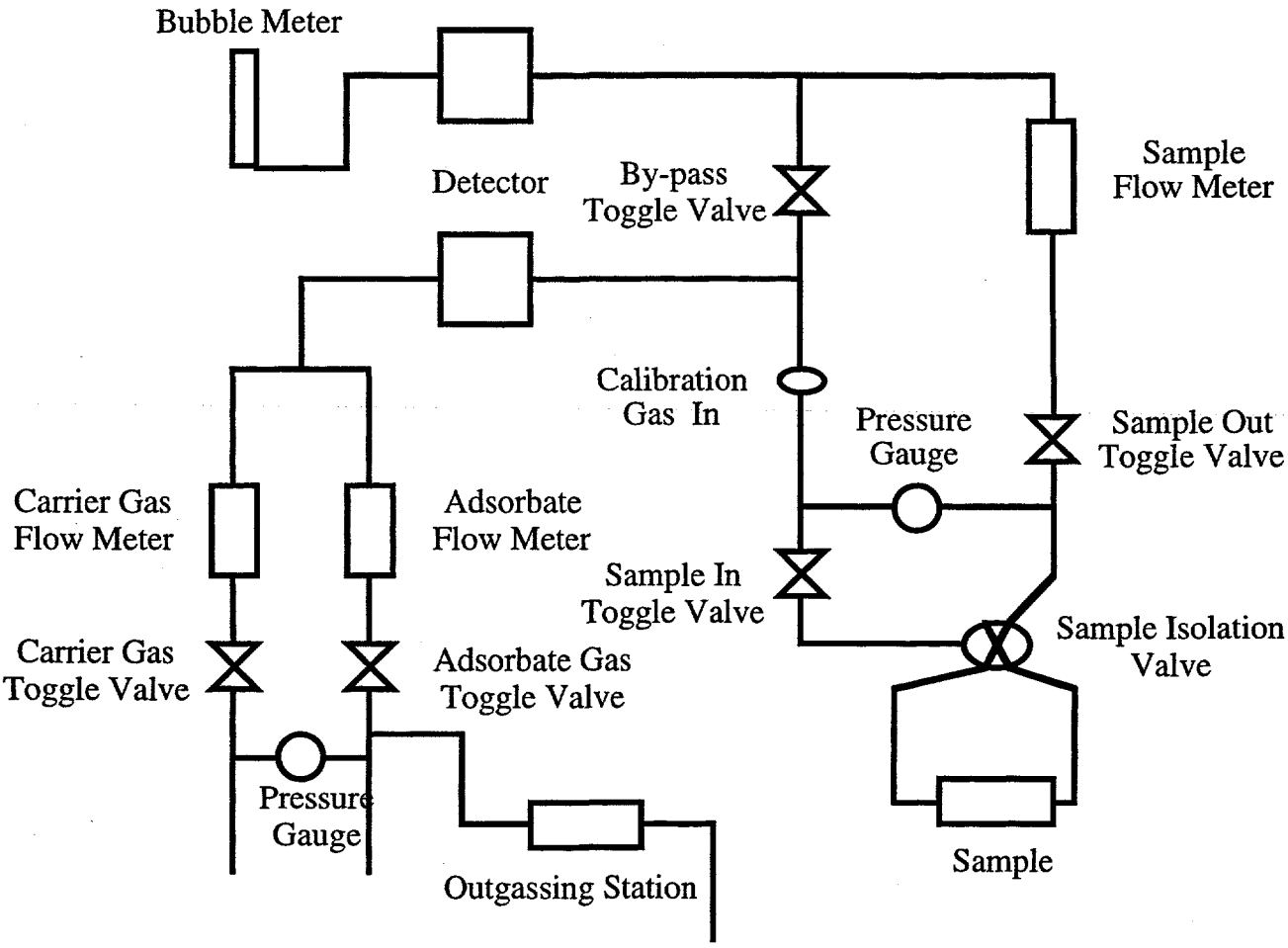

Figure 2.1. Schematic of the gas flow circuit of the Quantasorb surface area analyzer.

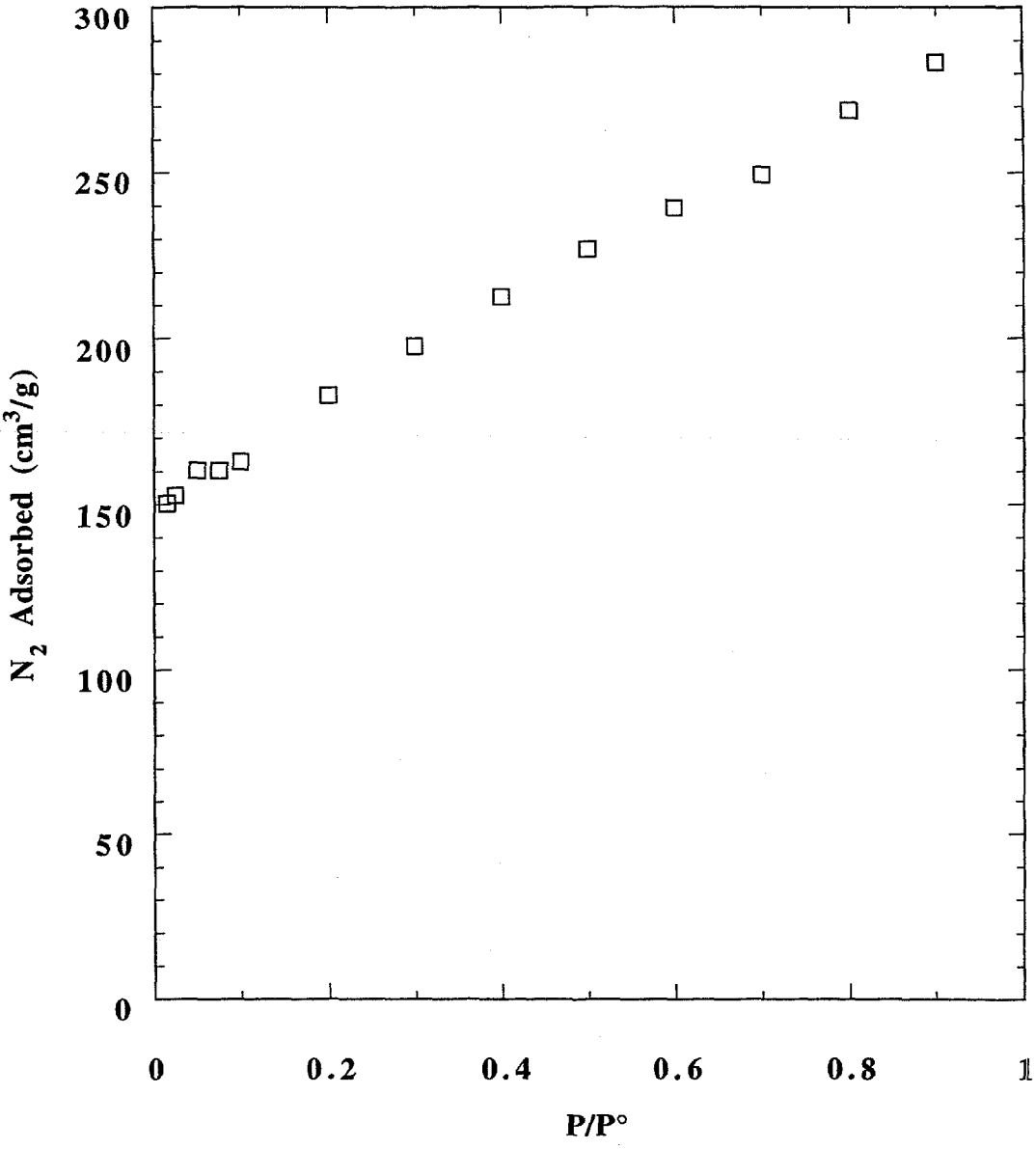

Figure 2.2. Nitrogen uptake at 77 K on Wyodak coal char gasified in oxygen at 420°C to 30% burn-off.

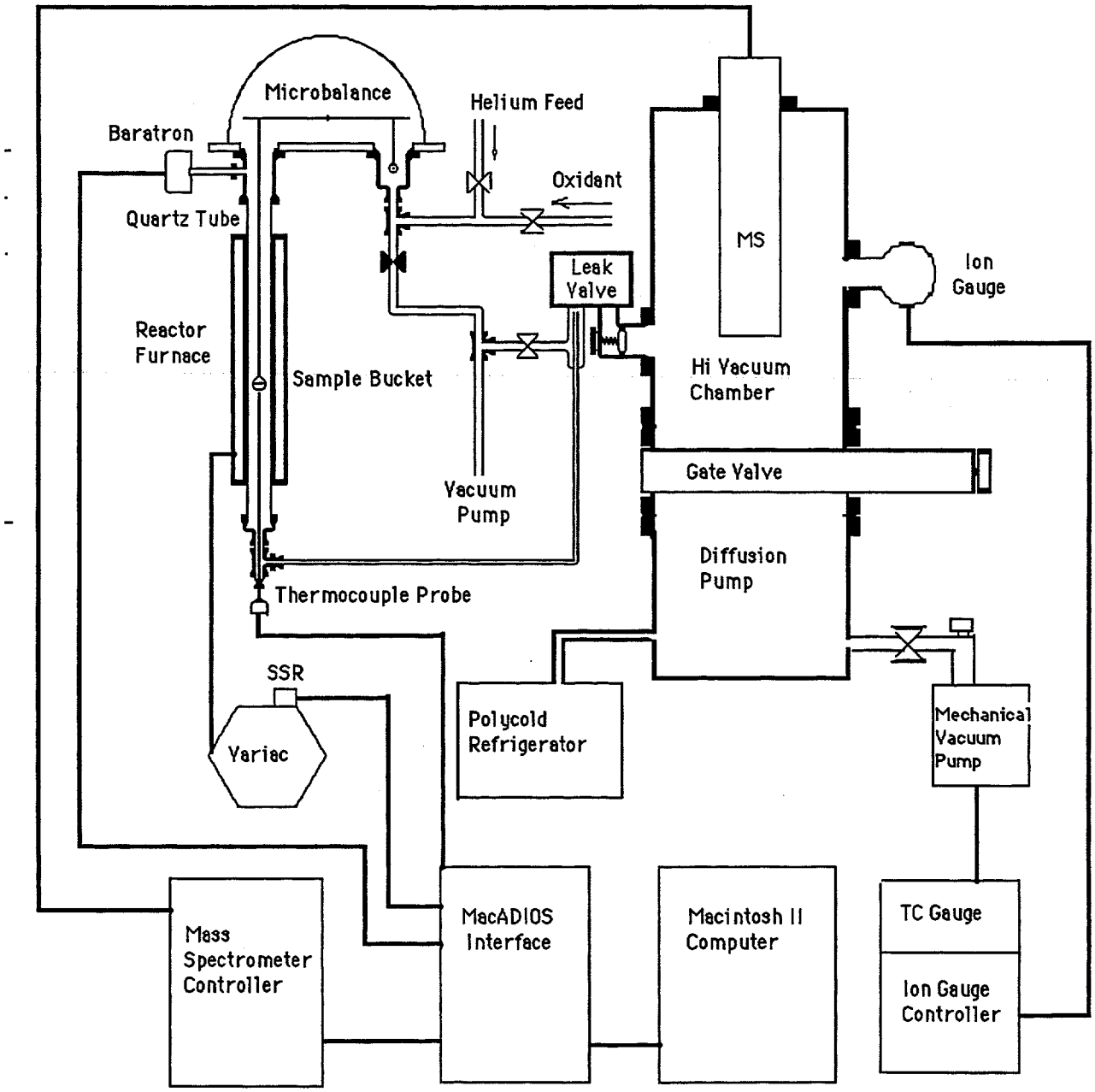

Figure 2.3. Schematic of the TPD-MS/TGA apparatus.

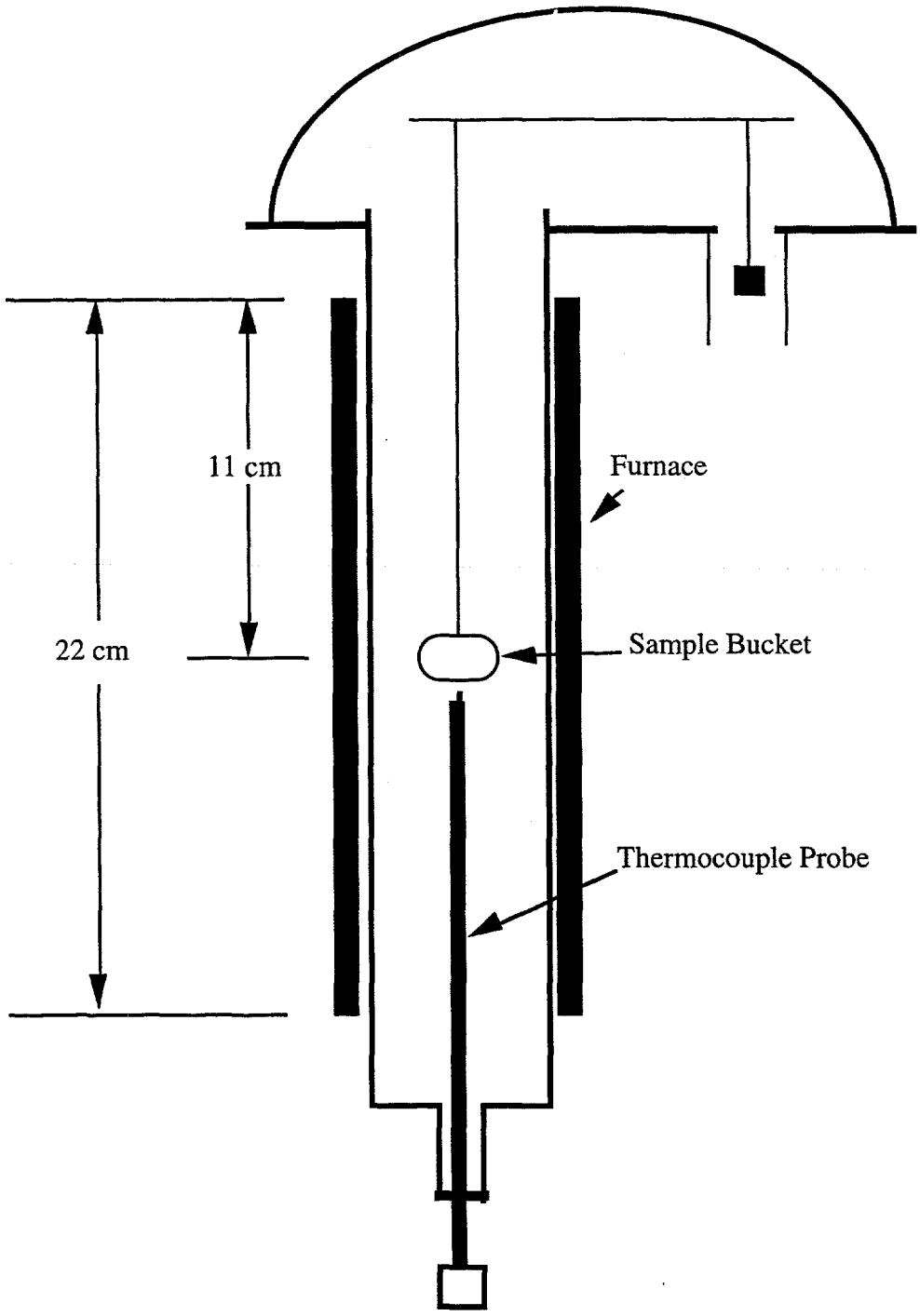

Figure 2.4. Schematic of the TPD-MS/TGA reactor hangdown tube.

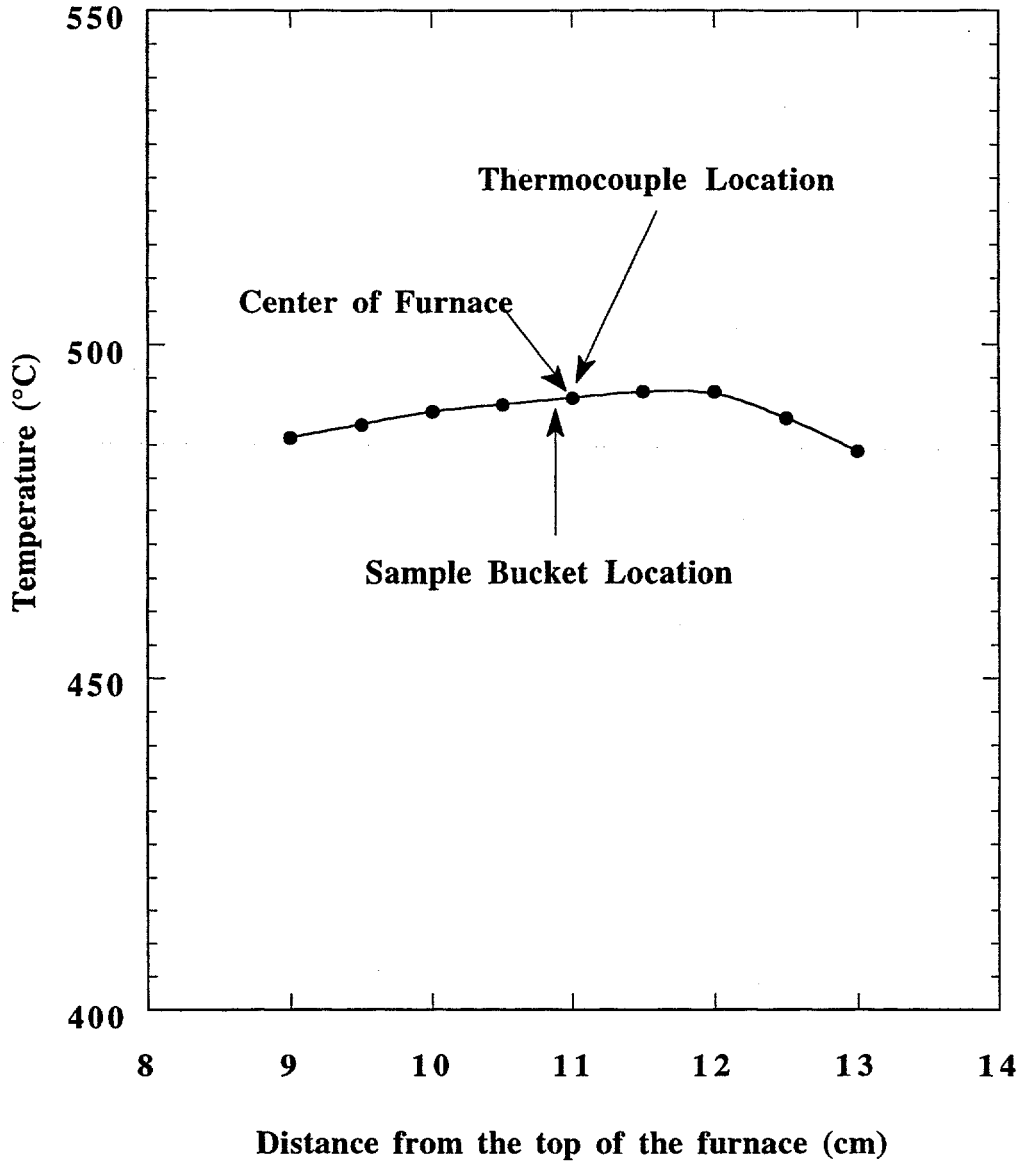

Figure 2.5. Temperature profile in the reactor hangdown tube.

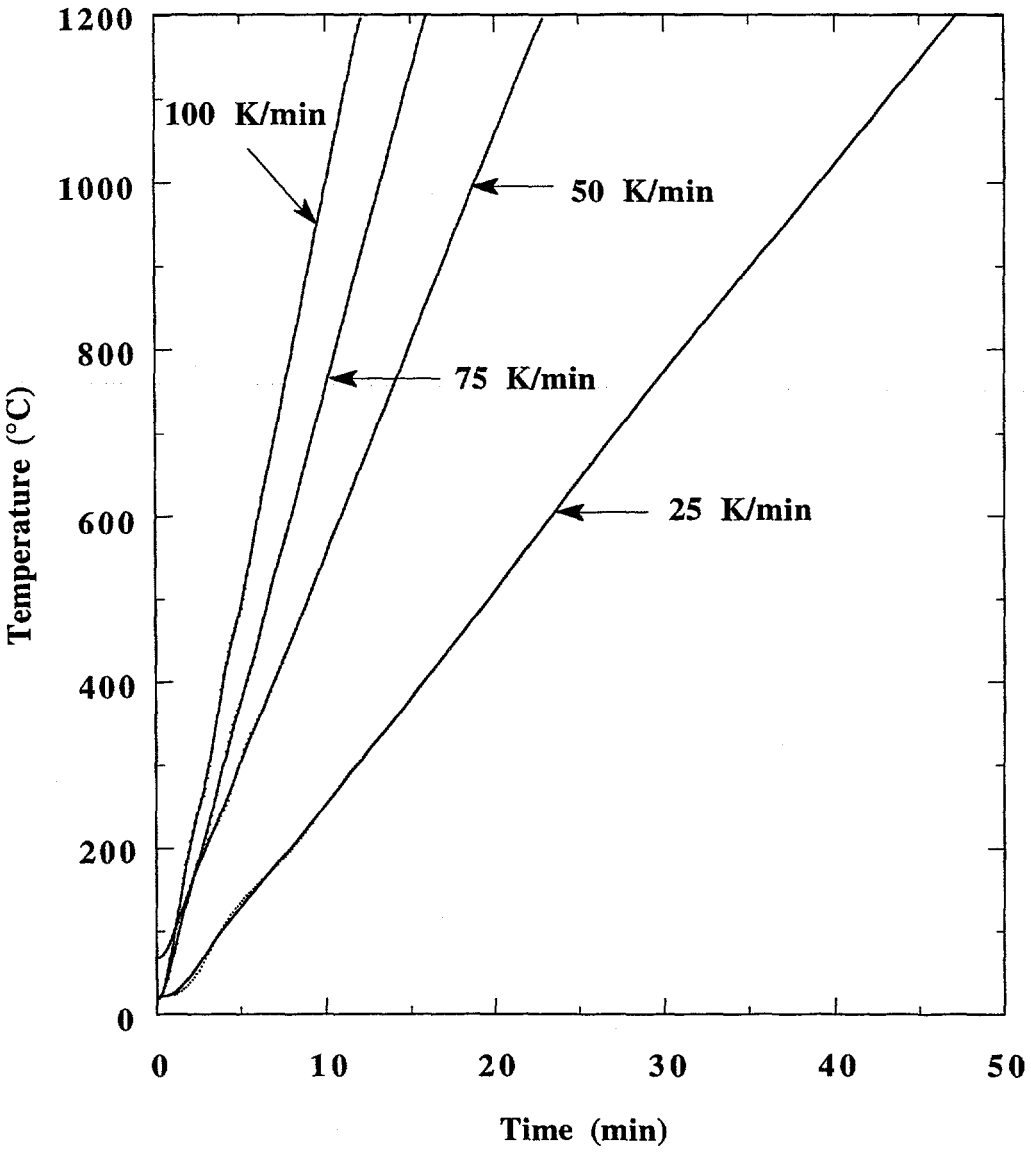

Figure 2.6. Temperature programs at different heating rates.

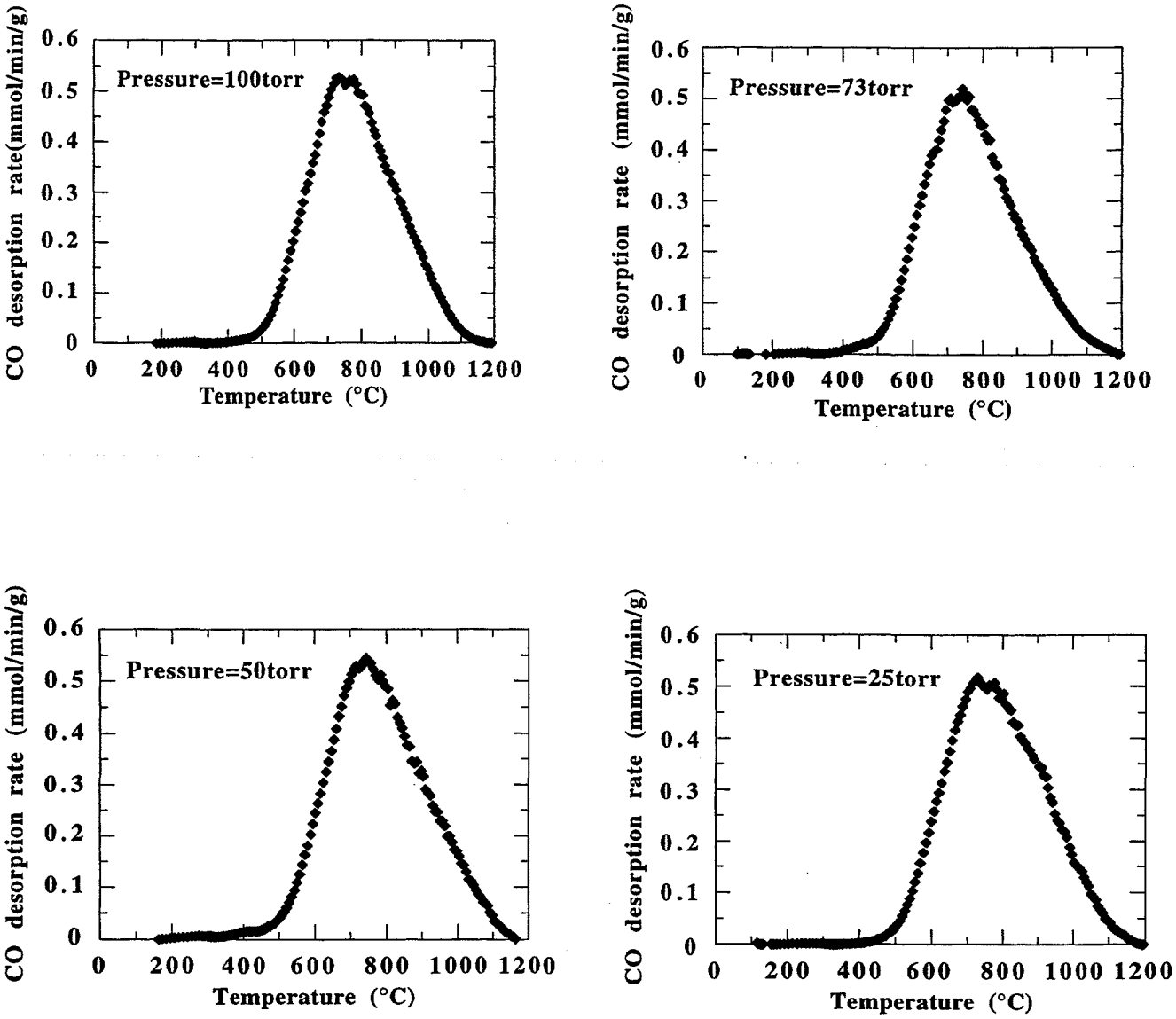

Figure 2.7. 50K/min CO TPD spectra as a function of helium carrier gas pressure for resin char gasified in oxygen at 470°C to 10% burn-off.

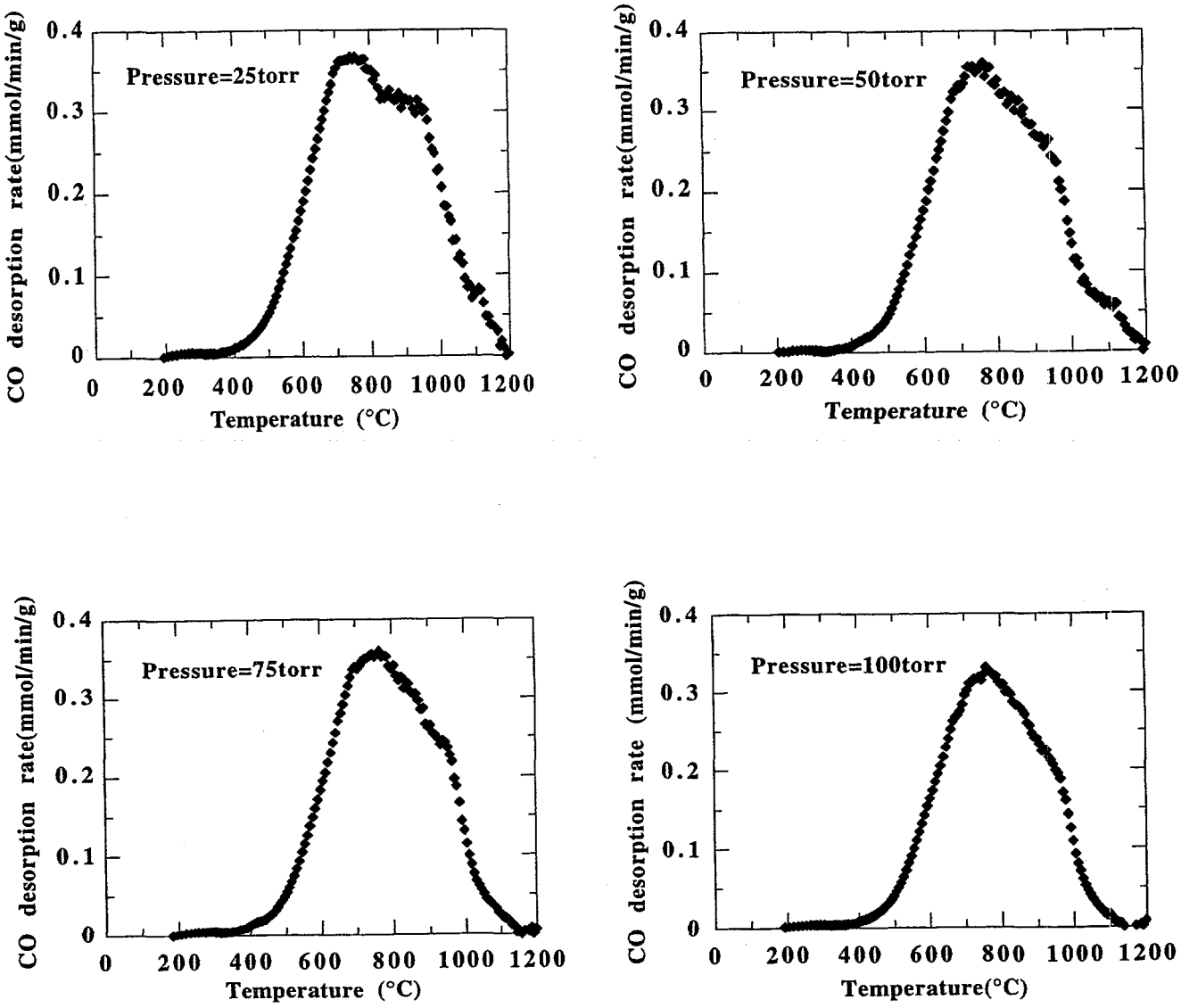

Figure 2.8. 50K/min CO TPD spectra as a function of helium carrier gas pressure for natural Wyodak coal char gasified in oxygen at 380°C to 10% burn-off.

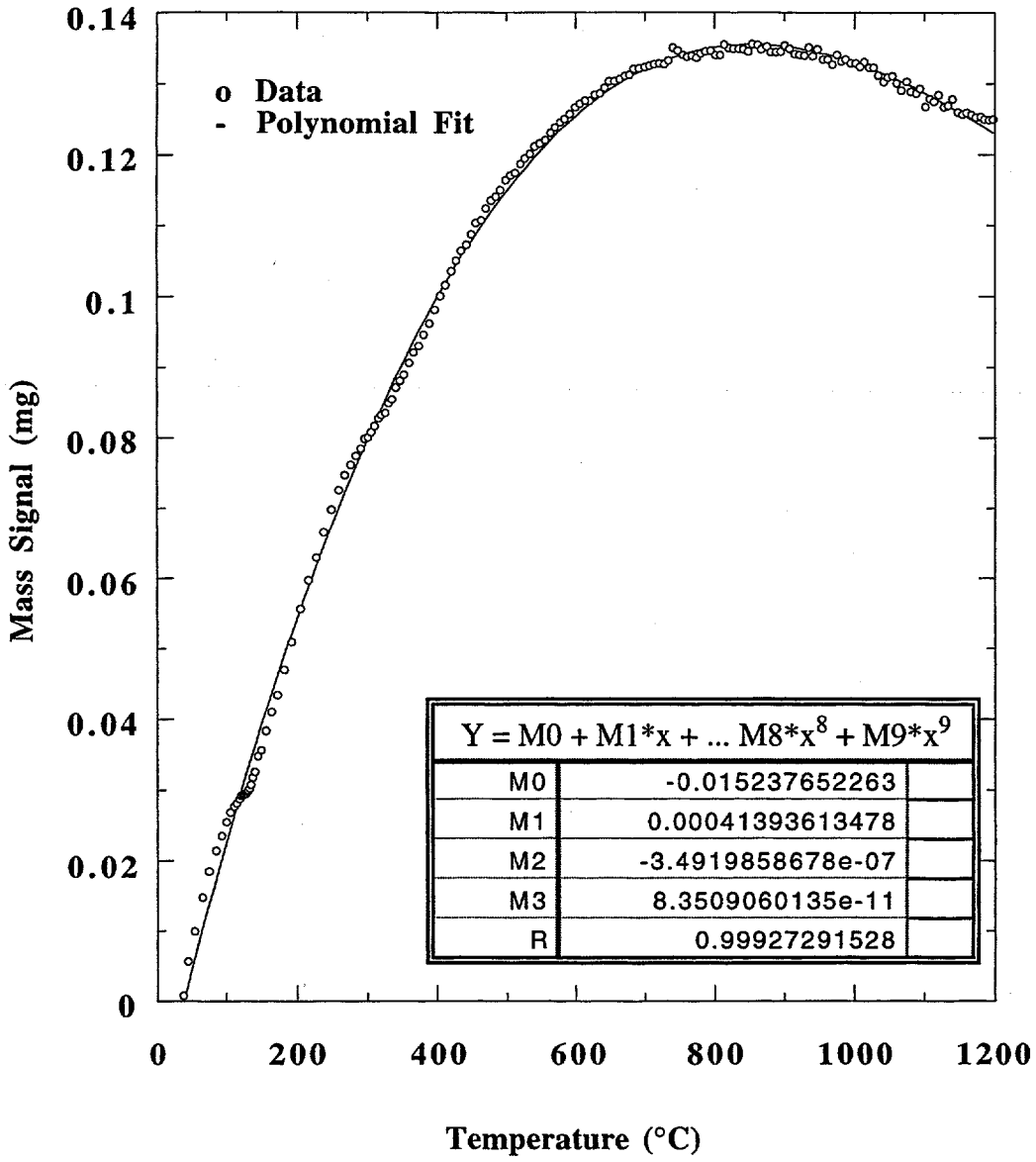

Figure 2.10. Mass signal for the empty sample bucket as a function of temperature at a heating rate of 50 K/min.

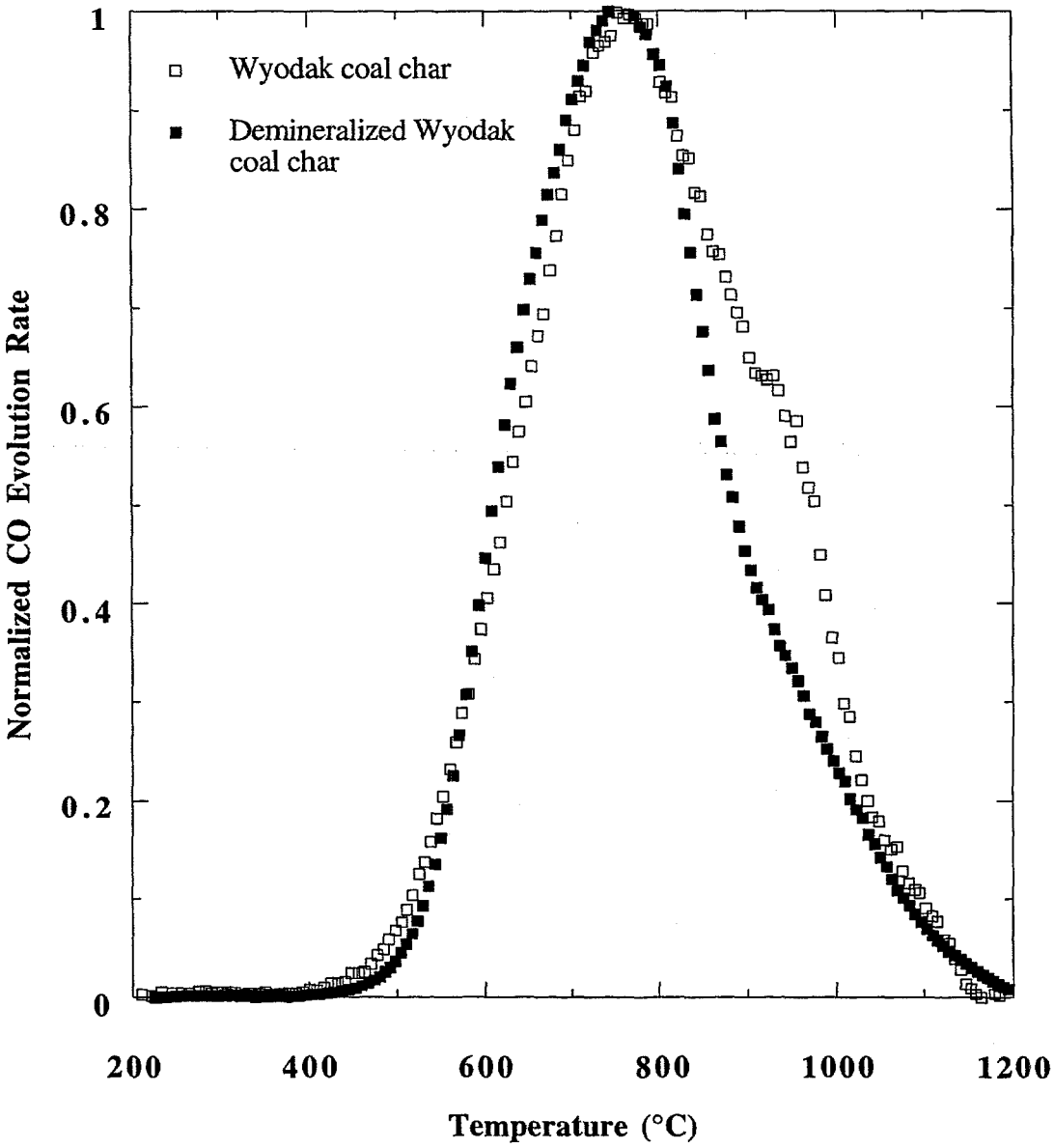

Figure 2.9. Comparison of 50K/min TPD spectra from natural Wyodak coal char and demineralized Wyodak coal char gasified in oxygen at 420°C to 30% burn-off, for a helium carrier gas pressure of 25 torr.

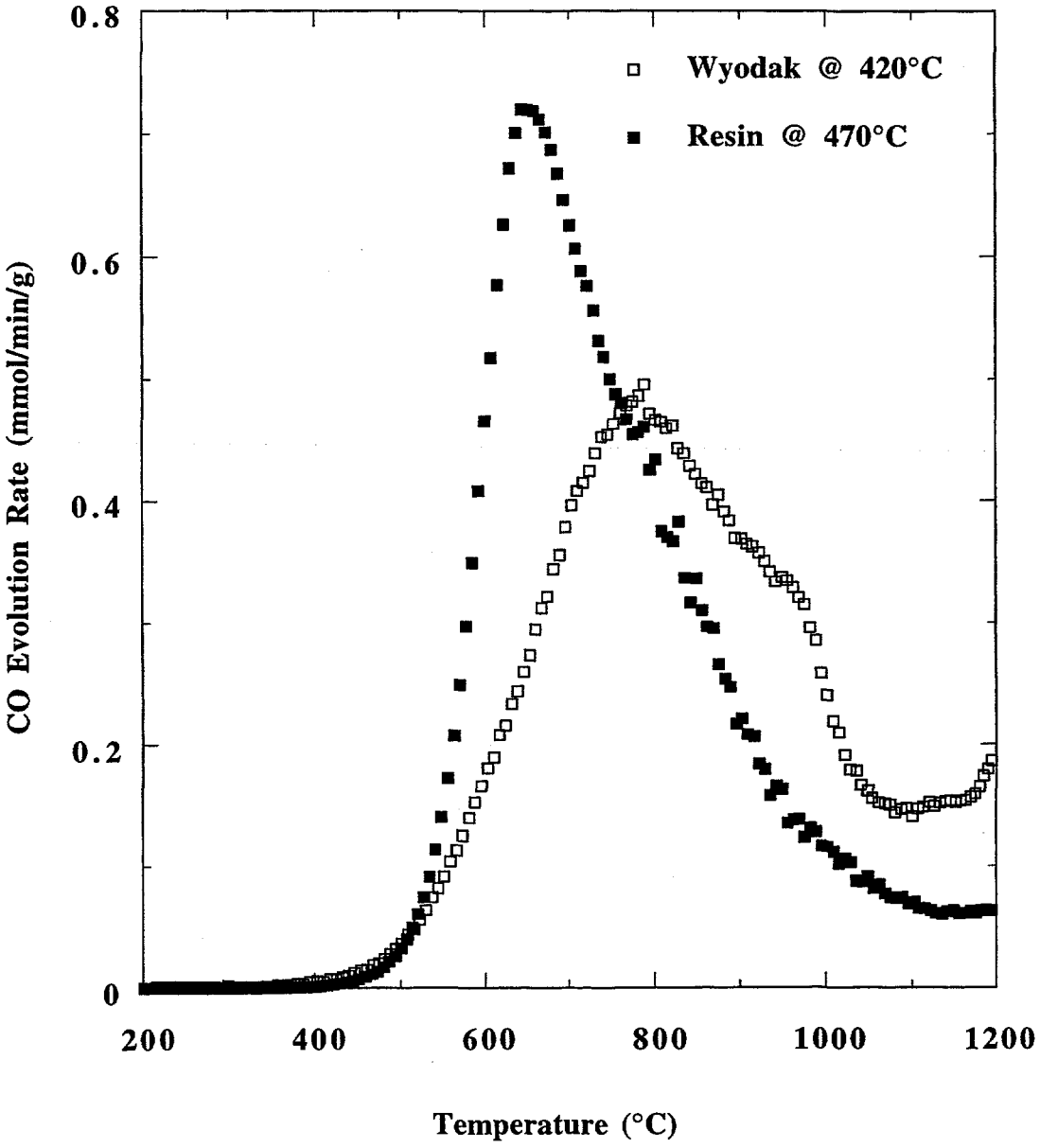

Figure 2.11. CO desorption spectra from Wyodak coal char and resin char gasified in 1 atm of oxygen to 15% burn-off.

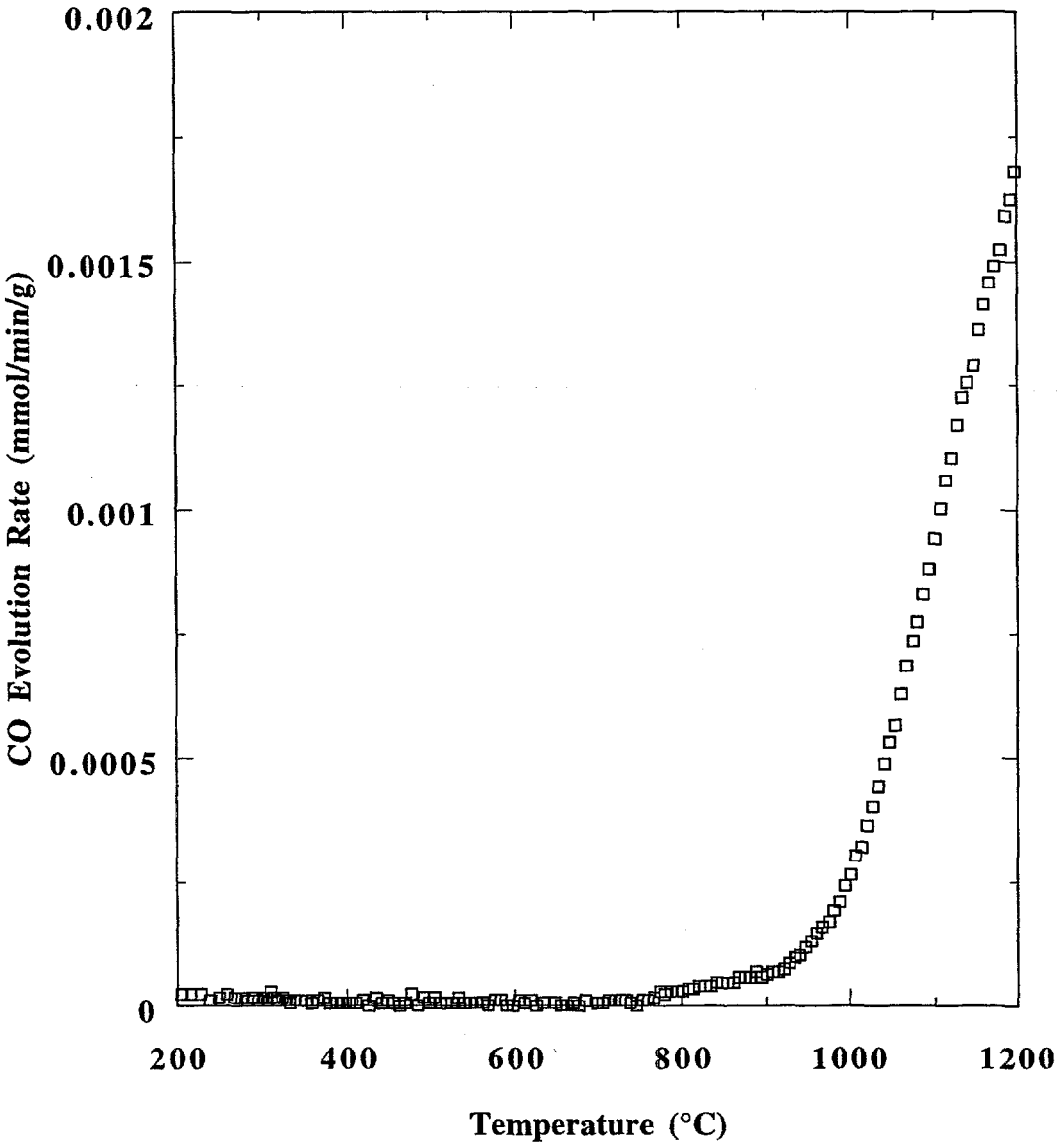

Figure 2.12. 50K/min CO Evolution curve for "empty" contaminated quartz sample bucket.

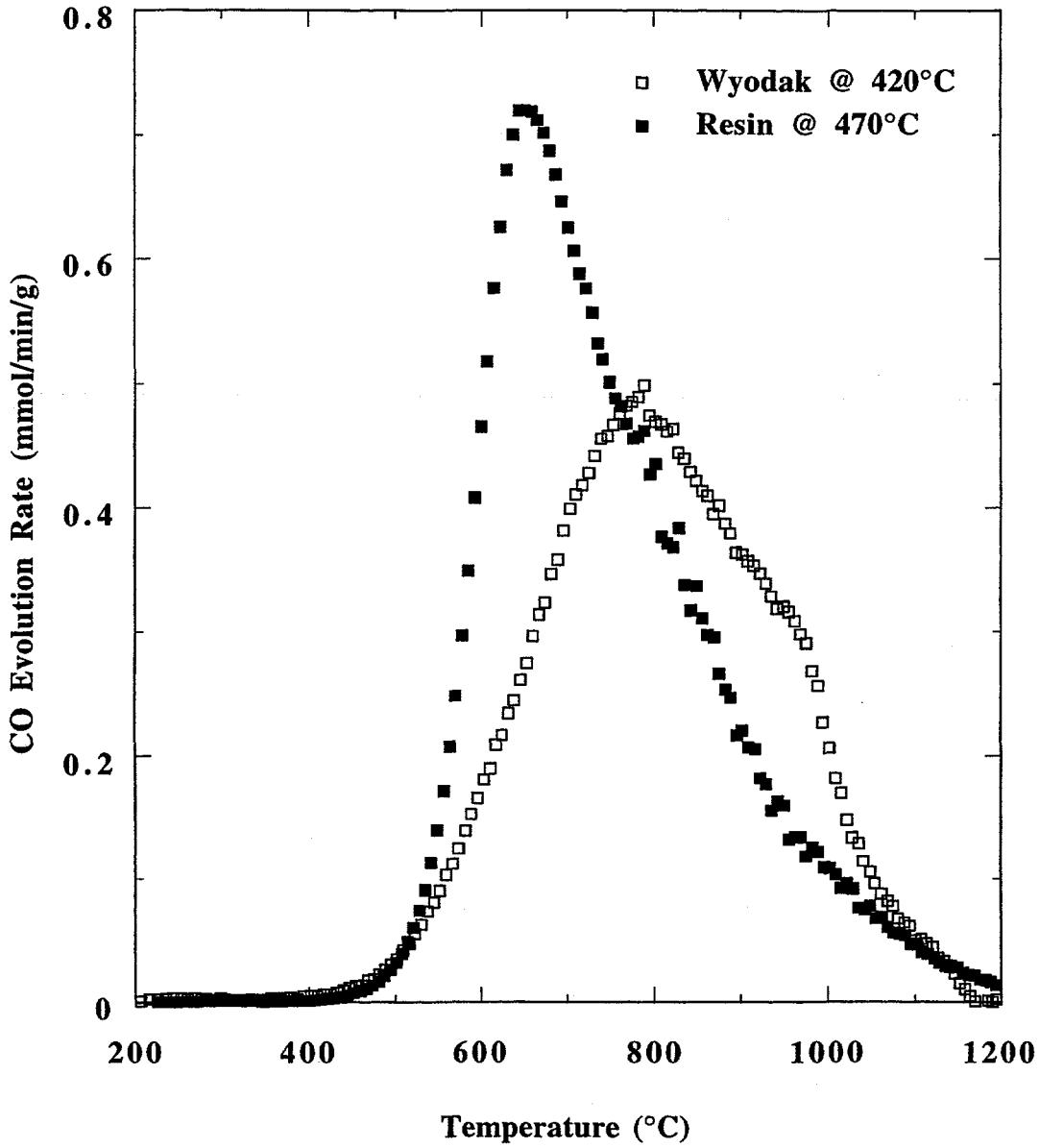

Figure 2.13. "Corrected" 50K/min CO desorption spectra from Wyodak coal char and resin char gasified in 1 atm oxygen to 15% burn-off.

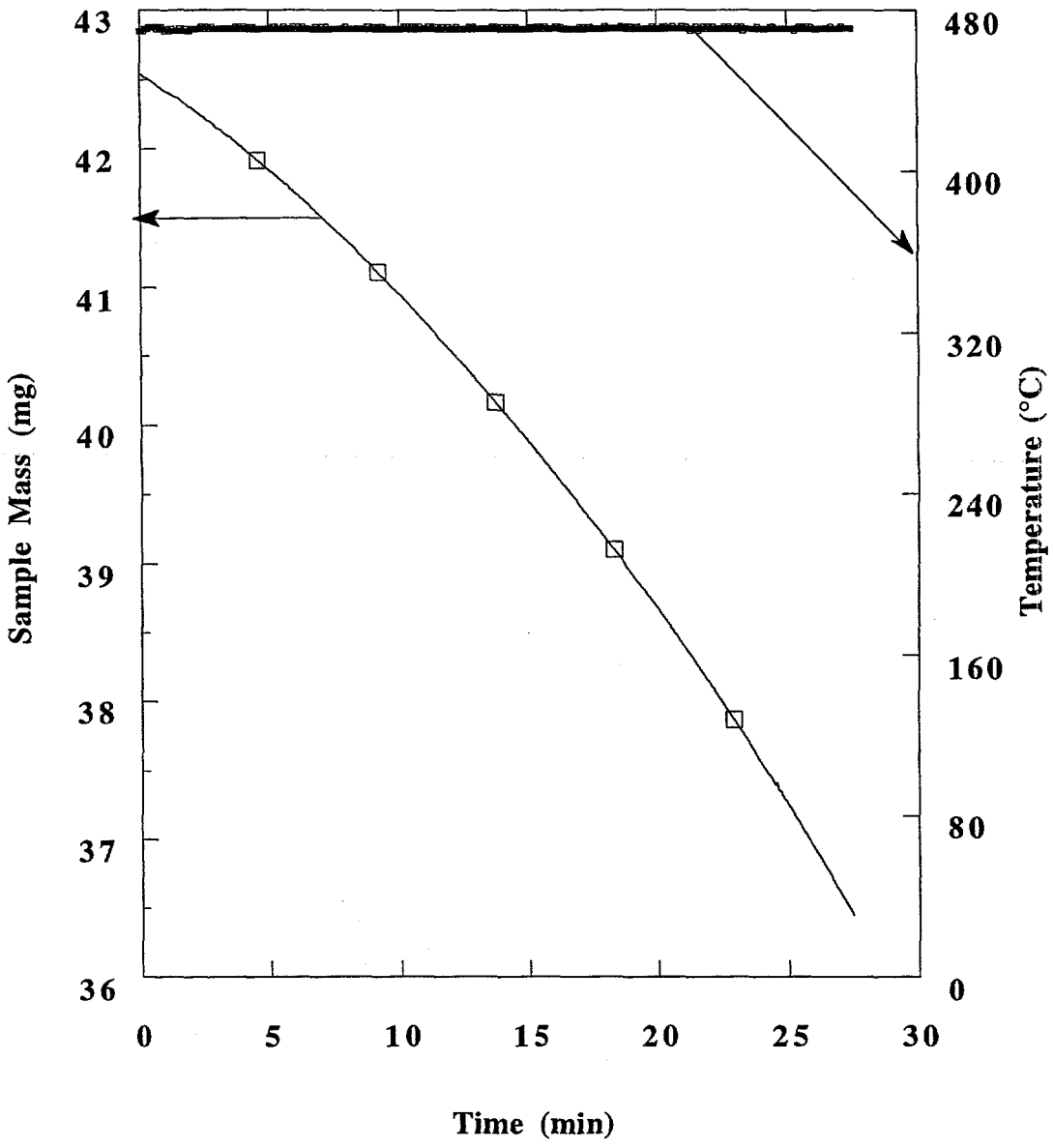

Figure 2.14 Typical TGA data for resin char in 1 atm of oxygen, gasified at 470°C to 15% burn-off. The data were corrected for buoyancy.

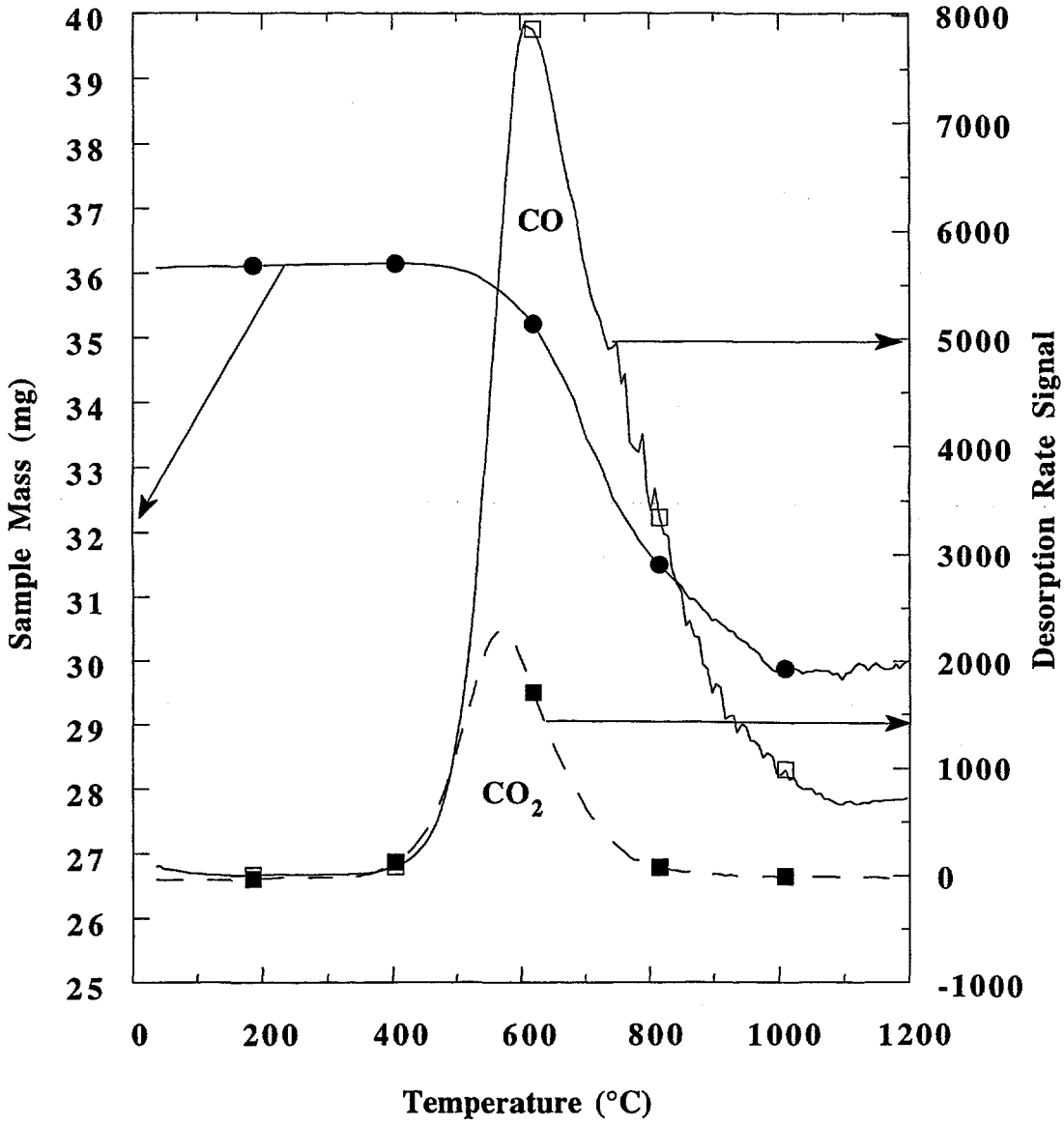

Figure 2.15. Typical raw data obtained during 50K/min TPD run at a reactor pressure of 25 torr for resin char gasified in oxygen at 470°C to 15% burn-off. The sample mass data were not corrected for buoyancy.

3.0. CHAR POROSITY CHARACTERIZATION AND DEVELOPMENT *VIA* TPD TECHNIQUES

3.1. Introduction.

In the current project, a new approach has been explored for the characterization of porosity and the study of porosity development during gasification or activation processes. This approach involves the interpretation of post-activation temperature programmed desorption (TPD) spectra. As discussed previously in Section 1.2, TPD has become a standard technique for investigating the physico-chemical state of adsorbed species on carbon surfaces. In the current work, the technique involves first forming oxygen complexes on a carbon surface by oxygen gasification. Subsequently, the sample temperature is raised in an inert carrier gas (e.g., helium) at a programmed heating rate, during which the rate of evolution of CO and CO_2 are measured. The results presented here show that there exist both qualitative and quantitative relationships among porosity development, rate of reaction, and post-reaction desorption features of oxygen surface complexes formed during the activation process. In addition, a random pore model (Gavalas, 1980) is extended and applied to the current problem.

3.2. Experimental.

As presented in Section 2.0, the samples used in the experiments were chars produced from Wyodak subbituminous and Pittsburgh #8 bituminous coal samples, obtained from Argonne Premium Coal Sample Bank (Vorres, 1993). Resin char samples produced from phenol-formaldehyde resin were also used, for a total of three different carbon materials. All the chars used in the current work were produced in a tube furnace at 1000°C for 2h in flowing ultrahigh purity helium, as described in Section 2.0.

All the oxidation and thermal desorption experiments were carried out in the TPD-MS/TGA apparatus described in Section 2.0. For gasification, the samples were exposed to one atmosphere of

oxygen at the desired temperature, and burned-off to varying extents. The thermal desorptions were all carried out at a heating rate of 50K/min to 1200°C in ultrahigh purity helium carrier gas. The operating pressure for TPD was about 25 torr.

The ash contents of Wyodak and Pittsburgh #8 coal chars were measured by reacting the samples in oxygen to 100% burn-off; i.e., "ashing" them. The burn-offs reported for these samples were based on the carbon content.

The adsorption isotherms of the various char samples were obtained using a Quantachrome Quantasorb surface area analyzer with nitrogen at 77K.

3.3. Nitrogen Adsorption Isotherm Data.

3.3.1. Wyodak Coal Char.

The nitrogen adsorption isotherms for Wyodak coal char are presented in Figure 3.1. These isotherms cover the total range of relative pressure, $0 < P/P^\circ < 1$. The results show that increasing burn-off results in an increase of nitrogen uptake up to about 40% burn-off, following which the amount of nitrogen uptake begins to decrease. At low burn-offs, the nitrogen adsorption isotherms exhibit classical Type I isotherm behavior, consistent with the low burn-off Wyodak coal char being primarily microporous. As the burn-off increases, however, the isotherms gradually take on Type II behavior, indicative of mesoporosity development.

Although the microporosity accounts for the bulk of the porosity of activated carbons and chars, the contribution of the nonmicroporous structure (mesopores and/or macropores) may also be important in highly activated materials for which the isotherm has a relatively steep slope at $P/P^\circ > 0.3$. And, as can be seen in Figure 3.1, at the higher burn-offs the linear portions of the isotherms at high relative pressures become steeper. This is reflective of a significant contribution from the nonmicroporous structure.

As presented in Section 1.0, the nitrogen isotherm data were analyzed using the α_s-plot method (Lippens *et al.* 1964; Lippens and de Boer, 1965; Gregg and Sing, 1982) to separate the

contribution of the microporosity from that of the nonmicroporous porosity of the chars. As previously discussed, from an α_s-plot: the slope of the extrapolated line from the first few experimental points at low α_s values to the origin provides a measure of the total surface area; the slope of the upper linear branch gives the nonmicroporous surface area; and extrapolation of this latter branch to $\alpha_s = 0$ provides the total micropore volume. In the current work, α_s-plots were constructed from the adsorption isotherms using the standard nonporous carbon proposed by Rodriguez-Reinoso *et al.* (1987). The results of this procedure are presented as the curves in Figure 3.2, and a sample calculation for the total surface area, micropore volume, and nonmicroporous surface area is presented in Appendix A.

Figures 3.3 and Figure 3.4 present the variation of total specific surface area and micropore volume, respectively, with burn-off for Wyodak coal char, as determined by the α_s-plot method. As shown, for Wyodak coal char gasified in oxygen at 420°C, both the surface area and the micropore volume increase with burn-off, and then pass through maxima around 40% burn-off. Similar behavior has been observed for other carbonaceous materials (Walker, 1986). As the burn-off proceeds, the nonmicroporous (i.e., larger porosity) surface area increases continuously but more rapidly prior to 40% burn-off, and less rapidly at higher degrees of burn-off, as shown in Figure 3.5 (Sample calculations are presented in Appendix A). This behavior indicates that the microporosity continues to develop up to about 40% burn-off, and decreases thereafter; while, the larger porosity develops continuously with burn-off. These results are consistent with the classical picture of microporosity development at low conversions, followed by pore wall collapse and concomitant surface area loss at higher conversions (e.g., Miura and Hashimoto, 1984).

Figure 3.6 presents mesopore size distributions of Wyodak coal char as a function of burn-off, as determined by the method of Roberts (1967). As is evident from this figure, the Wyodak coal char is initially almost entirely microporous, and eventually develops some mesoporosity evident at 50% and 66%, which then disappears by about 80% burn-off. These results are entirely consistent with the preceding conclusions concerning the behavior of this char.

3.3.2. Pittsburgh #8 Coal Char.

The nitrogen adsorption isotherms for Pittsburgh #8 coal char are presented in Figure 3.7, and the corresponding α_s-plots in Figure 3.8. The trend of these isotherms as a function of burn-off is qualitatively similar to that of the Wyodak coal char. However, the amount of adsorbed nitrogen at zero burn-off is considerably less than for the Wyodak coal char, indicating that prior to activation, this coal char is essentially almost totally nonporous with very low surface area. Figures 3.9 and 3.10 present the surface area and micropore volume as a function of burn-off for Pittsburgh #8 coal char, as determined by the α_s-plot method from Figure 3.8. These figures also clearly show that the surface area and micropore volume corresponding to 0% burn-off are quite low and that the char is essentially nonporous. However, both the surface area and the micropore volume increase progressively with burn-off, and then pass through maxima around 40% burn-off. At the same time, as the burn-off proceeds, the portion of the nonmicroporous surface area increases continuously, as shown in Figure 3.11.

It is concluded that Pittsburgh #8 coal char is essentially nonporous prior to oxygen gasification, and that the microporosity is created and continues to develop up to about 40% burn-off, whereupon it begins to decrease. Meanwhile, the larger porosity develops continuously with degree of burn-off. After about 60% burn-off, the majority of the total surface area lies in the larger porosity.

Figure 3.12 presents mesopore size distributions of the Pittsburgh #8 coal char as a function of burn-off, as determined by the method of Roberts (1967). These results support the preceding conclusions of almost zero initial porosity, followed by development of micro- and then mesoporosity, ultimately culminating in pore wall collapse at high burn-off and loss of all porosity.

3.3.3. Resin Char.

The nitrogen adsorption isotherms for resin char are presented in Figure 3.13. As shown, all the isotherms are essentially of Type I with a sharp "knee" at low P/P°. This means that these chars are essentially microporous with little or no mesoporosity development. Figures 3.14 to 3.16 show that the total surface area and micropore volume continue to increase up to about 45% burn-off,

whereupon they both begin to decrease at a relatively low rate. However, it should be noted that even though the larger porosity increases with degree of burn-off, the majority of the porosity is still microporous over the entire activation process. Even at 72% burn-off, the surface area contribution from the larger porosity is only about 5% of the total surface area.

3.4. Correlations With Temperature Programmed Desorption (TPD) Spectra.

The CO and CO_2 TPD spectra for Wyodak coal char are presented in Figures 3.17 and 3.18, respectively, as a function of burn-off. Although both species exhibit two principal desorption features, there are still some differences between the two. The total integrated amount of CO obtained from the data in Figure 3.17 initially increases, and then decreases with degree of burn-off, approaching a maximum in the burn-off range between 35% and 50%. This is the same as the trend indicated by the nitrogen isotherms presented in Figure 3.1. There are at least two major desorption features evident in these data. It is noted that the first peak accounts for the bulk of the desorbed CO, and thus it follows the same trend as the total integrated CO; i.e., it exhibits a maximum around 40% burn-off. In addition, the first peak gradually shifts to lower temperatures, and the second peak remains at essentially the same temperature with burn-off.

The CO_2 TPD spectra, summarized in Figure 3.18, exhibit increasing total integrated gas evolution with burn-off. The spectra also appear to be comprised of at least two features, each of which appears just before the two corresponding CO peaks.

There are at least two theories which can explain the major CO desorption peaks: (1) that they represent the desorption of two chemically-different types of oxygen surface complexes formed during gasification prior to TPD (Otake and Jenkins, 1993; Zhuang *et al.*, 1994); and (2) that a significant portion of the "high temperature" feature is due to CO which is re-chemisorbed during TPD, and that some of the CO_2 is from secondary reactions of the type (Calo and Hall, 1989):

$$CO(g) + C(O) <==> C_f + CO_2(g) \qquad [3\text{-}1]$$

where: CO(g) represents free, gaseous carbon monoxide resulting from the desorption of a surface oxygen complex; C(O) is a surface bound oxygen complex; and C_f is an unoccupied surface active site.

In order to test whether secondary reactions were significant during TPD in the current work, a series of preliminary experiments were performed in which oxygen-oxidized chars were subjected to TPD at various heating rates. For example, four TPD runs at 25, 50, 75, and 100°C/min were conducted on Wyodak coal char samples obtained from the same batch of char oxidized in the apparatus to 10% burn-off in oxygen at 390°C. The experimental results are summarized in Table 3.1. It is shown that the total amounts of each gas evolved are virtually the same for the four different heating rates, suggesting that the TPD processes were essentially free of secondary reactions of this type. Thus the gas evolution data appear to be representative of the oxygen surface complexes formed during gasification. Possible reasons for the apparent absence of secondary reactions are that the operating pressure for TPD was very low (25 torr) in the current work, in comparison to atmospheric pressure as used by Calo and Hall (1989), and CO was rapidly removed once it was desorbed from the sample surface.

Otake and Jenkins (1993) concluded that the lower temperature CO_2 peak arises from nonadjacent carboxylic acid oxygen complexes formed at dangling carbon sites, and the higher temperature CO_2 peak is from carboxylic acid anhydrides, which are adjacent acidic oxygen complexes formed at dangling carbon sites. By combining diffuse reflectance infrared Fourier transform spectroscopy (DRIFTS) with transient kinetics (TK), and TPD techniques, Zhuang *et al.* (1994) have also found that lactone (and/or acid anhydride), carbonyl, and ether type complexes are formed on the carbon surface during oxygen gasification, and CO_2 evolution arises from the decomposition of lactone and/or acid anhydride complexes, whereas CO desorption is mainly from carbonyl and ether type complexes. In a DRIFTS study of the formation of surface groups on carbon by oxygen, Fanning and Vannice (1993) also reported that initial exposure to oxygen produces ether

structures, and that additional exposure develops cyclic anhydride groups.

Table 3.2 summarizes all the experimental results from gasification, nitrogen adsorption isotherms, and TPD for Wyodak coal char. A comparison of total CO evolution and total surface area for Wyodak coal char (Figure 3.19) reveals very similar trends with burn-off. On the other hand, both the amount of total CO_2 evolved and the nonmicroporous surface area both increase with burn-off for Wyodak coal char, as shown in Figure 3.20, and they correlate quite well.

The same behavior is also apparent for both Pittsburgh #8 coal char and resin char. The experimental data for both chars are listed in Tables 3.3 and 3.4, respectively. Figures 3.21 and 3.22 present a comparison of total CO evolved and total surface area for Pittsburgh #8 coal char and resin char gasified in oxygen, respectively. Again, it is observed that the total surface area and total CO evolved during TPD are well correlated. As shown in Figures 3.23 and 3.24, the amount of CO_2 evolution upon TPD and the nonmicroporous surface area for both chars both increase with burn-off, and, once again they correlate quite well.

It is apparent that just like nitrogen which is adsorbed in all the porosity (i.e., micro-, meso- and macroporosity), oxygen can also penetrate all the porosity during gasification to form surface complexes over the entire carbon surface. The obvious conclusion that one can draw from these results is that the apparent specific surface area is responsible for the CO evolution, and that most (if not all) of the CO_2-evolving surface complexes are formed only on the surface area in the larger porosity.

In a study of the effect of nonreacting gases on the desorption of reaction-created surface complexes on carbon, Britten *et al.* (1985) concluded that the surface transport process was involved in the desorption of CO, but that no influence of the nonreactive gases on the CO_2 desorption rate was observed. These results support the conclusion that the CO_2-evolving surface complexes are formed on the surface area in the larger porosity, and, therefore, there is also probably much less of an effect on the intrapore transport resistance.

Otake and Jenkins (1993) have shown that the CO_2 complexes present on an air-oxidized char are responsible for the acidic nature of the surface, and CO_2 evolution is a result of the thermal

decomposition of carboxylic acid anhydride surface complexes. Marchon *et al.* (1988) concluded that CO evolution arose from semiquinones, and CO_2 evolution from lactones in a study of oxygen adsorption on polycrystalline graphite. Zhuang *et al.* (1994) have also hypothesized that the CO_2 evolved is from the decomposition of lactone and/or acid anhydride surface groups, whereas CO desorption is mainly from carbonyl and ether-type complexes formed during oxygen gasification. The detection of carboxylic acid groups on oxidized carbon surfaces using FTIR spectroscopy by Starsinic *et al.* (1983) proves that such functionalities do exist, but not necessarily within the micropore structure. The size of carboxylic acid groups may restrict their presence to the surface of the larger pores. These workers also found that carboxylic acid anhydride complexes increase in number with degree of burn-off.

The structure of the various oxygen surface complexes are schematized below.

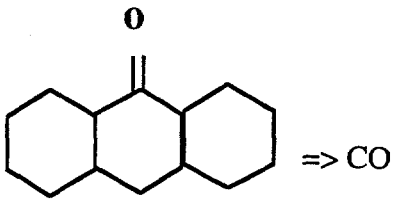

Semiquinone

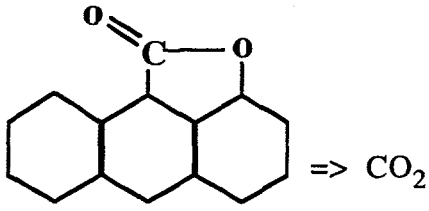

Lactone

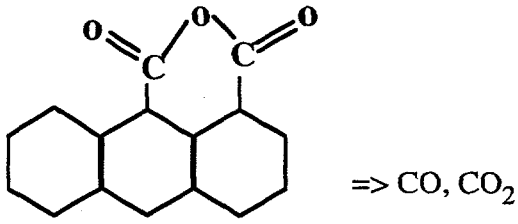

Carboxylic acid anhydride

The carboxylic acid anhydride {O=(C)-O-(C)=O} and lactone {O=(C)-O} surface complexes are larger than the CO-evolving semiquinone and ether-type complexes. Thus, the former may be

sterically hindered from forming in the smaller microporosity, while the latter are capable of forming on the surface of all the porosity. The nitrogen isotherm results show that the nonmicroporous portion of the porosity increases with burn-off for all three chars investigated. As a result, when the degree of burn-off increases, the capacity of the char porosity to host CO_2-evolving surface complexes also increases.

The conclusion that the apparent specific surface area is responsible for the CO evolution, and that the CO_2-evolving surface complexes are formed only on the surface area in the larger porosity is further supported by the data in Figures 3.25 to 3.27, which compare micropore volumes to "corrected" CO evolution, for Wyodak coal char, resin char, and Pittsburgh #8 coal char, respectively. Here the "corrected" CO was obtained by subtracting the total CO_2 desorption from total CO desorption during TPD. Since the carboxylic acid anhydride complexes decompose into one CO and one CO_2 molecule, at least some of the CO must arise from this source in the larger porosity. Therefore, "corrected" CO desorption data for the expected contribution from the carboxylic acid anhydrides should better follow the microporosity if the carboxylic acid anhydride complexes indeed exist only on the surface area in the larger porosity. As shown in Figures 3.25 to 3.27, the "corrected" CO improves the correlation with micropore volume for all three chars.

3.5. The Random Pore Model.

Random pore models have been used for analyzing gas-solid reaction systems by a number of workers (e.g., Hashimoto and Silveston, 1973; Simons and Finson 1979; Bhatia, 1985; Gavalas, 1980). Gavalas (1980) proposed a random pore model in which the number of intersections, length of pore segments, and evolution of pore volume and surface area are exactly and consistently derived from a single probability-density function characterizing the porous solid. He also applied this model to char gasification under conditions of chemical reaction rate control.

The purpose of the current work is to examine the feasibility of applying this type of model to the current data in order to determine the surface area variation with extent of gasification, and to

extend this model to the determination of pore size development during the gasification process.

3.5.1. Background and Theory.

In this model, the porous structure is assumed to consist of infinitely long, straight, cylindrical pores of radii in the range $R_* \leq R \leq R^*$. The axes of the pores are located completely randomly; that is, without any anisotropy or spatial correlation. With these assumptions, a fundamental relationship can be obtained :

$$1 - \varepsilon = \exp(-2\lambda\pi R^2) \qquad [3.2]$$

in accordance with the Poisson density distribution:

$$p(dS_L) = e^{-dN} \qquad [3.3]$$

where dS_L is a differential surface area element, dN is the lines of pores originating from an element dS_L and intersecting the sphere S, p is the probability that no lines of pores emanating from dS_L intersect the sphere S, λ is the density of pore numbers, ε is the void fraction, and R is the pore radius. Eq.[3.2] can be extended to the case of a continuous pore size distribution with the pore radius varying over the interval $[R_*,R^*]$ to yield the total void fraction, e_T:

$$\varepsilon_T = 1-\exp\left[-2\pi\int_{R_*}^{R^*} R^2\lambda(R)dR\right] \qquad [3.4]$$

If q(t) is the increase in pore radius over the time from zero to t, then the pore radius at time t is given by:

$$R(t) = R_o + q(t) \qquad [3.5]$$

The radius of the char particle must then decrease by the same amount:

$$R_p(t) = R_{po} - q(t) \qquad [3.6]$$

The probability density function at time t, given in terms of the original probability density function, $\lambda_{o,}$ is:

$$\lambda(R) = \lambda_o(R-q) = \lambda(R_o), \qquad [3.7]$$

and thus the total void fraction from Eq.[3.4] is given by:

$$\varepsilon_T(q) = 1-\exp\left[-2\pi\int_{R_*}^{R^*}(R_0+q)^2\lambda_0(R_0)dR_0\right] \qquad [3.8]$$

which may be rewritten as:

$$\frac{1-\varepsilon_T(q)}{1-\varepsilon_{T0}} = \exp[-2\pi(B_0q^2+2B_1q)] \qquad [3.9]$$

where

$$B_0 = \int_{R_{0*}}^{R_0^*}\lambda(R_0)dR_0 \qquad [3.10]$$

$$B_1 = \int_{R_{0*}}^{R_0^*}R_0\lambda(R_0)dR_0 \qquad [3.11]$$

The zeroth order moment, B_0, is the total number of pore axes which intersect a unit surface area, while the first moment, B_1, is equal to the product of B_0 and the mean pore radius.

As q increases by a length dq, the pore volume increases by $d\varepsilon_T = S(q)\,dq$, where S(q) is the total pore surface area. Hence:

$$S(q) = \frac{d\varepsilon_T}{dq} = 4\pi[1-\varepsilon_T(q)](B_0 q + B_1) \qquad [3.12]$$

The conversion, or burn-off, x_c, is defined by the amount of carbon reacted divided by the initial amount of carbon; that is:

$$x_c(q) = \frac{m_{t=0} - m_t}{m_{t=0}} = 1 - \left(1 - \frac{q}{R_p^0}\right)^3 \left[\frac{1-\varepsilon_T(q)}{1-\varepsilon_{T0}}\right] \qquad [3.13]$$

Substituting Eq.[3.9] into Eq.[3.13] yields:

$$x_c(q) = 1 - \left(1 - \frac{q}{R_{p0}}\right)^3 \exp[-2\pi(B_0 q^2 + 2B_1 q)] \qquad [3.14]$$

Under conditions of chemical reaction rate-control, it can be shown that $q << R_{po}$ (Gavalas, 1980). Therefore Eq.[3.14] can be reduced to the following form after neglecting the small correction due to the slight change in particle size:

$$x_c(t) = 1\text{-}\exp[-2\pi\,(B_0\, q^2 + 2B_1 q)] \qquad [3.15]$$

Combining Eqns. [3.9], [3.12] and [3.15] results in the following relationship between total pore surface area and conversion rate:

$$S(q) = 4\pi\,(1-\varepsilon_{To})(B_0 q + B_1)[1-x_c(t)] \qquad [3.16]$$

Here q can be expressed as:

$$q = v\,t \qquad [3.17]$$

where v is the velocity with which a pore surface element recedes due to reaction. Taking the derivative of Eq.[3.15] with respect to time yields:

$$\frac{dx_c}{dt} = 4\pi(B_0 v^2 t + B_1 v)\exp[-2\pi(B_0 v^2 t^2 + 2B_1 vt)] \qquad [3.18]$$

By eliminating t between Eqns. [3.15] and [3.18], the final relationship between reaction rate and the conversion or burn-off is obtained as:

$$\frac{dx_c}{dt} = 4\pi(1-x_c)\left[(B_1 v)^2 + \frac{B_0 v^2}{2\pi}\ln\left(\frac{1}{1-x_c}\right)\right]^{\frac{1}{2}} \qquad [3.19]$$

3.5.2. Extension of the Random Pore Model.

The random pore model proposed by Gavalas (1980) provides relationships among rate of reaction and total surface area and total void fraction. It is not capable of distinguishing microporosity from total porosity. The objective of the current work is to extend this random pore model to separate the microporosity from the larger porosity.

In order to achieve this goal, the probability density function, λ, for pore numbers has to be

determined first. Several models have been proposed to describe the pore size distribution of carbons. Laine and Yunes (1992) used a bimodal pore size distribution featuring both the widest macropores and the narrowest micropores among the samples they studied. Choma (1988) proposed a function associated with the gamma-type distribution to describe the distribution of micropores with respect to their dimension. A bimodal log-normal distribution was also used by Seaton *et al.* (1989) over both the micropore and mesopore size range. By assuming the formation of micropores to be a random process, Dubinin *et al.* (1986, 1987, 1990) proposed a normally-distributed micropore volume distribution for physical vapor adsorption in micropores of carbon. In the current study, the probability density function for the chars prior to oxidation, λ, was derived assuming a normally-distributed micropore volume distribution since the nitrogen adsorption data show that prior to activation, both Wyodak coal char and resin char are essentially microporous materials. The detailed derivation follows.

Let V(r) and N(r) be the volume and total numbers of pores over the radius range (r, r+dr), respectively, and V_T and N_T be the total pore volume and total pore numbers, respectively. Then:

$$N(r) \propto \frac{V(r)}{r^2} \qquad [3.20]$$

Therefore, if the probability density function for pore volume is a normal distribution:

$$\frac{V(r)}{V_T} = c_1 \exp\left[-\frac{(r_m - r)^2}{2\delta^2}\right], \qquad [3.21]$$

where c_1 is a constant, r_m is the mean pore radius, δ is the variance, and the probability density function for pore numbers, $\lambda(r)$, is given by:

$$\lambda(r)=\frac{N(r)}{N_T}=c_2\exp\left[-\frac{(r_m-r)^2}{2\delta^2}\right]\left(\frac{1}{r^2}\right), \qquad [3.22]$$

where c_2 is a constant.

Substituting Eq.[3.22] into the zeroth order moment, Eq.[3.10], and the first order moment, Eq.[3.11], yields:

$$B_0=\int_{R_{1micro}}^{R_{2micro}}\lambda(r)dr=c_2\int_{R_{1micro}}^{R_{2micro}}\frac{1}{r^2}\exp\left[-\frac{(r_m-r)^2}{2\delta^2}\right]dr \qquad [3.23]$$

and

$$B_1=\int_{R_{1micro}}^{R_{2micro}}r\lambda(r)dr=c_2\int_{R_{1micro}}^{R_{2micro}}\frac{1}{r}\exp\left[-\frac{(r_m-r)^2}{2\delta^2}\right]dr \qquad [3.24]$$

where $[R_{1micro}, R_{2micro}]$ is the micropore size range.

The initial void fraction (prior to oxidation), ε_{To} is determined by setting t = 0 and substituting Eq.[3.22] into Eq.[3.8]:

$$\varepsilon_{T0}=1-\exp\left\{-2\pi c_2\int_{R_{1micro}}^{R_{2micro}}\exp\left[-\frac{(r_m-r)^2}{2\delta^2}\right]dr\right\} \qquad [3.25]$$

Since the normalized probability function should be unity, or:

$$\int \frac{1}{\sqrt{2\pi}\delta} \exp\left[-\frac{(r_m - r)^2}{2\delta^2}\right] dr = 1 \quad , \qquad [3.26]$$

the constant for the probability density function is given by Eq.[3.25] as:

$$c_2 = \frac{\varepsilon_{T0}}{(2\pi)^{3/2}\delta} \qquad [3.27]$$

Therefore, the three parameters for the pore number probability density distribution are c_2, the mean radius, r_m, and the variance, δ, which are determined from Eqns. [3.23], [3.24], and [3.27].

Eq.[3.9] from the random pore model of Gavalas (1980) relates the total pore void fraction, ε_T, to the pore radius change q; and Eq.[3.12] relates the total surface area, pore size variation, and total void fraction. But this model is not capable of determining the fractions of surface area and void fraction contributed by the individual porosity type, such as the microporosity. The relationships among micropore void fraction and mean micropore radius change are developed here to describe microporosity development.

The total micropore void fraction, ε_{Tmicro}, at time t over the micropore size range [R_{1micro}, R_{2micro}] can be expressed, from the basic relationship Eq.[3.4], as:

$$\varepsilon_{Tmicro} = 1 - \exp\left(-2\pi \int_{R_{1micro}}^{R_{2micro}} r^2 \lambda(r) dr\right) \qquad [3.28]$$

If Δr is the radius change of micropores over the time [0, t], (i.e., $\Delta r = r - r_0$ by assuming the probability density function, λ, does not change with time, i.e.,

$$\lambda(r) = \lambda(r_0 + \Delta r) = \lambda_0(r_0) \qquad [3.29]$$

where λ_0 is the initial probability density function), then Eq.[3.28] can be rewritten as:

$$\varepsilon_{Tmicro}=1-\exp\left[-2\pi\int_{R_{1micro}}^{R_{2micro}}(r_0+\Delta r)^2\lambda_0(r_0)dr_0\right] \qquad [3.30]$$

Since the initial micropore void fraction, $(\varepsilon_{Tmicro})_0$, is expressed as:

$$(\varepsilon_{Tmicro})_0=1-\exp\left[-2\pi\int_{R_{1micro}}^{R_{2micro}}r_0^2\lambda_0(r_0)dr_0\right] \qquad [3.31]$$

The following relationship can be obtained by combining Eqns.(3.30) and (3.31):

$$\frac{1-\varepsilon_{Tmicro}}{1-(\varepsilon_{Tmicro})_0}=\exp\left\{-2\pi\int_{R_{1micro}}^{R_{2micro}}[(\Delta r)^2\lambda_0(r)dr+2r\Delta r\lambda_0(r)]dr\right\} \qquad [3.32]$$

Since Wyodak coal char and resin char are already microporous materials as pyrolyzed prior to oxidation (t = 0), for these chars it is feasible to set:

$$B_0=\int_{R_{1micro}}^{R_{2micro}}\lambda_0(r)dr \qquad [3.33]$$

$$B_1=\int_{R_{1micro}}^{R_{2micro}}r\lambda_0(r)dr \qquad [3.34]$$

Eq.[3.32] can be written as:

$$\frac{1-\varepsilon_{Tmicro}}{1-(\varepsilon_{Tmicro})_0}=\exp\{-2\pi[B_0(\Delta r)^2+2B_1\Delta r]\} \qquad [3.35]$$

The micropore surface area can then be calculated from:

$$S_{micro}=\frac{d\varepsilon_{Tmicro}}{d(\Delta r)}=4\pi(1-\varepsilon_{Tmicro})[(B_0\Delta r+B_1) \qquad [3.36]$$

Once the micropore void fraction, ε_{Tmicro}, is known, the mean micropore radius change, Δr, can be determined, (or vice versa), and the micropore surface area can be calculated.

3.5.3. Application of the Random Pore Model.

The samples used for the application of the random pore model are Wyodak coal char gasified in oxygen at 420°C, and resin char gasified in oxygen at 470°C. (A computer program for performing the detailed calculations is presented in Appendix D).

The theory for the reaction process is compared to the experimental data for Wyodak coal char and resin char. For both cases, linear regressions were performed using Eq.[3.19] in the form:

$$\left[\frac{1}{4\pi(1-x_c)}\frac{dx_c}{dt}\right]^2 = A_0 \ln\frac{1}{1-x_c}+A_1^2 \qquad [3.37]$$

where $A_0 = B_0v^2/(2\pi)$ and $A_1^2 = (B_1v)^2$. The linear fits for both chars in Figures 3.28 and 3.29 show that the data do indeed follow the form of the model.

A_0 and A_1 are determined from these plots as the slope, A_0, and the intercept, A_1^2. From these values and the surface area at one point, such as at 5% burn-off, the parameters B_0, B_1 and v can be obtained. The apparent surface area can then be determined from the reaction rate data by the general expression of Eq.[3.16]. Figures 3.30 and 3.31 present comparisons of the surface areas predicted

from the random pore model with those determined from nitrogen isotherm data for Wyodak coal char and resin char, respectively. As shown, the agreement between the two is quite good. Therefore, it is concluded that the random pore model satisfactorily correlates the specific surface area evolution with burn-off from the reaction rate data.

Eq.[3.35] relates the total micropore void fraction, ε_{Tmicro}, to the mean micropore radius change, Δr; and Eq.[3.36] relates the total micropore surface area, S_{micro}, the mean micropore radius change, Δr, and total micropore void fraction, ε_{Tmicro}. These expressions are used here for the determination of the microporosity. The micropore void fraction, ε_{Tmicro}, was determined from nitrogen adsorption isotherm data, the mean micropore radius change, Δr, is given by Eq.[3.35], and the total micropore surface area, $S_{micro,}$ is determined by Eq.[3.36]. The difference between total surface area and micropore surface area is the nonmicroporous surface area.

The adsorption data show that as gasification proceeds, the micropores continue to develop to the maximum in the surface area, and thereafter some of these micropores become mesopores (or even macropores); i.e., the population of micropores begins to decrease. The application of the random pore model to these chars indicates a similar trend. Figure 3.32 presents the change of the mean micropore size, Δr, as a function of burn-off for both Wyodak coal char and resin char. As can be seen, at low burn-off, the mean micropore radius increases, and reaches a peak value around 40% burn-off, and then as the burn-off increases, the mean micropore radius decreases. At the same time, the larger porosity develops and some of the pore walls collapse as the burn-off proceeds, thereby causing surface area loss at high conversion.

These results can be seen more clearly in Figure 3.33, which presents the mean micropore radius as a function of burn-off for both Wyodak coal char and resin char. Here the initial mean pore radius (prior to oxidation) was determined from Eqns [3.25] to [3.27], assuming a normal micropore volume distribution. The resultant mean pore radius prior to oxidation is 1.04 nm for Wyodak coal char, and 0.64 nm for resin char. The variance of the normal distribution is 0.24 nm for Wyodak coal char, and 0.18 nm for resin char. These results indicate that the pore size is larger, and the pore

distribution is broader for Wyodak coal char than for resin char before activation.

The corresponding mean pore radius and variance were not able to be found from Eqns. [3.15] to [3.27] for Pittsburgh #8 coal char prior to oxidation. This is most probably due to the initially nonporous nature of the char, and that the assumption of a normal micropore volume distribution is not suitable for the unactivated Pittsburgh #8 coal char.

It is noted that the rate of mean micropore radius decrease with burn-off at high conversion is much slower for resin char than for Wyodak coal char. This result suggests that the percentage of micropores converted to larger pores is smaller for resin char than for Wyodak coal char; i.e., resin char remains more microporous with burn-off. This conclusion is also apparent from Figures 3.34 and 3.35, which present the nonmicroporous surface area for both chars.

It is concluded that the random pore model theory is capable of providing reasonable predictions of the porosity upon gasification for both resin char and Wyodak coal char. This model can also be extended to determine porosity development. Since the surface areas obey the master curve of Eq.[3.19], and the total surface area and total CO surface complex desorbed during TPD are correlated, it is possible to determine the surface area just from the TPD data. If the data for the micropore volume are available, the nonmicroporous and microporous surface area, and microporosity development can be determined.

3.6. Correlation/Prediction of Porosity Development *via* TPD.

From the preceding discussions, it has been concluded that CO is formed over the surface area of all porosity, and the total CO evolution from TPD and total surface area are correlated. Figures 3.36 and 3.37 present the measured total surface area as a function of the total CO evolution for resin char and Wyodak coal char, respectively. As can be seen, the relationship between the total surface area and total CO evolution is close to linear for both chars, and can be expressed as:

$$S_{total} = a_1 + a_2 \times m_{CO} \qquad [3.37]$$

where S_{total} is the total surface area, m_{CO} is the total amount of CO evolved during TPD, a_1 and a_2 are constants.

It has been also concluded that "corrected" CO desorption (= total CO - total CO_2 evolved) data for the expected contribution from the carboxylic acid anhydrides improves the correlation with the microporosity. Therefore the "corrected" CO and the micropore volume should be correlated. Figures 3.38 and 3.39 present the micropore volume as a function of "corrected CO" evolution. As shown, the relationship between them is also near linear for both chars, and can expressed as:

$$V_{micro} = b_1 + b_2 \times m_{(CO\text{-}CO_2)} \qquad [3.38]$$

where V_{micro} is the micropore volume, $m_{(CO\text{-}CO_2)}$ is the "corrected" CO evolution from TPD, and b_1 and b_2 are constants.

By knowing the total surface and micropore volume at any two points (for example, by obtaining nitrogen isotherms), the constants, a_1, a_2, b_1, b_2, can be determined. This is equivalent to *calibrating* the gas evolution from TPD. Following this, the total surface area as a function of CO evolution from TPD, and micropore volume as a function of CO_2 evolution from TPD can be determined. This approach then constitutes a new method for the characterization of the porosity of carbons and chars.

As discussed above, development of the porosity, such as the microporosity, can be further examined using the random pore model, knowing the requisite information about the total surface area and micropore volume. Therefore, the combination of desorption methods with the extended random pore model can be used to monitor porosity development.

3.7. Summary and Conclusions

Oxygen gasification, and subsequent temperature programmed desorption (TPD) have been carried out for resin char, Wyodak coal char and Pittsburgh #8 coal char samples. The rate of conversion and the features of desorption were examined. The porosity characteristics of these chars

were obtained using the α_s-plot method from nitrogen isotherm data.

The results from nitrogen adsorption isotherm data show that Wyodak coal char is microporous prior to activation in oxygen. Its porosity develops continuously with burn-off, and about half of the total surface area is due to the larger pores at 80% burn-off. The resin char is also a microporous material before activation in oxygen, but the rate of pore size development is slower with burn-off, and at 72% burn-off, only 5% of the surface area is contributed by the larger porosity. Pittsburgh #8 coal char is essentially a nonporous material prior to activation in oxygen, but as gasification proceeds, the porosity creates and develops rapidly, and at 80% burn-off, more than half the surface area (about 61%) is due to the larger porosity. The total surface area of these char samples increase with degree of burn-off at low conversion, attain a maximum at about 40% burn-off, and then decrease as gasification proceeds. At the same time, the percentage of nonmicroporous surface area increases continuously with burn-off. The correlation between the total surface area and total amount of CO evolved upon TPD is almost linear. The surface area of larger pores (mesoporosity, or even macroporosity) and the total CO_2 evolved upon TPD are also correlated.

It is concluded from these results that the CO complexes are formed over the entire surface area of the chars during gasification, but that the surface area in the larger porosity is responsible for the formation of CO_2-evolving complexes.

The favorable comparison of the random pore model theory with the nitrogen adsorption isotherm data supports the feasibility for the application of this theory to these samples. Therefore, the total surface area during the entire burn-off history can be determined from the information of conversion rate *via* a master curve obtained from Eq.[3.16]. The random pore model predicts that at low conversion, the mean micropore radius increases, and attains a peak value around 40% burn-off, and then decreases with burn-off. At the same time, the larger pores develop and some of the pore walls of the smaller porosity collapse as the burn-off proceeds. This causes surface area loss at high conversion.

The total surface area and total CO surface complex desorbed during TPD are correlated, and as

are nonmicroporous surface area and CO_2 desorbed during TPD. The relationship between micropore volume and the "corrected" CO for the expected contribution from the carboxylic acid anhydrides is linear. It is possible to predict total surface area and micropore volume from TPD spectra. From the extended random pore model, additional information about the micropore surface area, the nonmicroporous surface area, and the mean micropore size development as a function of reaction time (or burn-off) can be predicted. Therefore, combining the TPD technique and the extended random pore model sets a new method for characterization of the porosity for carbons.

Table 3.1. Summary of experimental results for TPD of Wyodak coal char gasified in oxygen at 390°C and 10% burn-off.			
Heating rate (K/min)	**Total integrated CO (mmol/g)**	**Total integrated CO_2 (mmol/g)**	**$\frac{CO_2}{CO+2CO_2}$**
25	2.51	0.69	0.177
50	2.56	0.67	0.165
75	2.33	0.58	0.164
100	2.55	0.65	0.169

Table 3.2. Summary of experimental results for Wyodak coal char.							
Burn-off(%)	0	5	17	33	50	66	80
Reaction time(min)	0	18	47	86	120	165	210
Rate of conversion (g/g/hr)		0.18	0.26	0.27	0.24	0.21	0.14
Apparent surface area $A_t(m^2/g)$	180	275	339	377	319	275	174
Micropore volume V_m (cm^3/g)	0.097	0.156	0.205	0.242	0.202	0.124	0.066
Nonmicropore surface area $A_{ex}(m^2/g)$	27.5	46.3	75.3	92	92.7	105	88.3
A_{ex}/A_t	0.15	0.18	0.22	0.24	0.29	0.38	0.51
Total CO from TPD (mmol/g)		1.45	3.28	3.92	4.07	3.09	1.98
Total CO_2 from TPD (mmol/g)		0.4	0.74	0.99	1.16	1.14	1.23
CO_2/CO		0.28	0.22	0.25	0.29	0.37	0.62

Table 3.3. Summary of experimental results for Pittsburgh #8 coal char.

Burn-off (%)	0	5	17	33	50	66	80
Reaction time (min)	0	13	39	60	78	114	178
Rate of conversion (g/g/hr)		0.28	0.45	0.50	0.42	0.26	0.13
Apparent surface area $A_t(m^2/g)$	2.9	30	42.3	54.2	36.2	27.8	23.9
Micropore volume V_m (cm^3/g)	0.001	0.015	0.021	0.027	0.015	0.01	0.005
Nonmicropore surface area $A_{ex}(m^2/g)$	0.5	4.63	14.8	18	16.2	15.6	14.6
A_{ex}/A_t	0.17	0.174	0.35	0.33	0.45	0.56	0.61
Total CO from TPD (mmol/g)		0.65	0.77	1.15	0.91	0.92	0.86
Total CO_2 from TPD (mmol/g)		0.137	0.143	0.234	0.253	0.258	0.305
CO_2/CO		0.21	0.185	0.203	0.278	0.28	0.354

Table 3.4. Summary of experimental results for resin char.

Burn-off(%)	0	5	15	30	45	60	72
Reaction time(min)	0	14	31	45	66	92	130
Rate of conversion (g/g/hr)		0.23	0.38	0.50	0.54	0.43	0.22
Apparent surface area $A_t(m^2/g)$	61	269	365	455	504	455	451
Micropore volume V_m (cm^3/g)	0.038	0.161	0.246	0.308	0.38	0.30	0.30
Nonmicropore surface area $A_{ex}(m^2/g)$	2.1	9.9	15.1	22		23	23.4
A_{ex}/A_t	0.034	0.037	0.041	0.048		0.051	0.052
Total CO from TPD (mmol/g)		3.06	3.73	5.04	5.38	5.19	5.13
Total CO_2 from TPD (mmol/g)		0.3	0.37	0.74	0.89	0.93	0.99
CO_2/CO		0.099	0.098	0.146	0.166	0.179	0.193

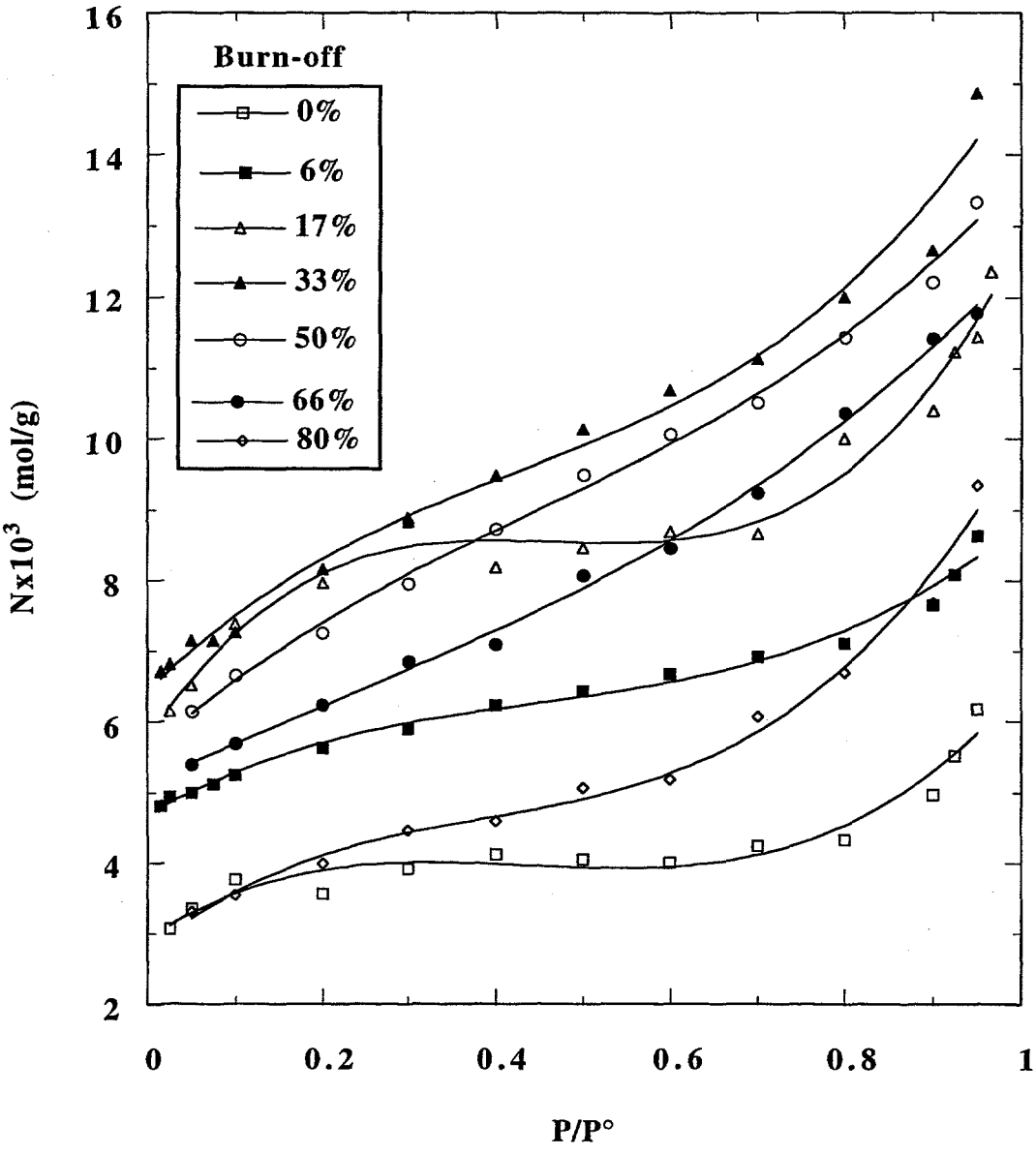

Figure 3.1. Nitrogen desorption isotherms for Wyodak coal char samples as a function of burn-off in oxygen at 420°C.

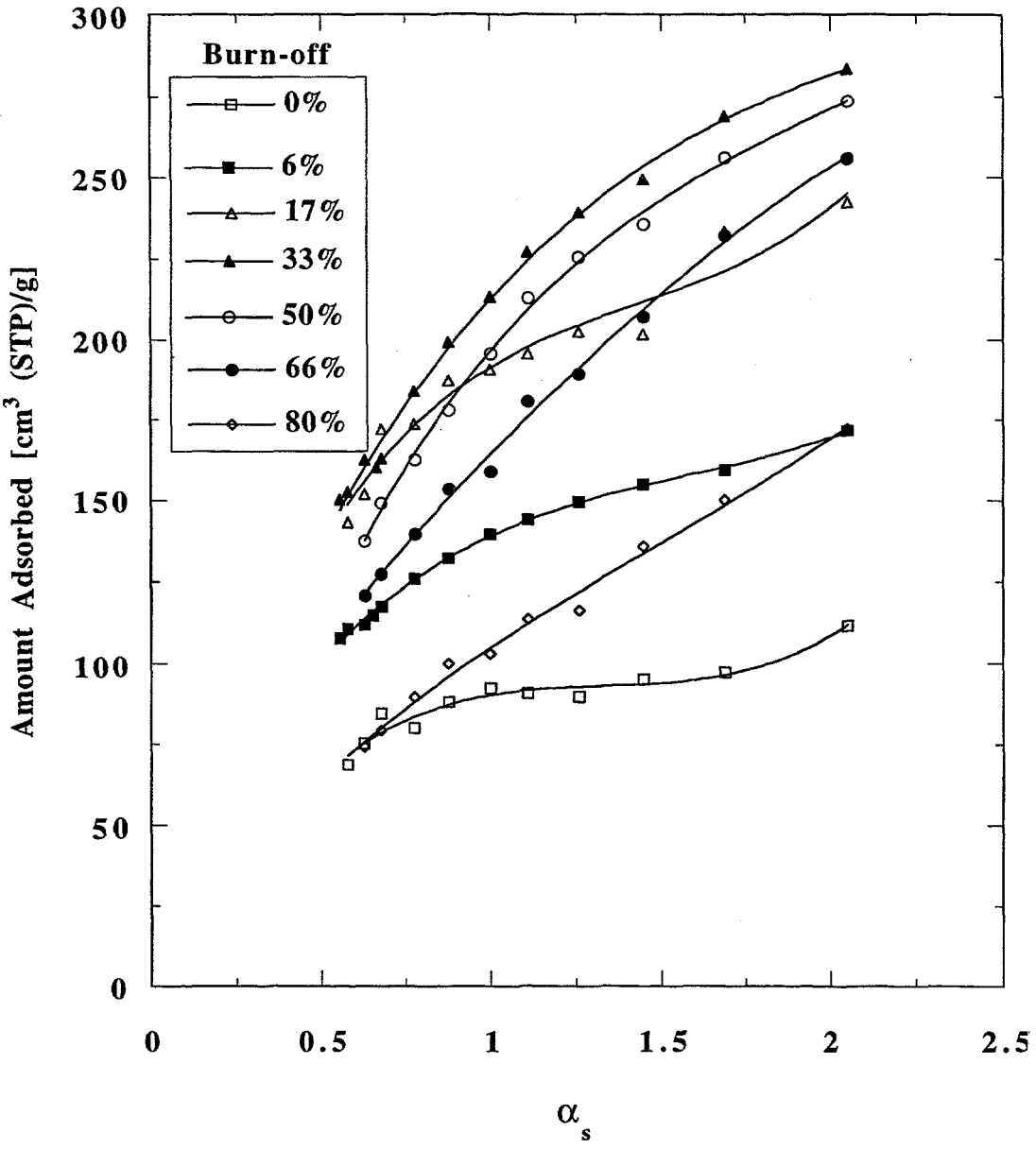

Figure 3.2. α_S-plots for Wyodak coal char samples constructed from the nitrogen desorption isotherm data presented in Figure 3.1.

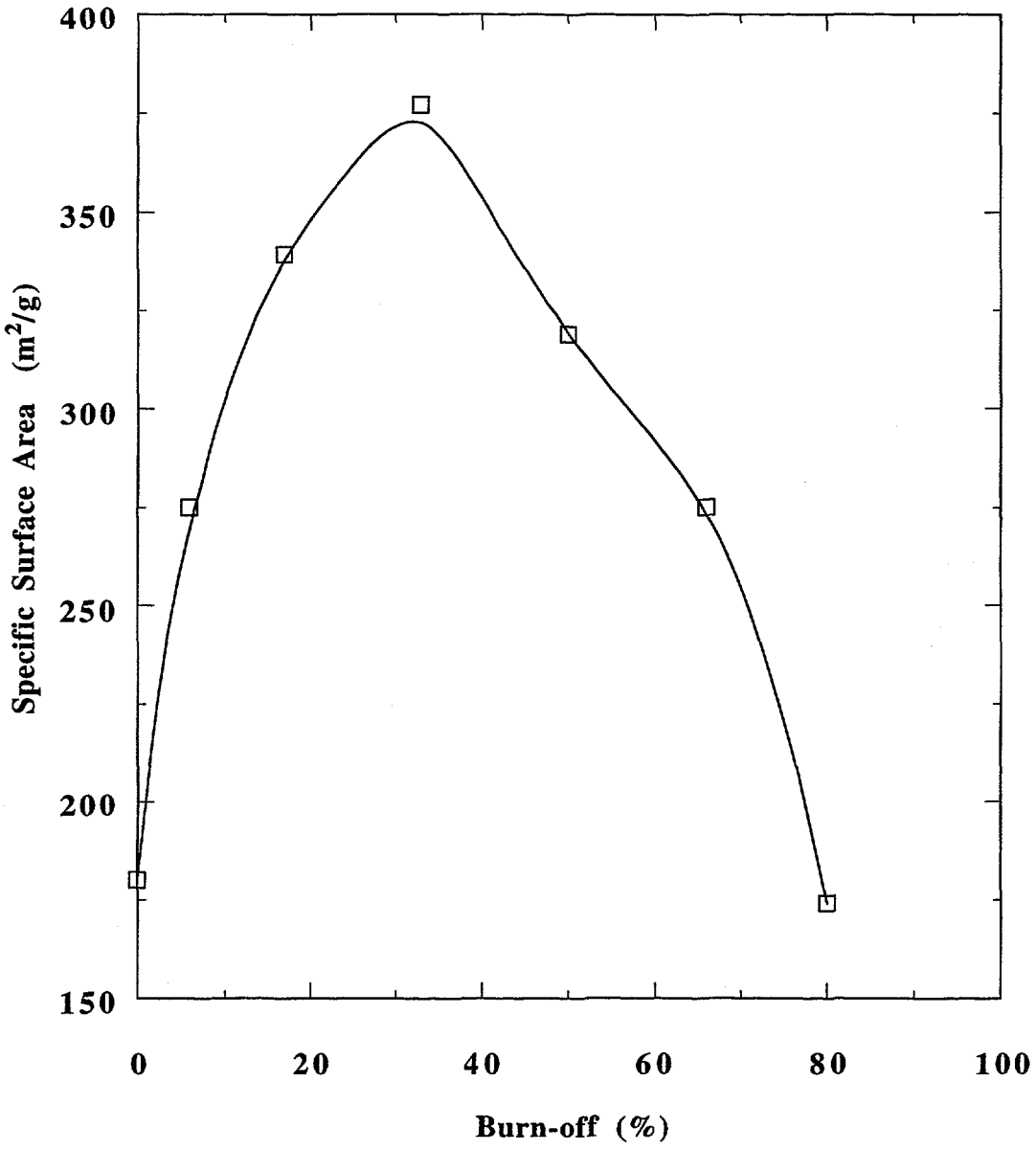

Figure 3.3. Variation of total specific surface area with burn-off for Wyodak coal char, obtained from the α_s-plots presented in Figure 3.2.

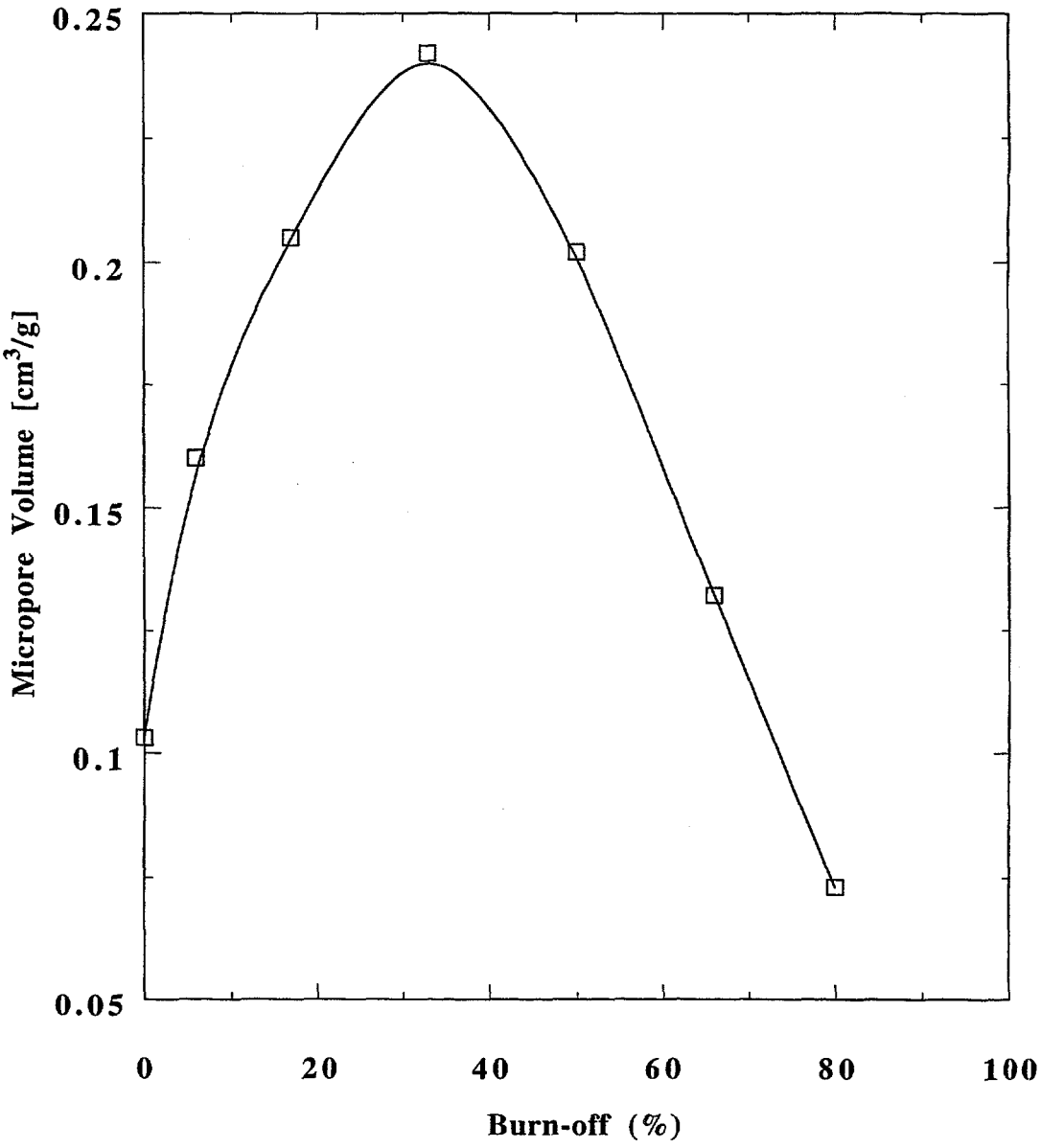

Figure 3.4. Variation of micropore volume with burn-off for Wyodak coal char, obtained from the α_s-plots presented in Figure 3.2.

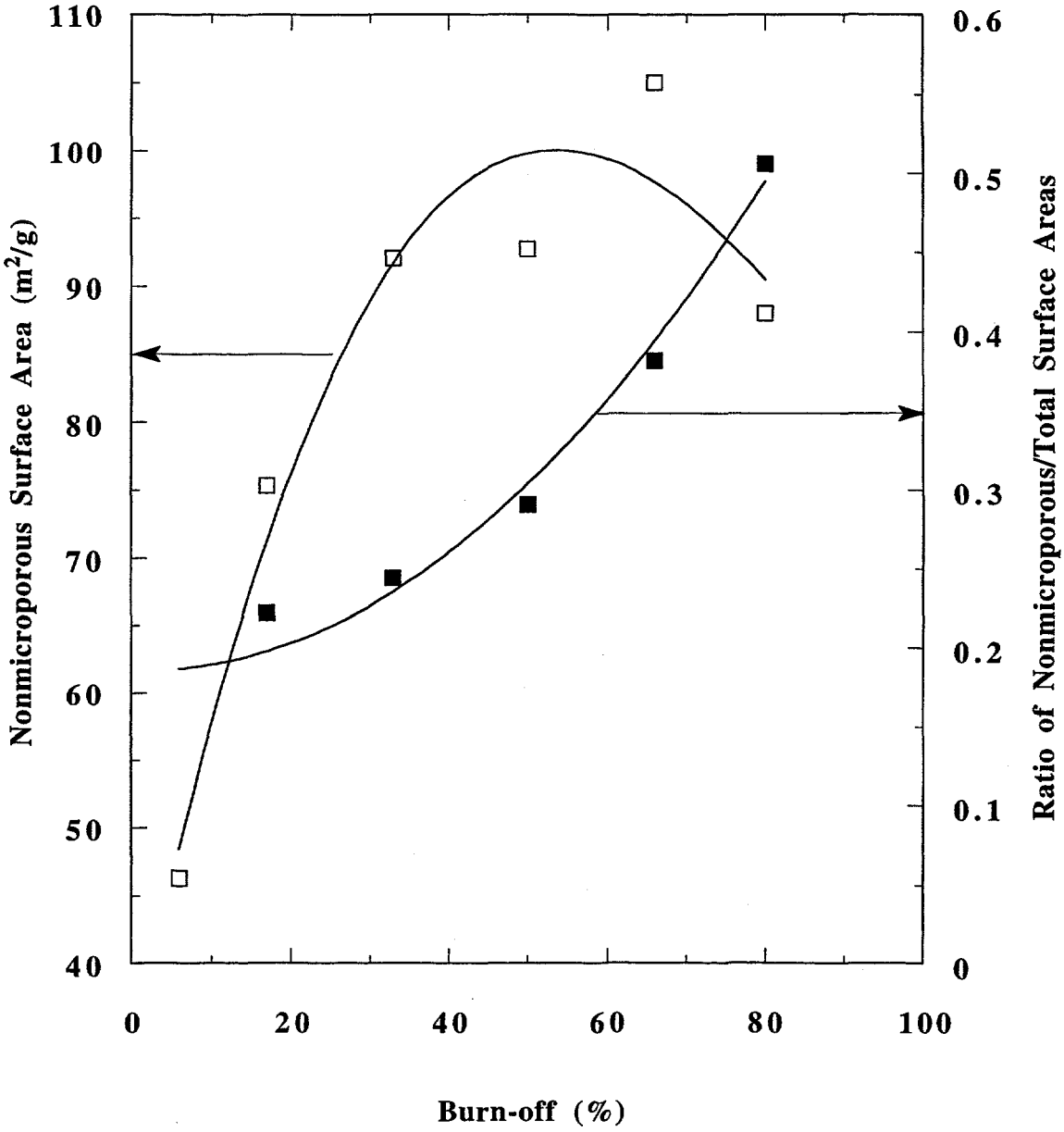

Figure 3.5. Variation of nonmicroporous surface area with burn-off for Wyodak coal char, obtained from the α_S-plots presented in Figure 3.2.

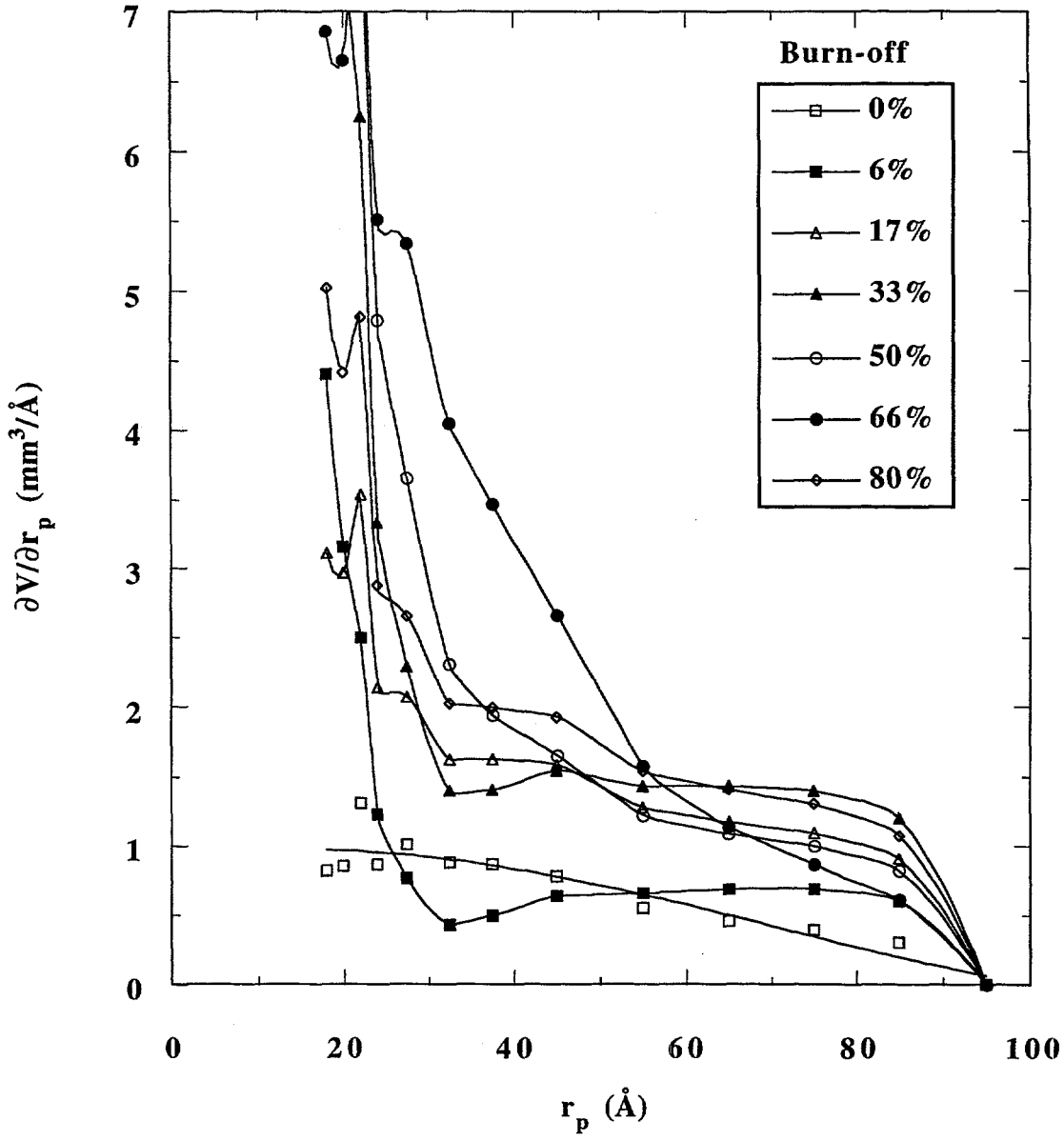

Figure 3.6. Mesopore size distributions for Wyodak coal char, as determined by the method of Roberts (1967) from the nitrogen desorption isotherm data presented in Figure 3.1.

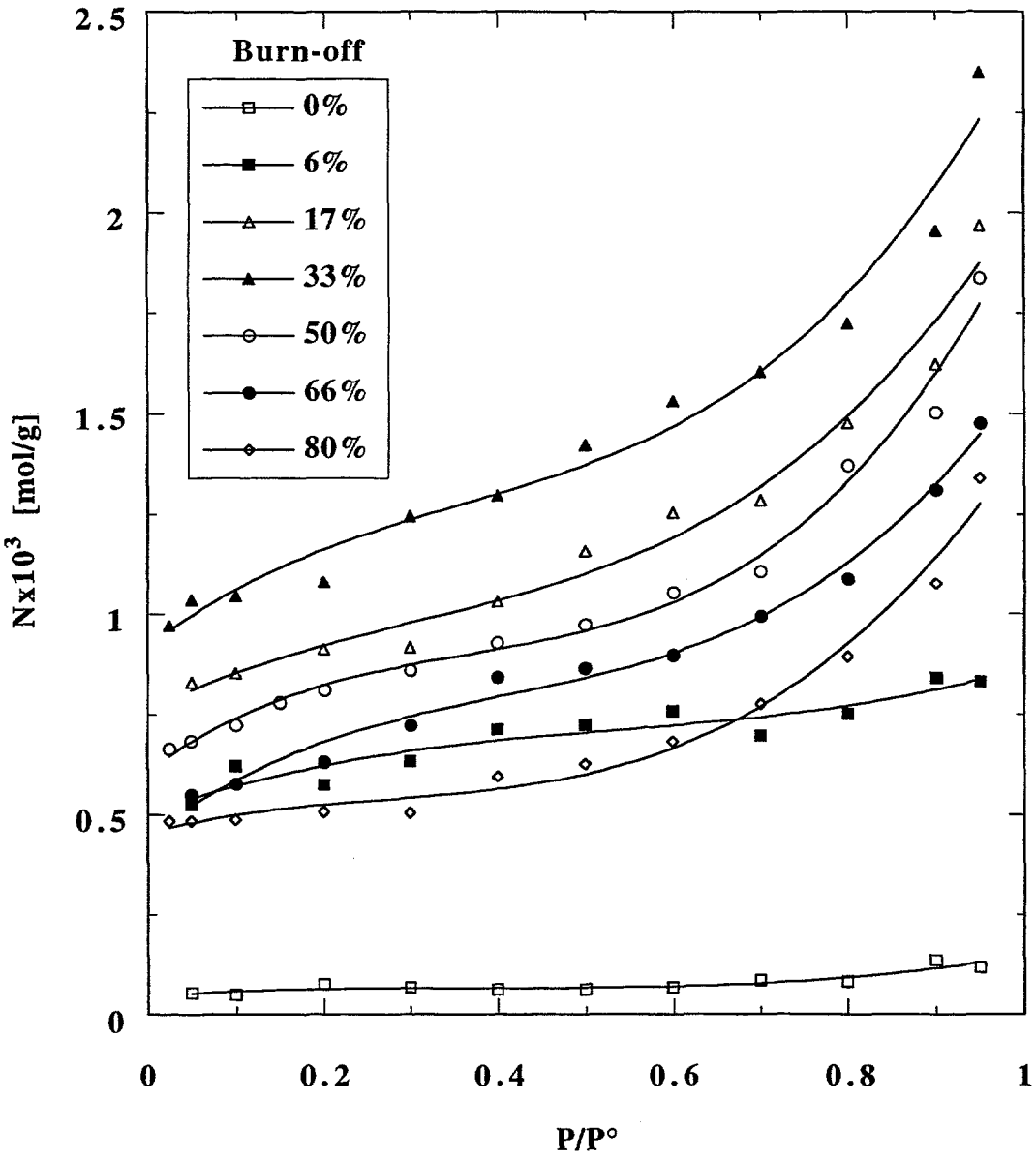

Figure 3.7. Nitrogen desorption isotherms for Pittsburgh #8 coal char samples gasified in oxygen at 470°C.

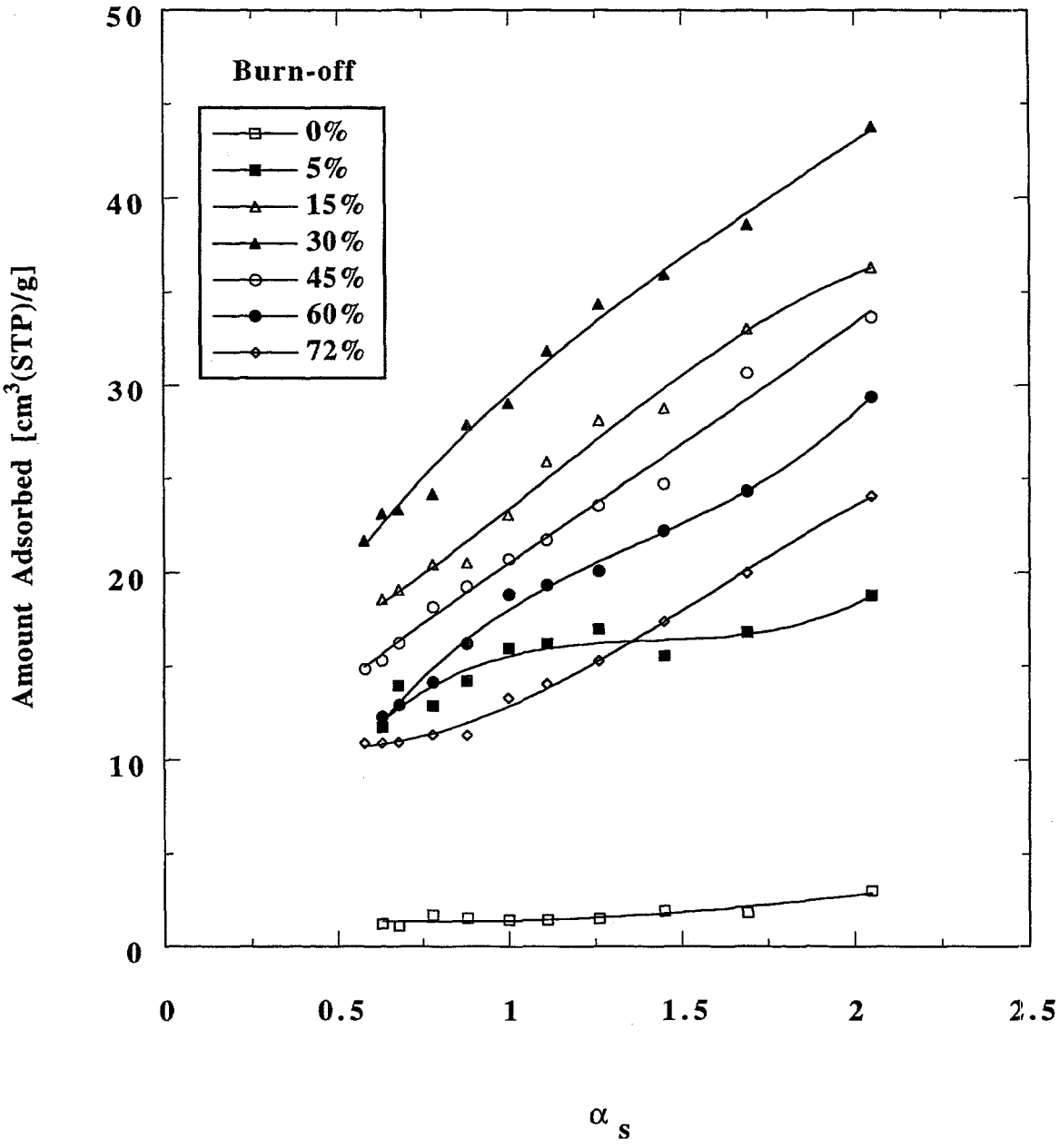

Figure 3.8. α_s-plots for Pittsburgh #8 coal char samples constructed from the nitrogen desorption isotherm data presented in Figure 3.7.

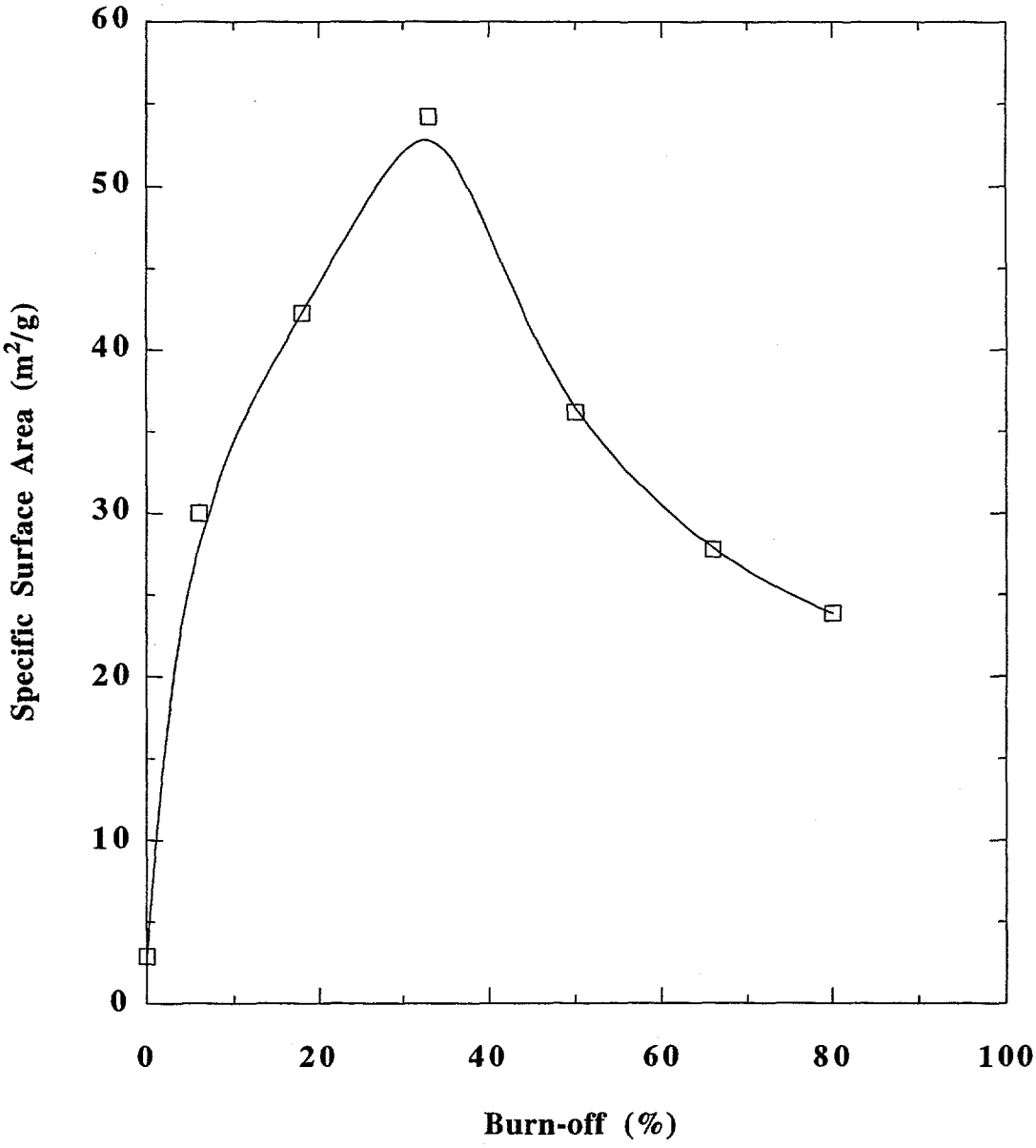

Figure 3.9. Apparent specific surface area as a function of burn-off for Pittsburgh #8 coal char, obtained from the α_s-plots presented in Figure 3.8.

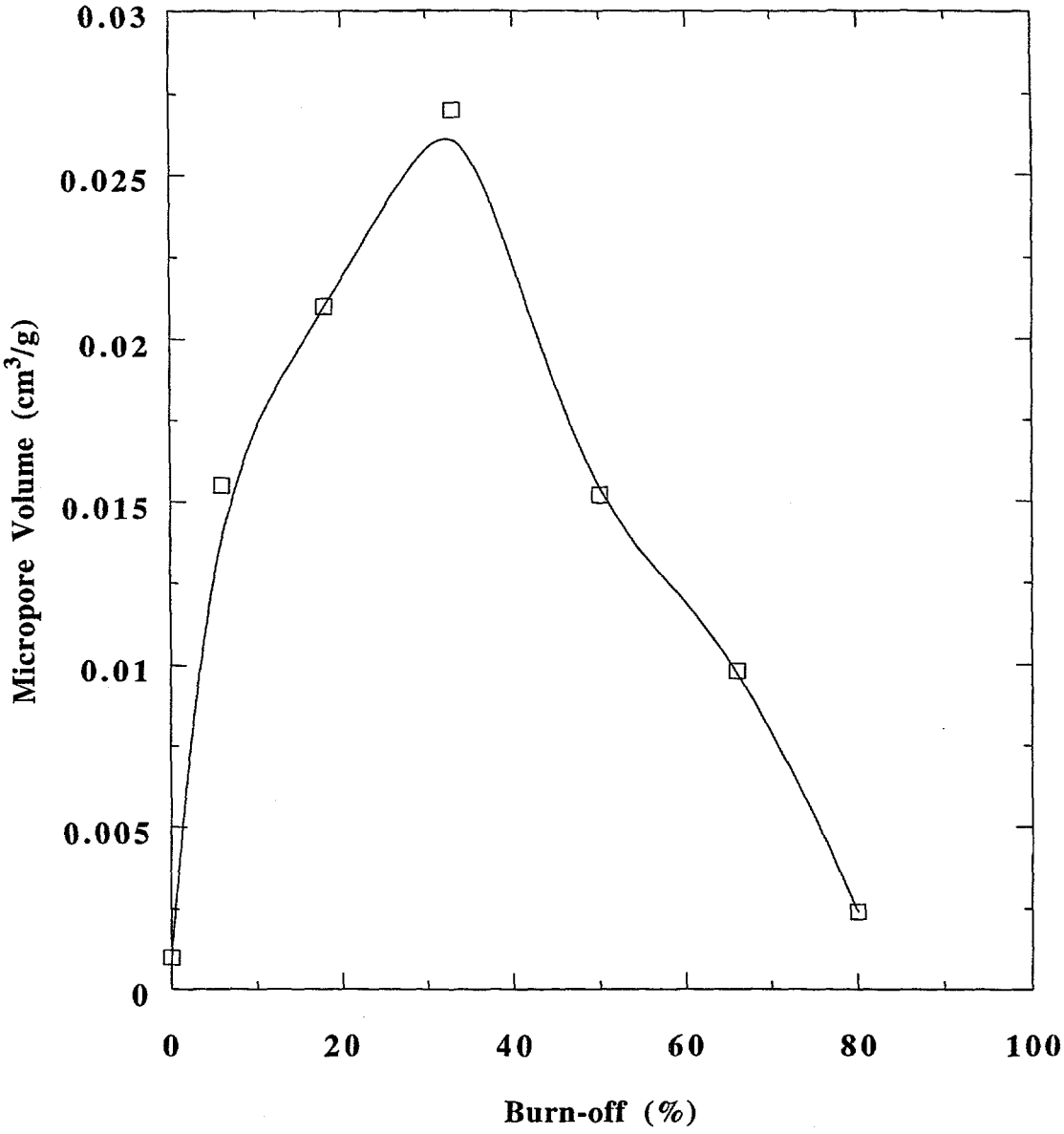

Figure 3.10. Micropore volume as a function of burn-off for Pittsburgh #8 coal char, obtained from the α_S-plots presented in Figure 3.8.

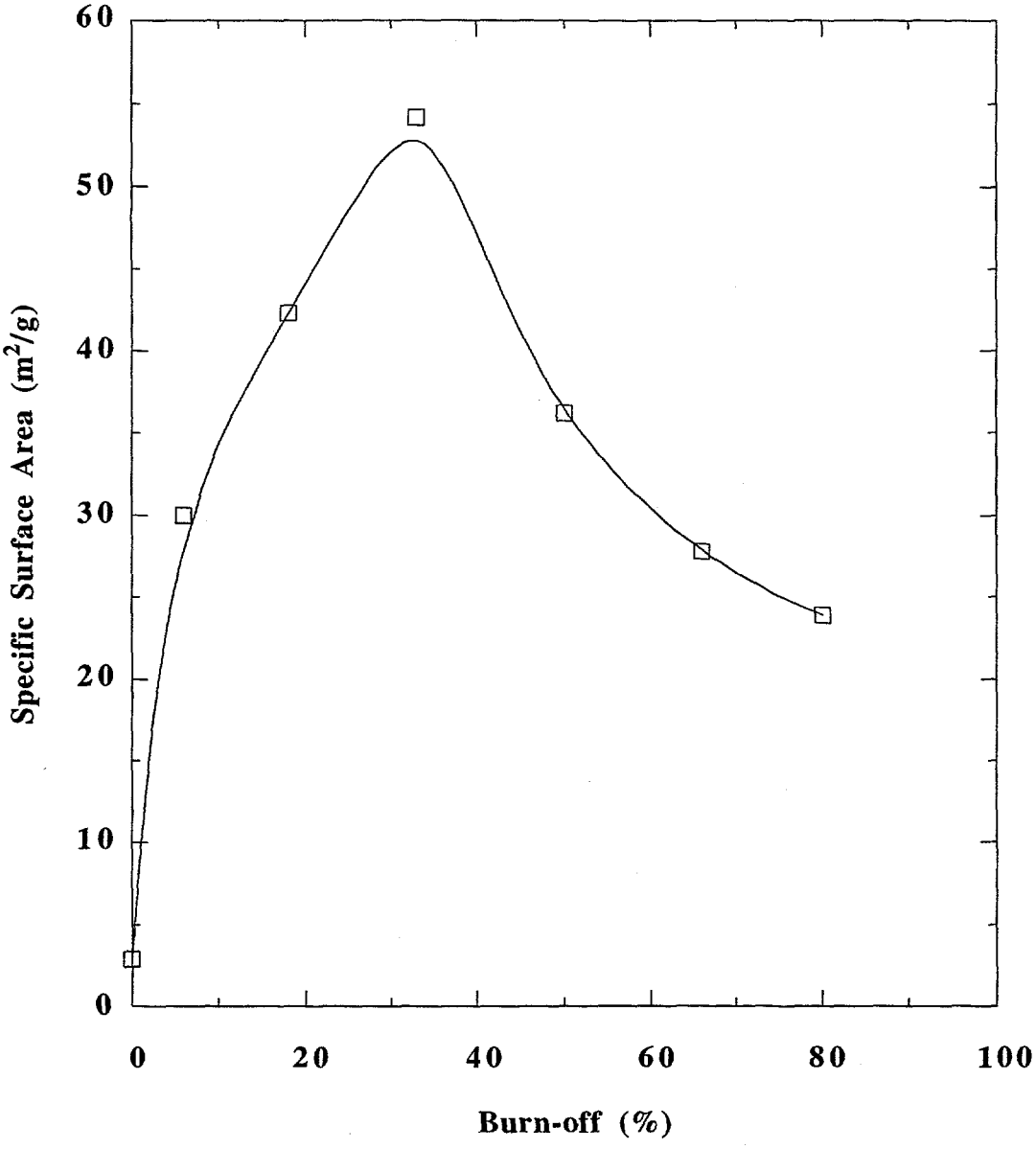

Figure 3.11. Apparent specific surface area as a function of burn-off for Pittsburgh #8 coal char, obtained from the α_s-plots presented in Figure 3.8.

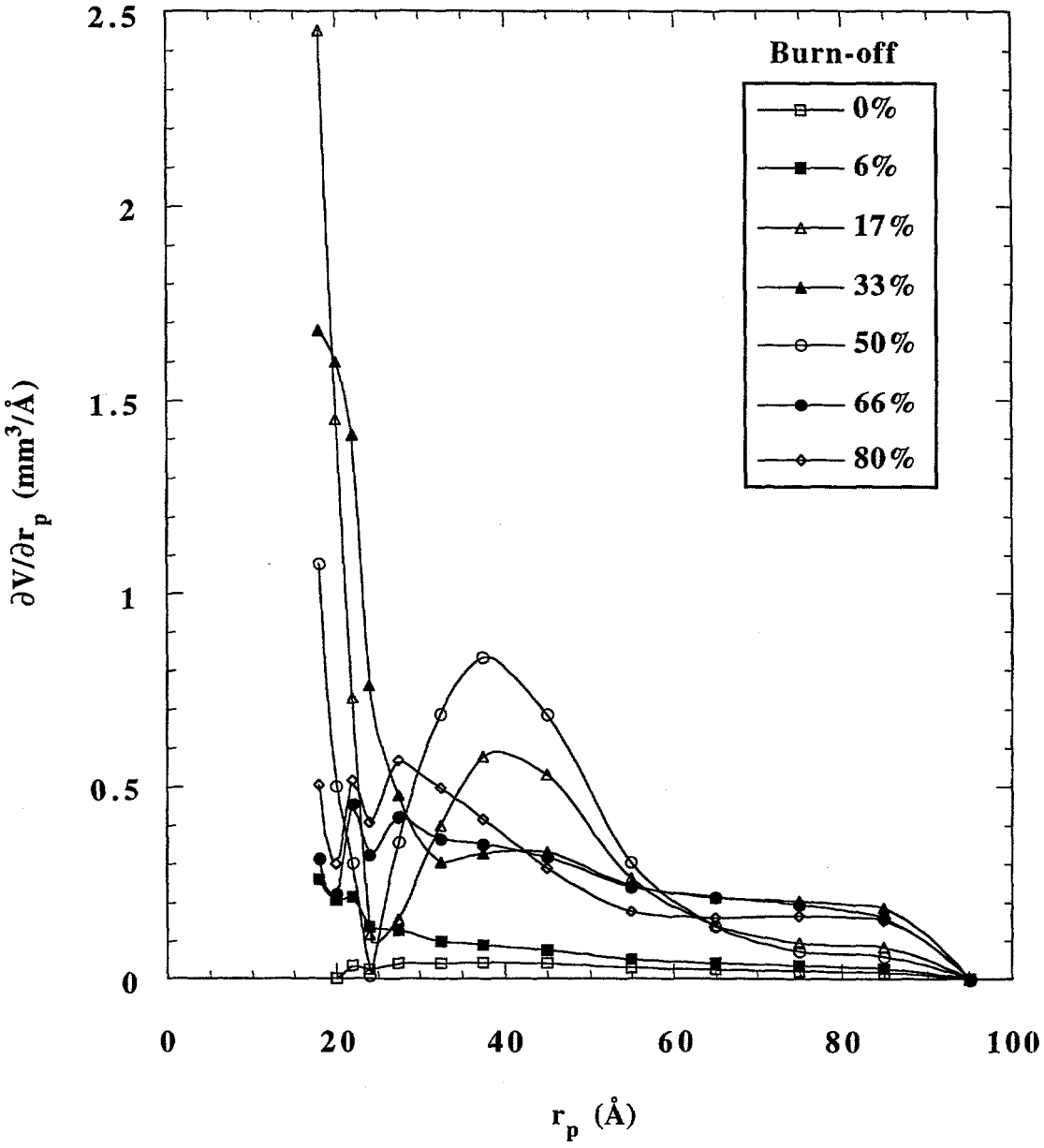

Figure 3.12. Mesopore size distributions for Pittsburgh #8 coal char gasified in oxygen at 470°C, as determined by the method of Roberts (1967).

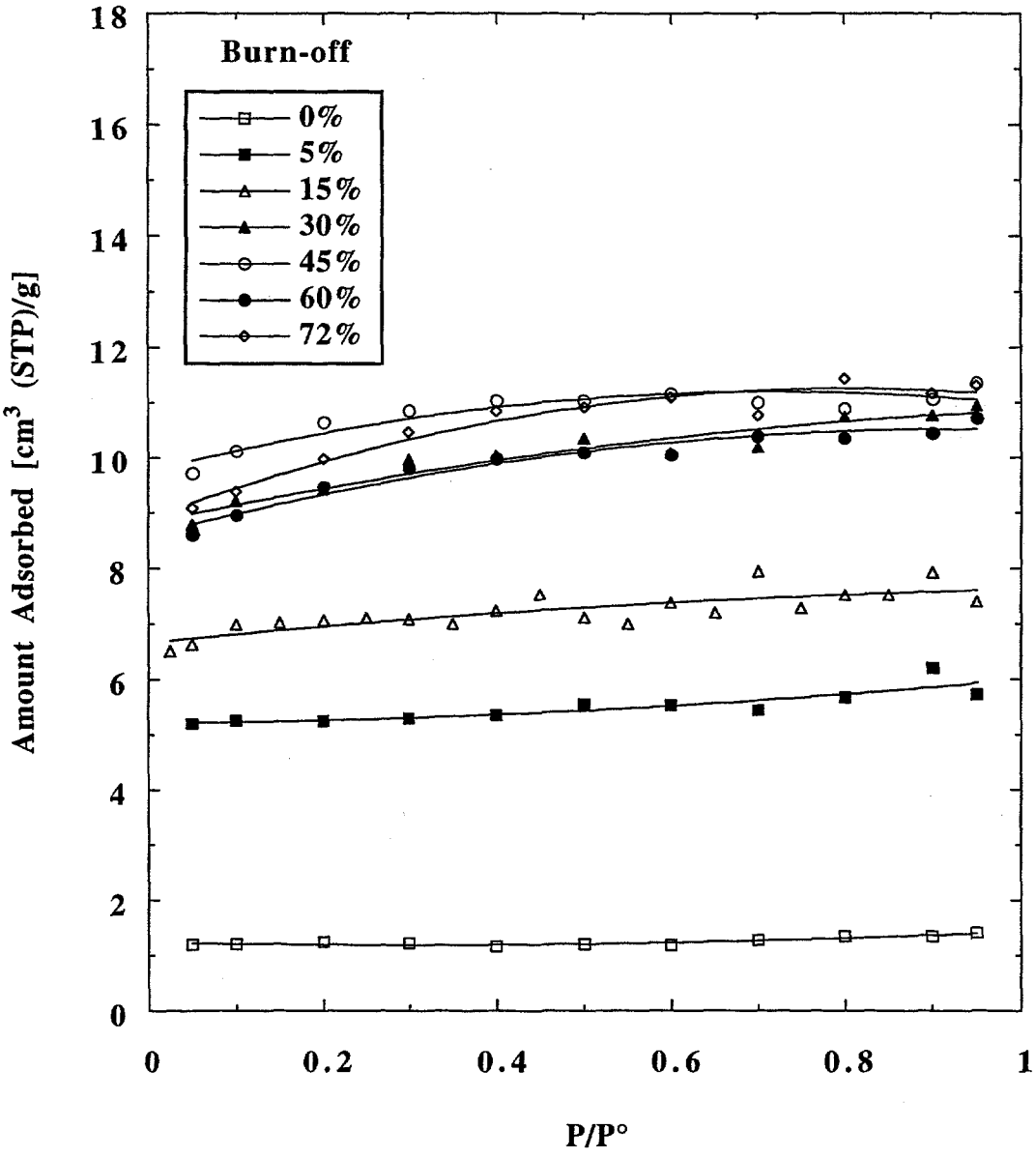

Figure 3.13. Nitrogen desorption isotherms for phenol-formaldehyde resin coal char gasified in oxygen at 470°C.

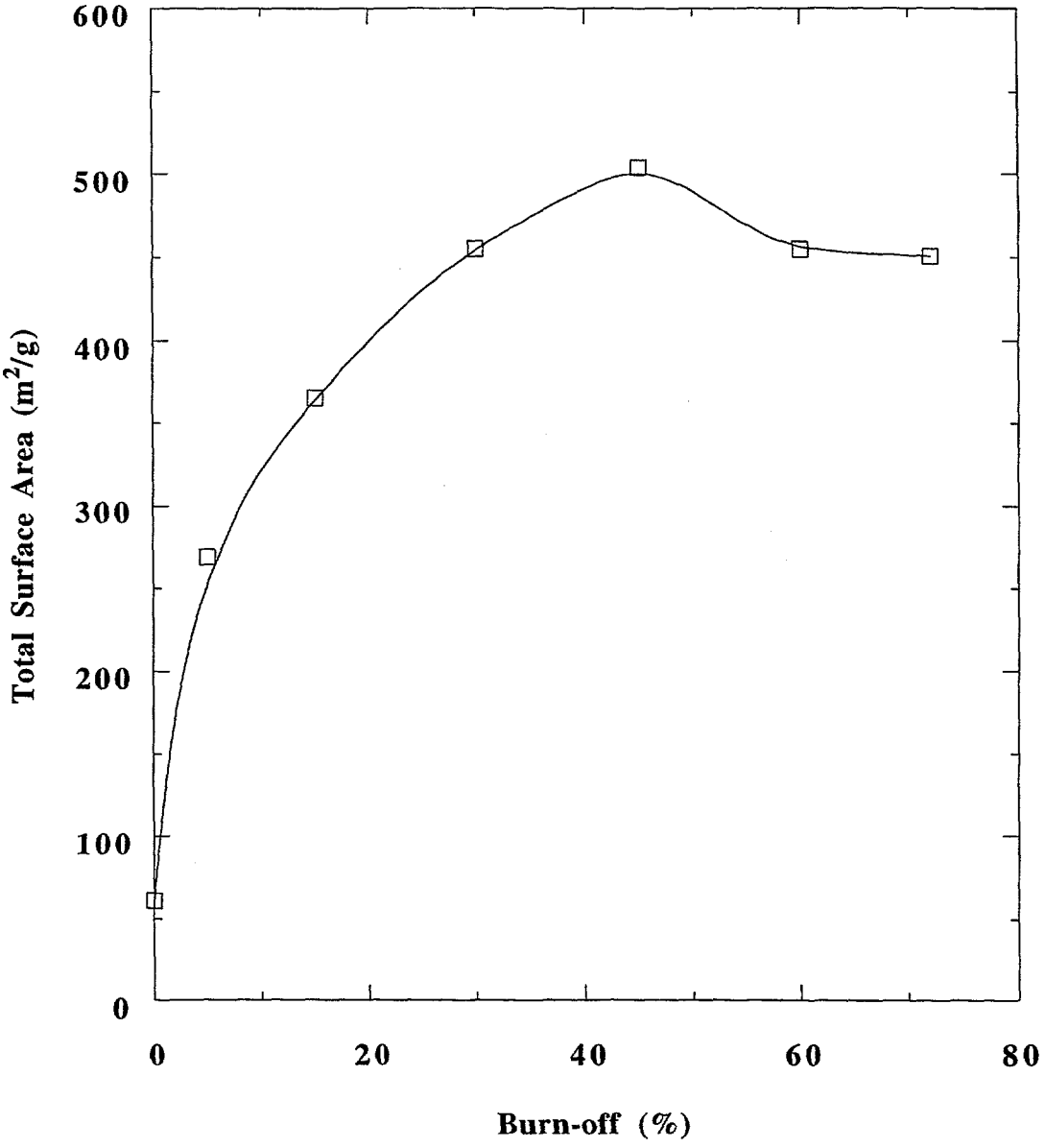

Figure 3.14. Total surface area as a function of burn-off for resin char gasified in oxygen at 470°C.

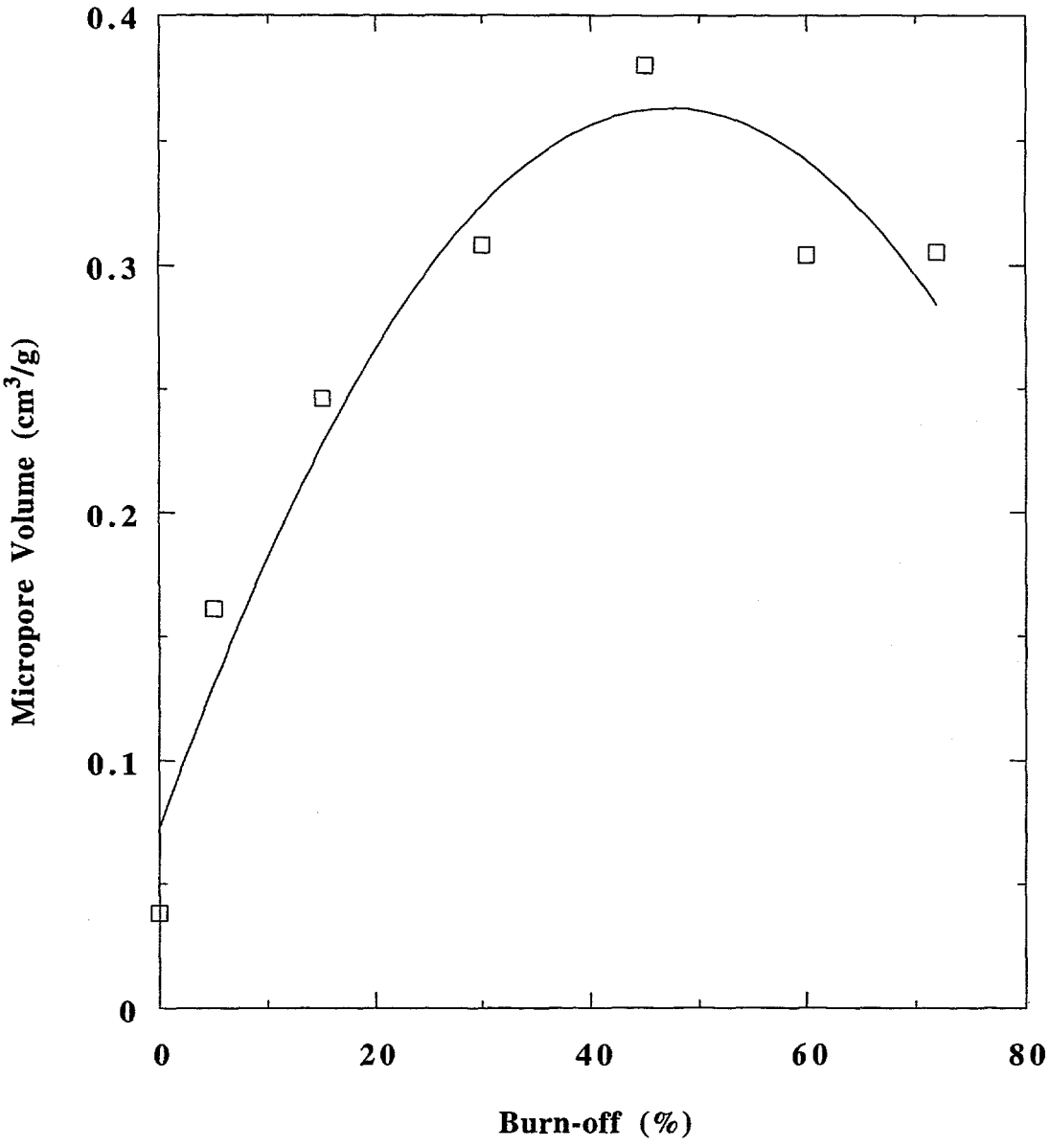

Figure 3.15. Micropore volume as a function of burn-off for resin char gasified in oxygen at 470°C.

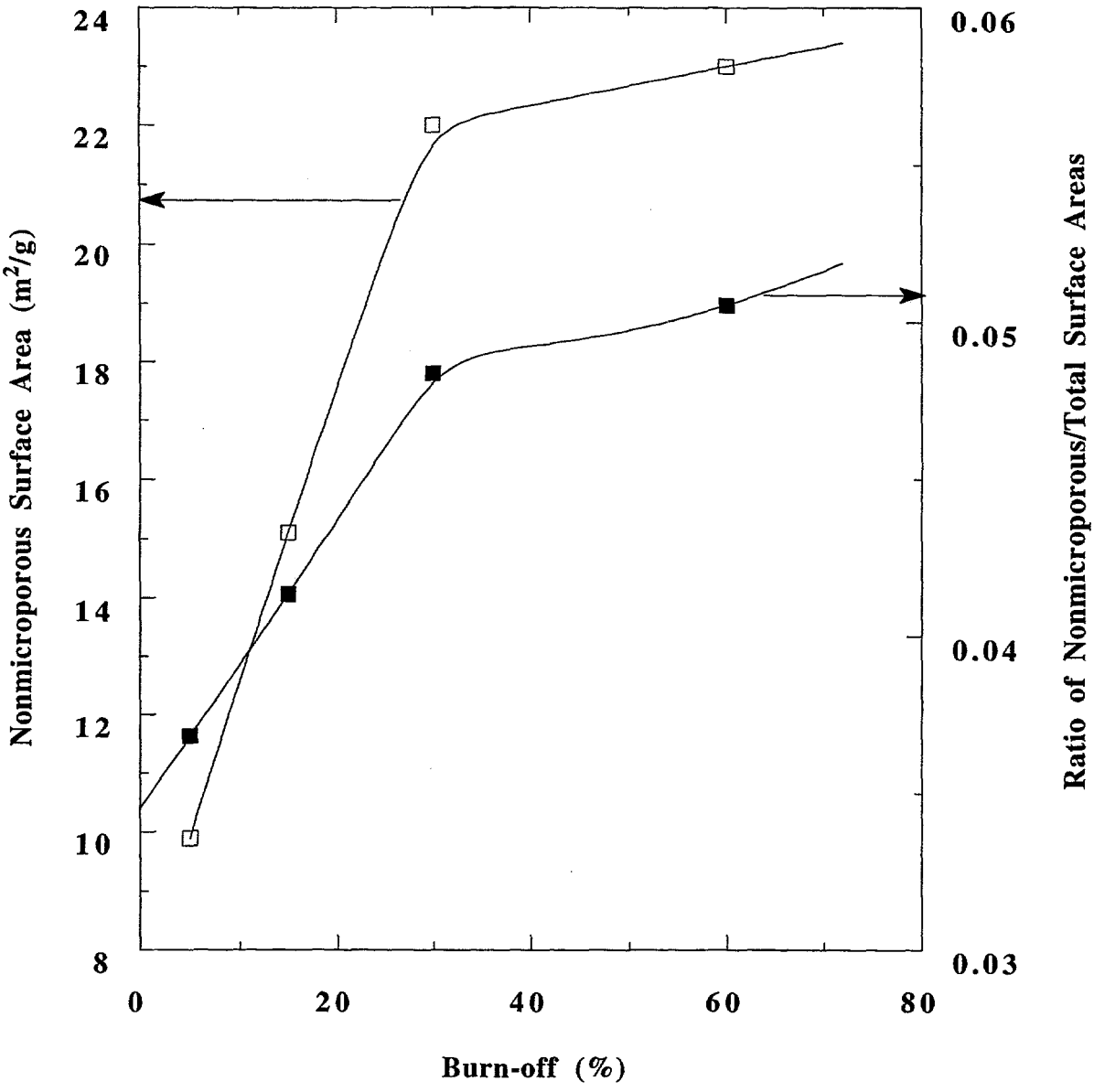

Figure 3.16. Nonmicroporous surface area as a function of burn-off for resin char gasified in oxygen at 470°C.

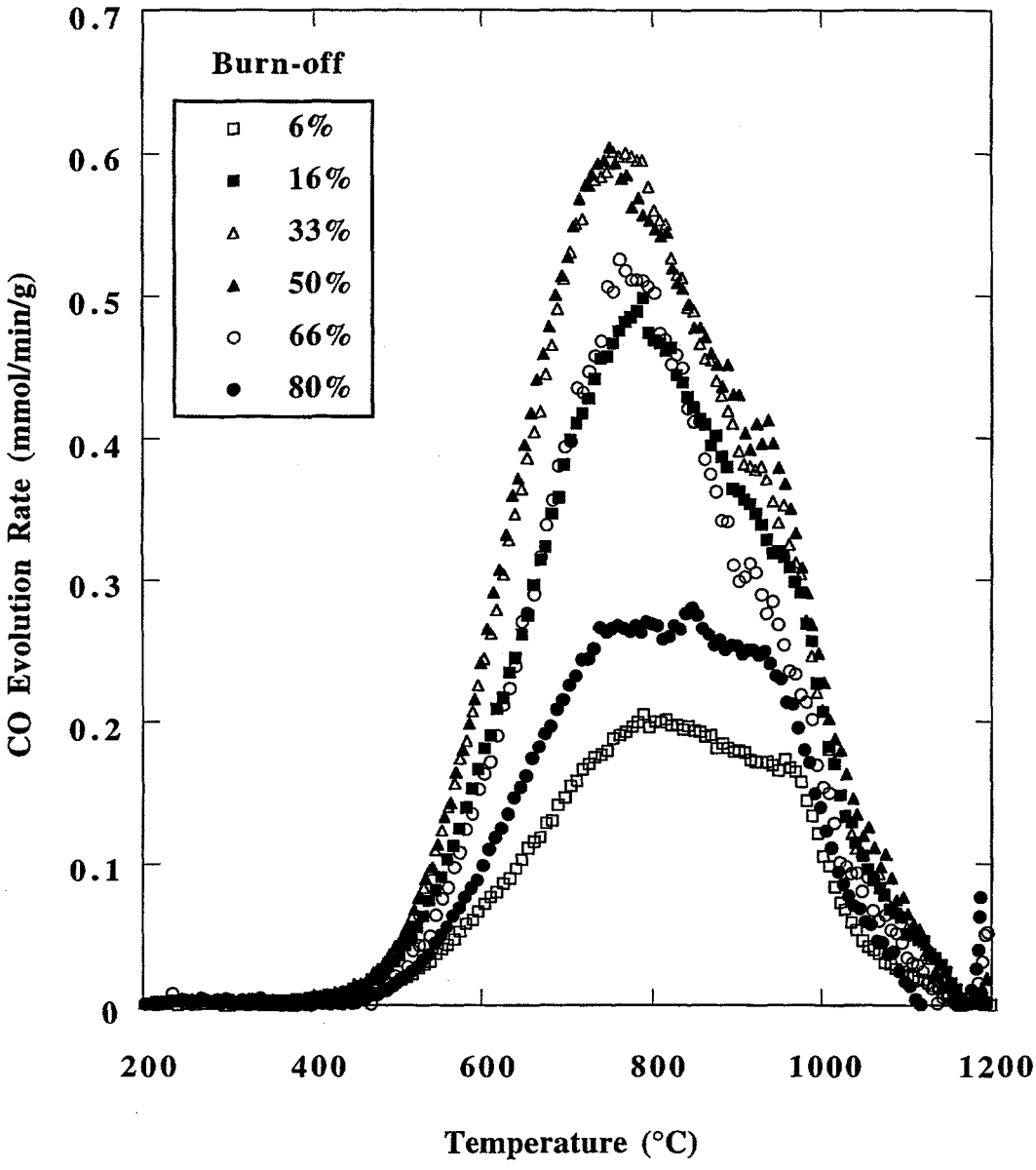

Figure 3.17. 50K/min CO TPD spectra from Wyodak coal char as a function of burn-off in oxygen at 420°C.

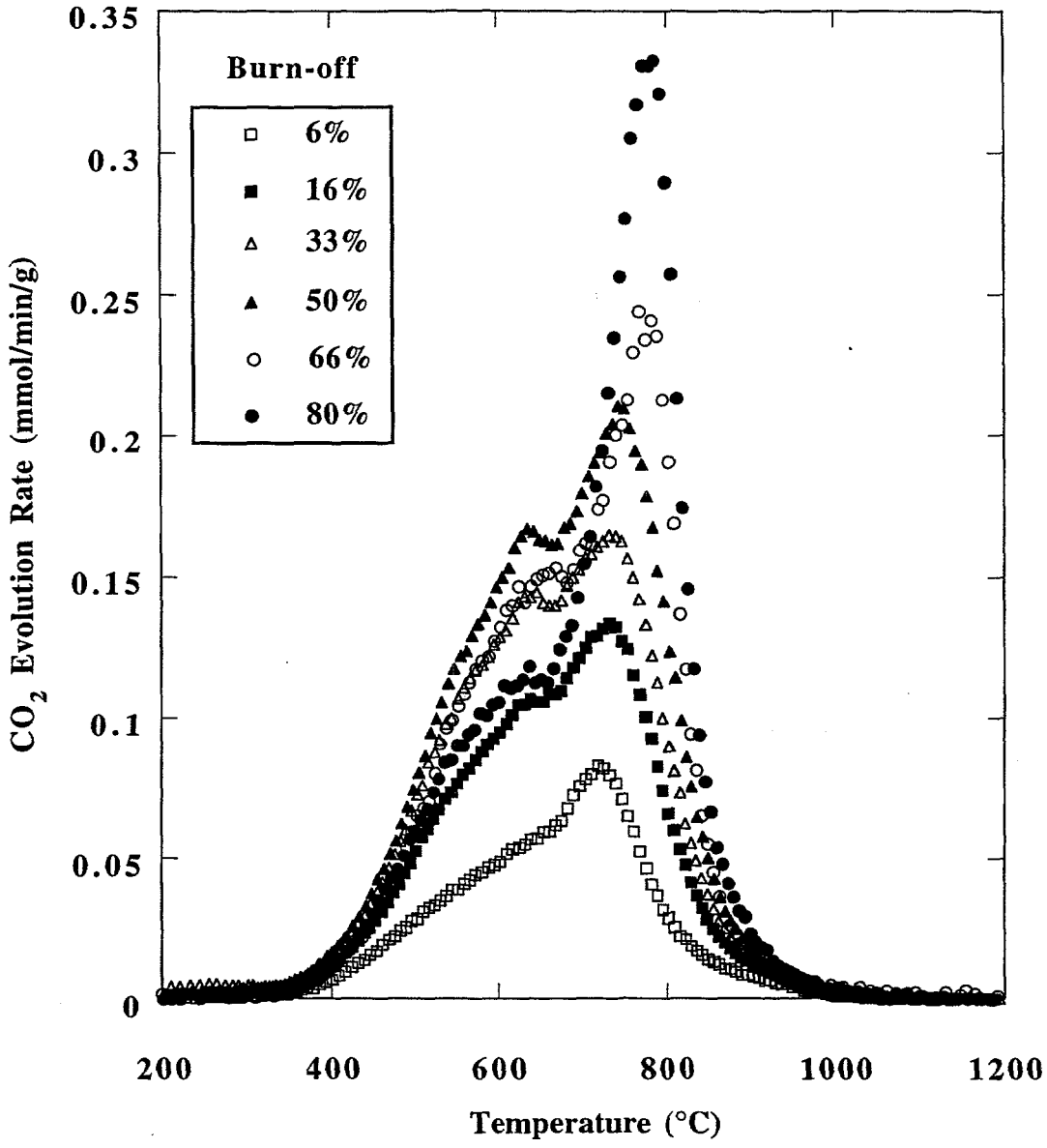

Figure 3.18. 50K/min CO_2 TPD spectra from Wyodak coal char as a function of burn-off in oxygen at 420°C.

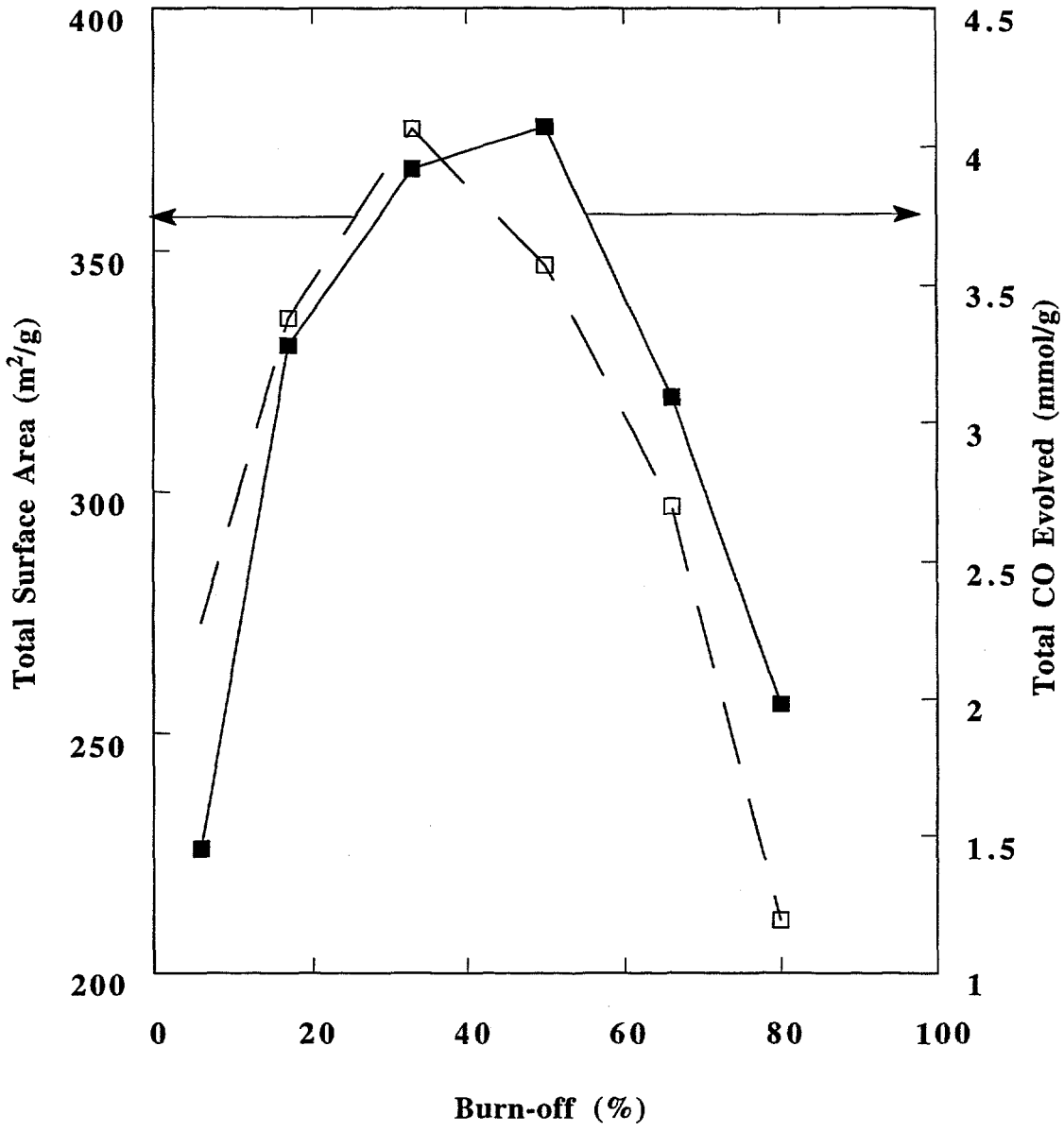

Figure 3.19. CO evolved and specific surface area as a function of burn-off for Wyodak coal char gasified in oxygen at 420°C.

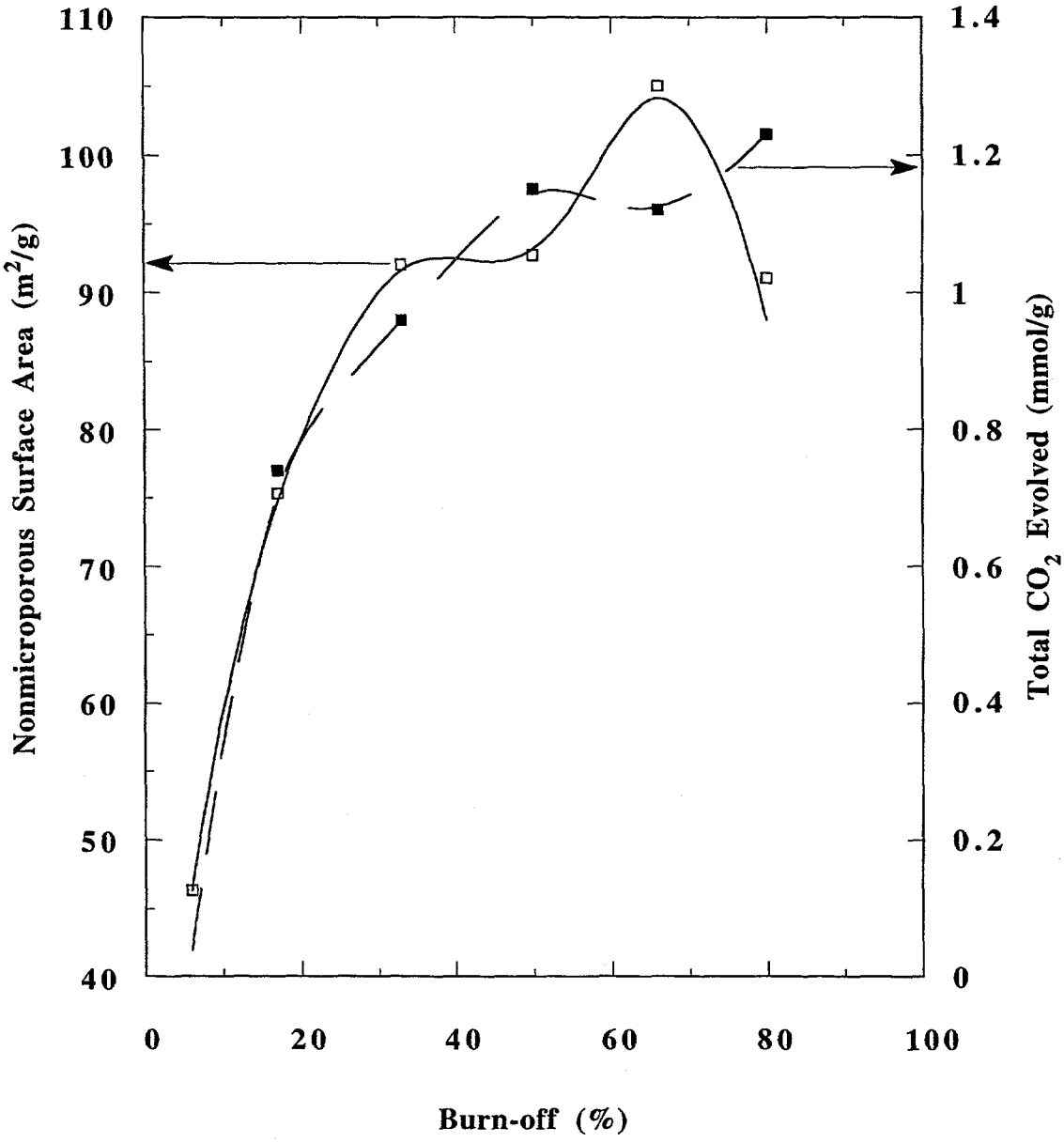

Figure 3.20. Comparison of nonmicroporous surface area with total CO_2 evolved as a function of burn-off for Wyodak coal char gasified in oxygen at 420°C.

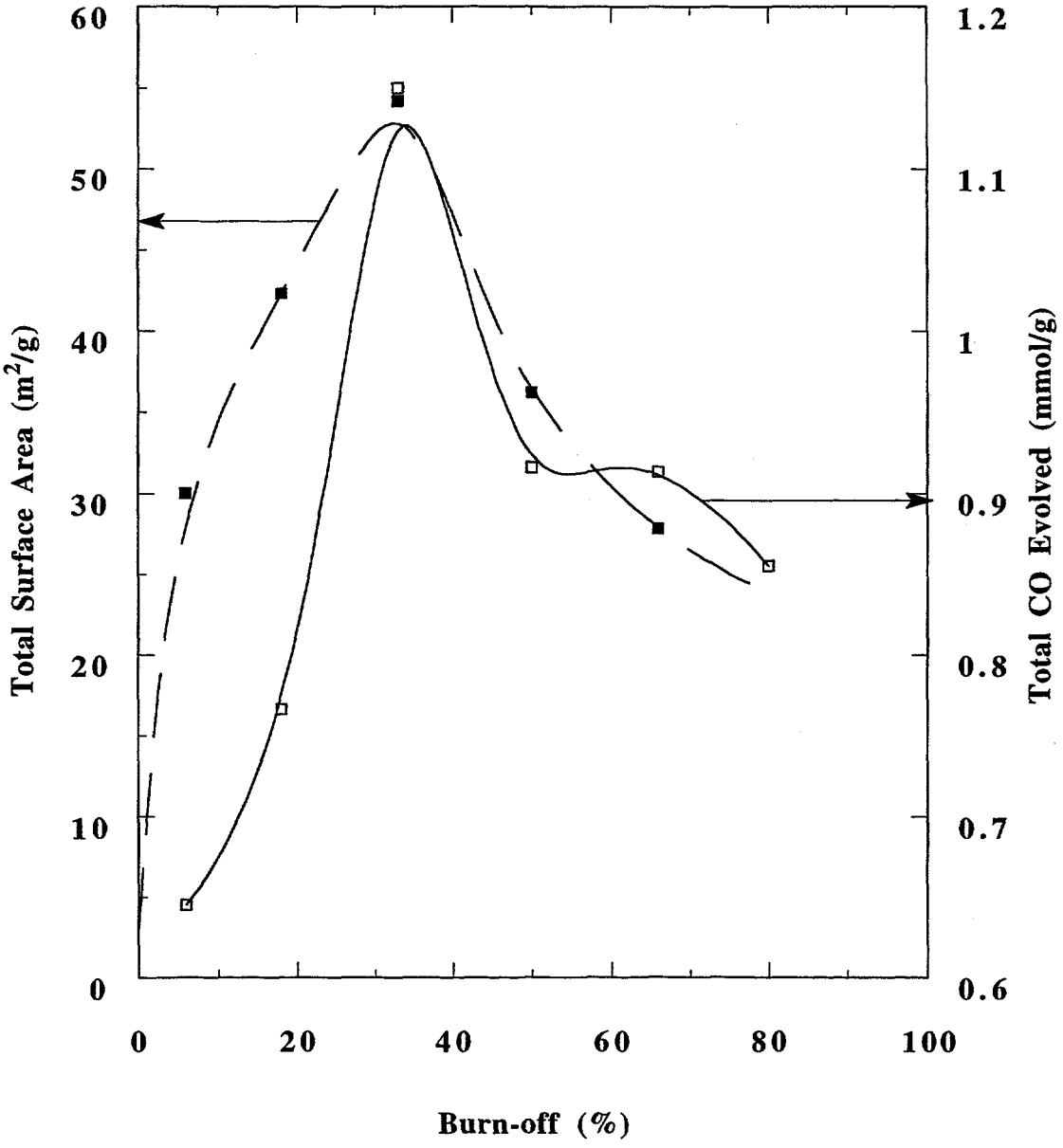

Figure 3.21. Comparison of total CO evolved with specific surface area for Pittsburgh #8 coal char gasified in oxygen at 470°C.

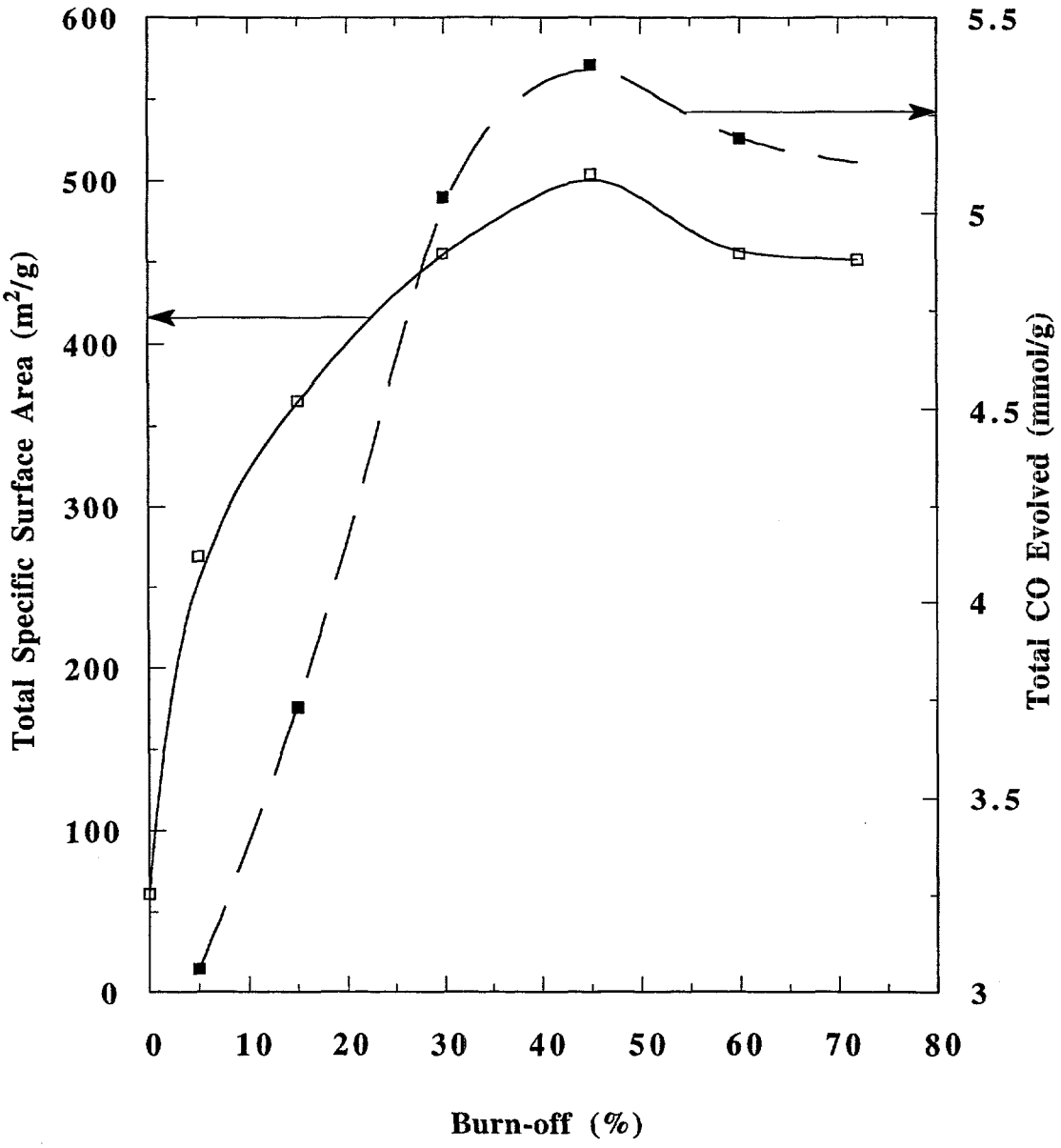

Figure 3.22. Comparison of CO evolution with specific surface area for resin char gasified in oxygen at 470°C.

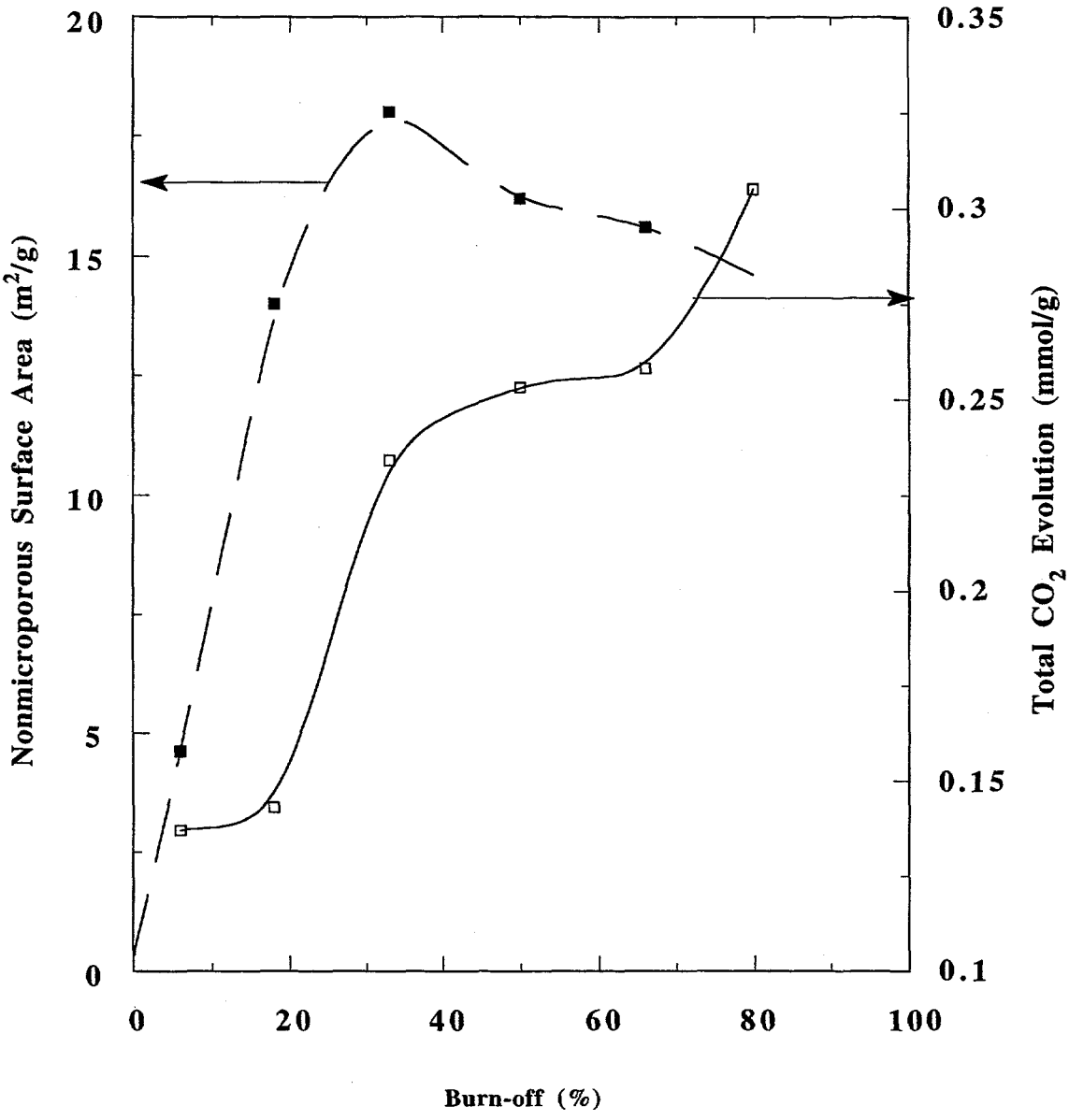

Figure 3.23. Comparison of total CO_2 evolved with nonmicroporous surface area for Pittsburgh #8 coal char gasified in oxygen at 470°C.

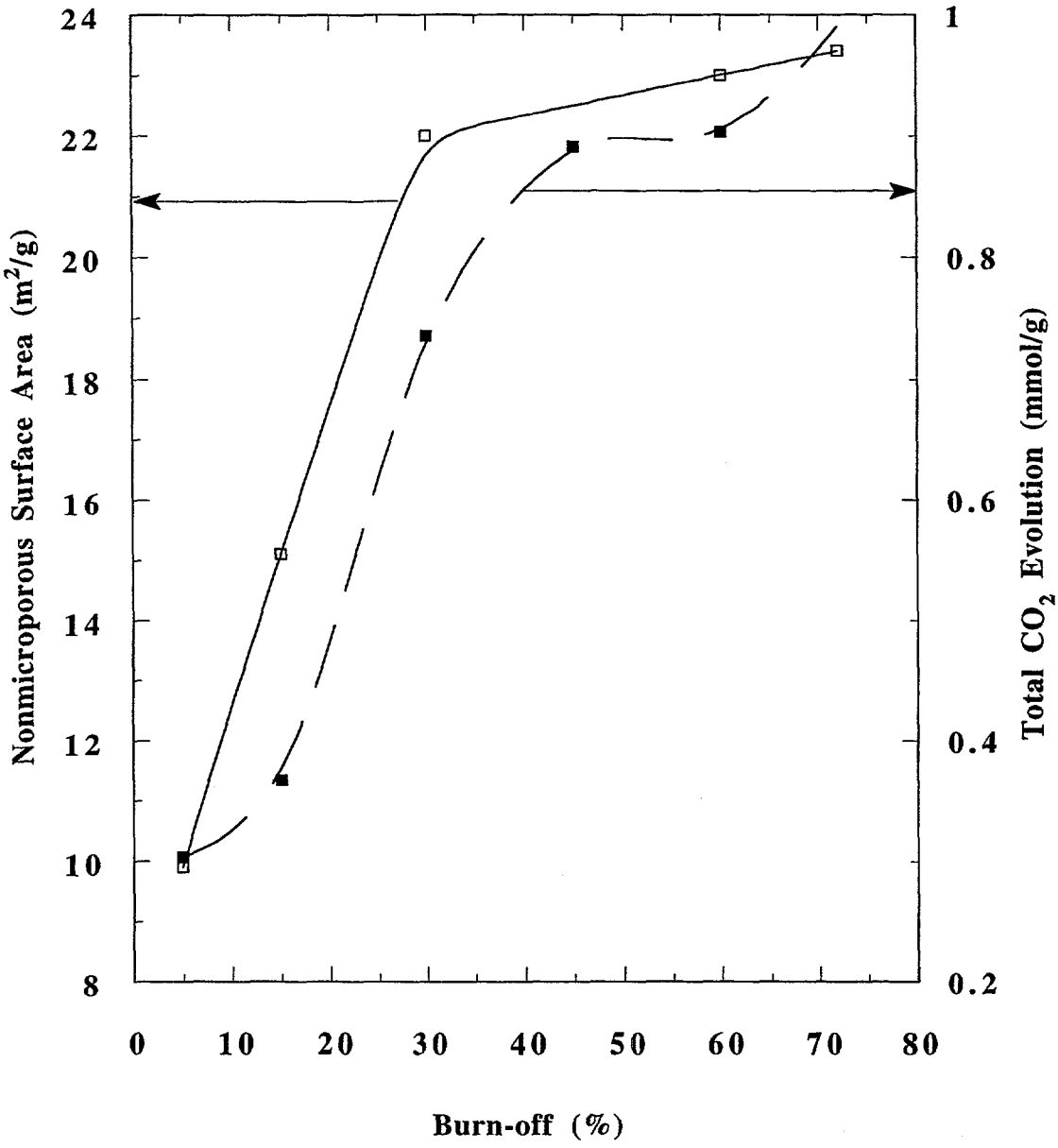

Figure 3.24. Comparison of total CO_2 evolution with nonmicroporous surface area for resin char gasified in oxygen at 470°C.

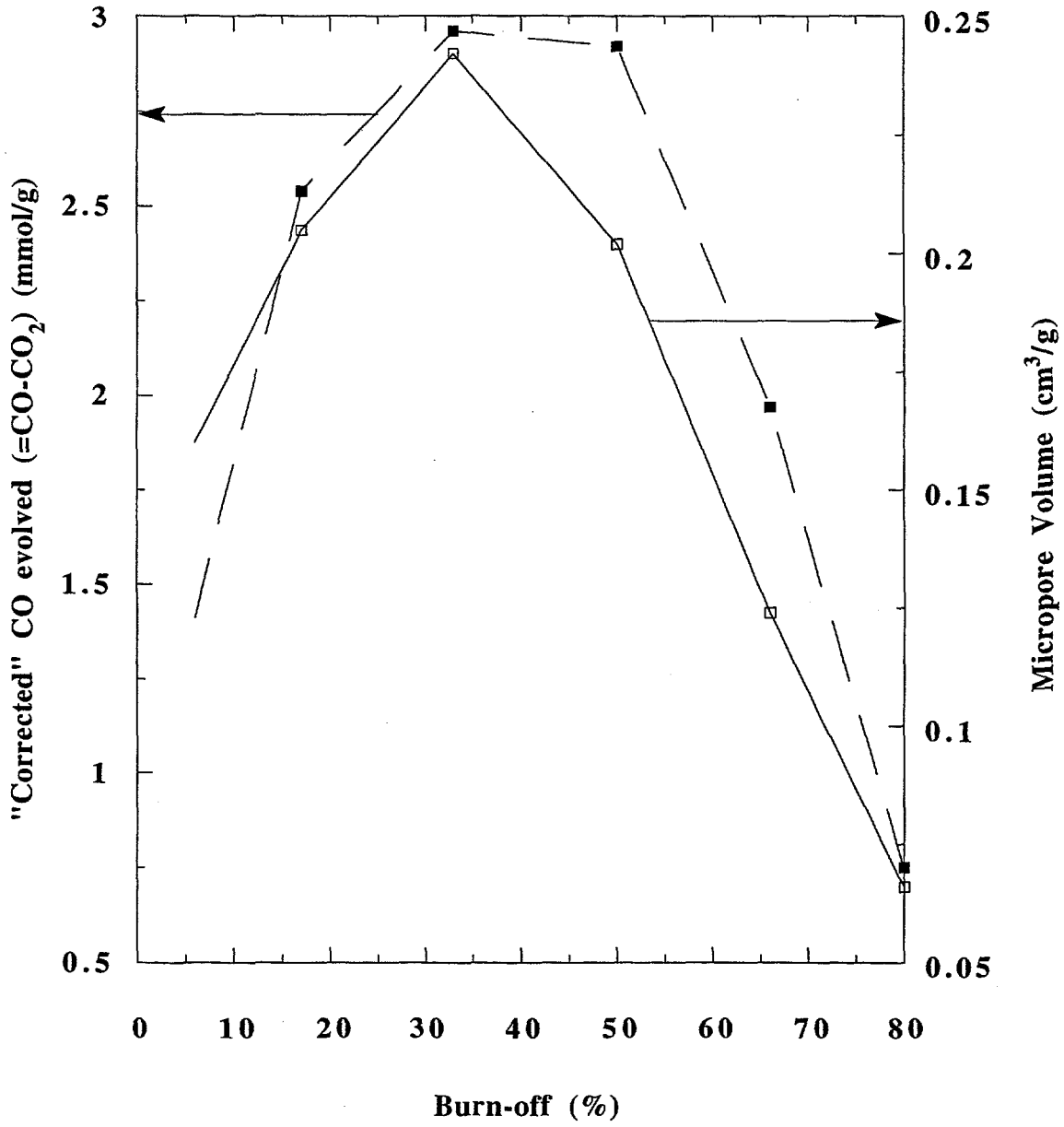

Figure 3.25. Comparison of micropore volume with "corrected" CO evolved from Wyodak coal char gasified in oxygen at 420°C.

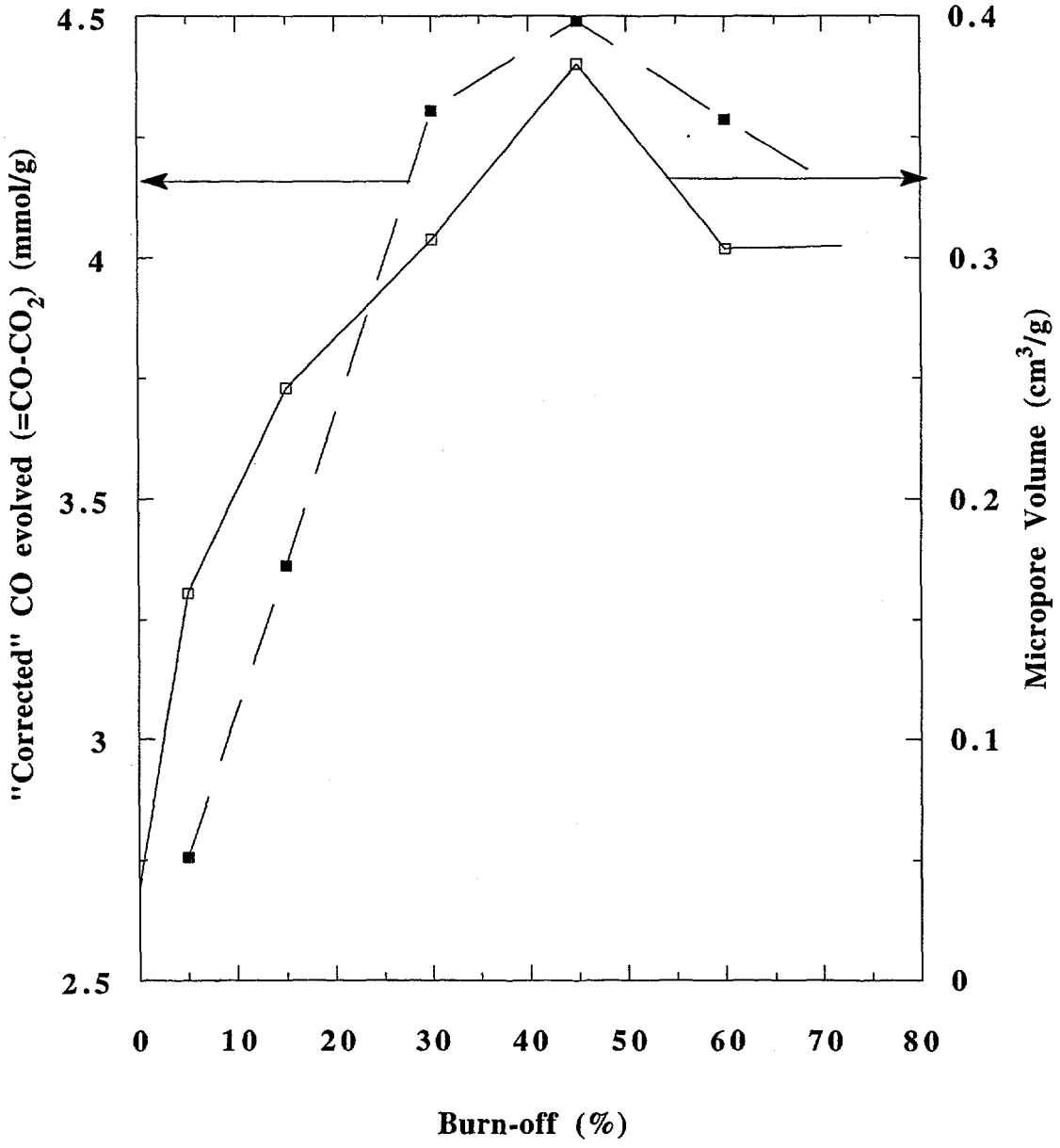

Figure 3.26. Comparison of micropore volume with "corrected" CO evolved from resin char gasified in oxygen at 470°C.

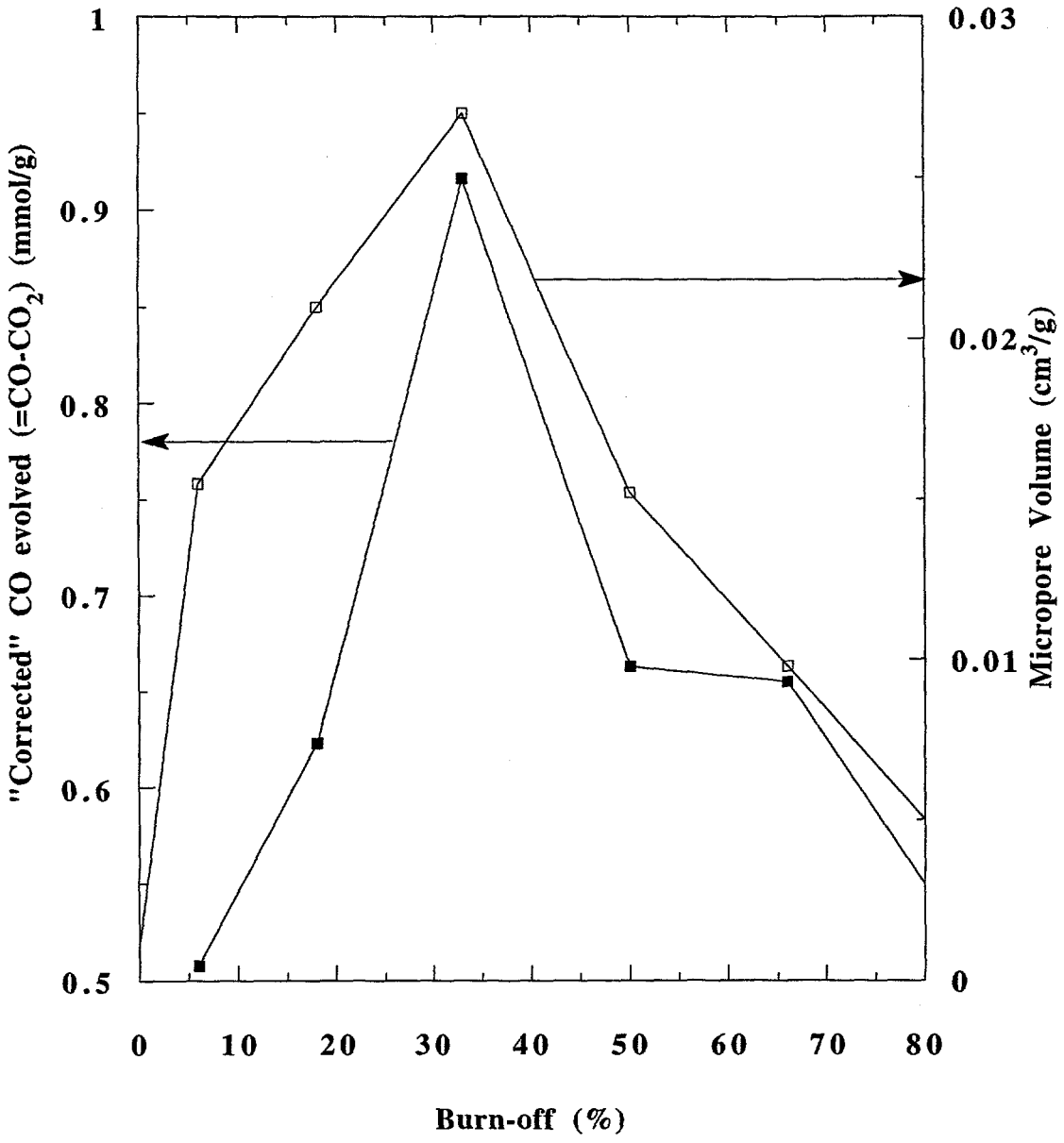

Figure 3.27. Comparison of micropore volume with "corrected" CO evolved from resin char gasified in oxygen at 470°C.

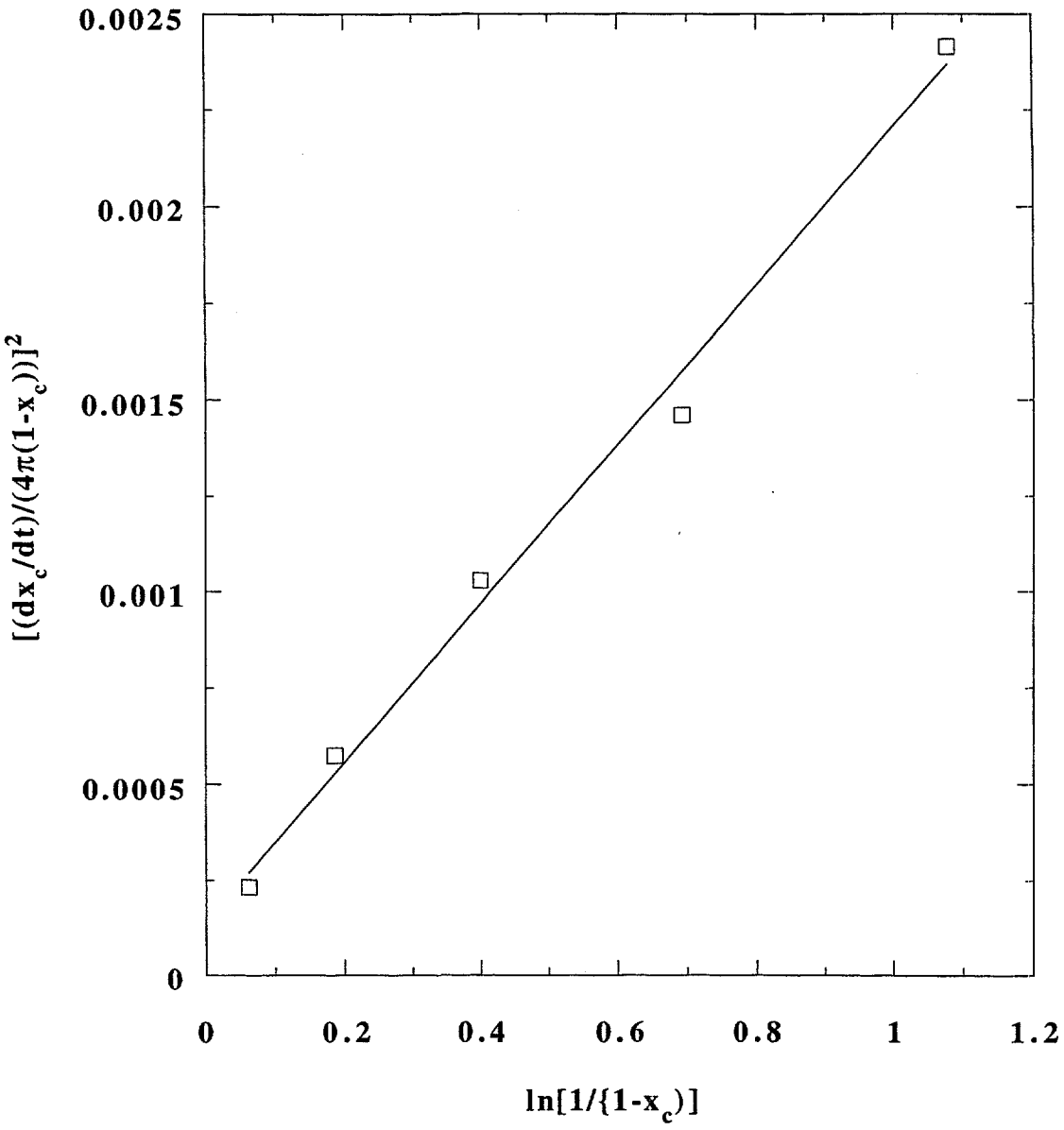

Figure 3.28. Comparison of random pore model predictions (Eq.[3.37]) with experimental gasification data for Wyodak coal char in oxygen at 420°C.

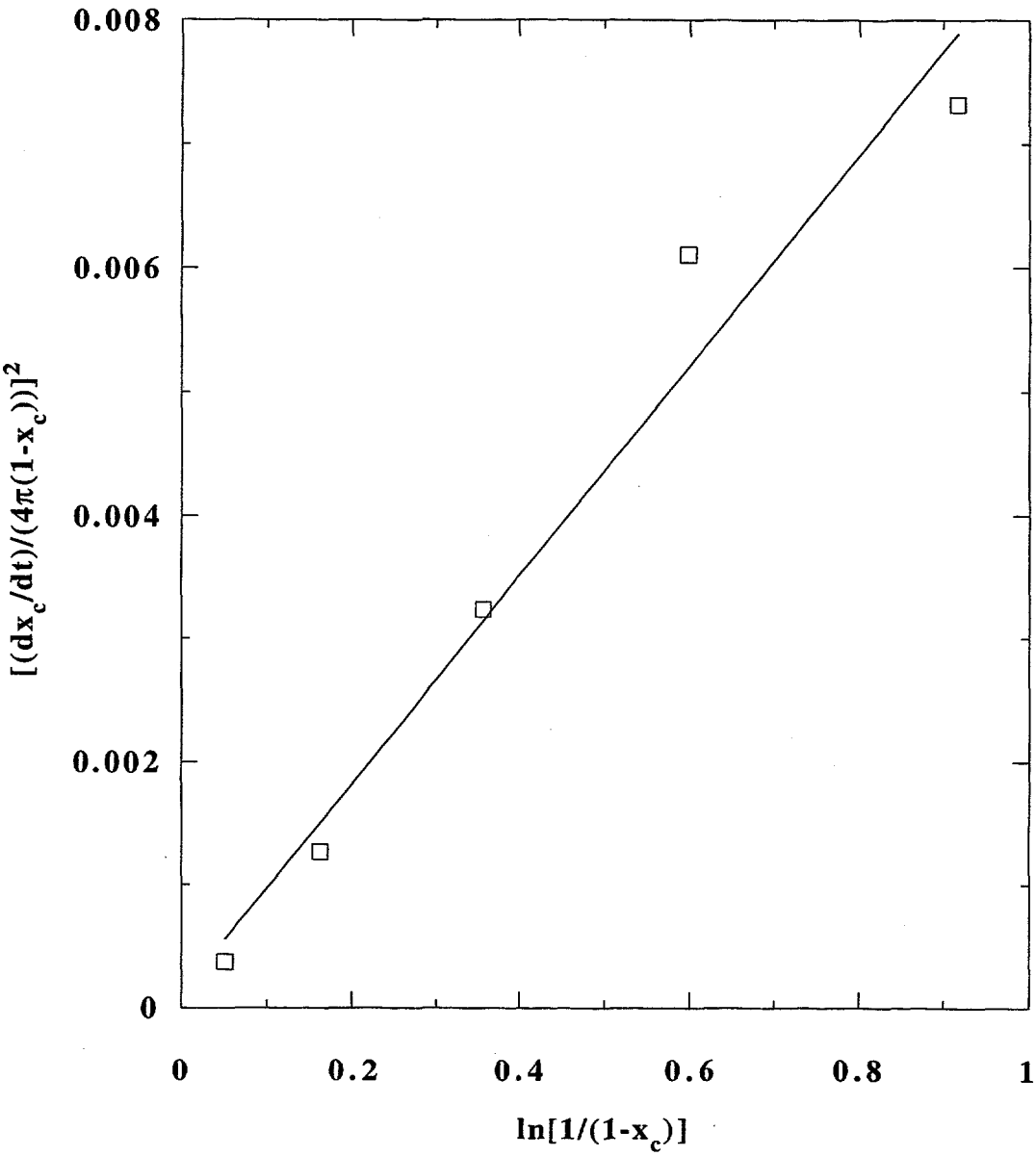

Figure 3.29. Comparison of random pore model predictions (Eq.[3.37]) with experimental gasification data for resin char in oxygen at 470°C.

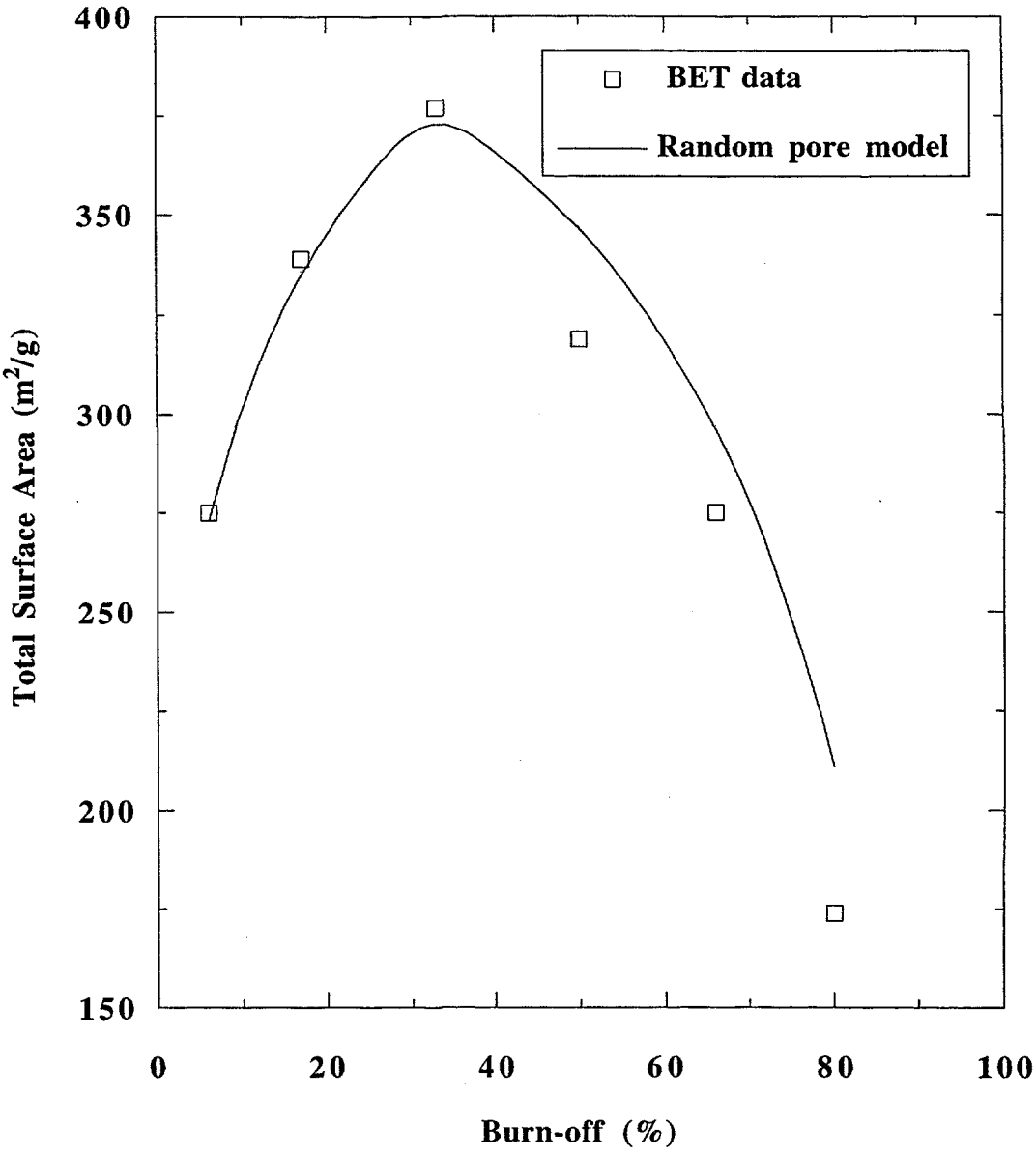

Figure 3.30. Comparison of random pore model predictions with BET surface area for Wyodak coal char gasified in oxygen at 420°C.

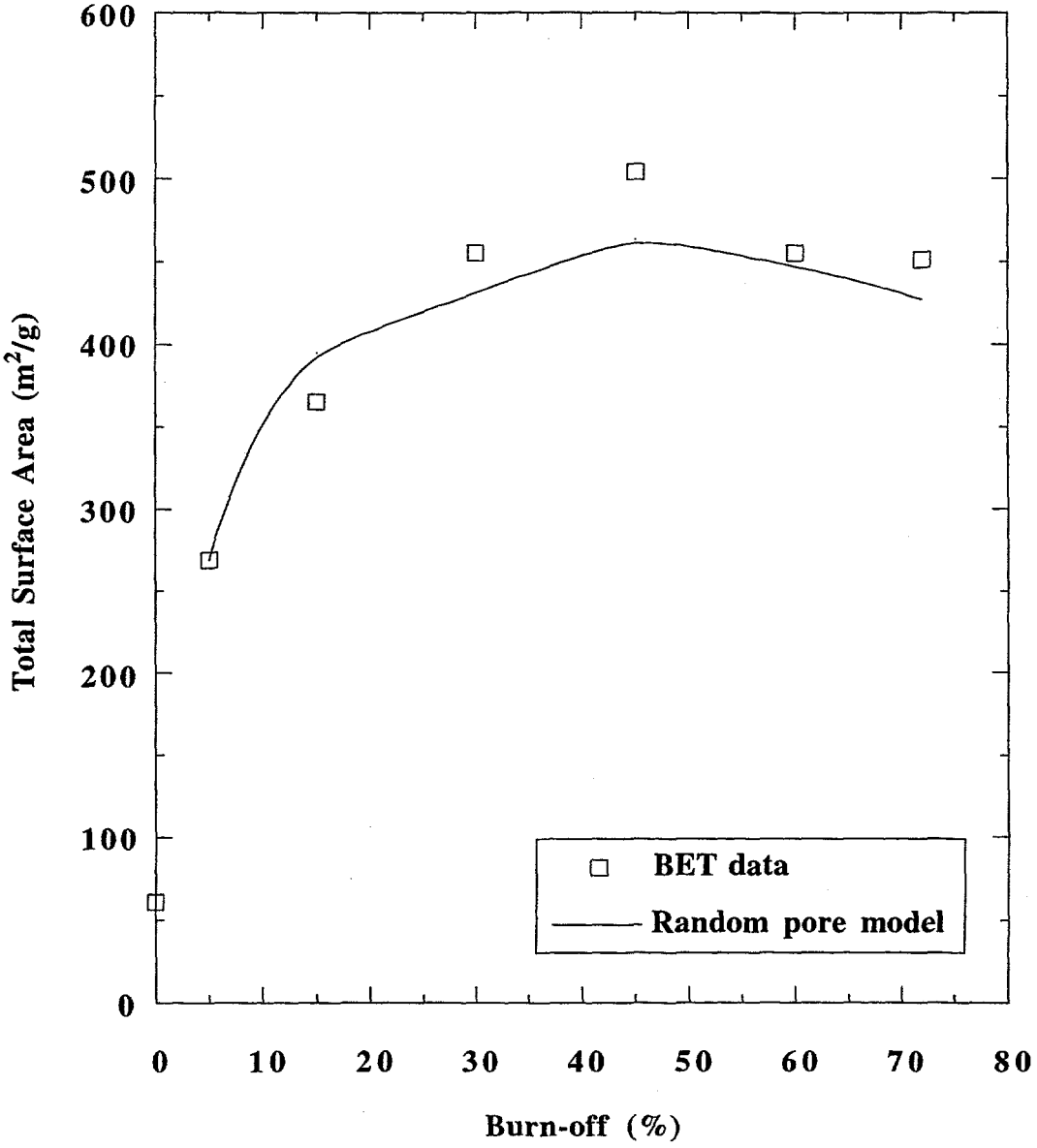

Figure 3.31. Comparison of random pore model predictions with BET surface area for resin char gasified in oxygen at 470°C.

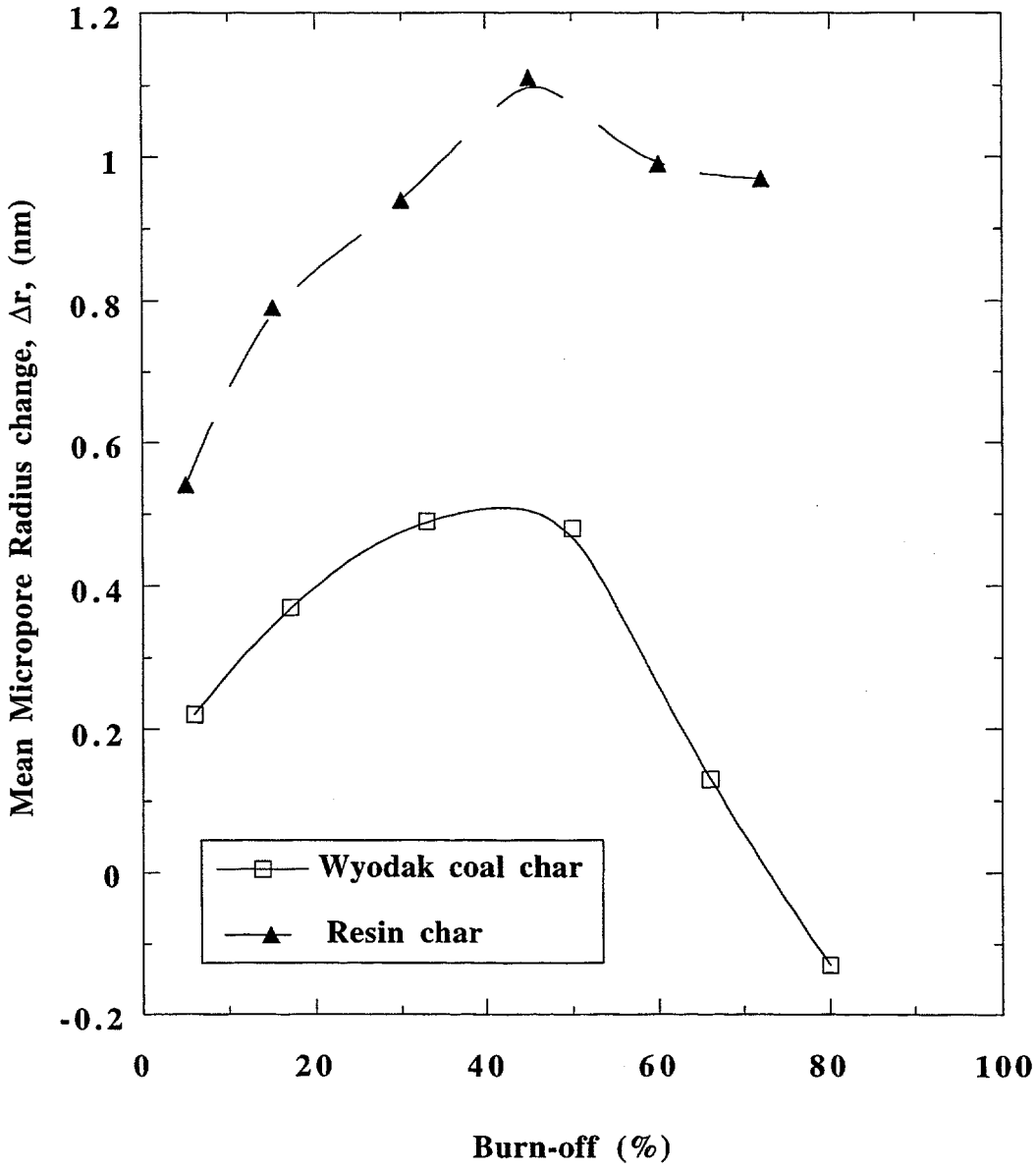

Figure 3.32. Mean micropore radius change as a function of burn-off.

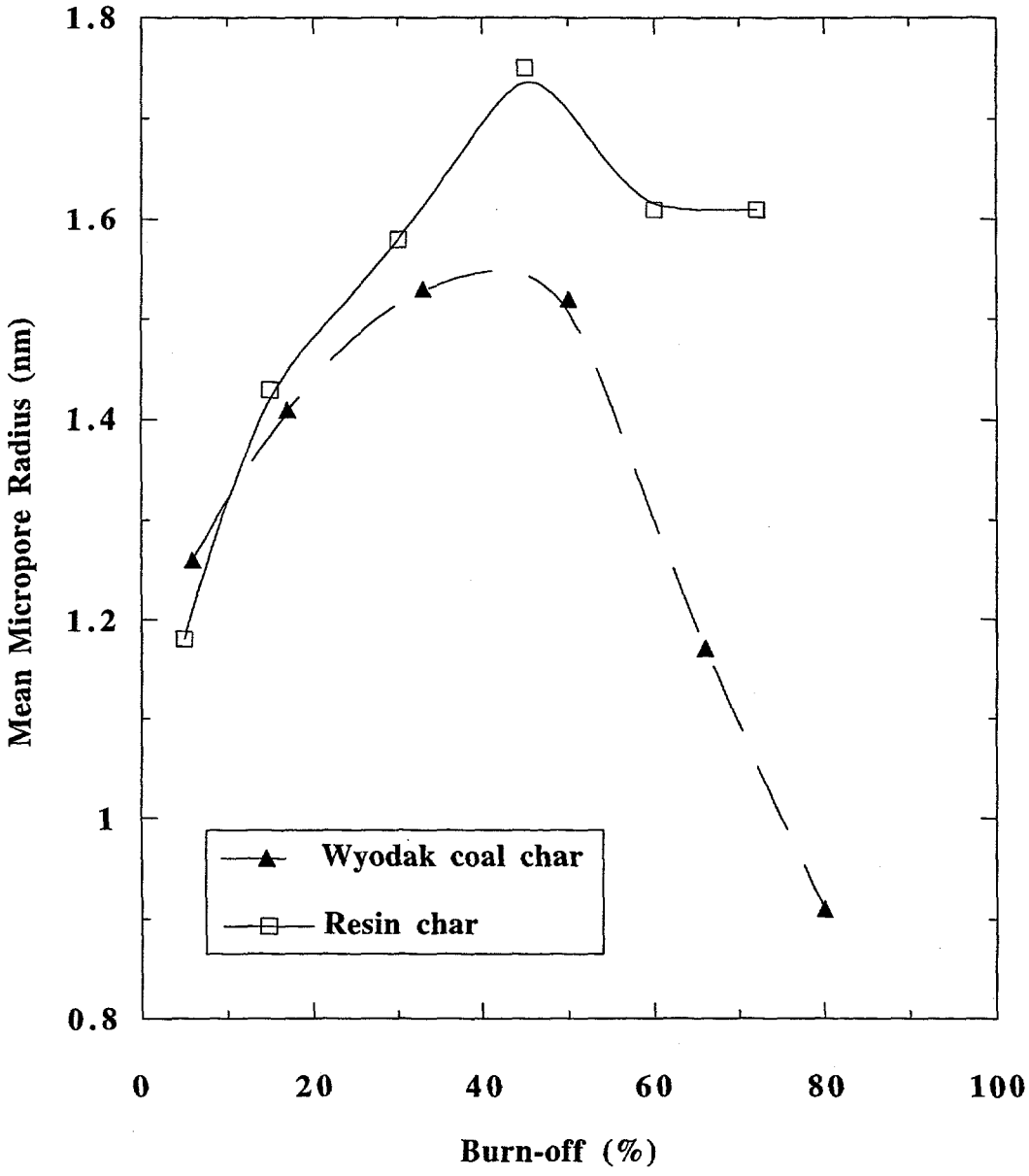

Figure 3.33. Mean micropore radius as a function of burn-off.

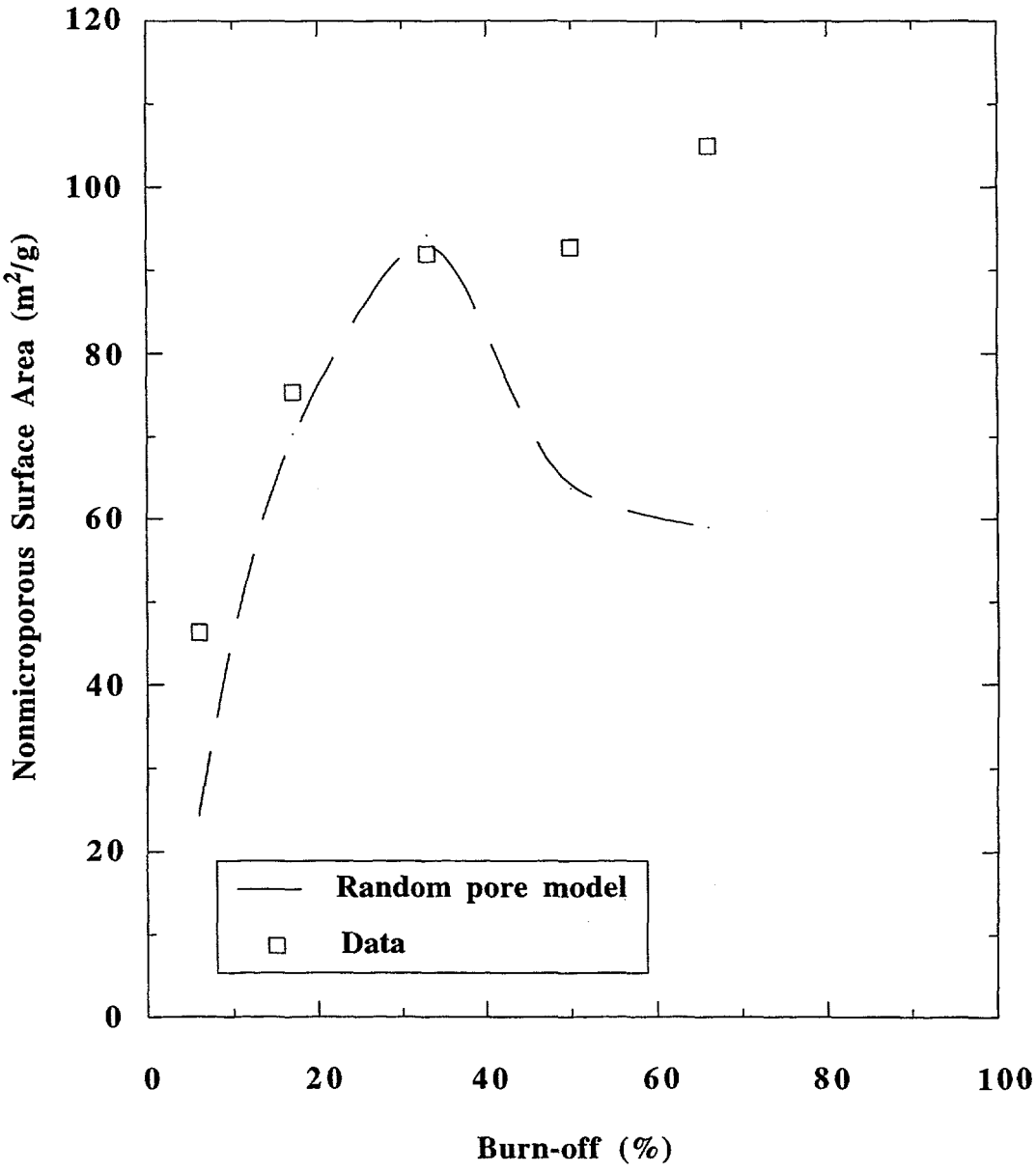

Figure 3.34. Comparison of random pore model with experimental nonmicroporous surface area for gasification of Wyodak coal char in oxygen at 420°C.

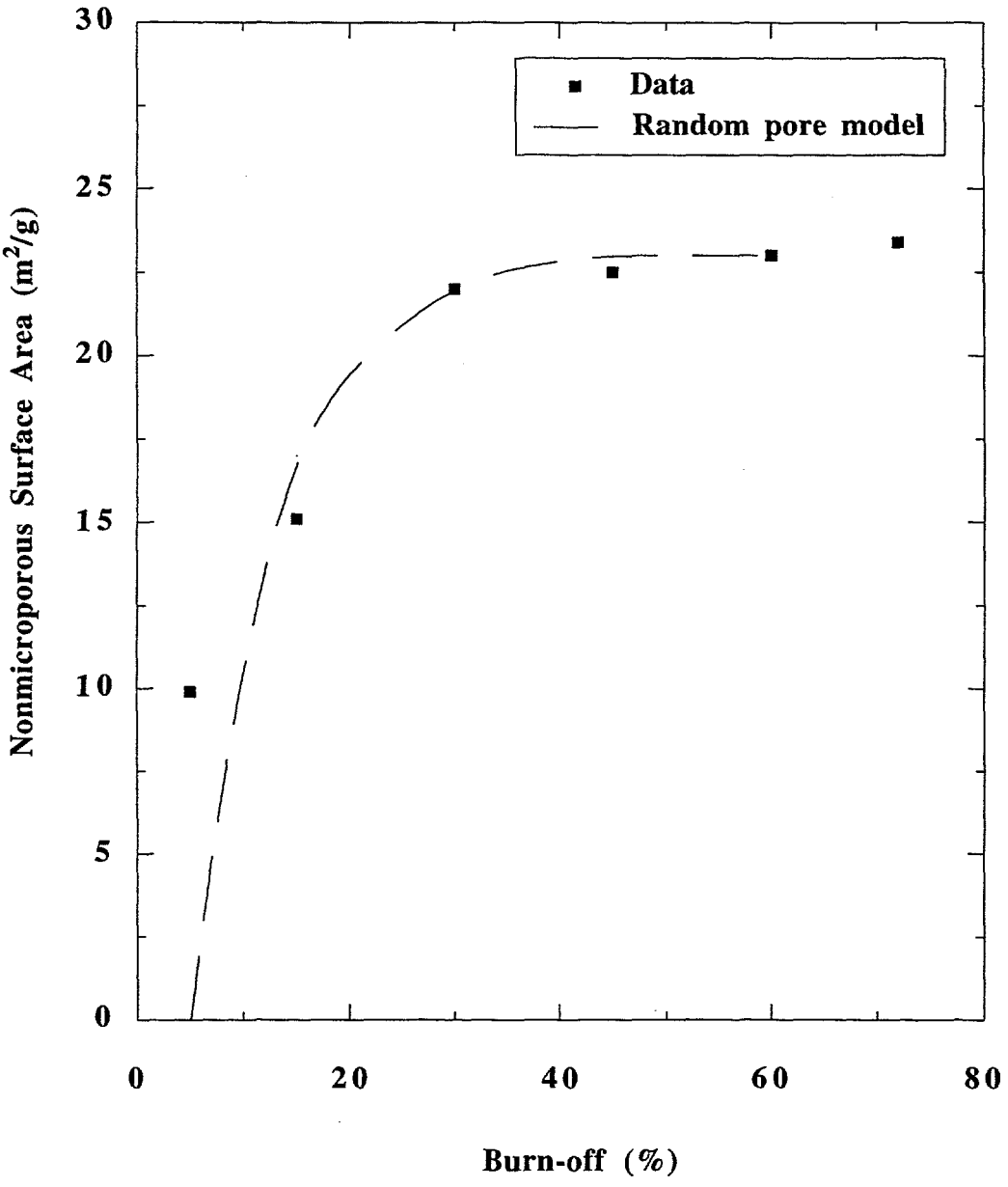

Figure 3.35. Comparison of random pore model predictions with experimental nonmicroporous surface area for resin char gasified in oxygen at 470°C.

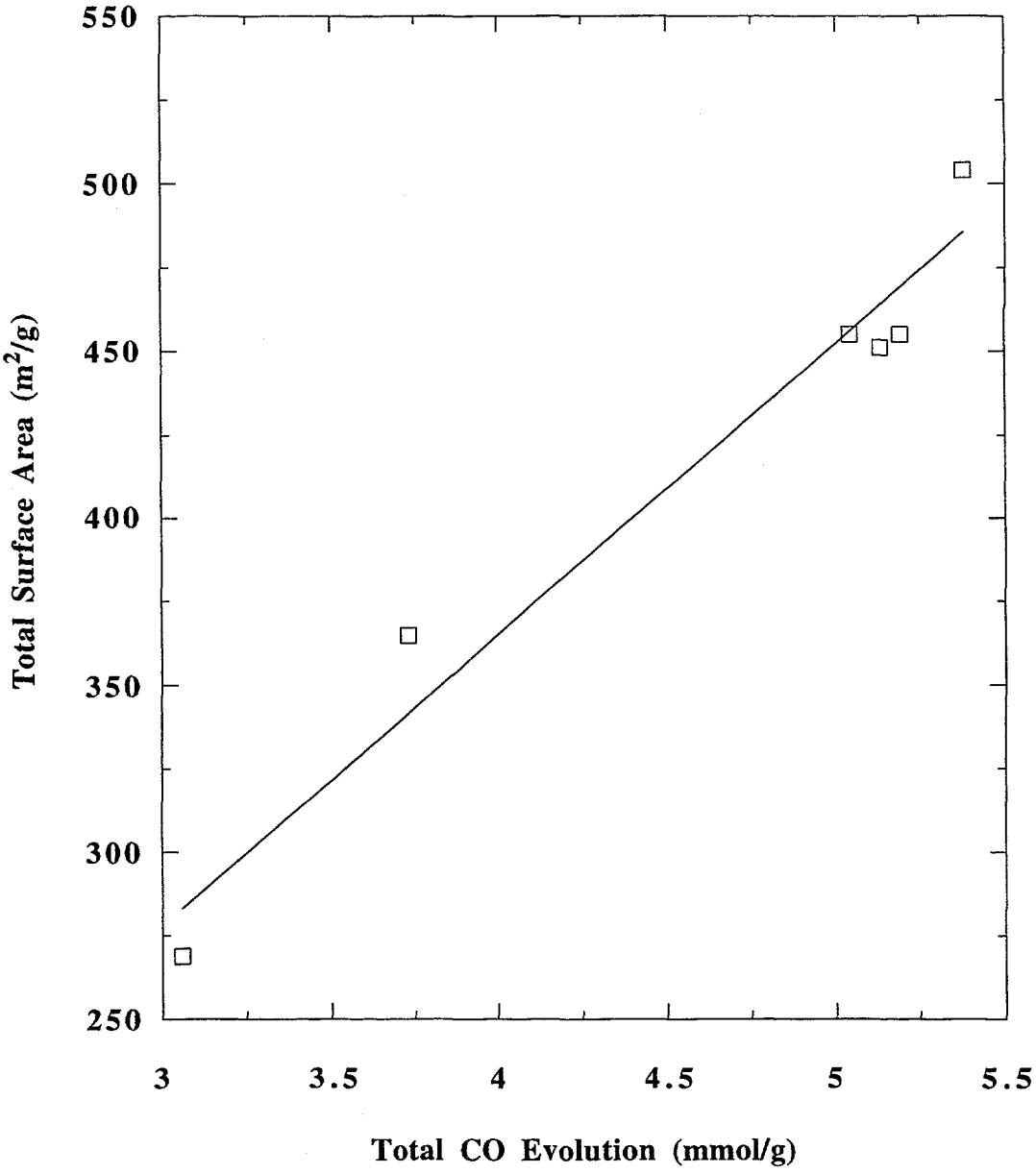

Figure 3.36. Total Specific area as a function of total CO evolution for resin char gasified in oxygen at 470°C.

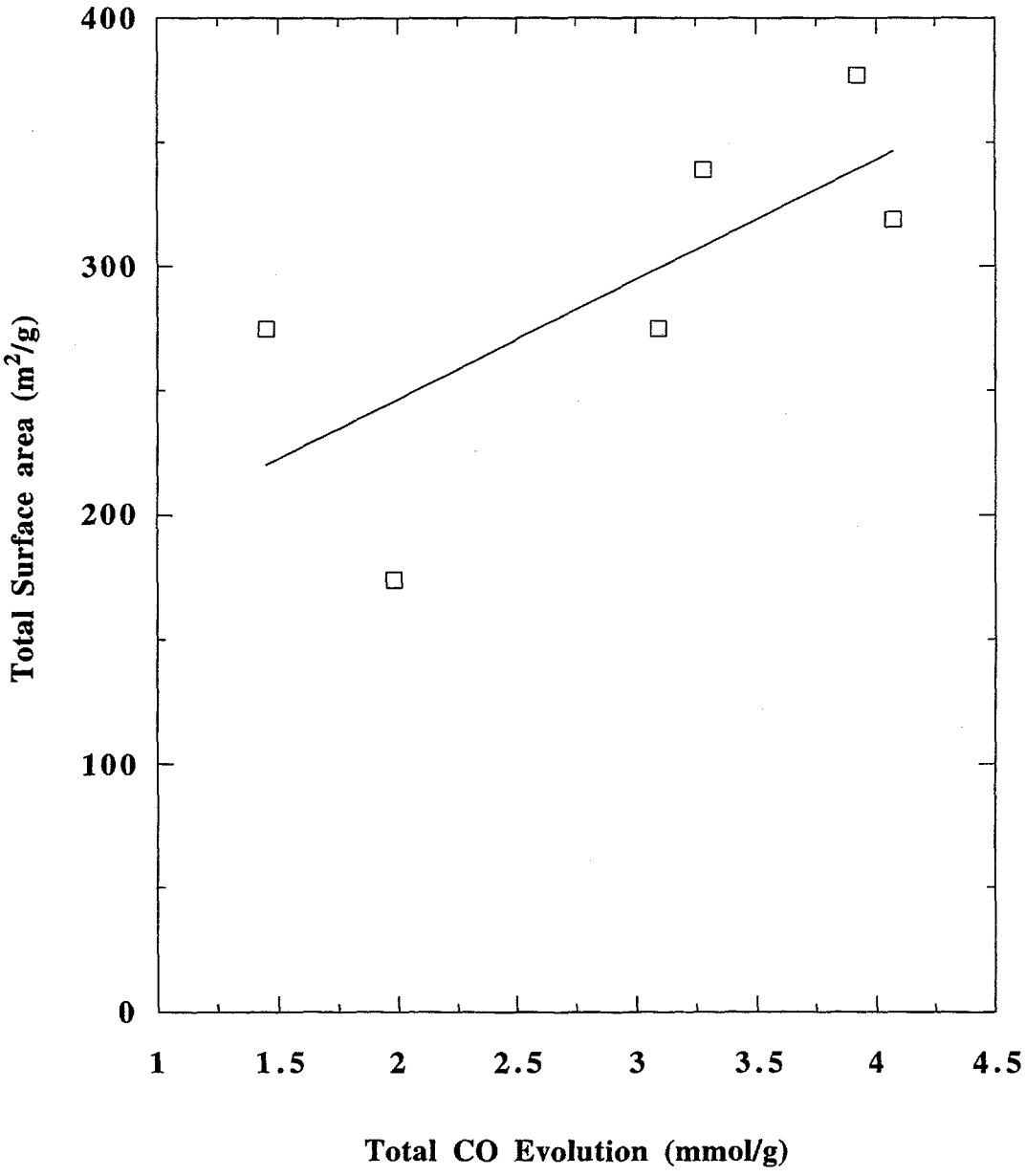

Figure 3.37. Total Specific area as a function of total CO evolution for Wyodak coal char gasified in oxygen at 470°C.

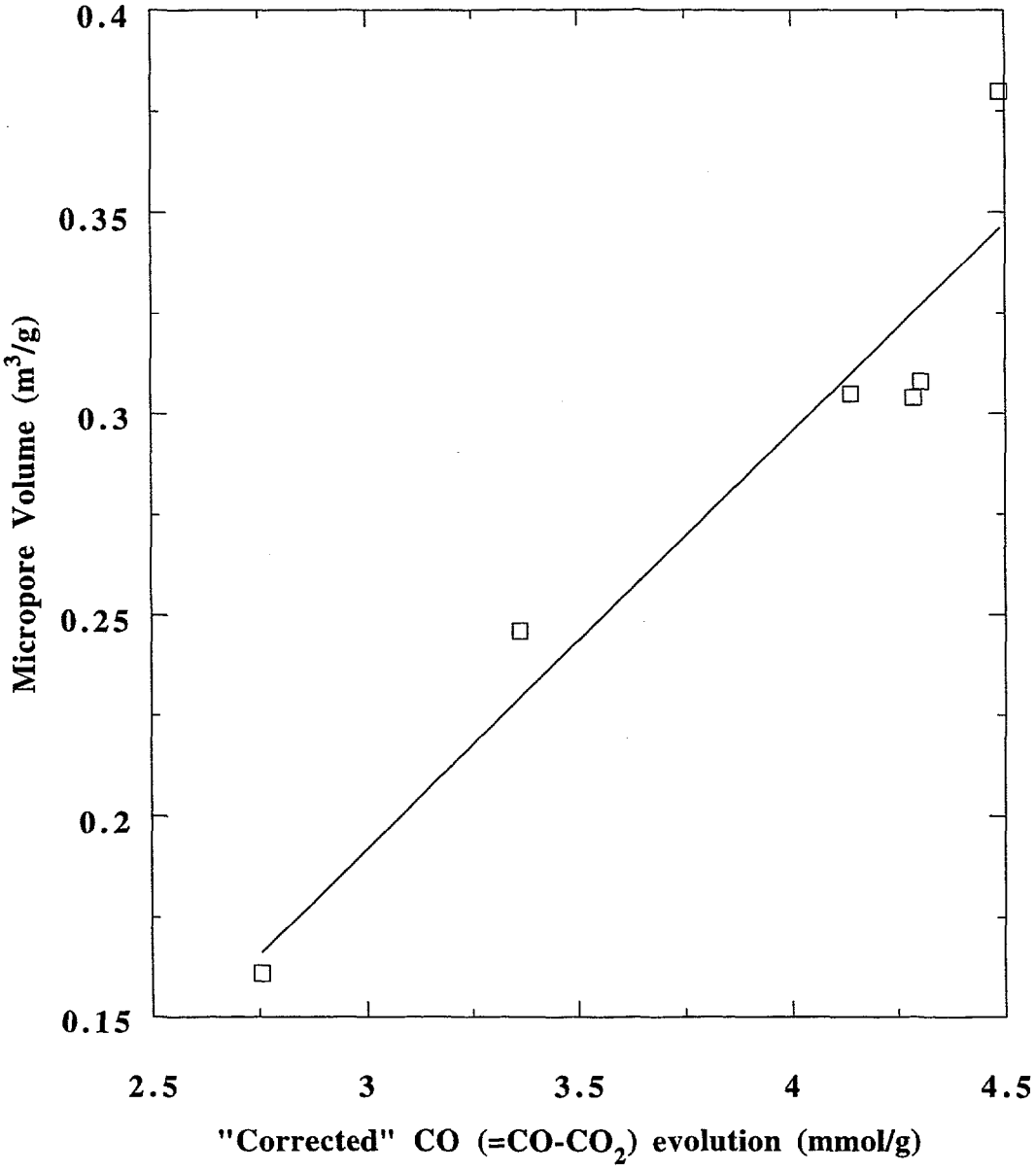

Figure 3.38. Micropore volume as a function of "corrected" CO evolution for resin char gasified in oxygen at 470°C.

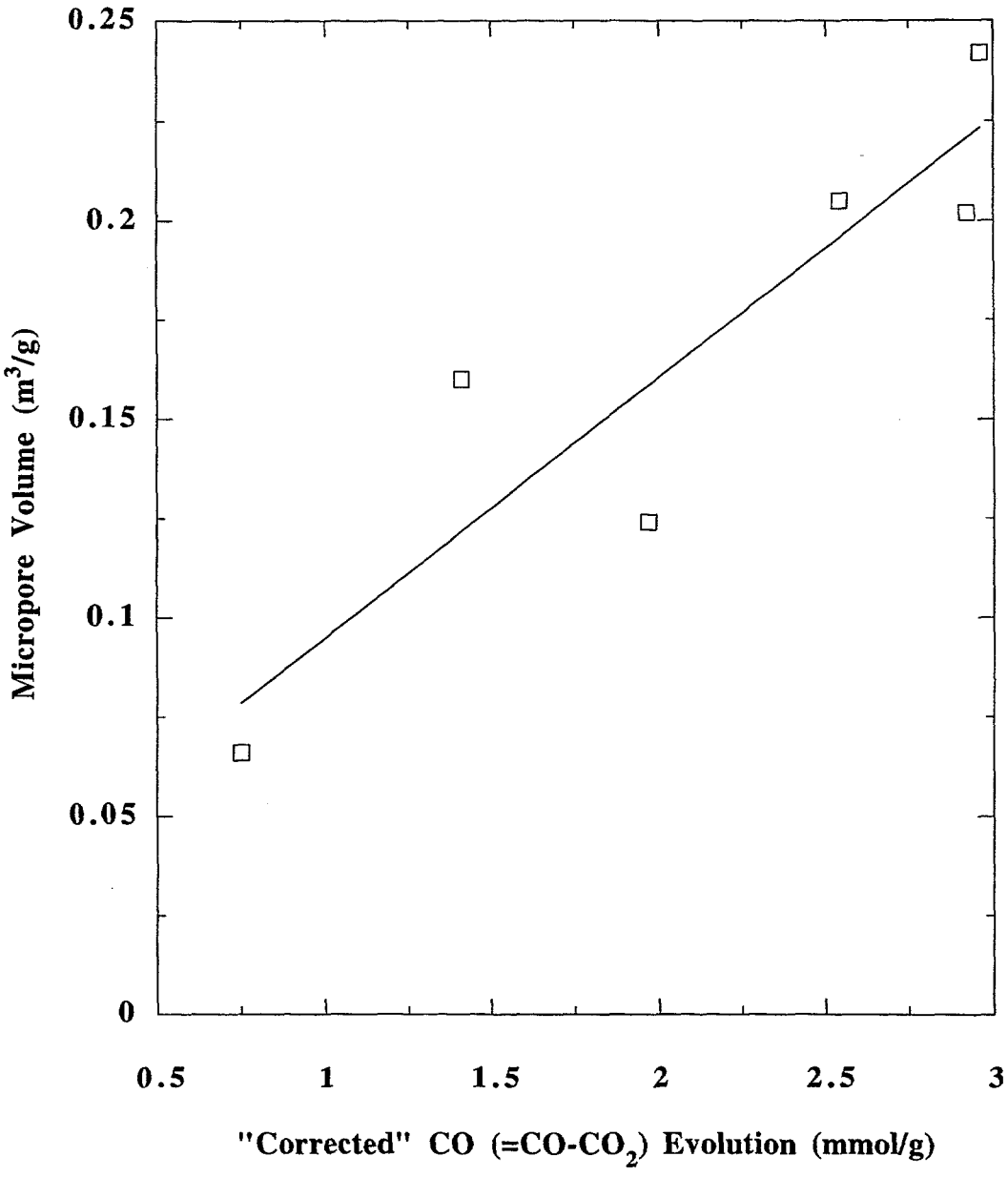

Figure 3.39. Micropore volume as a function of "corrected" CO evolution for Wyodak coal char gasified in oxygen at 420°C.

4.0. POROSITY CHARACTERIZATION *VIA* SMALL ANGLE NEUTRON SCATTERING (SANS)

4.1. Overview.

As indicated in Section 1.0, one of the techniques that has been applied to the characterization of char porosity in the current project is small angle neutron scattering (SANS). Even though it is well known that small angle scattering (SAS) methods rely upon the models that are used in the interpretation of the data, they are still quite useful in assessing whether experimental observations are consistent with other techniques. In addition, a robust analysis that yields realistic values for the model parameters can be used to infer other properties of the porous structure that can be invaluable in assessing other data, such as that provided by gas adsorption techniques, as well as, in the present case, thermal desorption data.

4.2. Porosity Development in Chars.

4.2.1. Background.

Although most small angle scattering (SAS) investigations of porous materials have used X-rays, there are a number of important differences between the use of X-rays and neutrons in small angle scattering experiments. Primarily, the scattering cross section for X-rays increases with atomic number. In this regard, it is difficult to monitor light atoms in the presence of heavier ones. Neutron scattering cross sections exhibit no simple systematic variation with atomic number; thus in many cases it is possible to detect the presence of light atoms (Higgins and Benoît, 1994). Neutron scattering cross sections can vary greatly between isotopes of the same material. In the current work, this characteristic is used to "contrast match" the solid carbonaceous structure.

The analysis of SANS data is complex. A good discussion of some of the problems is provided by Higgins and Benoît (1994). For a two phase system, the scattering intensity, I(q), is given by:

$$I(q) = b_v^2 \phi V^2 P(q) \qquad [4.1]$$

where q is the scattering wave vector:

$$q = \frac{4\pi}{\lambda} \sin(\theta) \qquad [4.2]$$

in which λ is the neutron wavelength, and θ is half of the scattering angle. In Eq. [4.1], V is the sample volume, b_v is the contrast factor per unit volume between the solid material and the (empty) pore, ϕ is the void volume fraction, and P(q) is known as the form factor which is characteristic of the size and shape of the scatterers.

The situation for scattering from hard spheres is relatively simple since the scattering intensity does not depend on the orientation of the scatterers. For this case, it can be shown (Higgins and Benoît, 1994) that the form factor becomes:

$$P(q) = [9/(qR)^6] [\sin(qR) - qR \cos(qR)]^2, \qquad [4.3]$$

where R is the sphere radius. Substituting this expression into Eq. [4.1] yields:

$$I(q) = b_v^2 \phi V^2 [9/(qR)^6] [\sin(qR) - qR \cos(qR)]^2, \qquad [4.4]$$

Evaluating the quadratic expression and replacing $\cos^2(qR)$ and $\sin^2(qR)$ by 1/2 (their average values), and $\sin(qR)\cos(qR) = (1/2)\sin(2qR) \approx 0$, yields:

$$I(q) = b_v^2 \phi V^2 [9/2] [1/(qR)^4 + 1/(qR)^6], \qquad [4.5]$$

Now, for spheres, $V^2/R^4 = (16/9)(\pi R)^2 = 4\pi S/9$, where $S = 4\pi R^2$. Substituting back into Eq.

[4.5], and keeping only the first term:

$$q^4 I(q) = b_v^2 2 \pi S_T \qquad [4.6]$$

where $S_T = NS$ is the total surface area of the spheres. This result is the well known Porod scattering law, and indicates that at sufficiently high q values, the scattering intensity is proportional to q^{-4}, and $q^4 I(q)$ is proportional to the total surface area of the sample.

Another useful parameter for the analysis of porous materials is the Porod invariant, Q, defined as:

$$Q = \int q^2 I(q)\, dq, \qquad [4.7]$$

The Q is related to the void fraction of the material under investigation, ϕ, *via* the following relation:

$$2 \pi^2 b_v^2 \phi (1-\phi) = \frac{1}{V} \int_0^\infty I(q)\, q^2\, dq \qquad [4.8]$$

The relationship between ϕ and the interfacial scattering surface area depends upon the assumption of a particular pore geometry and pore size distribution. In general this is a complex proposition, especially if, as is generally the case, the system is polydisperse. Normally, Q values are not formally calculated from SANS data due to deviations from the resultant q^{-4} (Porod) behavior, and also because the q range of most instruments means that the maximum in scattering cannot be detected at the lowest q values available. Nevertheless, Q values provide a useful comparison as to how the void fraction of materials change following treatment.

One model that has been widely used to interpret scattering data from porous materials is a combined fractal and polydisperse spheres. The fractal portion of the scattering dominates at low q values and accounts for scattering from meso- and macroporosity. The polydisperse spheres portion

of the model dominates at high q, and, therefore, accounts for scattering from microporosity. This model has been used by Hall *et al* (1996) for scattering from microporous polymers. Jensen *et al* (1988) also used a similar model for heavily defected nickel that had been sputtered by krypton gas.

For surface fractals Schmidt (1991) and Teixeira (1988) have shown that

$$I(q) = I_o\, \Gamma(5-D) \sin [\pi(D-1)/2]\, q^{-(6-D)} \qquad [4.9]$$

where I_0 is a constant, $\Gamma(5\text{-}D)$ is a gamma function, and D is the surface fractal dimension.

The results of scattering from monodisperse spheres has been summarized above. In order to generalize this result to polydisperse spheres, a kind of normalized average intraparticle structure factor, P(R), exhibiting polydispersity (Foster and Jensen, 1990), must be defined:

$$P(R) = (1/\Gamma(b))(b/R_o)^b\, R^{b-1} \exp(-b\, R/R_o) \qquad [4.10]$$

where R_0 is the mean sphere radius and b is a parameter that increases with the sharpness of the distribution; in other words, it is something like an inverse variance.

The preceding modelling approach can be summarized as:

$$I(q) = (\text{Fractal}) + (\text{Spherical Polydispersity}) \qquad [4.11]$$

The mass fractal dimension, D_m, is defined by the relationship:

$$I(q) \propto q^{-Dm} \qquad [4.12]$$

where $2 \leq D_m \leq 3$.

Heenan (1989) has written a comprehensive program for the fitting of SANS data to a number

of different models, called FISH. This program was used to interpret the data here in terms of Eq. [4.11].

Neutron scattering can be a more flexible technique than X-ray scattering in the sense that b_V can be varied easily by using isotopic substitution. For example, the scattering cross sections of hydrogen and deuterium are very different; and, by using what is termed "contrast matching" it is possible to set b_V=0. This fact has important implications for the examination of porous materials and can be used to distinguish closed from open porosity in materials.

In SAXS experiments and SANS experiments on dry samples, scattering occurs from both closed and open porosity. If a liquid that contrast-matches the char or carbon sample fills the open porosity, then in SANS experiments scattering would be observed only from the "closed" porosity. Of course, if there were no "closed" porosity present then the scattering would disappear entirely.

Contrast matching SANS (CM-SANS) has been applied by Hall *et al.* (1996) to investigate the presence of closed porosity in a series of styrene-divinylbenzene resins produced with varying amounts of porogen during polymerization. A porogen is a chemically inert substance added during polymerization to produce porosity within polymers. Contrast matching with a (non-swelling) mixture of ethanol and [$^2H_6$]-ethanol reduced scattered intensities in all of the resins as the contrast matching liquid eliminated scattering from open porosity. Following contrast matching there was still residual scattering which Hall *et al.* (1996) interpreted as scattering from closed porosity. It was demonstrated that resins produced with small amounts of porogen had high levels of closed porosity and were therefore ineffective as ion exchange resins.

The presence of closed porosity is important to a number of chars and carbons, and the increase of surface area during the production of some active carbons may actually involve the opening of closed porosity. Therefore, the technique of CM-SANS and its ability to decouple open and closed porosity has considerable potential in the production and control of porosity in carbons. The objective here is to use CM-SANS on a char of known low porosity, to investigate the porosity developed during gasification and to compare the SANS results to nitrogen BET measurements.

4.2.2. Experimental.

The same chars used for the TPD and nitrogen adsorption experiments were also used for the SANS studies reported here. The preparation procedures for the Pittsburgh #8 and Wyodak coals char, and the resin char samples are described in Section 2.1. For the current work, all the chars were activated in air in a tube furnace at 400°C.

The char density of the phenolic resin char (PRC) is 1.67 g/cm^3, as determined by mercury intrusion porosimetry. This value is quite close to the true "skeletal" density of carbon, which yields a neutron scattering density of 5.6 x 10^{10} cm^{-2}. [$^2H_8$] toluene also has a scattering density of 5.6 10^{10} cm^{-2}, which, therefore, makes it suitable as a neutron contrast matching material for the resin char samples. Due to similarities with respect to density, deuterated toluene was also used as the contrast medium for the coal chars.

BET surface areas were obtained from nitrogen desorption isotherms at 77K using the Quantachrome Quantasorb apparatus over the range $0.01 < P/P^\circ < 0.95$, as described in Section 2.2. For all of the chars investigated here, the surface area determined by CO_2 adsorption at 273K was the same as the 77K N_2 adsorption isotherms, indicating the absence of extremely narrow porosity with molecular sieve properties.

SANS was performed at the Intense Pulsed Neutron Source (IPNS) at the Argonne National Laboratory at the small angle diffractometer (SAD) (Epperson *et al.*). This instrument has a wave vector range of $0.0058 < q < 0.249$ Å. The sample holders were made of low boron Suprasil with a path length of 0.2 cm. The scattering data were corrected for scattering from the sample holder and other instrumental backgrounds. Normalization for the sample thickness and transmission were made and the data were scaled to yield an absolute calibration.

4.2.3. Results and Discussion.

4.2.3-1. Pittsburgh #8 Coal Char. Figure 4.1 presents the 77K nitrogen adsorption isotherms for the Pittsburgh #8 coal char samples. For clarity, the isotherm for the ungasified char is shown on an expanded scale. The nitrogen BET surface area of the ungasified char was 8 m^2/g which suggests no significant open microporosity, or a small amount of macroporosity. This has

been previously observed by Hall and Calo (1990) and is typical of chars from coking coals. The isotherm is of Type II according to the BDDT classification (Brunauer *et al.,* 1940) which is typical for nonporous materials or materials which have pore systems with significant amounts of meso- or macroporosity. However, as noted previously, gas adsorption techniques can give no indication as to the possible existence of closed porosity, or whether porosity development proceeds by opening porosity or developing new porosity.

Mesopore size distributions from the adsorption isotherms calculated by the Roberts (1967) method are presented in Figure 4.2. As shown, the unactivated char has a fairly broad distribution of pore sizes peaking *ca.* 25 Å in radius. At 0.8% burn-off there is a broad distribution of large porosity and the development of significant microporosity. The 4.5% burn-off sample shows that the distribution has shifted dramatically to smaller pores <18 Å in radius. The 13.5% burn-off sample shows the formation of larger pores with a shift to significantly larger pore sizes.much larger pore sizes.

Small angle neutron scattering data for the ungasified char are presented in Figure 4.3. As shown, the scattering intensity increases monotonically even at the lowest q values. This behavior suggests that the size of the largest scatterer cannot be resolved. Guinier (1955) has shown that scattering due to spherical particles of a single size is given by:

$$I(q) = I(0) = \exp(-q^2 R_g^2/3), \qquad [4.13]$$

where I(0) is the scattering intensity at zero scattering wave vector, and the scattering radius of gyration, R_g, is a measure of the size of the particles. Hence, a plot of ln[I(q)] *vs.* q^2 should be linear if the size of the scatterers is unimodal. Figure 4.4 is such a Guinier plot of the "dry" scattering data in Figure 4.3. Since it obviously exhibits curvature over the entire q range, this is suggestive of a very broad range of pore sizes. This is consistent with the pore size distributions obtained from the nitrogen isotherm data in Figure 4.2.

From Figure 4.3 it can be seen that the effect of contrast matching by the addition of deuterated toluene significantly reduced the scattering intensity at all q-values. To illustrate this more graphically, the scattering intensity is shown on a linear scale in the inset in Figure 4.3. The Porod invariant (i.e., Eq. [4.7]) of the "dry" scattering curve is 5.04×10^{-3}, and 2.5×10^{-4} for the contrast matched curve. This means that the interfacial scattering surface area has been reduced by a factor of about 20. The CM curve in Figure 4.3 also shows that there is no significant scattering for $q > 0.078$ Å, which suggests the absence of porosity less than about 75Å. It is probable, therefore, that the residual scattering following contrast matching is due to a small number of large pores within the structure, or due to inhomogeneities such as mineral matter. The size of these scatterers cannot be resolved because of the q-range limit of the instrument. The result is that the dry and difference curves in Figure 4.3 are very similar. Therefore, in accordance with the generally accepted behavior of Pittsburgh No. 8 coal char, it has a very low level of porosity.

As described above, the "difference" curve of Figure 4.3 represents scattering from open porosity. This curve has been fit to a fractal model, which dominates the scattering at low q values. The resultant (surface) fractal dimension is $D_s = 2.13$, which suggests scattering from a globally smooth surface. The upward deviation from the fractal fit at large q is due to the presence of micropores, which are also evident in Figure 4.2. It was not possible to fit this residual scattering to a polydisperse spheres model, perhaps because the pore size distribution does fit a Schulz type distribution very well; e.g., the level of porosity is quite low and the distribution is very broad. Other distributions were tested but with similarly poor results.

Gasification to 0.8% burn-off increases the BET surface area to 80 m^2/g, which suggests the development of some microporosity. This is confirmed by the nitrogen isotherm pore size distribution data in Figure 4.2. The SANS data for the 0.8% burn-off char are shown in Figure 4.5. As with the ungasified char, contrast matching significantly reduces the scattered intensity, which suggests that there is very little closed porosity. These scattering data suggest that deuterated toluene can access all of the porosity developed during gasification.

Comparison of the scattering from the contrast matched samples in Figures 4.3 and 4.5 (shown in the inset in Figure 4.5) shows that they are very similar. Therefore, the scattering data from the 0% and 0.8% samples indicate that gasification proceeds by the creation of new porosity, rather than the opening of closed porosity, as is the case for phenolic resin char, as discussed below.

The dry scattering curve in Figure 4.5 is typical of a material with a well developed micropore system. The scattering behavior for a fractal surface is also shown in Figure 4.5, and the upward deviation from the fractal behavior is due to the presence of micropores formed during gasification. The fractal dimension is 2.1, which is similar to the ungasified char, and represents scattering from a relatively flat surface. Scattering from the micropores appears to follow the Schulz polydisperse sphere distribution reasonably well, with a mean micropore radius of 27 Å b = 3. This is in reasonable agreement with the pore size distribution data in Figure 4.2, which is also consistent with a fairly narrow distribution of micropores

The SANS results at higher burn-offs are presented in Figure 4.6, which also includes the 0.8% data for comparison. The difference scattering curve for the 4.5% sample shows an enhancement in scattering at the highest q values over the 0.8% sample. Somewhat unexpectedly, this suggests a reduction in the mean micropore size. Analysis of the 4.5% curve using the model in Eq. [4.11] yields a fractal dimension of 2.1, and Schulz distribution parameters of 24 Å mean pore size with b = 4. The SANS evidence for a reduction in the mean micropore size is confirmed by the pore size distribution data plot in Figure 4.2 which shows a shift to a narrower pores at a lower mean pore size.

Gasification to 13.5% burn-off produces a linear plot which suggests the formation of a fractal surface; the slope is -3 and the surface fractal dimension is therefore also 3, indicative of a highly convoluted surface. The nitrogen isotherm data data in Figure 4.2 show a large reduction in the level of microporosity and the production of a wide range of pore sizes. It is known that fractal surfaces are associated with wide pore size distributions. Therefore, there is agreement between the SANS and adsorption data.

In summary, contrast matching SANS shows that Pittsburgh #8 char has very little closed

porosity, and, consequently, that pore development during gasification proceeds by the creation of new pores. In the early stages of gasification (<4.5% burn-off), a pore system with significant microporosity is produced. In later stages of gasification (4.5%-13.5% burn-off) the tendency is to open these micropores, producing a pore system with a broad range of sizes.

4.2.3-2. Phenol-Formaldehyde Resin Char (PRC). It is well known that phenolic resins form a low density and highly microporous char. The apparent surface area of the unactivated char is very low (generally < $2m^2/g$), which indicates that most of the surface area is external, and, therefore, the material has a very low amount of accessible porosity. It has been noted that low levels of activation (e.g., 1-2% burn-off) increase the BET surface area significantly for these types of chars. Therefore, it has been hypothesized that PRC has a large amount of closed porosity in its unactivated form. This hypothesis can be directly tested experimentally with CM-SANS. It is expected that the interpretation of scattering from PRC samples should be simpler than that from coal chars, because the resin chars have no mineral matter and no scattering from macerals.

Figure 4.7 shows SANS data obtained for an unactivated PRC sample. As discussed above, scattering from the dry sample (referred to as the "dry" curve) is the result of scattering from the entire sample. Conversely, scattering from the PRC char and perdeuterated toluene mixture (referred to as the "contrast matched" sample) should only be from the porosity present in the char, since the perdeuterated toluene contrast matches the carbon very closely. One test of this hypothesis is that the intensity of scattering from the contrast matched sample should be less than that from the dry sample. This effect is certainly evident Figure 4.7. Although it is not formally possible to calculate Porod scattering invariants, ($\int I(q)\, q^2\, dq$), because the intensity is increasing at the lowest q values, and there is no q^{-4} variation, nevertheless these values provide a comparative indication of the interfacial scattering surface areas in the samples. The scattering invariant for the dry curve is 2.15×10^{-3}. The nitrogen BET surface area of the unactivated PRC was determined to be 2.5 m^2/g. This indicates that most of the surface area is external; most probably in the form of macroporosity, which is typical for glassy carbons. The effect of contrast matching reduces the scattering invariant to 1.52×10^{-3}, a

factor of 0.29 less. This indicates that there is a considerable amount of closed porosity in the structure. This is almost the opposite of the result for the Pittsburgh #8 coal char, discussed above. In that case, the effect of contrast matching was to reduce the scattering invariant by a factor of 20. This was a demonstration of the fact that the unactivated Pittsburgh #8 coal char sample had no internal porosity. The scattering invariant of the difference curve for the PRC is 0.63×10^{-3}.

The dry and contrast matched scattering curves for the 0% burn-off sample in Figure 4.7 are typical of scattering from a microporous material. The scattering data were fit to Eq. [4.11], and the results are summarized in Table 4.1. The slope of the linear portion in the low q region of the dry sample is -2.4, indicating that the scattering is from a surface fractal of fractal dimension 2.6. As previously discussed, the upward deviation is due to the presence of micropores. When fit to a polydisperse spheres model with a Schulz distribution, the resultant mean micropore size is 8.6 Å with b = 1. Scattering from the fractal portion of the contrast matched sample is also from a surface fractal, but for this sample, the fractal dimension is 2.67. The mean size of the micropores is 9.1 Å with b = 1. Scattering for the difference curve is typical of scattering from a nonmicroporous material, or a material with a wide pore size distribution. The curve is linear on the log-log plot, indicating fractal scattering; the surface fractal dimension is 2.5.

Activation to 21% burn-off increases the nitrogen BET surface area to 31 m^2/g. This value was unexpectedly low for this class of materials, and the reasons for this are not clear but it may be that a significant part of the carbon is lost from the external surface. Figure 4.8 presents the dry, contrast matched and difference SANS data for PRC activated to 21% burn-off in air. As in Figure 4.7, the scattering from the contrast matched sample is less than from the dry sample, which is due to the elimination of scattering from open porosity, and also possibly from voids between the carbon particles. There is a difference in the relative scattering intensities in the curves in comparison to those in Figure 4.7. The scattering invariant of the dry curve is 1.75×10^{-3}, and the corresponding value for the contrast matched sample is 0.67×10^{-3}. This is a reduction of a factor of 0.64, which is greater than the corresponding reduction of 0.29 for the unactivated sample. This is explained by the

fact that the proportion of closed porosity has been reduced during activation. The scattering invariant of the difference curve is 1.08 x 10^{-3}, which suggests that there has been some development of closed porosity during activation. This is consistent with the increase in surface area determined from the nitrogen data. All three curves for the 21% burn-off sample exhibit properties of scattering from microporous materials. The resultant fit mean micropore sizes and fractal dimensions are given in Table 4.1.

Figure 4.9 compares the scattering results from the dry 0% and 21% samples. The corresponding Porod scattering invariants, presented in Table 4.2, are 2.15 x 10^{-3} and 1.75 x 10^{-3}, respectively. A conventional interpretation of these data would be to conclude that the effect of activation is to reduce the interfacial scattering area by a factor of 0.18, and gives no indication of the process of pore opening. Also, there is no significant change in the overall mean size of the micropores nor in the fractal dimension. Changes in the pore structure only become evident upon contrast matching.

The results of the contrast matched experiments on the 0% and 21% samples are presented in Figure 4.10. As discussed above, the reduction in the Porod invariants is explained by the opening of closed porosity. Another feature of interest in Figure 4 is the ratio of scattering intensity as a function of q for these samples (shown in the inset). As can be seen, this ratio is relatively constant over a large q range. This suggests that the form factor of the objects underlying the scattering is the same for both samples. In practical terms, this shows that the pore size distributions of the closed porosity for both samples is similar. This is not an unreasonable conclusion, given that the activation process cannot alter closed porosity, but shows that the process of activation in the PRC char does not selectively open large or small pores. Table 4.1 shows that the mean micropore sizes and fractal dimensions from the fits to the data are also similar.

Figure 4.11 presents a comparison of the difference curves for the 0% and 21% samples. It can be seen that the principal difference between the curves is an augmentation of scattering at high q values. This is the region of the scattering curve that is dominated by scattering from micropores. It was argued above that the difference curves provide information about open porosity. The scattering

curve for the 0% sample is characteristic of scattering from a char with no microporosity. The augmentation in scattering at high q values is due to the formation of microporosity. The fractal and polydisperse spheres model gave a mean micropore size of 10.4 Å, although the quality of the fit was not as good as for the other samples. This may be due to the fact that the micropore size distribution deviates significantly from the assumed Schulz polydisperse spheres distribution.

In summary, scattering from the dry samples provides information about the entire porosity of the sample. These data yielded a mean micropore size of 5.6 Å for 0% burn-off, and 5.9 Å for the 21% burn-off sample. The contrast matched samples provide information about the closed porosity present, and the difference between the dry and contrast matched samples yields information about open the porosity. The Porod scattering invariants for the contrast matched and difference 0% burn-off sample shows that most of the porosity is inaccessible from the external surface. The process of activation to 21% burn-off is shown to open previously closed porosity, and also that the mean micropore size of the open porosity is about 10.4 Å.

4.2.3-3. Wyodak Coal Char. Scattering curves for five Wyodak coal char samples (0, 9.2, 32.7, and 68% burn-off) are presented in Figures 4.12-16. Taken together, these plots illustrate the principal changes in the pore system that occur during gasification. Variation of the surface area, as determined by nitrogen uptake, and the Q values for the difference and contrast matched curves are given in Table 4.3.

The SANS data for the unactivated Wyodak coal char are presented in Figure 4.12. As shown, the scattering intensity of the difference curve (which represents scattering primarily from open porosity) is greater than that of the contrast matched curve (which represents scattering from "closed" or inaccessible porosity) for $q < 0.21$ Å^{-1}, but that scattering from from the contrast matched curve is greater than the difference for $q > 0.021$ Å^{-1}. The overall effect on the Q values is that the contrast matched value (3.13) is much greater than the difference value (1.03). Combined with the relatively low nitrogen BET surface area of the char sample (12 m^2/g), this suggests that the char has a significant amount of porosity which is inaccessible to the external surface. Apparent as well is the

linear portion of the difference scattering curve over the range 0.249 < q 0.027 $Å^{-1}$, with a slope of -4.0. This is characteristic of Porod scattering, indicating that the scattering is primarily from features with smooth surfaces. There is an upward deviation from this behavior at larger q values, which is typical of scattering from micropores. The latter scattering data were fit to a Schulz polydisperse distribution of spheres, with a mean pore size of 24.5Å and b = 4. The contrast matched curve also exhibits a linear portion with a slope of -3.0., indicating scattering from a fractal surface of dimension 3.0; in other words, from a highly convoluted surface. As for the difference curve, the upward deviation from the fractal scattering line at large q values was fit to the Schulz model with a mean pore size radius of 10.98 Å with b = 2.

Figure 4.13 presents the SANS data for the char burned off to 9.2%. For these data, the difference scattering curve is greater than or equal to the the intensity of the the contrast matched curve over the entire q range. Figure 4.16 shows that the Q for the difference curve (1.71) is greater than for the contrast matched curve (1.64). This is because the relative balance between closed and open porosity has decreased during activation. The difference curve was again deconvoluted into fractal and micropore distribution regions. The slope of the linear portion is -4.0, indicative of Porod behavior, and the mean pore radius is 18.2Å with b = 4. The contrast matched curve for the 9.2% burn-off sample also fits the model reasonably well. The results are similar to those for the unactivated sample. The slope of the fractal portion is -2.95, which is on the borderline between mass and surface fractal scattering, but is close to the value of -3.0 for the ungasified sample and a sample burned off to 7.4% (which is not discussed in detail here). the mean micropore size is 12.3 Å with b = 2. There is a slight increase in the micropore size from the ungasified sample, indicating perhaps that there is a propensity for the smallest pores to be opened.

The data in Table 4.3 shows that activation to 32.7% burn-off increases the nitrogen BET surface area to 270 m^2/g. The Q of the difference curve increases to 3.68, which is consistent with the increase in surface area. The Q of the contrast matched curve exhibits a further decrease to 1.47, which suggests a further decrease in the level of closed porosity. The scattering data for this sample

are presented in Figure 4.14. To illustrate the effect of contrast matching, the data is also presented on a linear scale for in the inset. It may be concluded that there is very little closed porosity in this sample. Indeed, there is probably a significant contribution to scattering in the contrast matched sample from the scattering contrast between the carbon/solvent and mineral matter present. It was not possible to fit the scattering data for the difference curve to Eq. [4.7]. Rather, it is possible to identify two linear regions with slopes of -2.9 at small q values, and -2.4 at large q values. These correspond to scattering from mass fractals. Fractals are associated with wide pore size distributions, and, as expected, the picture that emerges is that of the activation process widening the original porosity.

The maximum nitrogen BET surface area observed of 397 m^2/g was achieved at a burn-off of 58%. As shown in Table 4.3, this also corresponds to the maximum Q of 10.3 x 10^{-3}. The Q of the contrast matched sample decreases to the minimum value observed of 1.0 x 10^{-3}, and as can be seen in Figure 4.15, the difference and dry scattering curves are almost identical. In other words, there is no "closed" porosity in the sample. As previously discussed, the residual scattering in the contrast matched curve most probably results from the contrast difference between the mineral matter in the Wyodak coal char and the carbon/deuterated toluene. The difference curve is linear over the entire q range with a slope of -2.6, and, therefore, scattering occurs from a mass fractal.

The last sample investigated in the burn-off range was 68%. Table 4.3 shows that that the nitrogen BET surface area and the Q of the difference curve exhibit a decrease from the 58% burn-off sample.The Q of the contrast matched curve is the same as for the 58% sample, 1.3 x 10^{-3}, and again it is likely that that the origin of the scattering is primarily from mineral matter. The difference curve shown in Figure 4.16 exhibits two linear regions, one with a slope of -2.4 at low q, and the other with a slope of -3.3 at high q. The former is attributed to scattering from a mass fractal, and the latter to scattering form a surface fractal. The decrease in surface area is caused by a breakdown of the walls separating pores in the char structure at high burn-offs, as expected, and is accompanied by a decrease in the char particle size.

In the preceding discussion, a number of references have been made to the relationship between

the nitrogen BET surface area, the neutron scattering intensities, and the Porod invariants. Figure 4.17 presents the "difference" curves, taken as a measure of the accessible porosity, as a function of burn-off. It is quite evident that the degree of scattering correlates with the nitrogen BET surface areas presented in Table 4.3. In addition, as shown in Figure 4.18, there is a correlation between the nitrogen BET surface areas and the Porod invariants. This is also evident in Figure 4.19. However, although the Q values and surface areas appear to follow broadly similar trends, there is no constant ratio between them.

4.3. Modeling Porosity From SANS Data.

Although the model of Eq. [4.11] provides some insight into the interpretation of the SANS data from the char samples, a more robust model may be useful for extracting more information concerning the porosity of these materials. At least two criteria should be met when selecting a suitable porous structure model. The first is that the model incorporate as much of the essential characteristics of the real structure as possible. In the case of the types of porous structures under consideration, *connectedness* of the porosity is of particular concern, since small angle scattering is only sensitive to the local structure and is thus insensitive to *connectedness,* which is a global property. The other important criterion in model selection is mathematical tractability. If the model is too complex, the interpretation of model results may become difficult and the correspondence with other techniques may be difficult or impossible to draw.

One such model that seems to fulfill these two criteria in some sense is known as the Fully Penetrable Polydisperse Spheres (FPPS) model, as proposed by Foster and Jensen (1990), for example. Essentially, this model approximates porosity by randomly distributing spheres (e.g., voids) within a material (e.g., the solid phase). The interpenetration of these spheres imparts connectedness to the resultant pore structure. The size of these spheres can be distributed over a finite or infinite size range. Moreover, when the porosity is multimodal, as it is in many coal chars for example, more than one mode or distribution of spheres may be needed to describe the porosity. The software necessary to analyze the scattering data using a bimodal FPPS model has been developed.

An outline of the approach follows.

4.3.1. Analysis Procedures.

For a random, isotropic structure with two phases of uniform density, I(q) may be expressed in terms of the correlation function $\gamma(r,\mathbf{p})$:

$$I(q) = V\,(b_v^2)\,\phi_s\,(1 - \phi_s)\int_0^\infty \gamma(r,\mathbf{p})\,(\sin(qr)/q\,r)\,4\,\pi r^2\,dr, \qquad [4.14]$$

where ϕ_s the volume fraction of the solid phase. The correlation function, $\gamma(r,\mathbf{p})$ for a model with parameter values **p** represents the probability that a point at distance r in an arbitrary direction from a point in a given phase will also be in that phase.

The number of parameters **p** required to specify the correlation function depends on the form chosen for the frequency distribution of the sphere sizes, f(R), as well as the solid volume fraction, ϕ_s. The correlation function is closely related to the two-point conditional probability function $S_2(r; f(R),\phi_s)$; *viz.*,

$$\gamma(r; f(R),\phi_s) = [S_2(r; f(R),\phi_s) - \phi_s^2]/[\phi_s(1 - \phi_s)]. \qquad [4.15]$$

$S_2(r; f(R),\phi_s)$ has been derived for a general, single mode distribution, f(R), by Foster and Jenkins (1990). The evaluation of $S_2(r; f(R),\phi_s)$ involves integrations over the frequency distribution f(R). Hence, the application of Eq. [4-14] to calculate the scattering intensity requires a double integration over r. One useful frequency distribution for the sphere sizes, examined by Foster and Jenkins (1990), is the Schulz polydisperse spheres distribution, presented above in Eq. [4.10]. Plots of this distribution function for various values of b are presented in Figure 4.20. The requisite numerical integration for the evaluation of $S_2(r; f(R),\phi_s)$ can be simplified by making use of the fact that the integrals in the two-point conditional probability function for the Schulz distribution can be simply represented by incomplete gamma functions, P(c,x):

$$P(c,x) = \int_0^x t^{c-1} e^{-t} dt \qquad [4.16]$$

In this form, the expression for $S_2(r; f(R),\phi_s)$ for the Schulz distribution simplifies to:

$$S_2(r; f(R),\phi_s) = \exp[-\ln \phi_s (I_1 + I_2 - I_3)] \qquad [4\text{-}17]$$

where:

$$I_1 = 1 + P(b+3,x) \qquad [4.18a]$$

$$I_2 = (3/4)\, r\, (1-P(b+2,x))/[(b+2)^2\, (a_o/b)^2] \qquad [4.18b]$$

$$I_3 = (r^3/16)\, (1 - P(b,x))/\mu_3 \qquad [4.18c]$$

where,

$$x = b\, r/2\, R_o \qquad [4.18d]$$

where R_o is the mean sphere size of the distribution. Moreover, the incomplete gamma functions are related to one another by simple recursion relationships; i.e.,

$$P(b+1,x) = P(b,x) - A \qquad [4.19a]$$

$$P(b+2,x) = P(b+1) - x\, A/(b+1) \qquad [4.19b]$$

$$P(b+3,x) = P(b+2) - x^2 A/[(b+2)(b+1)] \qquad [4.19c]$$

where,

$$A = x^b e^{-x}/(b\, \Gamma(b)), \qquad [4.19d]$$

such that only one incomplete gamma function, P(b,x), and $\Gamma(b)$ need be evaluated for each value of x. This ultimately represents a considerable savings in computation time, since it essentially eliminates the inner integrations. The gamma function, $\Gamma(b)$, and the incomplete gamma functions, P(b,x), are evaluated using series approximations obtained from *Numerical Recipes* (Press *et al.*, 1987).

Most activated carbons and chars typically exhibit a bimodal distribution of pore sizes, typically

characterized as the micro- and mesoporosity. Consequently, in order to apply the preceding approach to determine the scattering function I(q) for a char with a bimodal porosity distribution, at least two modes must be incorporated into the distribution function of spheres. The total distribution will then be a linear combination of the two modes; i.e.,

$$f(R) = \varepsilon_1 f_1(R) + \varepsilon_2 f_2(R) \qquad [4.20]$$

where the ε_i are the relative weights, and $\Sigma \varepsilon_i = 1$.

A correlation function calculated for a bimodal Schulz distribution model for an arbitrary parameter set is presented in Figure 4.21, and the corresponding scattering intensities are presented in Figure 4.22 as a function of the scattering vector, q. As shown, the correlation function incorporates two distinct regions. The one at low ρ reflects the larger spheres, while the tail at large ρ is due to the small spheres. Likewise, the resultant scattering curve exhibits two regions. The scattering pattern for values of $q < 0.08\text{Å}^{-1}$ is controlled by the dimension of the larger spheres, while the scattering pattern at $q > 0.08\text{Å}^{-1}$ predominantly reflects the size of the smaller spheres. Since the scattered intensity from an object is proportional to the square of its volume, and thus to the sixth power of its characteristic dimension, the large spheres have a disproportionately strong effect on the observed scattering curve, although they are few in number (i.e., ε_1 near unity). In cases where the two modes are broader or the means closer, the presence of the second mode will be more difficult to discern in the correlation function. The "plateau" in the scattering curve due to the second mode will also be much less distinct, and may only appear as a "shoulder" in the steeply decreasing intensity from the larger spheres. If the contribution of the large spheres becomes greater (i.e., high ε_2), even the shoulder may disappear.

The objective in fitting small angle scattering data is to obtain parameters for a model that fit the experimental data best. For a bimodal FPPS Schulz distribution model, this becomes essentially a nonlinear, six-parameter fit; i.e., the parameter set is $R_{0,1}$, b_1, $R_{0,2}$, b_2, ϕ_s, and ε_1. The void fraction

parameter, ϕ_s, is related to the data in a self-consistent manner *via* the Porod invariant given in Eq. [4.8] (Higgins and Benoît, 1994):

$$Q \equiv \int_0^\infty q^2 I(q)\, dq = 2\pi^2 b_v^2 I_e V \phi_s (1 - \phi_s) \qquad [4.21]$$

Consequently, if the various parameters in Eq. [4.21] are known, the parameter ϕ_s can be determined from the data. However, the data actually obtained from an instrument may be "averaged" or "smeared" such that the invariant becomes, Q*:

$$Q^* \equiv \int_0^\infty q\, \hat{I}(q)\, dq = 4\pi^2 b_v^2 V \phi_s (1 - \phi_s) = 2\, Q \qquad [4.22]$$

where $\hat{I}(q)$ is the "averaged" data obtained from the instrument.

In general, the model prediction of I(q) or $\hat{I}(q)$ must be determined numerically and the reconciliation of the experimental and calculated scattering intensities then requires nonlinear regression. Although various objective functions can be formulated, in order to more equally weight evenly spaced data (in q), Foster and Jensen (1990) suggested an objective function based on the logarithms of the intensities:

$$\Phi = \sum_{i=1}^{N} [\ln(I^*(q)) - \ln(I(q))]^2, \qquad [4.23]$$

where the I*(q) and the I(q) are the experimental and calculated scattering intensities, respectively, and N is the total number of experimental values. A nonlinear least squares fitting algorithm can then be used to evaluate the model parameter set which minimizes the objective function, Φ.

For the current purposes, a Levenberg-Marquardt, or Marquardt method, was selected. This technique has become a standard for nonlinear least squares parameter estimation. The code was developed form a description in Numerical Recipes (Press *et al.*, 1987) and was written in

FORTRAN. In order to implement the Marquardt routine, the derivatives of the intensity integral, I(q), with respect to each of the model parameters must be determined. The corresponding derivatives, $\partial I/\partial R_{01}$, $\partial I/\partial b_1$, $\partial I/\partial R_{02}$, $\partial I/\partial b_2$, $\partial I/\partial \phi$, and $\partial I/\partial \varepsilon_1$, can all be determined analytically once P(b,x) has been evaluated numerically. The resultant Marquardt fitting program, SCATTER, is presented in Appendix E.1. The derivatives listed above can be found in SUBROUTINE FUNC in program SCATTER. The code was first tested against "data" synthesized using arbitrarily selected parameter sets, using the program SYNTHESIZE, presented in Appendix E.2. Such synthesized "data" were assigned 1% variances. The program was always successful in converging to the "correct" parameter set in typically less than one hundred iterations.

In practice, the fitting procedure was as follows. First the data set was roughly fit using the SYNTHESIZE program by iteratively guessing suitable parameter values until an approximate fit was obtained "by eye." A multiplicative scaling factor, I_o, was obtained by averaging the ratios of the experimental to the calculated scattering intensities over all the data points, N:

$$I_o = \sum_{i=1}^{N} [I(q)/I^*(q))]/N \qquad [4.24]$$

A comparison of Eqns. [4.14] and [4.22] indicates that I_o and Q or Q* are related *via:*

$$Q/(2\pi^2 I_o) = \phi_s (1 - \phi_s), \qquad [4.25]$$

or

$$Q^*/(4\pi^2 I_o) = \phi_s (1 - \phi_s), \qquad [4.26]$$

such that I_o and ϕ_s are not independent parameters. Thus an arbitrary value of ϕ_s (= 0.607, the theoretical minimum; Foster and Jensen, 1990) was used, and the corresponding value of I_o was obtained using the SYNTHESIZE program. These two values, along with the other five parameter values estimates arrived at using SYNTHESIZE were input into the Marquardt program, SCATTER, to "sharpen" the parameter set and obtain improved values of the parameters $R_{0,1}$, b_1, $R_{0,2}$, b_2, and ε_1. This set could then be used again in SYNTHESIZE to improve upon the values of I_o (and thus

also ϕ_s). In practice, however, this additional iteration was usually unnecessary.

4.3.2. Results and Discussion.

The resultant fits of the bimodal Schulz FPPS model to the SANS data for the unactivated PRC (discussed above in Section 4.2-3.2) are presented in Figure 4.23, and the corresponding parameter sets are presented in Table 4.4. As shown, the resultant fits are quite good. The resultant polydisperse distributions of spheres are presented in Figure 4.24. As shown, the distributions for the smaller porosity are quite sharp and peaked *ca.* $R_{0,1}$ = 5Å, for a characteristic mean pore size of about 10Å. In contrast to this, the distributions for the "larger porosity" are very broad, with mean values *ca.* 9Å. Although the resultant mean sizes are quite similar to those obtained with the fractal-single mode FPPS model above, the variance of the distributions for the small pores are quite different. In this case, the bimodal distribution is essentially unimodal, since the values of $R_{0,2}$ and b_2 are quite low, such that this mode is superimposed over the other. The two modes are presented on a logarithmic scale in Figure 4.24 to show that the "larger porosity" distribution provides the small "wing" at low values of R, which is necessary to fit the relatively broad "plateau" evident in the scattering intensity at high q-values. It also provides the relatively small amount of larger scatterers needed to account for the scattering intensity at low q-values. In other words, the unactivated PRC is essentially microporous, but the shape of the unimodal Schulz distribution is insufficient to account for the scattering intensity at both the highest and the lowest q-values; this is made up for by the other mode. The relatively low amount of large scatterers in the unactivated PRC is attributable to interparticle scattering, macropores, and/or cracks.

The resultant distributions of scatterers are presented in Figure 4.25 for the contrast matched (CM) and difference (Diff.) scattering intensities. The CM scattering intensities should represent the "closed" porosity, since all the "open" porosity should be filled with the contrast matching deuterated toluene. Consequently then, the "difference" between the dry and contrast matched scattering curves should represent the "open" porosity. As shown, for the unactivated PRC the "closed" porosity exceeds the "open" porosity by about a factor of 2.5. This is to be expected for a "glassy" carbon like

PRC.

It is of interest to determine whether the applicable Porod invariant is closer to the absolute value, Q, or the "smeared" value, Q*. Using the I_0 values from Table 4.4 indicates that the Q* values calculated from Eq. [4.26] agree quite closely with the Q* determined from the scattering data according to Eq. [4.22]. For the CM data, Eq. [4.26] yields Q* = 0.0145 in comparison to 0.0138 from Table 4.4. From the difference data, Q* = 0.0057 from Eq. [4.26], in comparison to 0.0071 from Table 4.4. Consequently, it is concluded that the scattering intensity data are "smeared" or "averaged."

The SANS data for the 21% burn-off PRC sample (discussed above in Section 4.2-3.2) were analyzed in a similar fashion. The resultant fits to the bimodal FPPS Schulz model are presented in Figure 4.26, and the corresponding parameter sets are presented in Table 4.5. Once again, the bimodal fits are quite similar to what was found for the unactivated PRC sample data. That is, the distributions of scatterers are essentially unimodal, indicative of a microporous char, with the mode representing the larger porosity superimposed on the narrower mode for the small porosity. Also as shown, Figure 4.26 appears to be similar to Figure 4.23, with the major exception that the contrast matched curve is now *less* than the difference curve. This indicates that there is considerably more "open" than "closed" porosity in this sample than in the unactivated PRC, as would be expected. The corresponding distributions of scatterers are presented in Figure 4.27, and, as shown, the "open" porosity distribution is a factor of 15 greater than the "closed" porosity.

In addition, as was also the case for the unactivated PRC, the Q* invariants for the 21 % burn-off PRC agreed much more closely with the values determined from Eq. [4.26], than the Q Porod invariants. Using the I_0 values from Table 4.5, Q* = 00604, in comparison to 0.00623 determined from Eq. [4.22] for the contrast matched data, while Q* = 0.00913 from Eq. [4.26] and 0.01045 from Eq. [4.22] for the difference data. Consequently, as previously, the data seem to be averaged or "smeared," and Q* is the more correct form of the invariant.

4.4. Summary and Conclusions.

Small angle neutron scattering (SANS) has been demonstrated to be a very useful technique for porosity characterization of carbons and chars. It is uniquely suited for the determination of the proportion of "closed," or inaccessible, *vs.* "open," or accessible porosity, as well as the elimination of interparticle scattering effects, which represent a problem for small angle X-ray scattering (SAXS) for example.

The apparent discrepancy between the fitting results for the fractal-unimodal FPPS Schulz model and the bimodal FPPS Schulz model remains to be resolved. However, it is anticipated that the bimodal model will ultimately provide a more useful description of char porosity.

Qualitatively, the behavior of porosity in the three chars investigated in this project -- Pittsburgh #8, Wyodak, and phenolic resin chars -- was determined to be the same as found using the new thermal desorption methods described in Section 3.0. That is, unactivated Pittsburgh #8 coal char has essentially no porosity, either "open" or "closed." It then progressively develops porosity with burn-off. Wyodak and phenolic resin chars, however, behave somewhat similarly in that they both are essentially microporous, with a greater proportion of "closed" than "open" porosity at 0% burn-off, which then "opens up" with progressive burn-off. Quantitatively, however, SANS techniques are much better developed than the thermal desorption methods which are new with the current project.

Table 4.1. Phenolic resin char (PRC) mean micropore sizes and fractal dimensions.

		Mean micropore size (Å)	Fractal Dimension D_s
0%	dry	8.6	2.6
	contrast matched	9.1	2.7
	difference	no micropores	2.5
21%	dry	8.9	2.6
	contrast matched	9.2	2.7
	difference	10.4	2.6

Table 4.2. Phenolic resin char (PRC) Porod scattering invariants ($Q \times 10^3, \pm 0.1$)

	0%	21%
Dry	2.1	1.7
Contrast Matched	1.5	0.7
Difference	0.6	1.1

Table 4.3. Wyodak coal char surface areas and Porod invariants (Q).

Burn-off (wt %)	Nitrogen BET Surface Area (m^2/g)	Q (x 10^3) (Diff.)	Q (x 10^3) (CM)
0	12	1.03	3.13
7.4	N.D.	1.49	1.60
9.2	140	1.71	1.64
32.7	270	3.68	1.47
58.0	397	10.3	1.30
68.0	268	4.86	1.30

Table 4.4. Parameter values for bimodal Schulz FPPS model for unactivated PRC.

Sample	R_{o1}	b_1	R_{o2}	b_2	ε_1	I_o (x10^3)	Q (x10^3)	Q* (x10^2)
Contrast Matched	5.5	50.	8.8	0.1	0.98	1.54	1.52	1.38
Difference	5.25	50.	10.	0.1	0.965	0.605	0.634	0.712

Table 4.5. Parameter values for bimodal Schulz FPPS model for PRC burned-off to 21%.

Sample	R_{o1}	b_1	R_{o2}	b_2	ε_1	I_o (x10^3)	Q (x10^3)	Q* (x10^2)
Contrast Matched	5.0	20.	8.	0.1	0.98	0.641	0.672	0.623
Difference	5.25	30.	25.	0.2	0.97	0.970	1.08	1.045

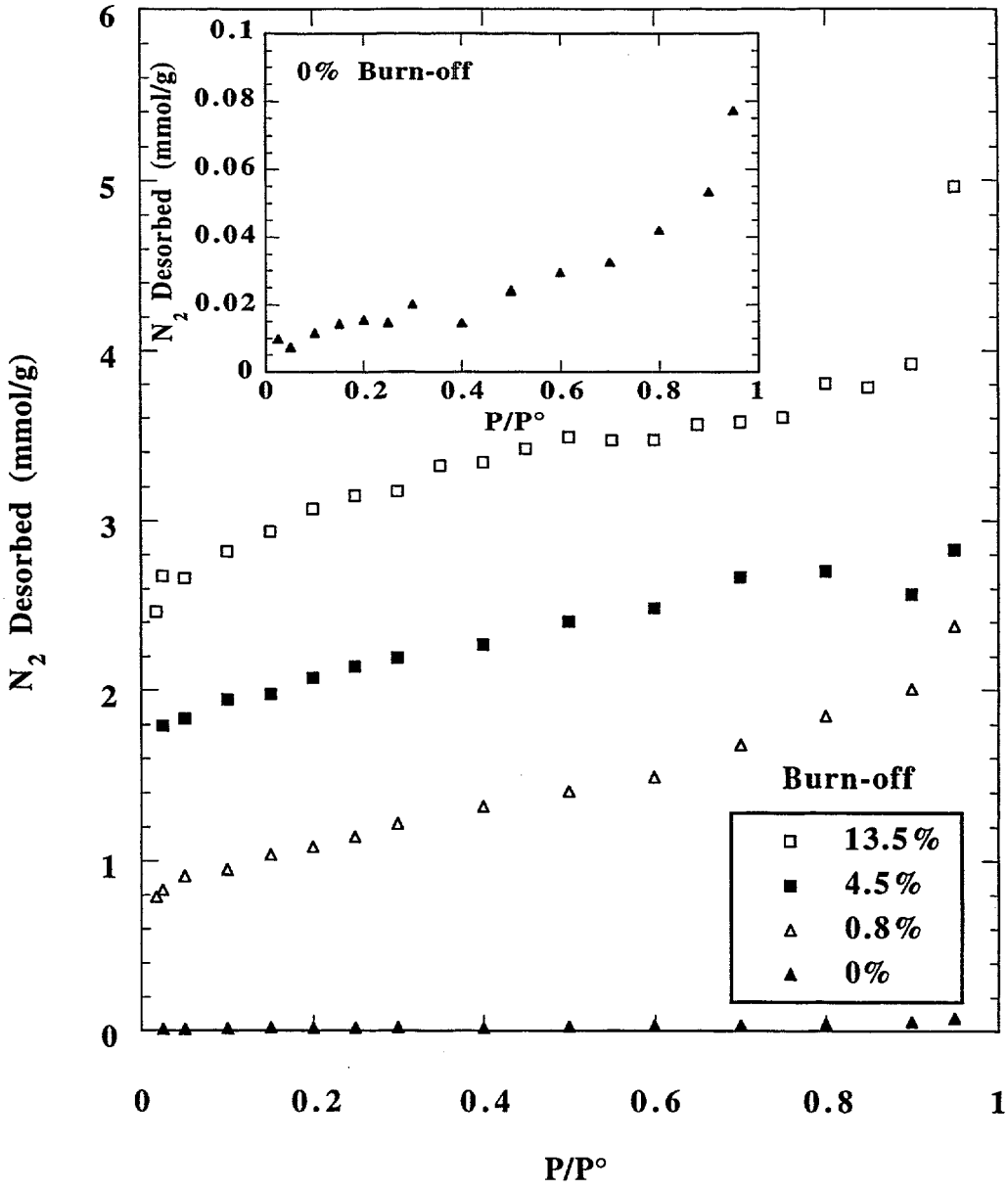

Figure 4.1. Nitrogen desorption isotherms for Pittsburgh #8 coal char samples as a function of burn-off in air at 400°C. The isotherm for the ungasified char (0% burn-off) is shown in the inset on an expanded scale.

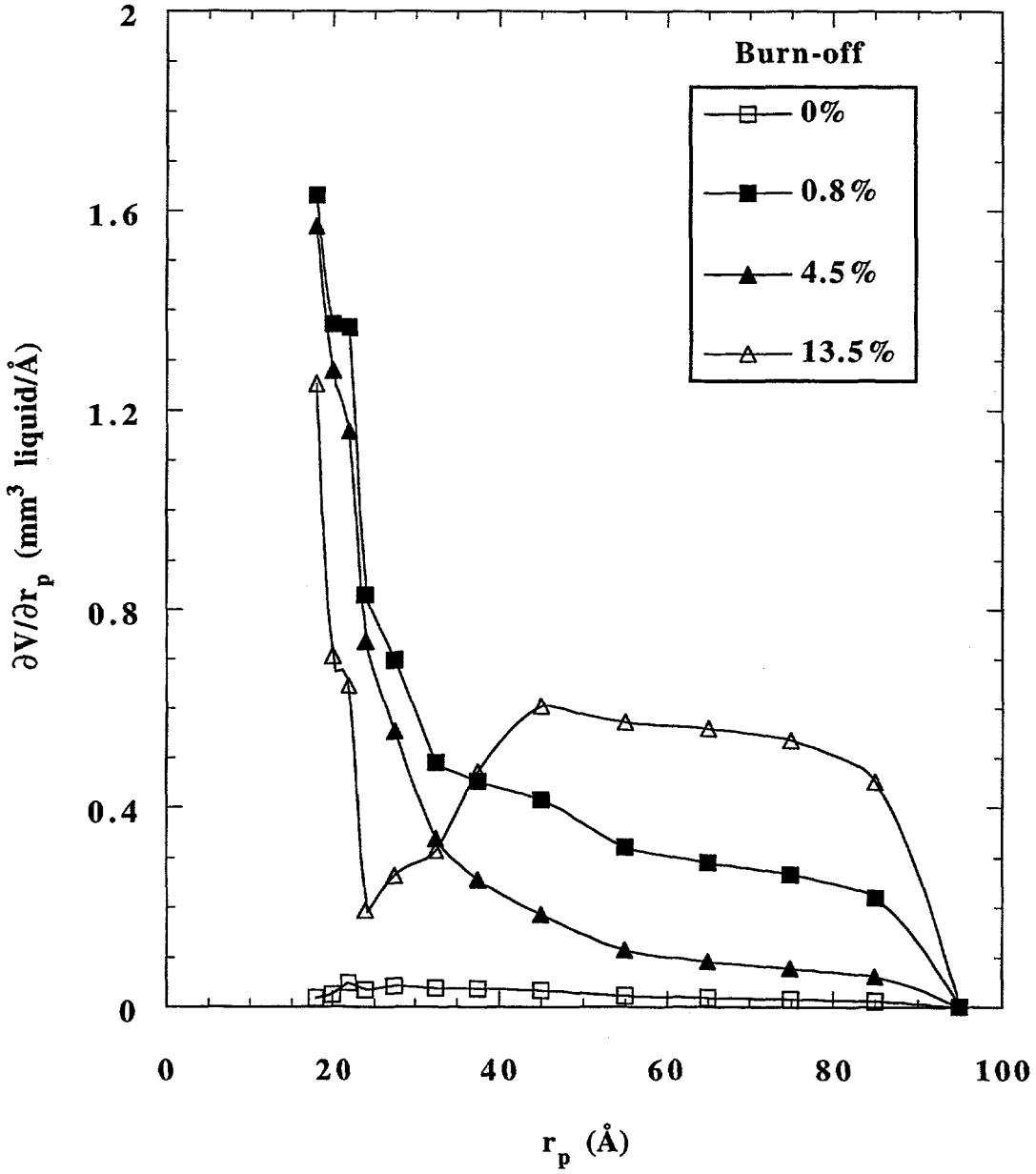

Figure 4.2. Mesopore size distributions for Pittsburgh #8 coal char, as determined by the method of Roberts (1967) from the nitrogen desorption isotherm data presented in Figure 4.1.

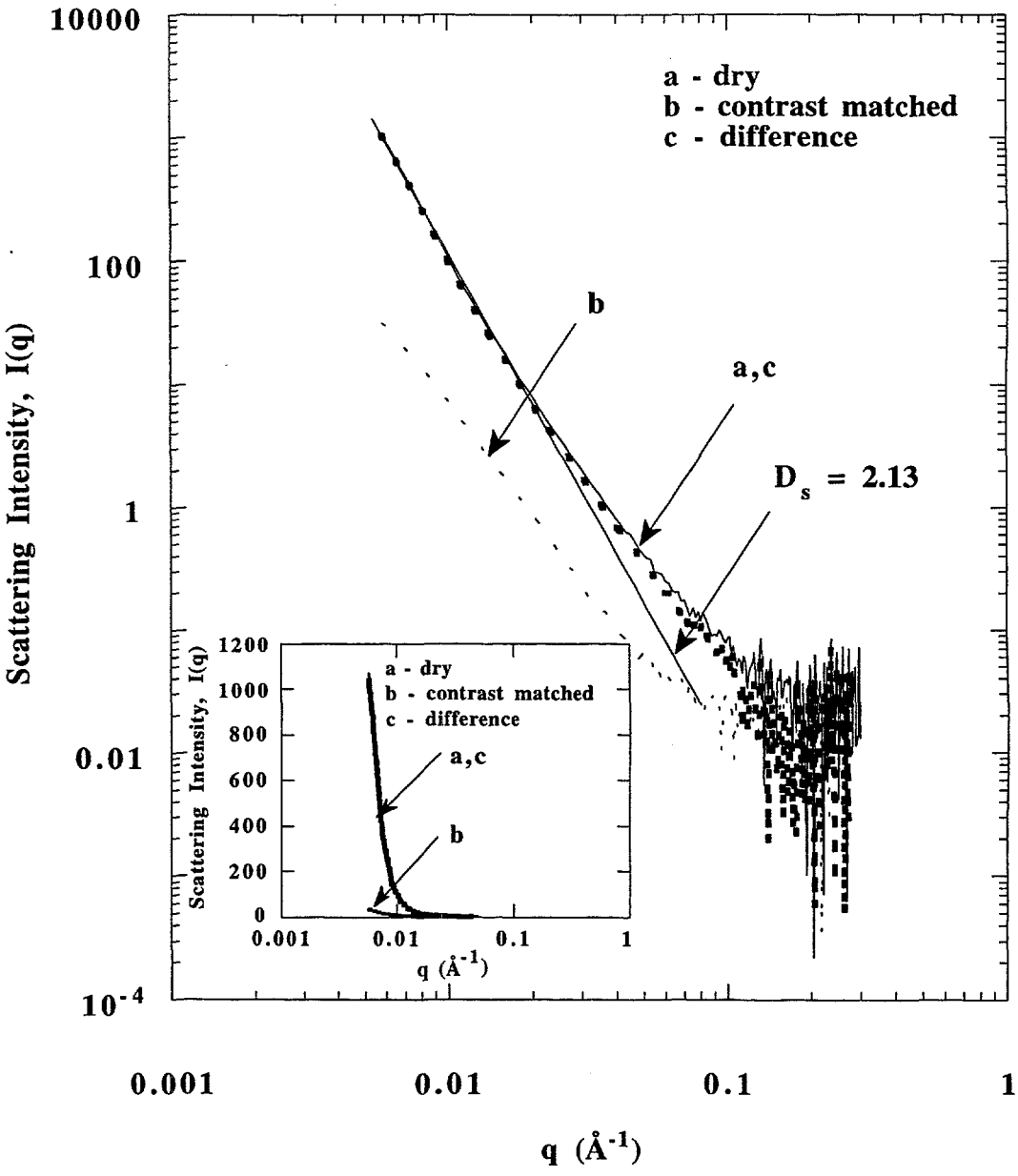

Figure 4.3. Small angle neutron scattering from unactivated (0% burn-off) Pittsburgh #8 coal char: (a) dry; (b) contrast matched with deuterated toluene; and (c) difference between scattering curves (a) and (b). The straight line is the fractal fit at low q values with D_s = 2.13. The same curves are shown on a linear scale in the inset.

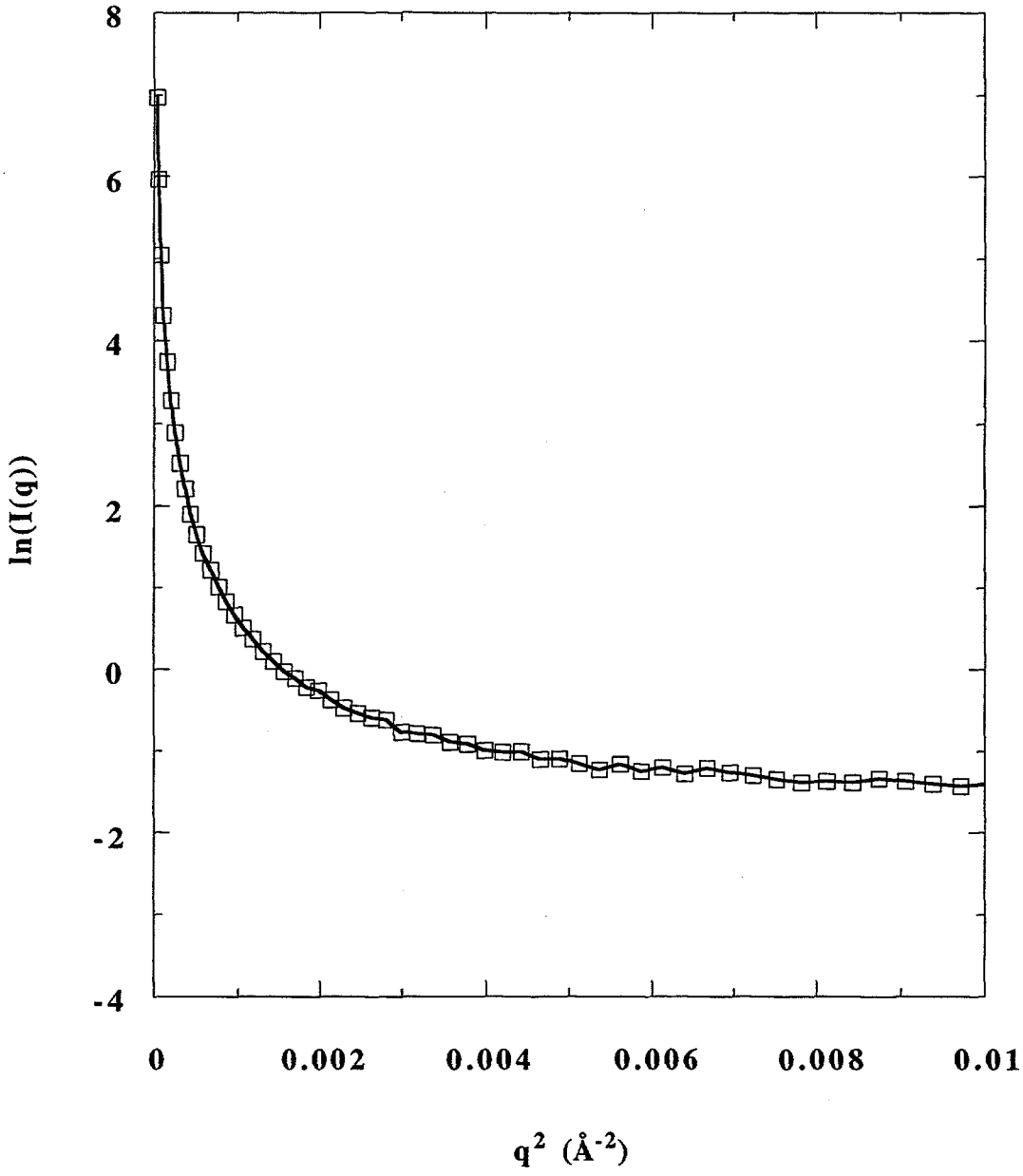

Figure 4.4. Guinier plot of the "dry" scattering intensity data presented in Figure 4.3 for the unactivated (i.e., 0% burn-off) Pittsburgh #8 coal char.

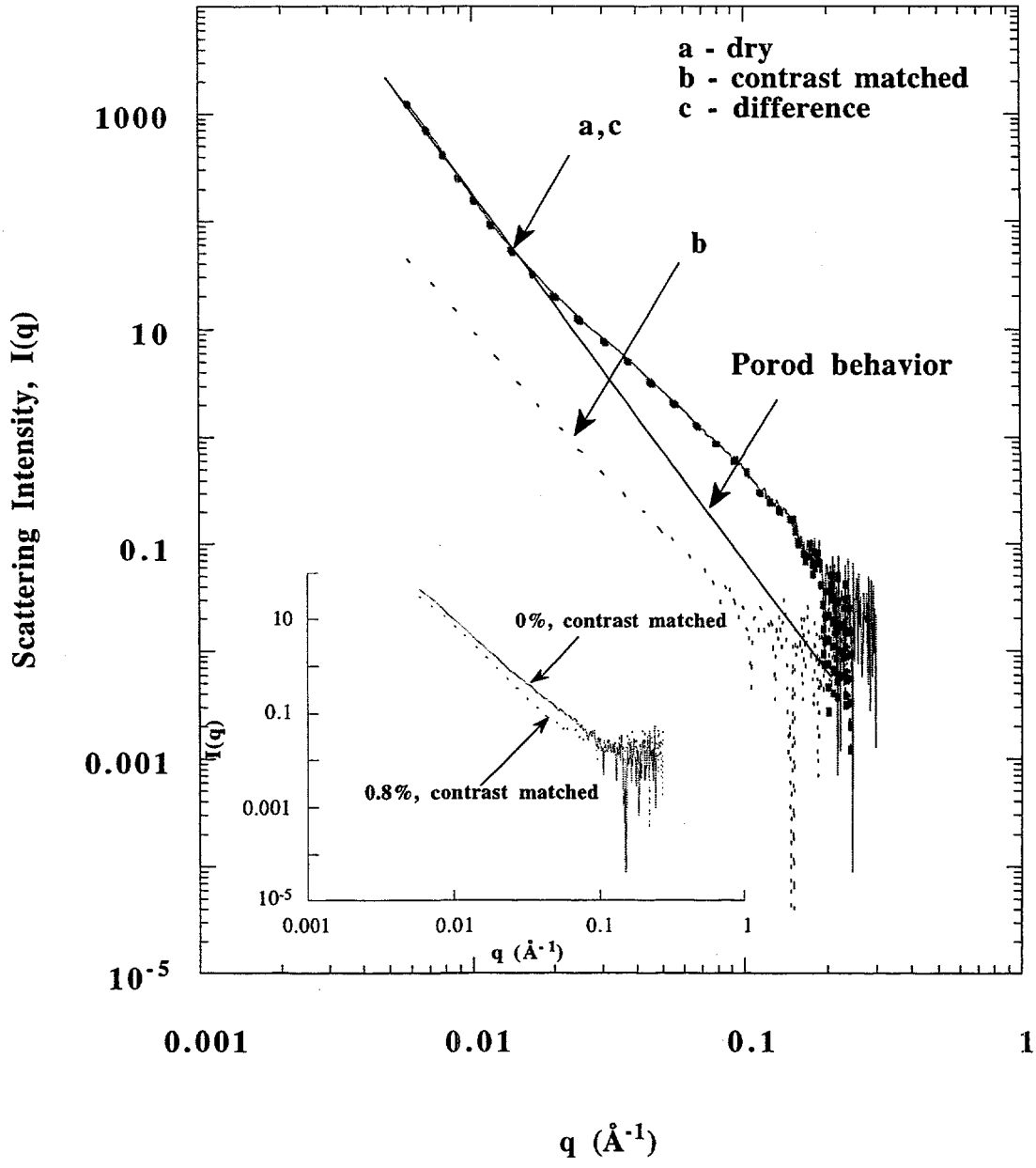

Figure 4.5. Small angle neutron scattering from Pittsburgh #8 coal char gasified to 0.8% weight loss in air at 400°C: (a) dry; (b) contrast matched with deuterated toluene; and (c) difference between scattering curves (a) and (b). A comparison of the scattering from the contrast matched ungasified and 0.8% gasified Pittsburgh #8 coal char samples is shown in the inset.

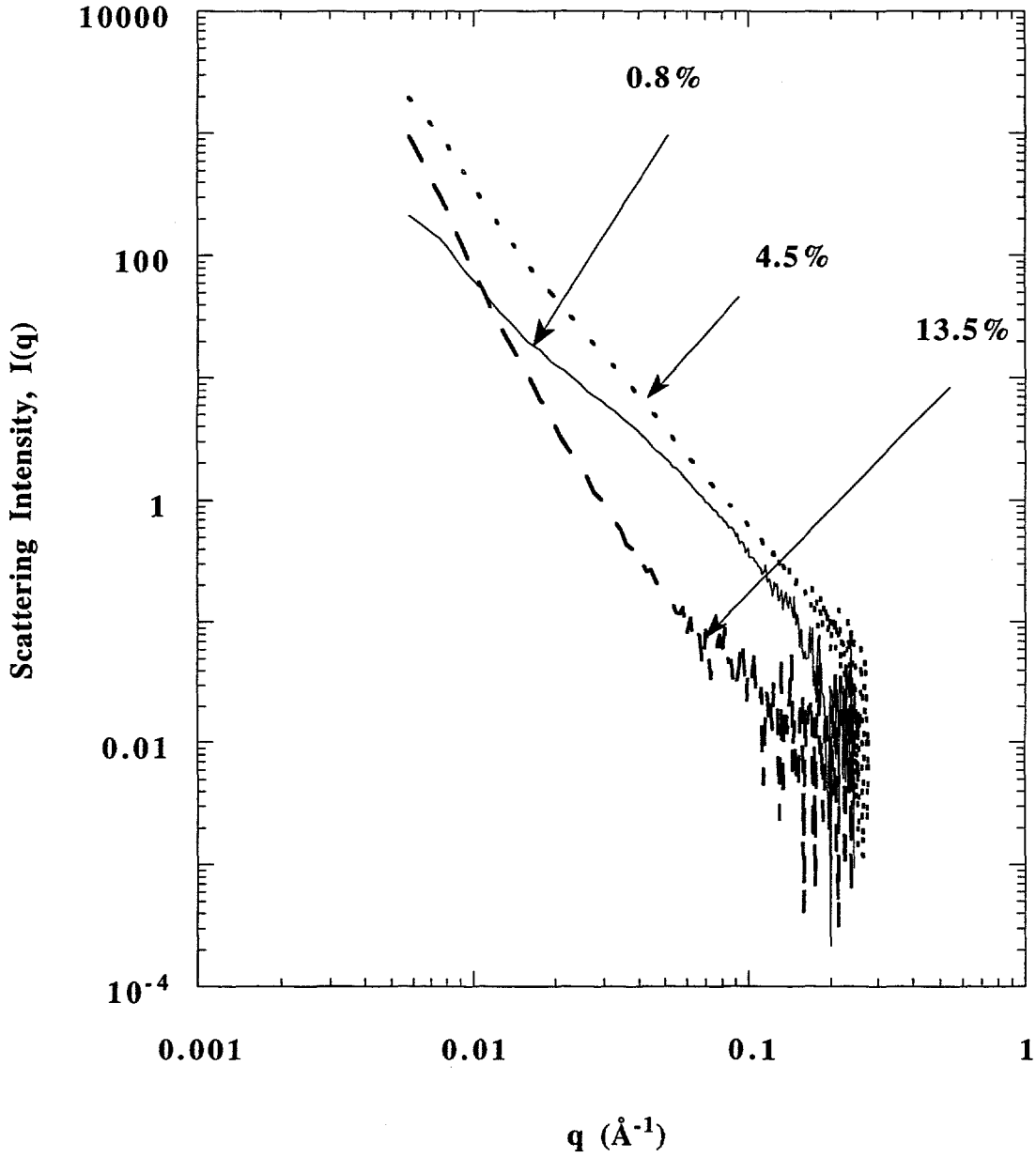

Figure 4.6. Small angle neutron scattering from Pittsburgh #8 coal char gasified to 0.8%, 4.5% and 13.5% weight loss in air at 400°C, dry.

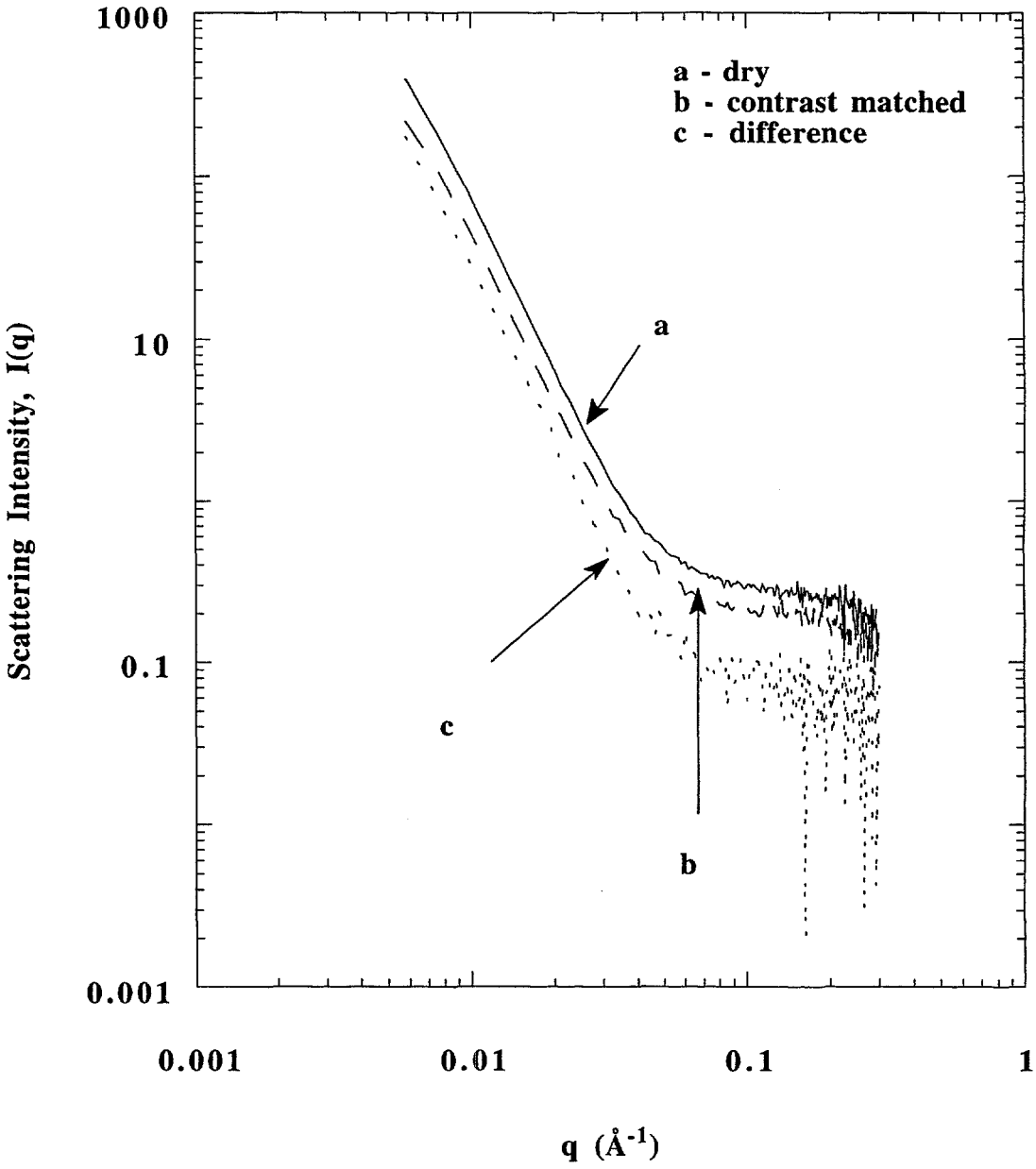

Figure 4.7. Small angle neutron scattering from unactivated (0% burn-off) phenolic resin char (PRC): (a) dry; (b) contrast matched with deuterated toluene; and (c) difference between scattering curves (a) and (b).

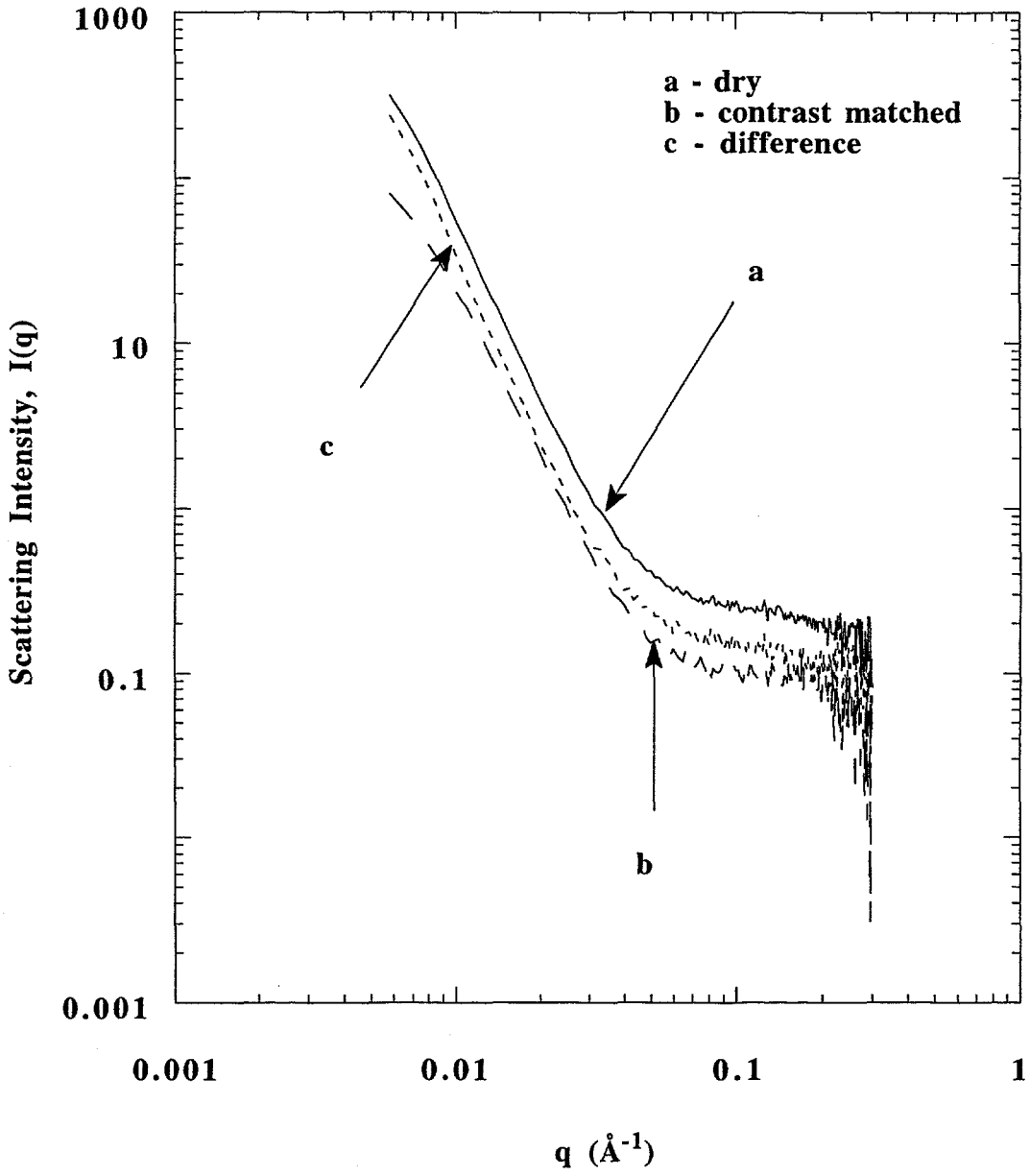

Figure 4.8. Small angle neutron scattering from phenolic resin char (PRC) activated in air at 400°C to 21% burn-off:: (a) dry; (b) contrast matched with deuterated toluene; and (c) difference between scattering curves (a) and (b).

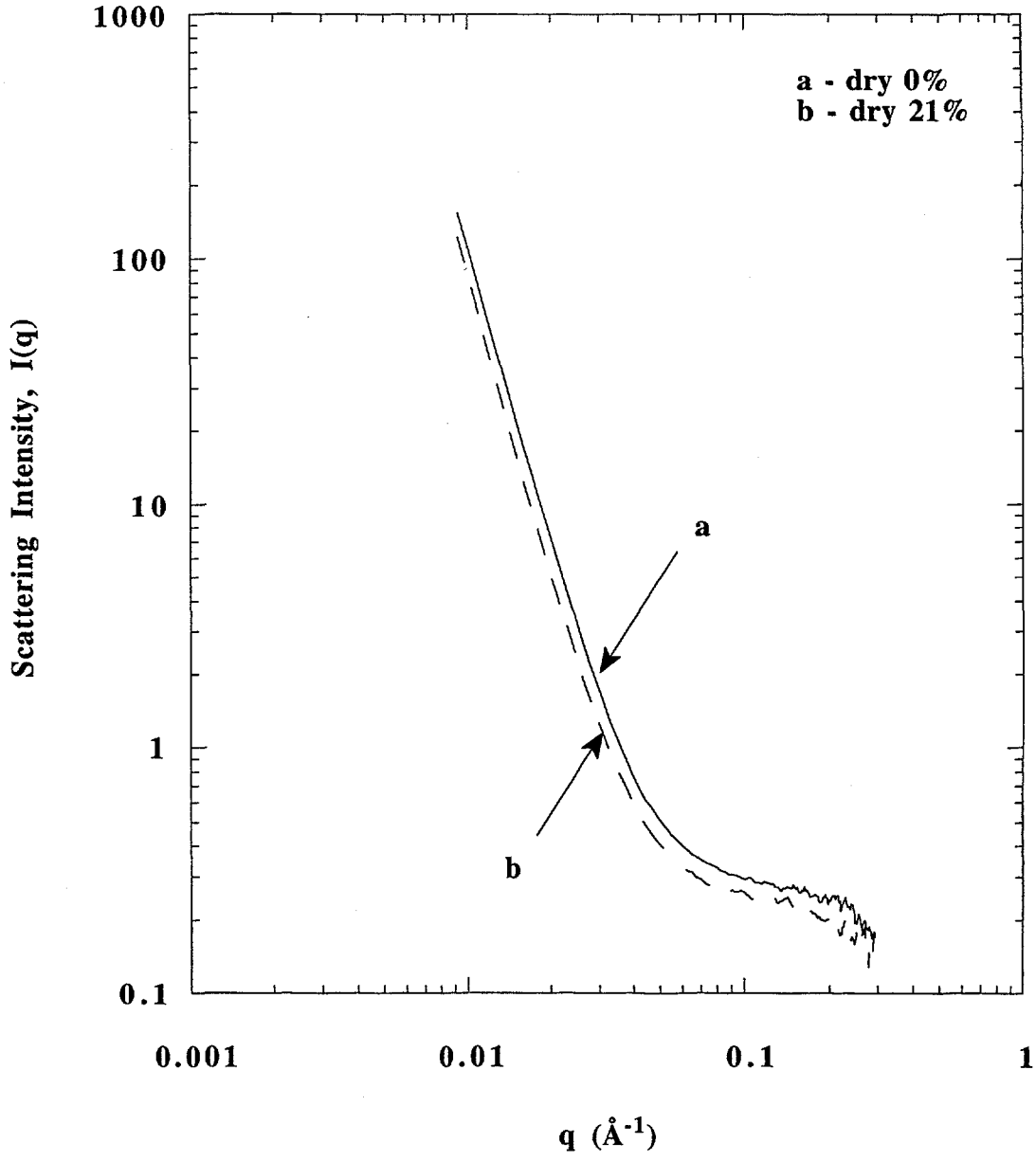

Figure 4.9. Comparison of the "dry" scattering curves for unactivated phenolic resin char and resin char activated to 21% burn-off from Figures 4.7 and 4.8.

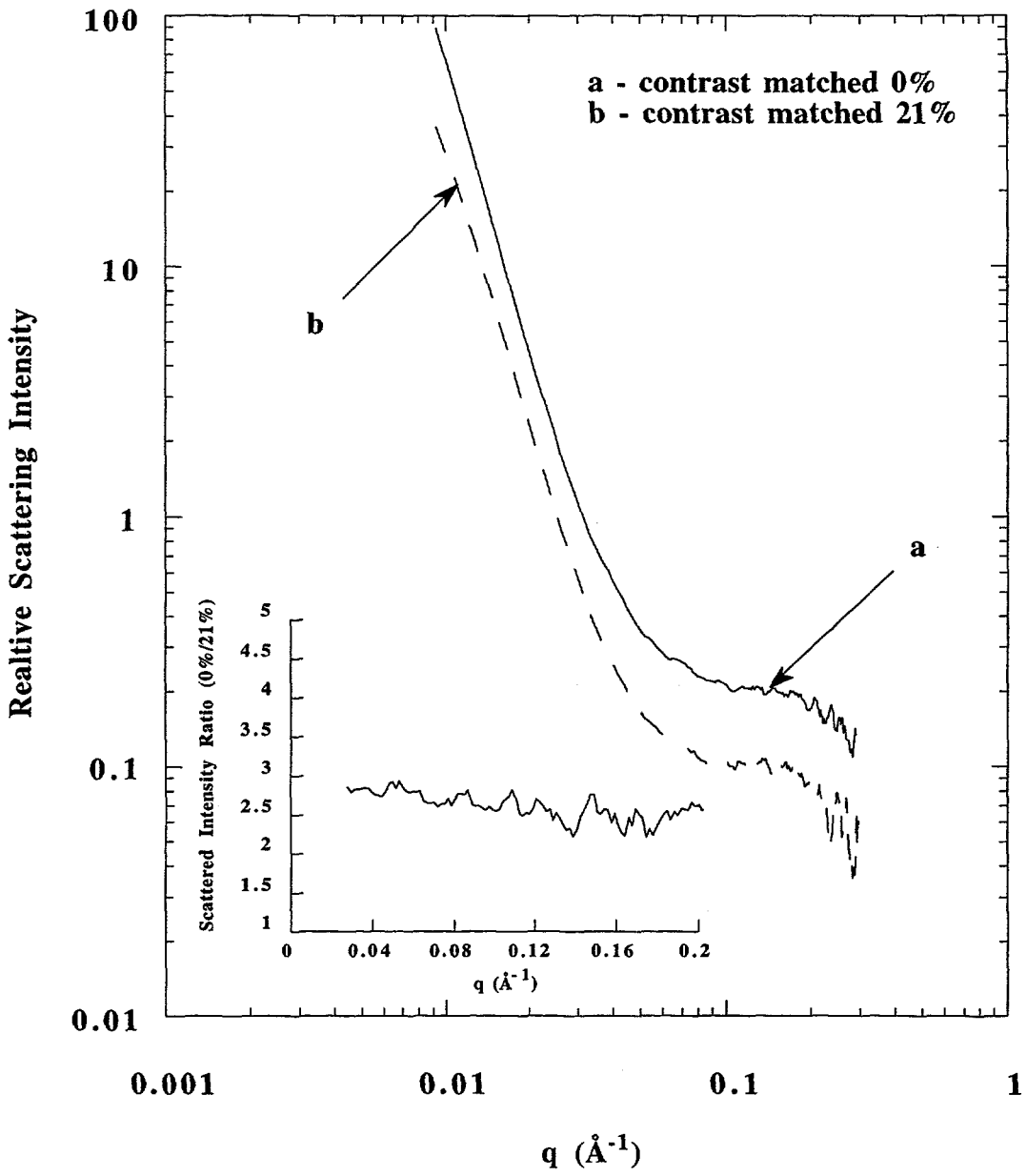

Figure 4.10. A comparison of small angle neutron scattering from unactivated phenolic resin char and phenolic resin char activated in air to 21% burn-off, that have been contrast matched by mixing with deuterated toluene. The relative intensity ratios of the two curves (0%/21%) are also shown in the inset.

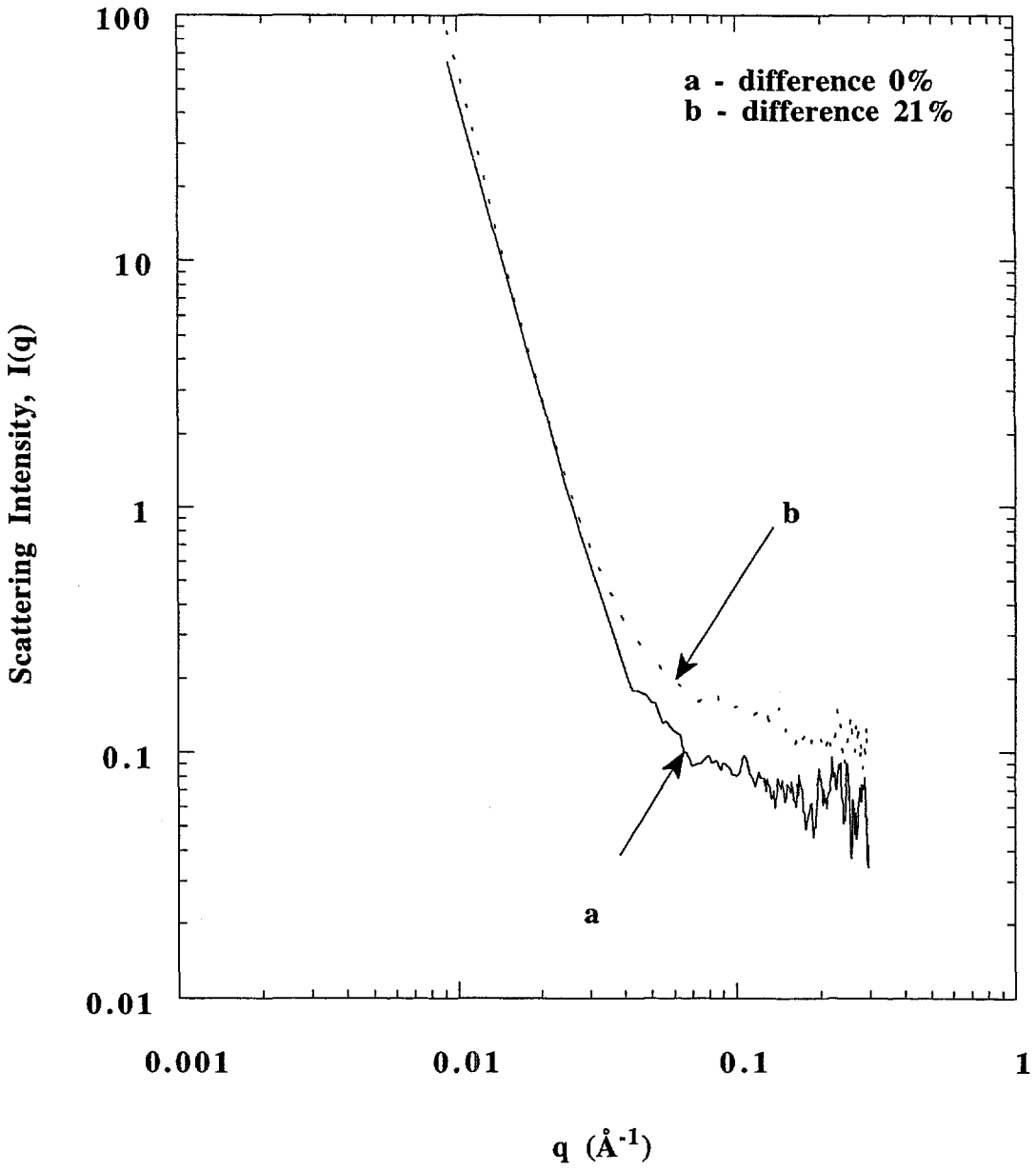

Figure 4.11. Comparison of the "difference" scattering curves for unactivated phenolic resin char and resin char activated to 21% burn-off from Figures 4.7 and 4.8.

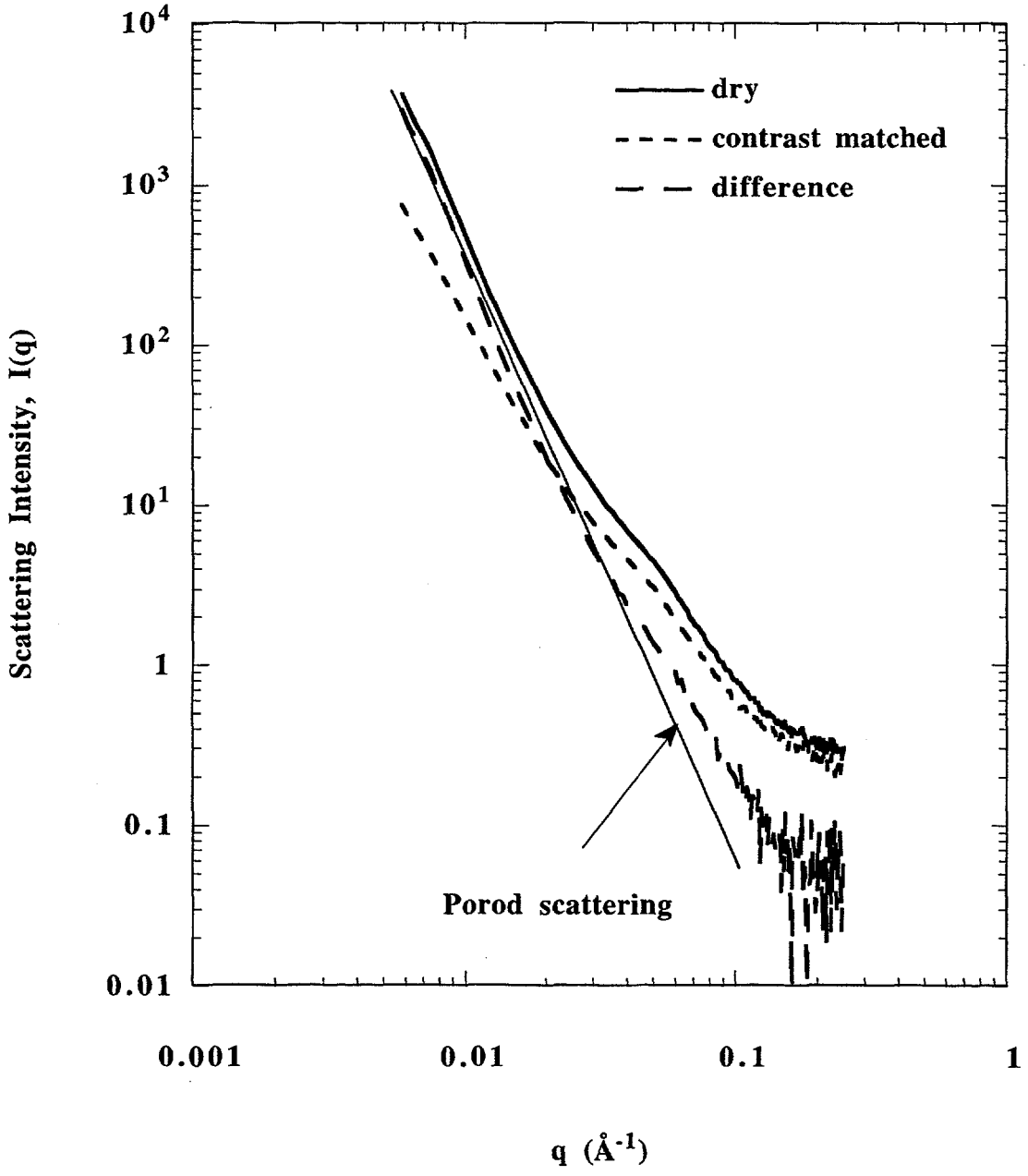

Figure 4.12. Small angle neutron scattering from unactivated (0% burn-off) Wyodak coal char.

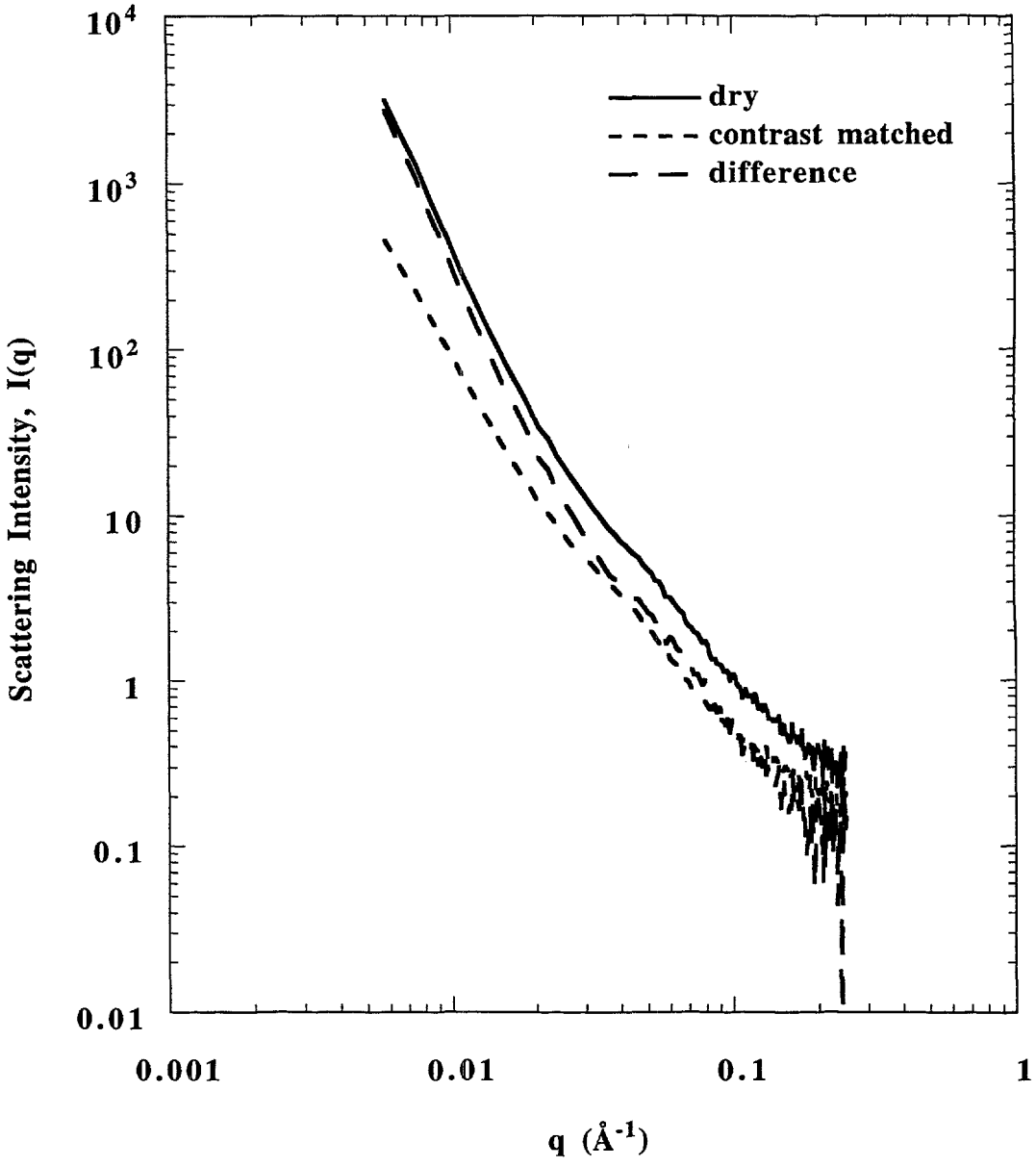

Figure 4.13. Small angle neutron scattering from Wyodak coal char activated to 9.2% burn-off in air at 400°C.

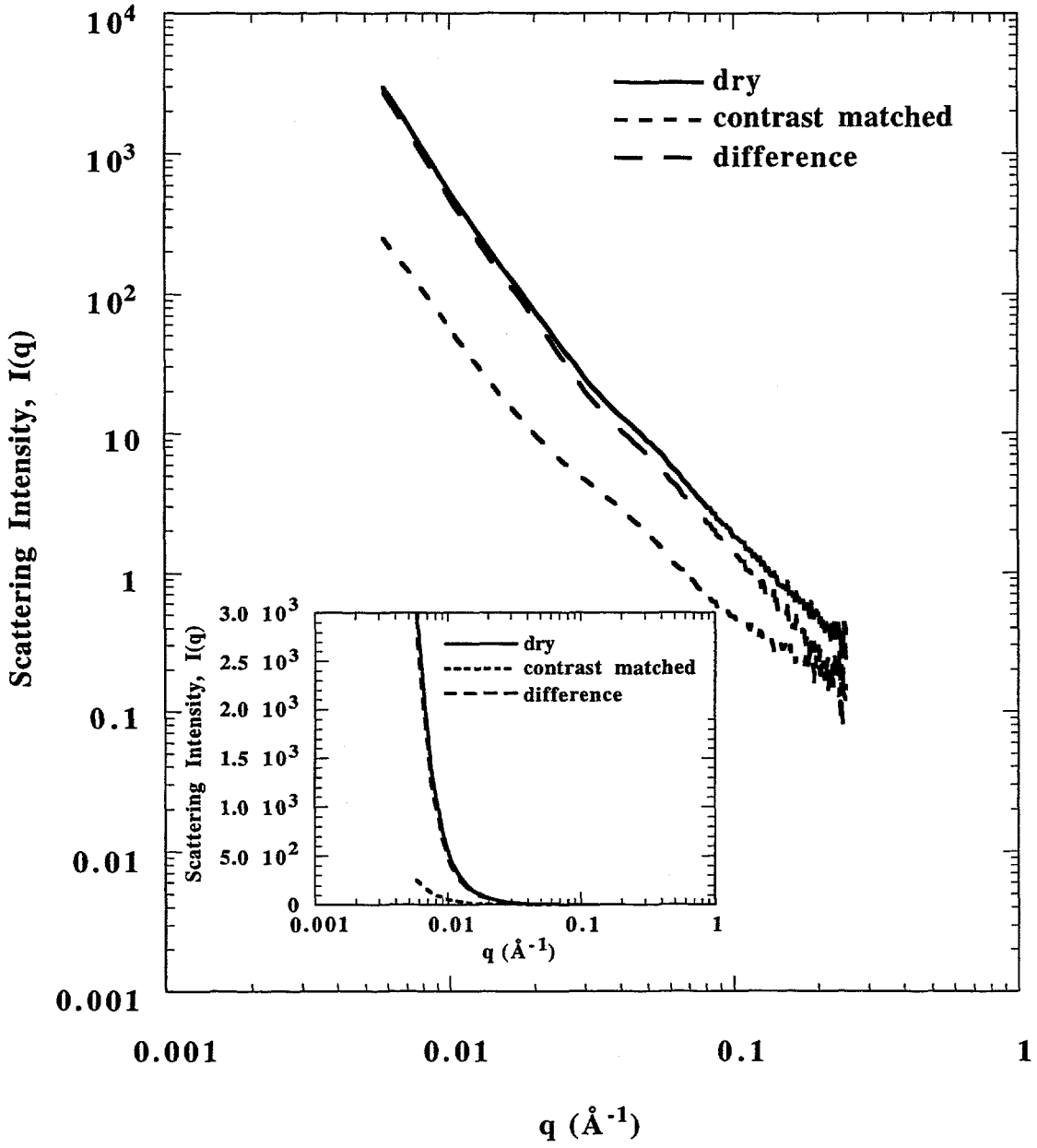

Figure 4.14. Small angle neutron scattering from Wyodak coal char activated to 32.7% burn-off in air at 400°C.

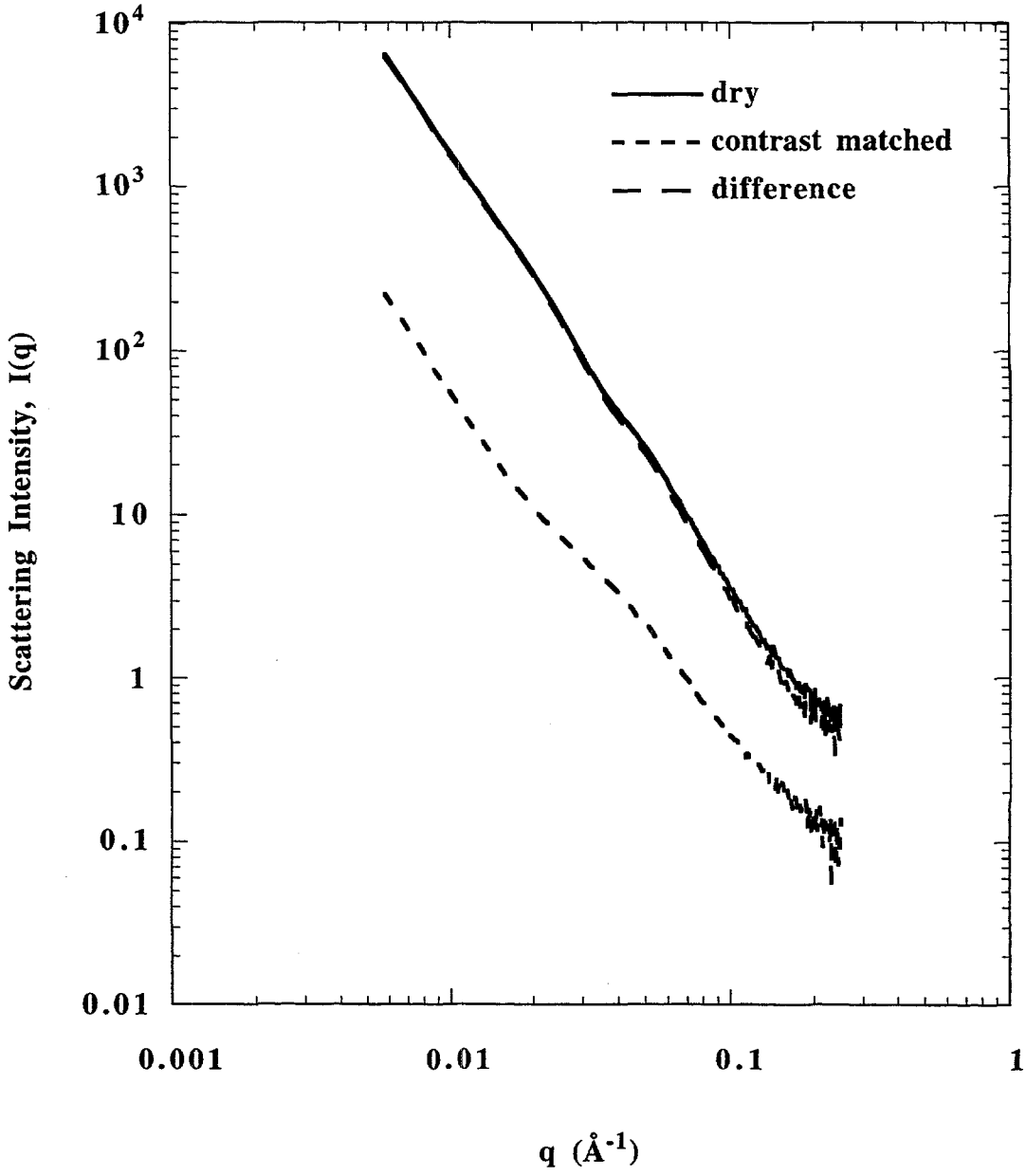

Figure 4.15. Small angle neutron scattering from Wyodak coal char activated to 58% burn-off in air at 400°C.

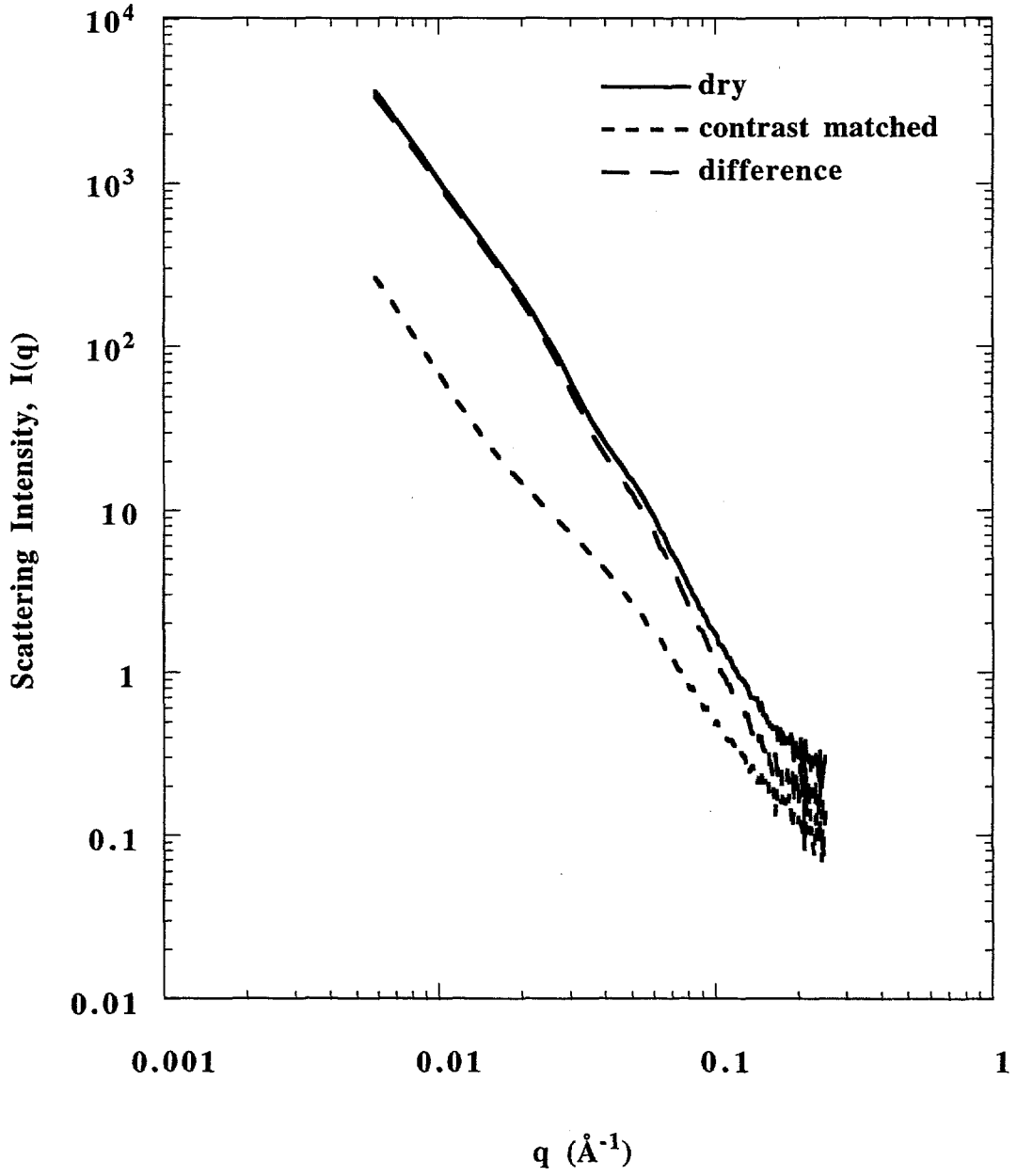

Figure 4.16. Small angle neutron scattering from Wyodak coal char activated to 68% burn-off in air at 400°C.

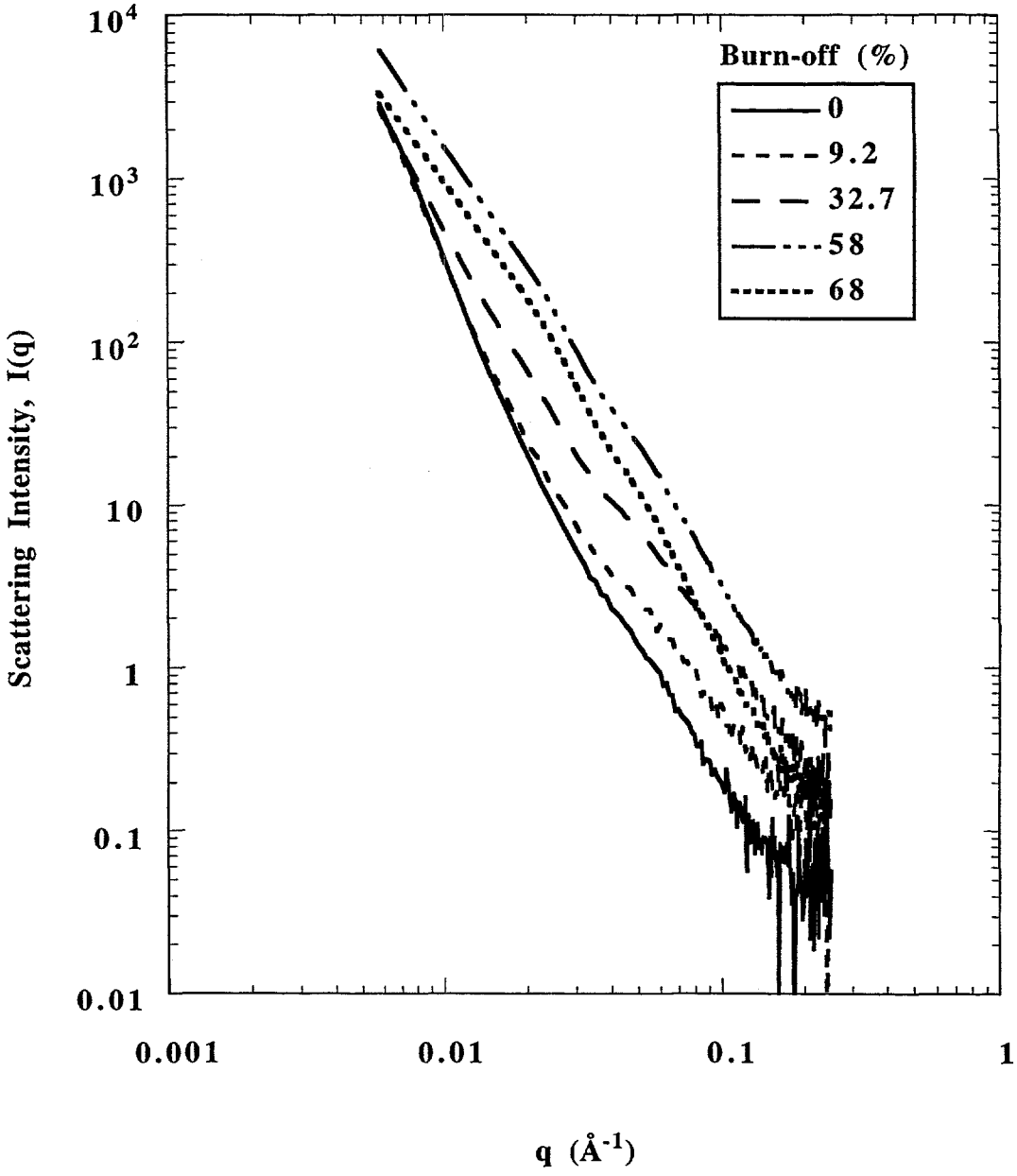

Figure 4.17. Small angle neutron scattering "difference" curves from Wyodak coal char as a function of burn-off in air at 400°C.

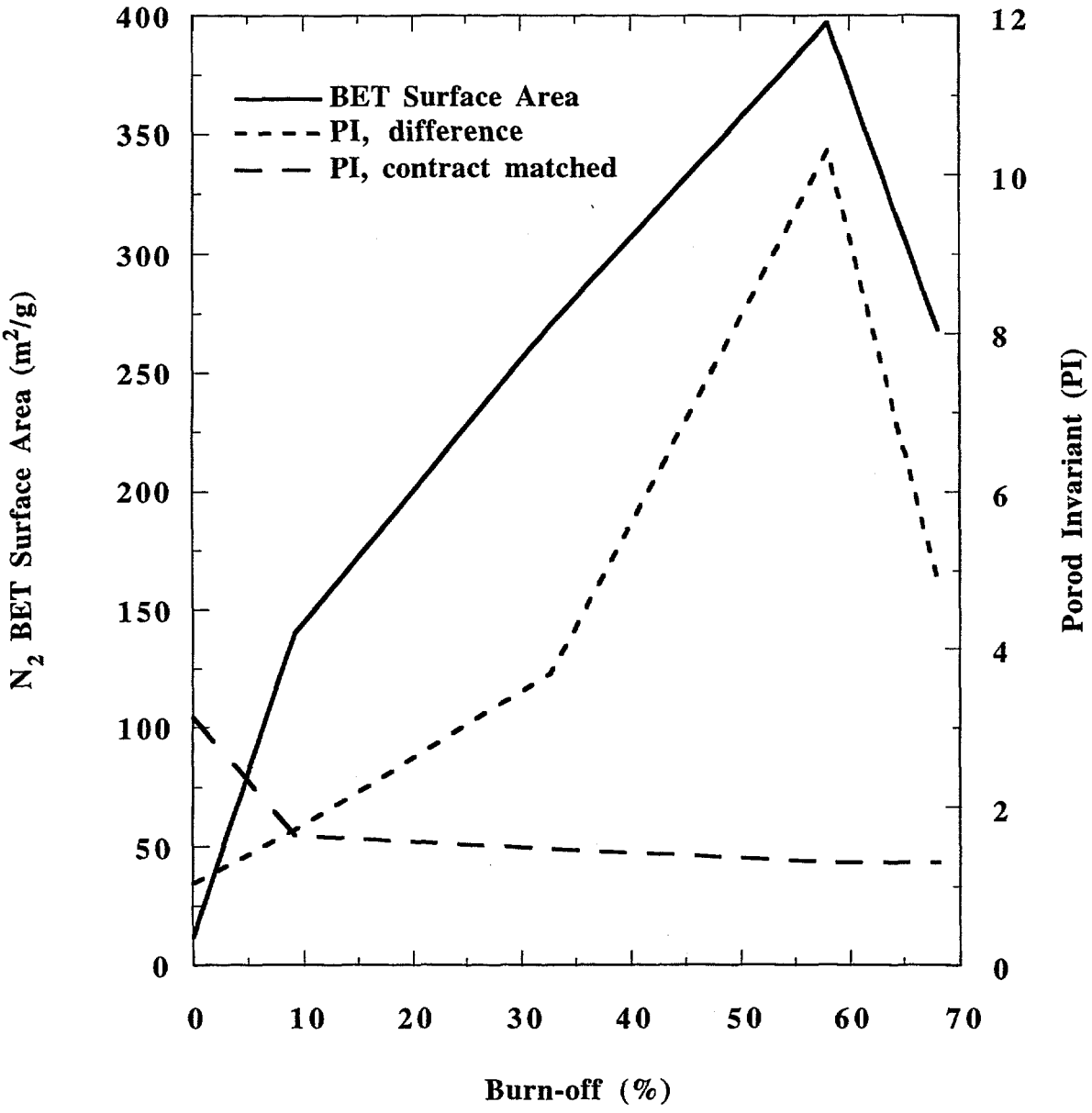

Figure 4.18. Comparison of nitrogen BET surface areas and Porod invariants for the difference and contrast matched SANS curves from Wyodak coal char as a function of burn-off.

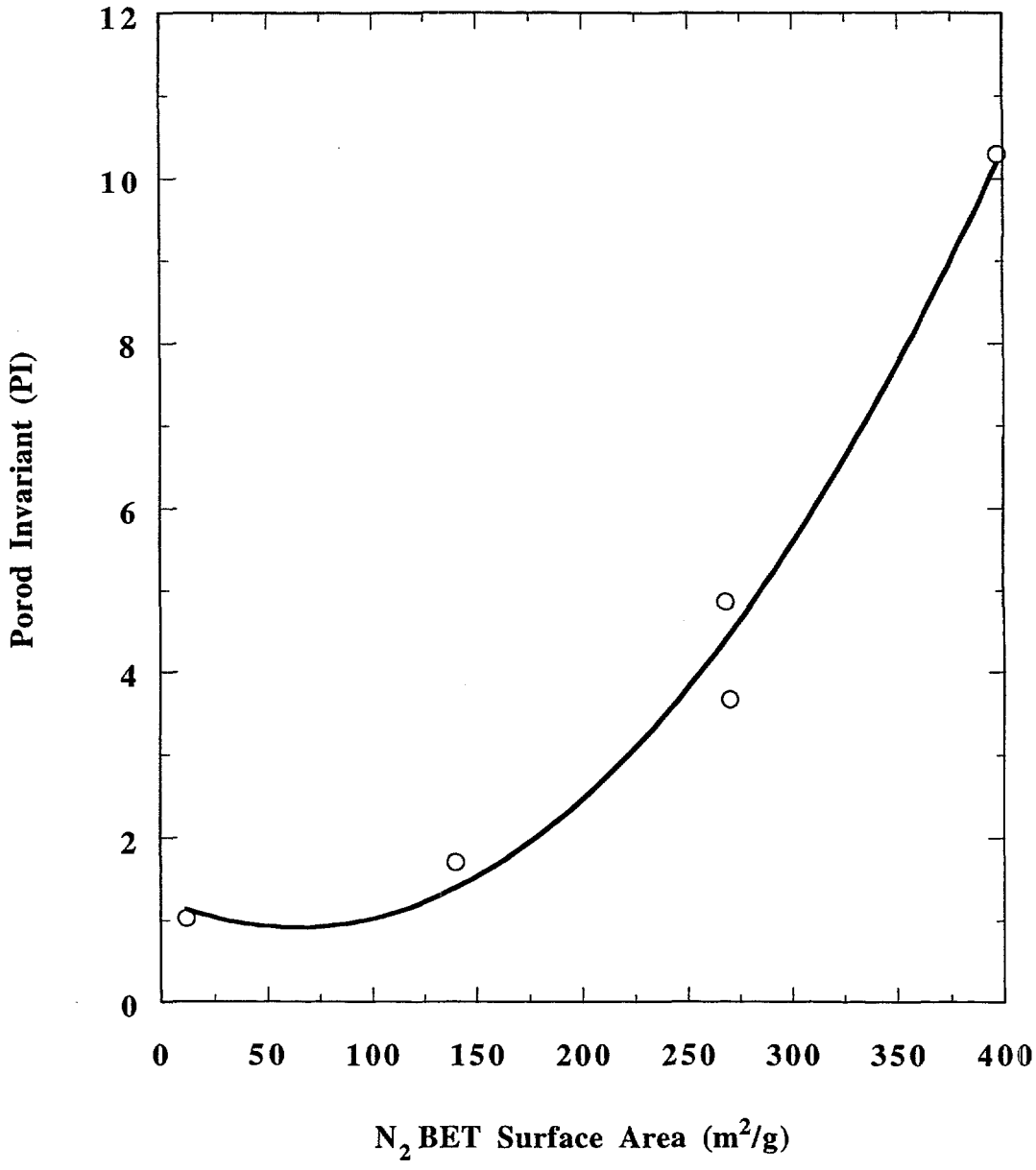

Figure 4.19. Comparison of nitrogen BET surface areas and Porod invariants for the difference SANS curves from Wyodak coal char.

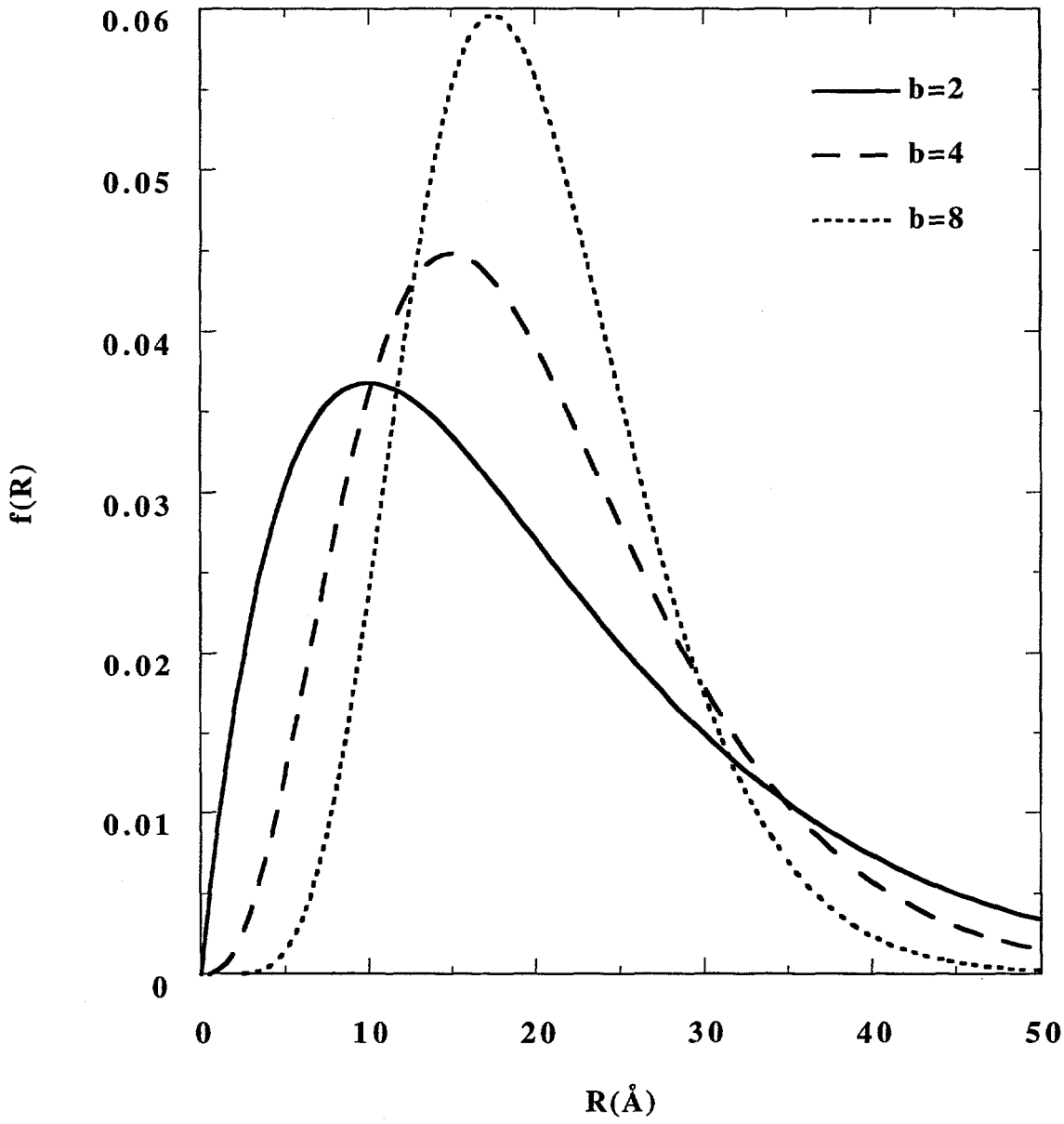

Figure 4.20. Schulz distribution functions for various values of b. R_o = 20Å.

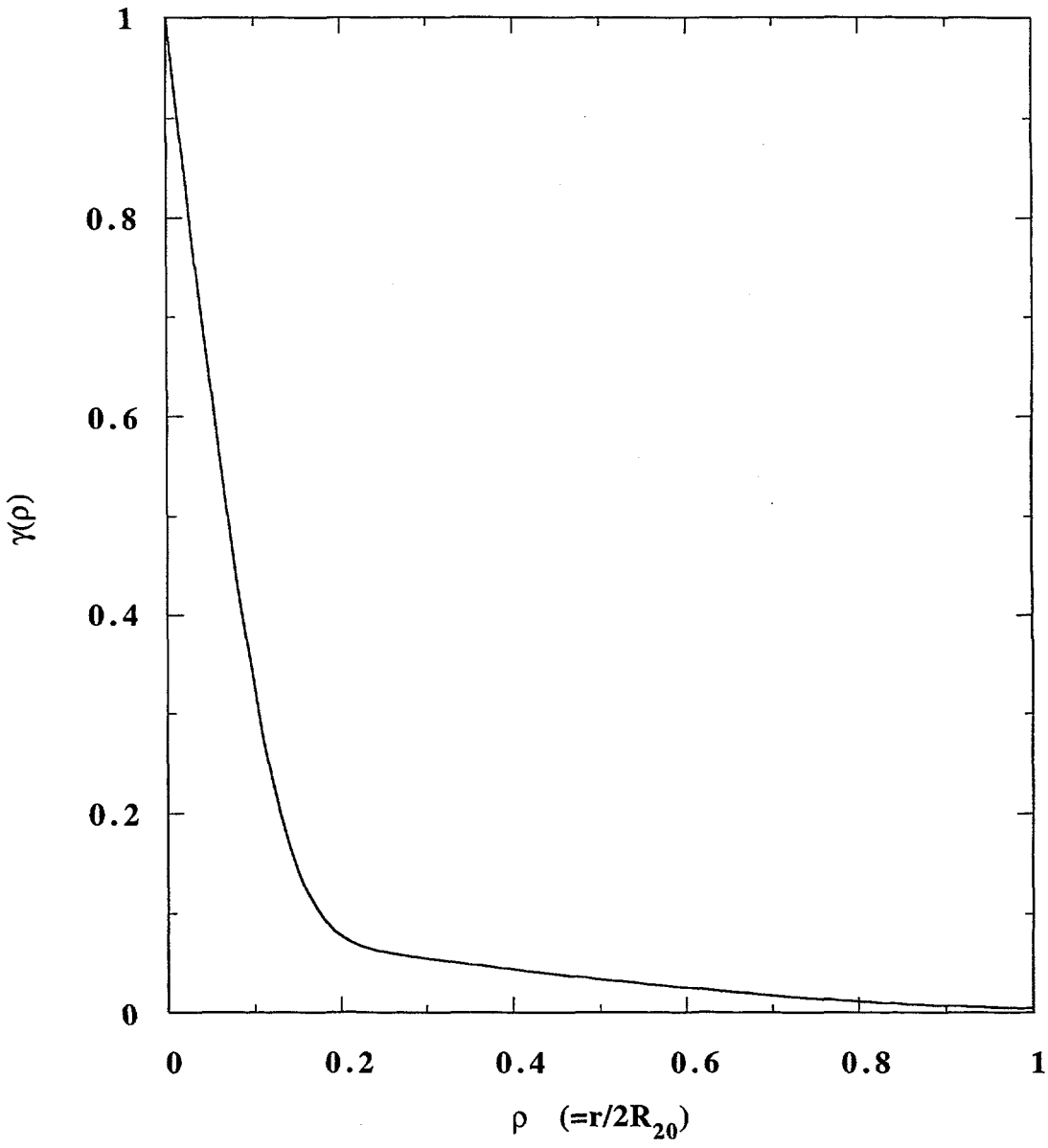

Figure 4.21. Correlation function, $\gamma(\rho)$, for the bimodal FPPS model with the following parameter set: R_{01} = 10Å; R_{02} = 60Å; $b_{1,2}$ = 20; ϕ_s = 0.99999; ε_1 = 0.9091. [Foster and Jensen, 1990].

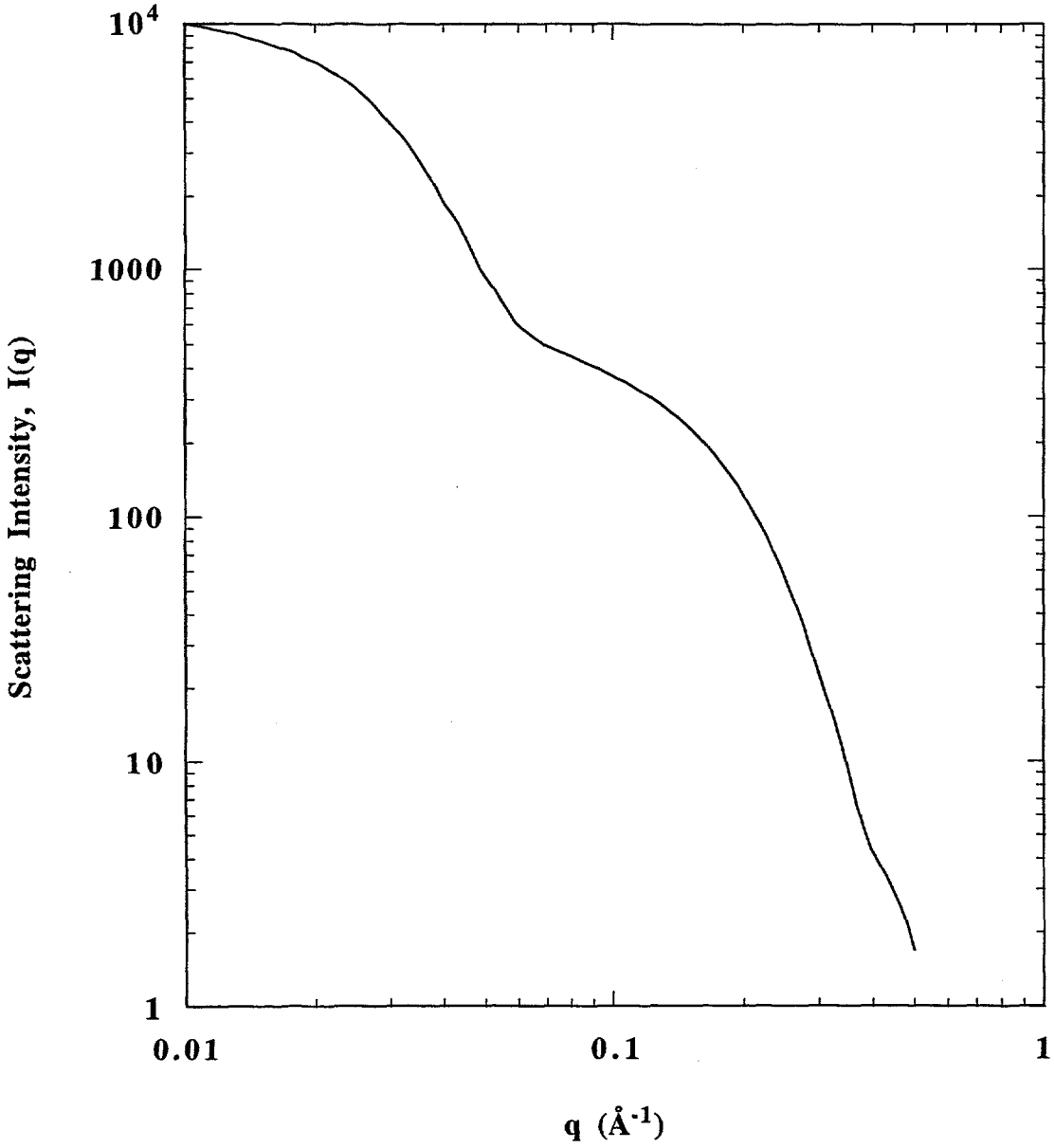

Figure 4.22. Scattering curve for the correlation function presented in Figure 4.20. The two distinct regions of the curve correspond to the two modes of the FPPS distribution. [Foster and Jensen, 1990].

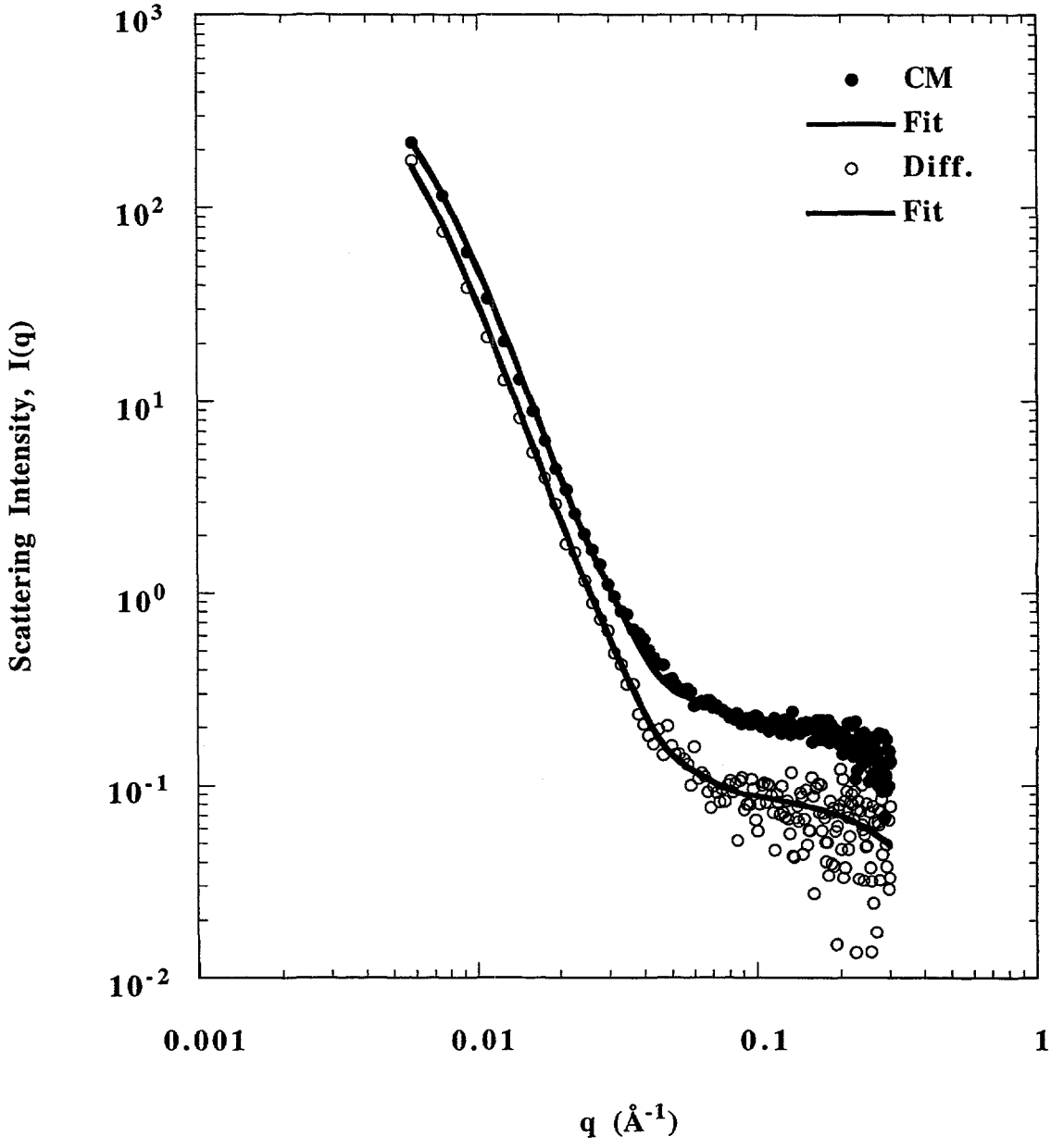

Figure 4.23. Contrast matched and difference scattering curves for unactivated PRC, and the corresponding bimodal FPPS Schulz model fits to the data.

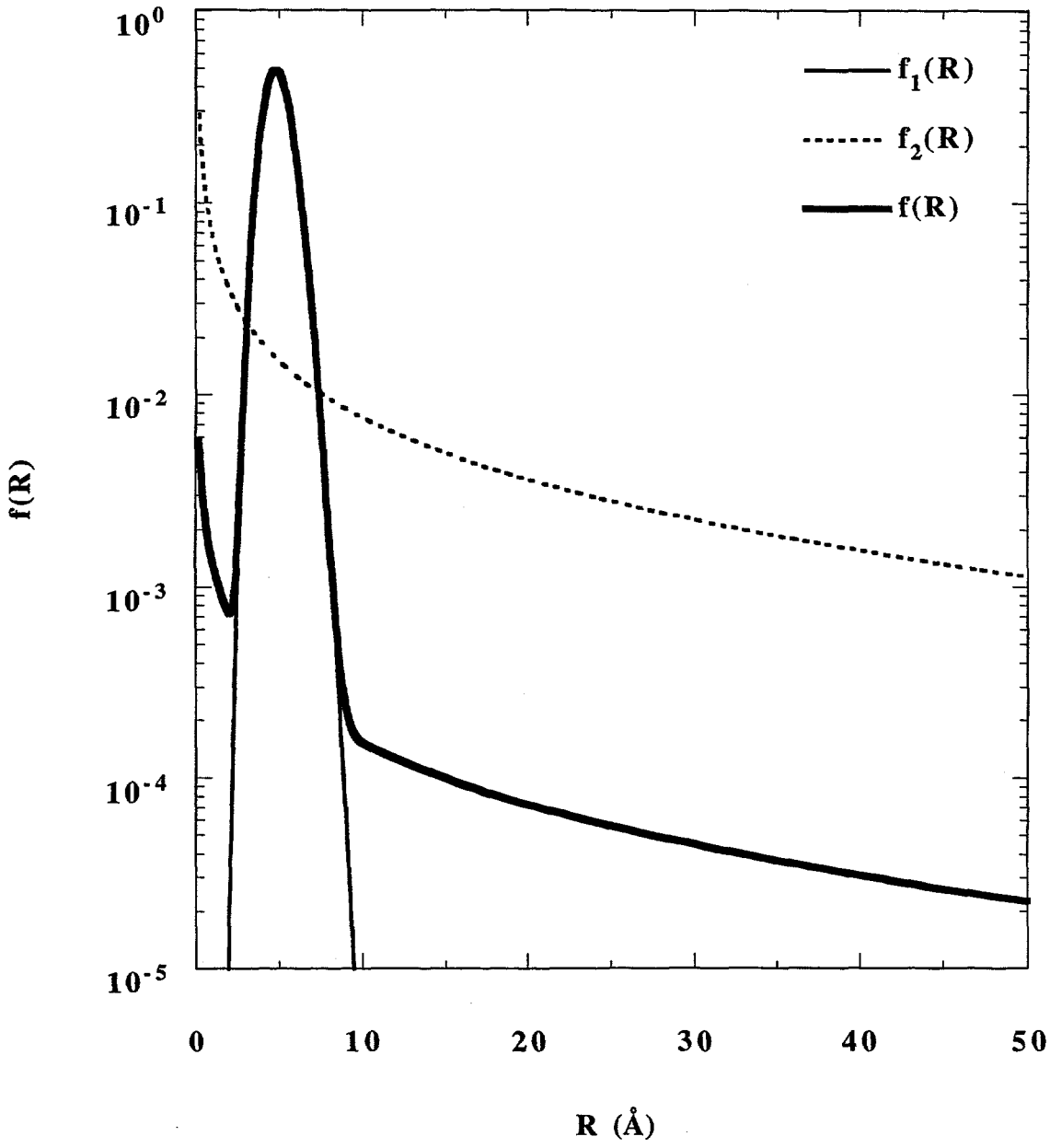

Figure 4.24. Both modes of the bimodal FPPS Schulz distributions for the contrast matched unactivated PRC sample, presented on a logarithmic scale.

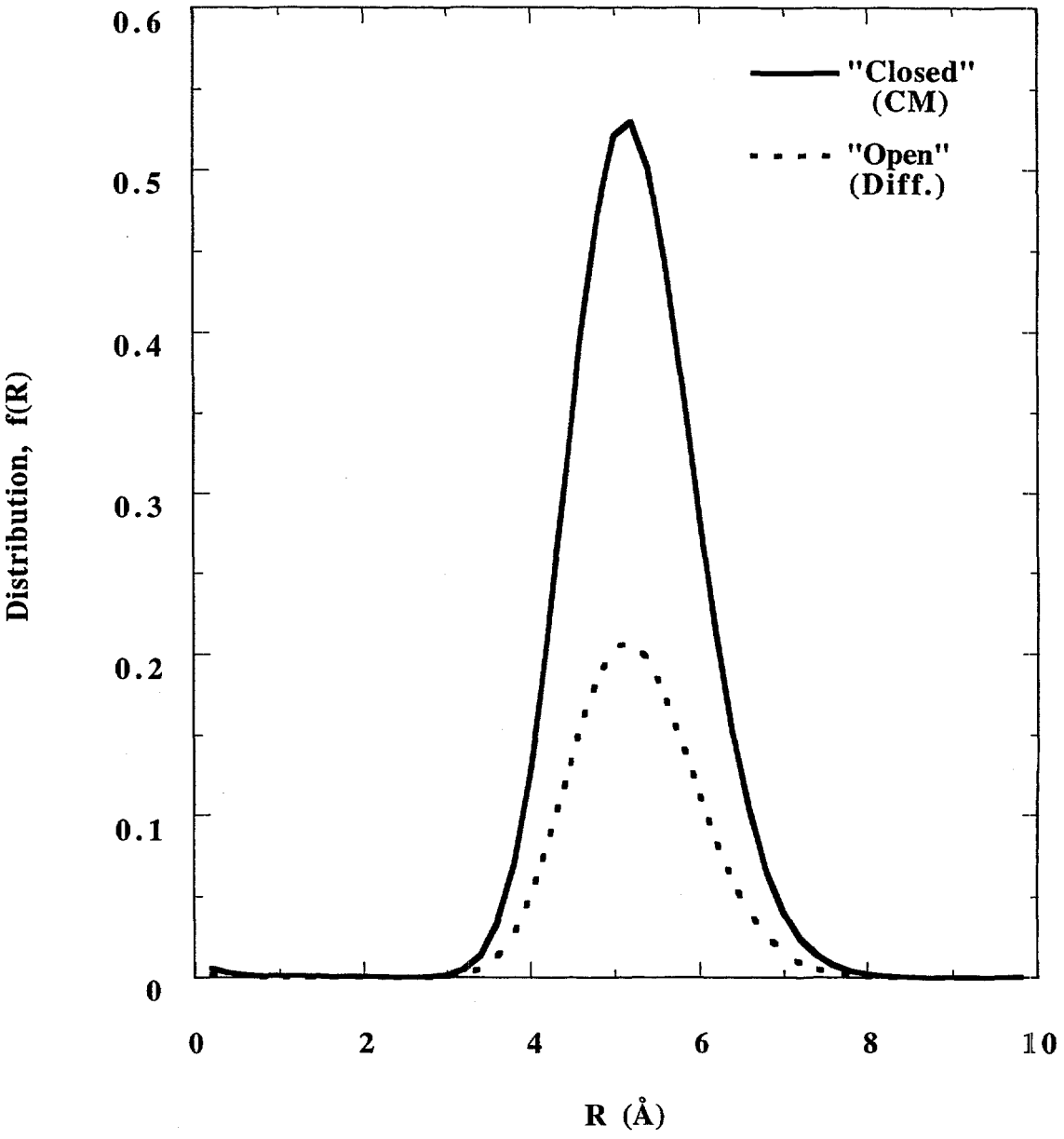

Figure 4.25. Distributions of scatterers for the contrast matched and difference scattering curves for the unactivated PRC sample.

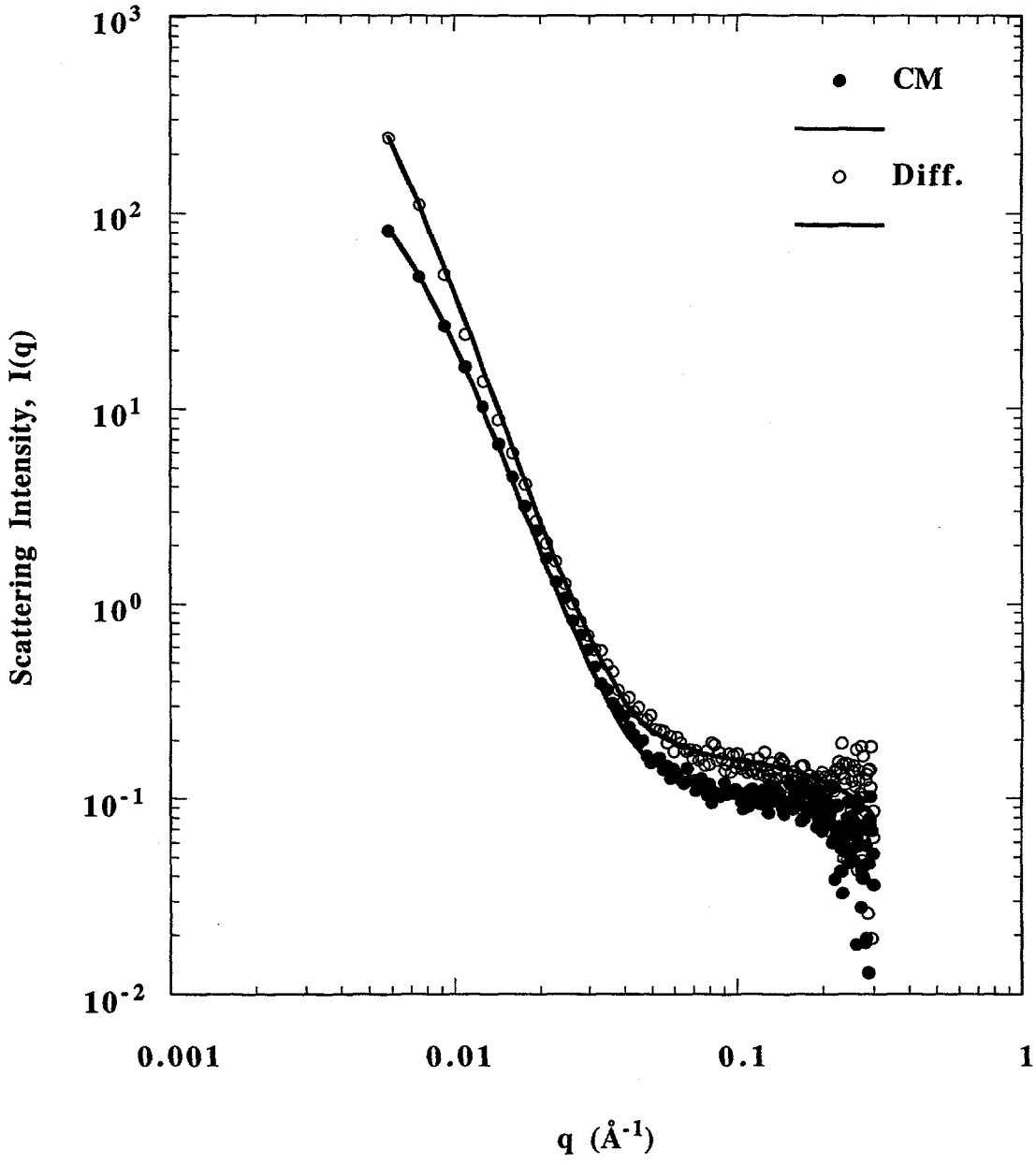

Figure 4.26. Contrast matched and difference scattering curves for PRC burned-off to 21%, and the corresponding bimodal FPPS Schulz model fits to the data.

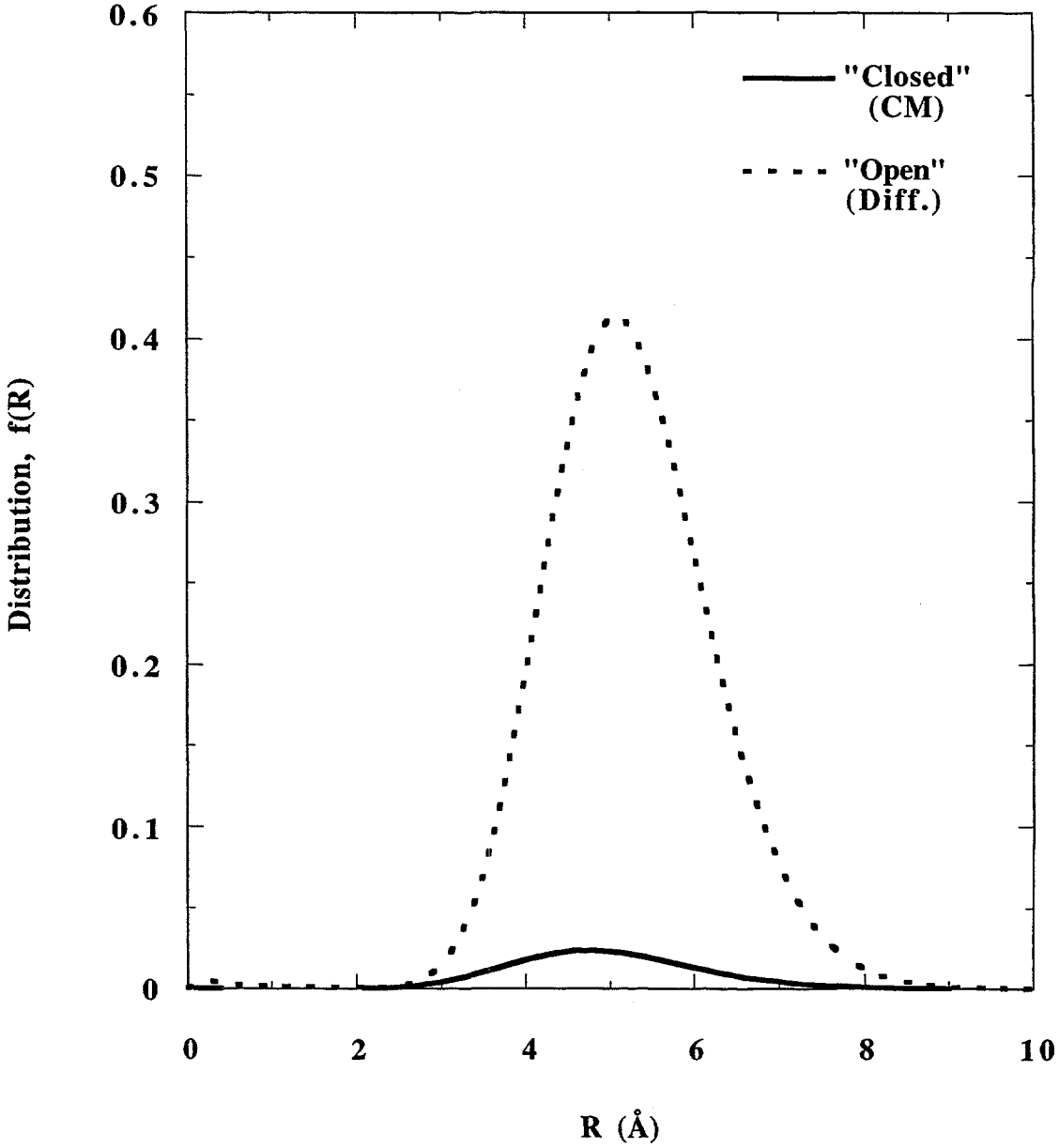

Figure 4.27. Distributions of scatterers for the contrast matched and difference scattering curves for the PRC sample burned-off to 21%.

REFERENCES

Agarwal, R. K., Amankwah, K. A. G. and Schwarz, J. A., *Carbon* **28**, 1, 169, (1990).

Barrer, R. M., *J. Coll. Intf. Sci.* **21**, 415 (1966).

Barton, S. S., Evens, M. J. B. and MacDonald, J. A. F., *Carbon* **29**, 8, 1099, (1991).

Bhatia, S.K., *AIChE J.* **26**, 3, 379 (1980).

Bradley, R. H., *Carbon* **29**, 7, 893, (1991).

Britten, J. A., Falconer, J. L. and Brown, L. F., *Carbon* **23**, 627 (1985).

Brunauer, S., Deming, L. S., Deming, W. S., and Teller, E., *JACS* **62,** 1723 (1940).

Brunauer, S., Emmitt, P. H., and Teller, E., *JACS* **60,** 309 (1938).

Calo, J.M., Hall, P.J., and Lilly, W.D., *A Mechanistic Study of the Energetic Heterogeneity of Coal Chars,* DOE/MC23284-F, DOE-METC Final Technical Report, 1989.

Calo,J.M., and Hall,P.J., *ACS Div. Fuel Chem. Prepr.* **34**, No.1,71(1989).

Calo, J.M. and Perkins, M. T., *Carbon* **25**, 395 (1987).

Calo, J.M. and Hall,P.J. NATO ASI Series, Series E, Vol. 192 (1991).

Cochrane, H., Walker, JR, P. L., Diethorn, W. S. and Friedman, H. C., *J. Coll. Intf. Sci.* **24**, 405, (1967).

Casquero-Ruiz, J. De D., Guil, J. M., Lopez-Gonzalez, J. De D. and Ruiz-Paniego, A., *Carbon* **26**, 5, 647, (1988).

Choma, J., Jaroniec, M., and Piotrowska, J., *Carbon* **26**, 1, 1, (1988).

Cranston, R. W., Inkley, F. A., *Advan. Catal.* **9**, 143 (1957).

Day, M. and Fletcher, R., *Characterization of Porous Solids,* Vol. 39, Amsterdam, Elsevier, 1988.

Dubinin, M. M., *Zhur. Phys. Chem.* **34**, 959 (1960).

Dubinin, M. M., *Chemistry and Physics of Carbon,* Vol. 2, New York, 1966, p.51.

Dubinin, M. M. and Radushkevich, L. V., *Proc. Acad. Sci. USSR* **55**, 331 (1947).

Dubinin, M. M., Russ. *J. Phys. Chem.* **39**, 697 (1965).

Dubinin, M. M., *Carbon* **25**, 5, 593 (1987).

Dubinin, M. M. and Kadlec, O., *Carbon* **25**, 3, 321 (1987).

Dubinin, M. M., Polyakov, N.S., and Kataeva, L.I., *Carbon* **28**, 481 (1990).

Ehrburger, P., Pusset, N. and Dziedzinl, P., *Carbon* **30**, 7, 1105 (1992).

Epperson, J.E., Thiyagarajan, P. and Klippert, T.E., *SAD Manual,* IPNS, Argonne National Laboratory, Argonne, IL 60439.

Evans, R., Marconi, U.M.B., and Tarazona, P., *J. Chem. Soc. Faraday Trans. II* **82**, 1763 (1986).

Fanning, P.E. and Vannice, M.A., *Carbon* **31**, 5, 721, (1993).

Floess, J. K., Kim, H. H., Edens, G., Oleksy, S. A. and Kwak, J., *Carbon* **30**, 7, 1025 (1992).

Foster, M.D., and Jensen, K.F., *J. Coll. Intf. Sci.* **135**, 132 (1990).

Glatter, O. and Kratky, O., *SAXS,* London: Academic Press, (1982).

Gregg, S. J., and Sing, K. S. W., *Adsorption, Surface Area and Porosity,* 2nd ed., Academic Press, 1982, p. 97.

Guinier, A. and Fournet, G., in *Small Angle Neutron Scattering,* translated by C.B. Walker and K.L. Kudowitch, Wiley, N.Y., 1955, pp: 19-23.

Hall P.J. and Calo, J.M., *ACS Div. Fuel Chem.Prepr.* **35(3)**, 705 (1990).

Hall, P.J., Ruiz Machado, W., Gascon Galan, D., Barrientos Barria E.L. and Sherrington, D.C.*Faraday Transactions* **92(14)**, 2607 (1996).

Heenan, R.K. "The FISH Data Fitting Manual" Rutherford Appleton Laboratory Report 89-129, UK, 1989.

Higgins, J.S. and Benoît, H.C. "Polymers and Neutron Scattering" Oxford Science Publications, Oxford, 1994.

Horvath, G., and Kawazoe, K., *J. Chem. Eng. Japan* **16**, 470 (1983).

Inners, R.W., Fryer, J.R. and Stoeckli, H.F., *Carbon* **27**, 71 (1989).

IUPAC Manual of Symbols and Terminology, Appendix 2, Pt. 1, Colloid and Surface Chemistry, *Pure Appl. Chem.* **31**, 578 (1972).

Jagiello, J., Sanghani, P., Bandosz, T. J. and Schwarz, J. A., *Carbon* **30**, 3, 507, (1992).

Janosi, A. and Stoeckli, H.F., *Carbon* **17**, 465, (1979).

Jenkins, R.G., Nandi, S.P., Walker, Jr., P.L., *Fuel* **52**, 288 (1973).

Jenkins, R. G., and Walker, P. L. Jr., *Carbon* **14**, 7 (1976).

Jensen, K.O., Eldrup, M., Pedersen, N.J. and Evans, J.H. *J. Phys F*, **18**, 1703 (1988).

Kiselev, A. V., *Disc. Far. Soc.* **40**, 205 (1965).

Kruk, K., Jaroniec, M., and Olivier, J.P., *Proc. 23rd Biennial Conf. Carbon,* Vol I, p. 106, Penn State University, July, 1997.

Laine, J. and Yunes, S., *Carbon* **30**, 4, 601 (1992)..

Langmuir, I., *JACS* **40**, 1361 (1918).

Lippens, B. C., Linsen, B. G., and de Boer J. H., *J. Cat.* **3**, 32 (1964).

Lippens, B. C. and de Boer J. H., *J. Cat.* **4**, 319 (1965).

Marchon, B., Tysoe, W.T., Carrazza, J., Heinemann, H., and Somorjai, G.A., *J. Phys. Chem.* **92**, 5447 (1988).

March, H., Grawford, D., O'Grady, T.M., and Wennerberg, A., *Carbon* **20**, 419 (1982).

Medek, J., *Fuel* **56**, 131, (1977).

Miura, K. and Hashimoto, K., *I&EC Proc. Des. Dev.* **23**, 138 (1984).

Miura, K. and Hashimoto, K., and Silveston, P.L., *Fuel* **68**, 1461 (1989).

Mittelmeijer-Hazeleger, M. C. and Martin-Martinez, J. M., *Carbon* **30**, 4, 695 (1992).

Morgan, M.E., Jenkins, R.G., Walker, P.L.Jr., *Fuel* **60**, 189 (1981).

Otake, Y. and Jenkins, R.G., *Carbon* **31**, 1, 109 (1993).

Pierce, C., *J. Phys. Chem.* **72**, 3673 (1968).

Polanyi, M., *Verb. Deutsch Physik. Ges.* **16**, 1012 (1914).

Porod, G. *Kolloid Zeitschrift* **124**, 83 (1951).

Press, W.H., Flannery, B.P., Teukolsky, S.A., and Ketterling, W.T., *Numerical Recipes - The Art of Scientific Computing,* Cambridge University Press, New York, 1987.

Roberts, B.F., *J. Coll. Intf. Sci.* **23**, 266 (1967).

Rodriguez-Reinoso, F., *Carbon and Coal Gasification,* Figueiredo and Moulijn, eds., 1986, p.601.

Rodriguez-Reinoso, F., Martin-Martinez, J. M., Prado-Burguete, C., and McEnaney, B., *J. Phys. Chem.* **91**, 515 (1987).

Seaton, N. A., Walton, J. P. R., and Quirke, N., *Carbon* **27**, 6, 853 (1989).

Schmidt, P.W. *J. Appl. Cryst.* **24**, 414 (1991).

Simons, G.A.,and Finson, M.L., *Comb. Sci.Tech.* **19**, 217 (1979).

Sing, K.S. W., in *Surface Area Determination,* D. H. Everett and R. H. Ottewill, eds., Butterworths, London, 1970, p. 25.

Shull, C. G., *JACS* **70**, 1405 (1948).

Starsinic, M., Taylor, R.L., Walker, P.L., Jr., and Painter, P.C., *Carbon* **21**, 69, (1983).

Stoeckli, H., *Carbon* **28**, 1 (1990).

Teixeira, J. *J. Appl. Cryst.* **21**, 781 (1988).

Vorres, K.S., *"Users Handbook for the Argonne Premium Coal Sample Program,"* ANL/PCSP-93/1, Argonne National Laboratory, USDOE, October, 1993.

Walker, P.L. Jr., in *Carbon and Coal Gasification,* Figueiredo, Moulijn, NATO ASI Series, 9.3, 1986.

Wojtowicz, M., *Ph.D. Dissertation,* Division of Engineering, Brown University, 1987.

Zhuang, Q-L, Kyotani, T., Tomita, A., *Energy and Fuels* **8**, 714 (1994).

Appendix A.

Sample Calculation of Specific Surface Area, External Surface Area, and Micropore Volume for a Char Sample.

A.1. Experimental Data.

A complete work-up of the nitrogen adsorption data is presented in this Appendix for a sample of Wyodak coal char gasified in O_2 at 420°C to 30% burn-off. The sample was pyrolyzed at 1000°C in helium for 2 hours. The adsorbate was N_2 at 77K. The experimental data for the nitrogen adsorption Isotherm are listed in Table A.1.

A.2. Reference Data.

Rodriguez-Reinoso *et al.* (1987) proposed a standard adsorption isotherm for the characterization of activated carbons, which is presented in Table A.2. An α_s-plot was constructed for an olive stone carbon using this standard material. The olive stone carbon was prepared by carbonization of olive stones in N_2 at 1123K followed by activation in CO_2 at 1098K to 34% burn-off. The resultant micropore volume deduced from the α_s-plot was 0.39 cm^3/g, and the nonmicroporous surface area was 21 m^2/g. The data from the olive stone carbon was used as a reference for the current work.

Figure A.1 presents the α_s-plot for the olive stone carbon, as determined by Rodriguez-Reinoso *et al.* (1987). As discussed in Section 1.3.2-4, the intercept on the ordinate axis of the extrapolated linear branch from an α_s-plot gives the micropore contribution, which when converted to liquid volume of nitrogen, is taken as the micropore volume. The intercept for the reference material is I_r = 11.4 mmol/g, or 255 cm^3/g, which when converted to standard conditions (0°C, 1 atm), yields a micropore volume of V_r = 0.39 cm^3/g. (The density of liquid N_2 at 77K is 0.808 g/cm^3.) The slope of the linear branch, S_r, is proportional to the area of the

mesopore walls together with the external surface area. For the reference material, S_r = 0.648 mmol/g, or 14.5 cm^3/g when converted to standard conditions, which corresponds to an external surface area $(A_{ex})_r$ = 21 m^2/g.

A.3. Sample Calculation.

The actual amount of N_2 adsorbed on a sample is:

$$N = A_{des} \times V_{cal}/A_{cal}/W_s \qquad [A.1]$$

where W_s is the mass of the sample; for the Wyodak coal char sample used here as an example, W_s = 0.013 g. The N_2 adsorbed at standard conditions (0°C, 1 atm) is:

$$N_{std} = N \times 273/(T_{amb.} + 273) \qquad [A.2]$$

So, for example, for P/P° = 0.9:

$$N_{std} = 993 \times 4 \times 273/998/0.013/(273+20) = 283.3 \text{ cm}^3/\text{g}.$$

Table A.3 presents the data for the adsorption of N_2 at 77K which was used for the construction of the α_s-plot for the Wyodak coal char sample. The value of $\alpha_s = n/n_{0.4}$ was obtained from the reference data.

Figure A.2 is the α_s-plot for the Wyodak coal char sample. The initial slope, S_s, extrapolated through the origin, line AB, yields the total surface area, A_s. Here S_s = 260 cm^3/g, so the specific surface area of the sample is calculated as:

$$A_s = S_s \times A_r/S_r = 377 \text{ m}^2/\text{g}$$

Since the slope of the extrapolated linear branch, CD, S_{ex}, is 54 cm^3/g, the nonmicroporous surface area can be obtained as:

$$A_{ex} = S_{ex} \times A_r/S_r = 78.2\ m^2/g$$

The intercept of the extrapolated linear branch, I_s, is 158 cm^3/g, so the micropore volume of the sample is given by:

$$V_s = I_s \times V_r/I_r = 0.242\ cm^3/g$$

Table A.1. Experimental nitrogen adsorption data for Wyodak coal char gasified in O_2 at 420°C to 30% burn-off.

P/P°	A_{des}*	A_{cal}*	$V_{cal}(cm^3)$*
0.9	993	998	4
0.8	922	977	4
0.7	1068	1220	4
0.6	1220	1089	3
0.5	1188	1118	3
0.4	1184	1190	3
0.3	1137	1229	3
0.2	980	1146	3
0.1	883	1159	3
0.075	859	764	2
0.05	869	773	2
0.025	772	721	2
0.015	767	767	2

* A_{des} is the integrator count from the sample adsorption signal;

A_{cal} is the integrator count from the calibration signal;

V_{cal} is the calibration volume.

Table A.2. Standard isotherm data for the adsorption of nitrogen at 77K on carbon.[†]

P/P°	n/n_m	α_s	P/P°	n/n_m	α_s
0.005	0.82	0.51	0.30	1.14	0.88
0.01	0.87	0.54	0.32	1.44	0.90
0.02	0.92	0.57	0.34	1.48	0.93
0.03	0.95	0.59	0.36	1.52	0.95
0.04	0.98	0.61	0.38	1.56	0.98
0.05	1.00	0.63	0.40	1.60	1
0.06	1.02	0.64	0.42	1.64	1.02
0.07	1.03	0.65	0.44	1.68	1.05
0.08	1.05	0.66	0.46	1.71	1.07
0.10	1.09	0.68	0.50	1.79	1.11
0.12	1.12	0.70	0.54	1.88	1.17
0.14	1.14	0.71	0.60	2.02	1.26
0.16	1.17	0.73	0.64	2.13	1.33
0.18	1.21	0.75	0.70	2.32	1.45
0.20	1.24	0.78	0.74	2.46	1.54
0.22	1.27	0.79	0.80	2.71	1.69
0.24	1.30	0.81	0.84	2.87	1.79
0.26	1.33	0.83	0.90	3.29	2.05
0.28	1.37	0.85	0.94	3.91	2.44

[†]Rodriguez-Reinoso *et al.* (1987).

Table A.3. α_s-plot data for the adsorption of N_2 at 77K on Wyodak coal char gasified in O_2 at 420°C to 30% burn-off.

P/P°	α_s	$N_2(cm^3(STP)/g)$
0.9	2.05	283.3
0.8	1.69	268.7
0.7	1.45	249.3
0.6	1.26	239.3
0.5	1.11	226.9
0.4	1.0	213.0
0.3	0.88	199.0
0.2	0.78	183.9
0.1	0.68	162.7
0.075	0.665	160.8
0.05	0.63	162.3
0.025	0.58	152.4
0.015	0.555	150.2

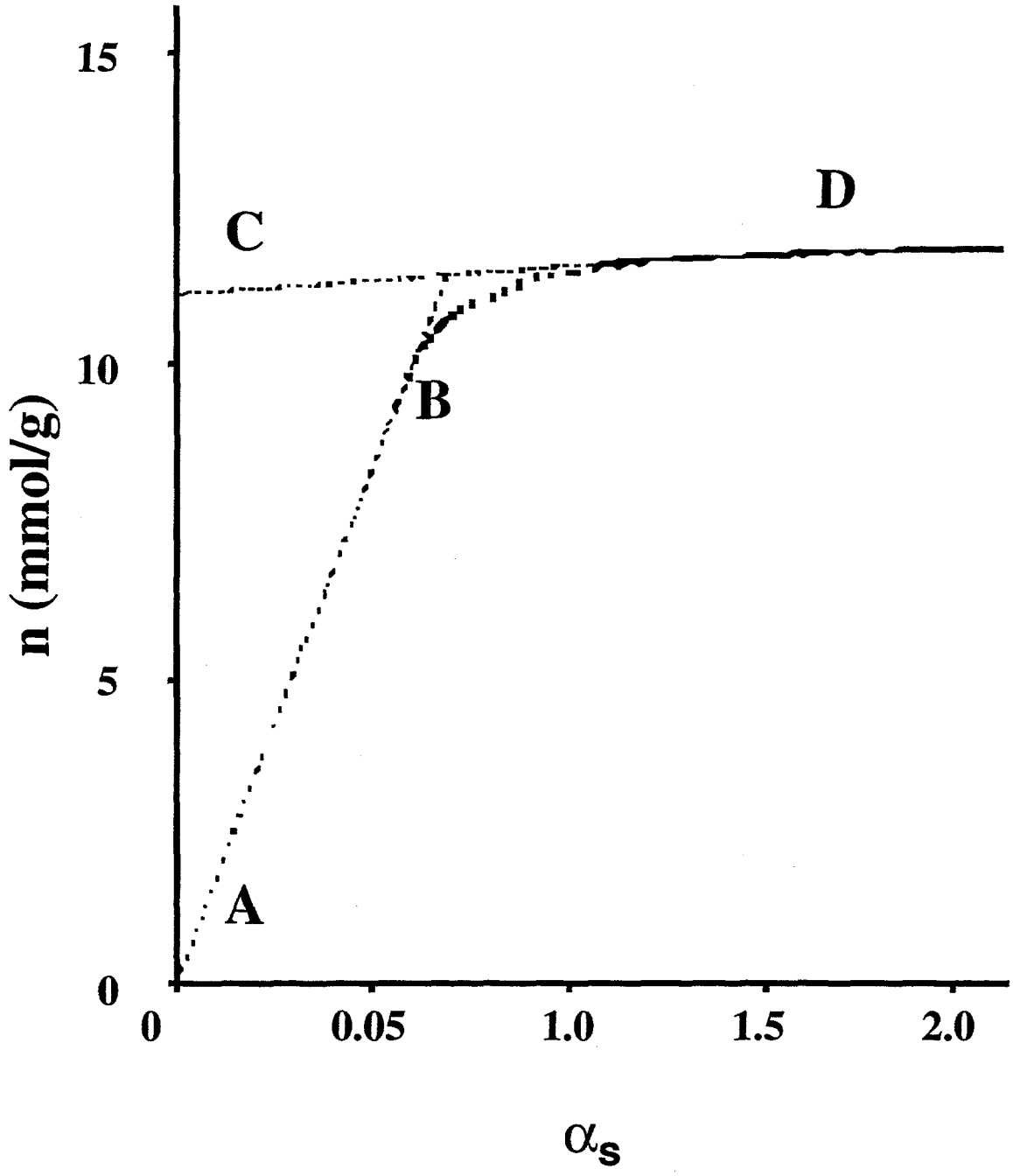

Figure A.1. α_s-plot for nitrogen adsorption at 77K on olive stone carbon activated to 34% burn-off [Rodriguez-Reinoso *et al.*, 1987].

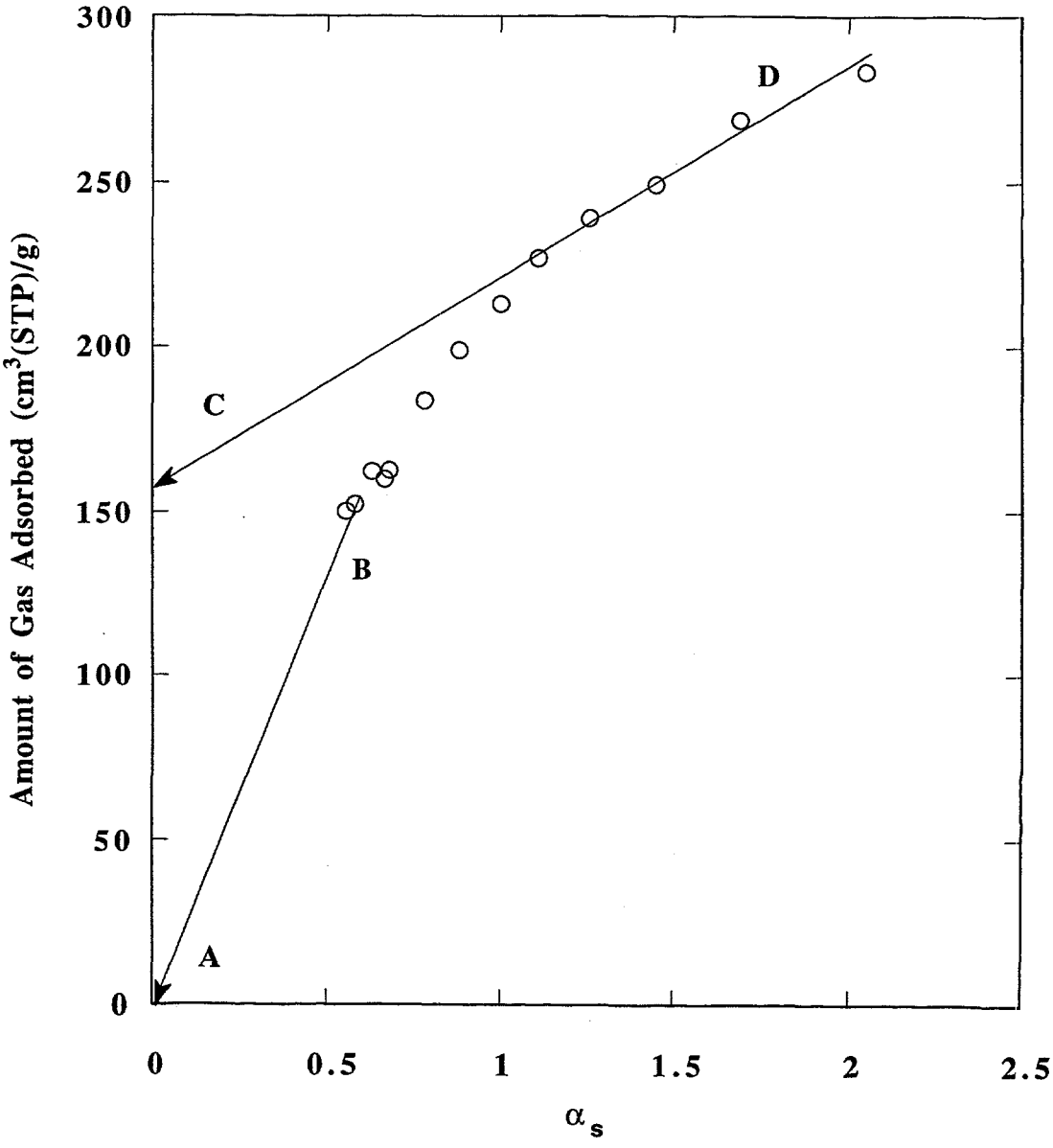

Figure A.2. α_s-plot for Wyodak coal char gasified to 30% burn-off at 420°C in oxygen.

Appendix B.

Roberts (1967) Method of Determining Mesopore Size Distributions

As discussed in Sections 1.3.3-2. and 2.2.2, mesopore size distributions were determined from nitrogen desorption isotherms for most of the samples in the current project. A method devised by Roberts (1967), as modified by Gregg and Sing (1982), was adopted for this purpose. In this method, the pore system is divided into 13 groups, in order to achieve a fairly uniform spacing in relative pressure, from mean pore radii of 100Å to 17Å. Allowance is made for the progressive thinning of the multilayer adsorbate in each pore as desorption proceeds. The calculation is most efficiently performed in a tabular format. Consequently a spreadsheet template was developed for this purpose. An example of the resultant template is presented for a Pittsburgh #8 sample burned-off to 15% is presented in Figure B-1.

The resultant pore size distributions for the Pittsburgh #8 and Wyodak coal char samples as a function of burn-off are presented in Figures 3 and 4, respectively. As indicated by these plots, the Pittsburgh #8 coal char develops a greater mesoporous fraction than the Wyodak char, and its microporosity never approaches the level of development evident for the Wyodak.

Pore Size Distribution Calculation - Roberts Method															
Pore group		13	12	11	10	9	8	7	6	5	4	3	2	1	0
rp/Å		17	19	21	23	25	30	35	40	50	60	70	80	90	100
rbp/Å		18	20	22	24	27.5	32.5	37.5	45	55	65	75	85	95	
t/Å		5.5	5.85	6.2	6.3	6.6	7.05	7.5	7.8	8.6	9.2	9.8	10.5	11.7	
p/p°		0.439	0.49	0.535	0.574	0.605	0.667	0.711	0.746	0.8	0.832	0.856	0.875	0.889	0.899
V/mm^3		36.8959	39.6048	41.3264	42.1437	42.4663	43.1893	44.6398	46.5961	50.358	52.2913	53.3656	54.0952	54.7447	55.3989
∂vp	**w/mm^3**	18.503	15.7941	14.0725	13.2552	12.9326	12.2095	10.7591	8.80282	5.04094	3.10755	2.03328	1.30369	0.65416	
2.900513	**12**	525.625													
		1.52458													
1.454606	**11**	562.5	538.889												
		0.81822	0.78387												
0.233271	**10**	594.184	571.914	550.069											
		0.13861	0.13341	0.12832											
0.782276	**9**	640	619.798	599.921	594.301										
		0.50066	0.48485	0.4693	0.46491										
1.998509	**8**	690.178	672.4	654.854	649.884	635.086									
		1.37933	1.3438	1.30873	1.2988	1.26923									
2.881898	**7**	728.178	712.336	696.668	692.224	678.976	659.344								
		2.09853	2.05288	2.00773	1.99492	1.95674	1.90016								
5.299227	**6**	770.494	756.9	743.427	739.6	728.178	711.211	694.444							
		4.08302	4.01099	3.93959	3.91931	3.85878	3.76887	3.68002							
2.638072	**5**	810	798.586	787.253	784.03	774.4	760.067	745.868	736.476						
		2.13684	2.10673	2.07683	2.06833	2.04292	2.00511	1.96765	1.94288						
1.4129	**4**	837.929	828.1	818.329	815.548	807.233	794.841	782.544	774.4	752.89					
		1.18391	1.17002	1.15622	1.15229	1.14054	1.12303	1.10566	1.09415	1.06376					
0.934823	**3**	858.711	850.084	841.5	839.056	831.744	820.836	810	802.816	783.815	769.714				
		0.80274	0.79468	0.78665	0.78437	0.77753	0.76734	0.75721	0.75049	0.73273	0.71955				
0.820815	**2**	874.775	867.09	859.438	857.258	850.735	840.997	831.315	824.891	807.884	795.244	782.704			
		0.71803	0.71172	0.70544	0.70365	0.6983	0.6903	0.68236	0.67708	0.66312	0.65275	0.64246			
0.850825	**1**	887.562	880.634	873.733	871.766	865.879	857.086	848.338	842.531	827.142	815.694	804.326	791.163	-	
		0.75516	0.74927	0.74339	0.74172	0.73671	0.72923	0.72179	0.71685	0.70375	0.69401	0.68434	0.67314	-	
Qii		2.0736	1.99778	1.93879	1.83855	1.7313	1.63076	1.5625	1.46332	1.40504	1.35693	1.32321	1.30174	1.30064	
∂rp		2	2	2	2	5	5	5	10	10	10	10	10	10	10
B		16.1396	14.3422	13.3222	13.1283	12.4807	10.984	8.91468	5.18145	3.16336	2.06631	1.3268	0.67314		
C = w - B		2.36335	1.45187	0.75026	0.12688	0.45184	1.2255	1.84441	3.62137	1.87757	1.04125	0.70648	0.63055		
∂vp=Qii C		4.90064	2.90051	1.45461	0.23327	0.78228	1.99851	2.8819	5.29923	2.63807	1.4129	0.93482	0.82082		
∂vp/∂rp		2.45032	1.45026	0.7273	0.11664	0.15646	0.3997	0.57638	0.52992	0.26381	0.14129	0.09348	0.08208		

Figure B.1. Spreadsheet template for mesopore size distribution calculation for Pittsburgh #8 coal char samples burned-off to 15% in oxygen @ 470°C, according to the method of Roberts (Gregg and Sing, 1982).

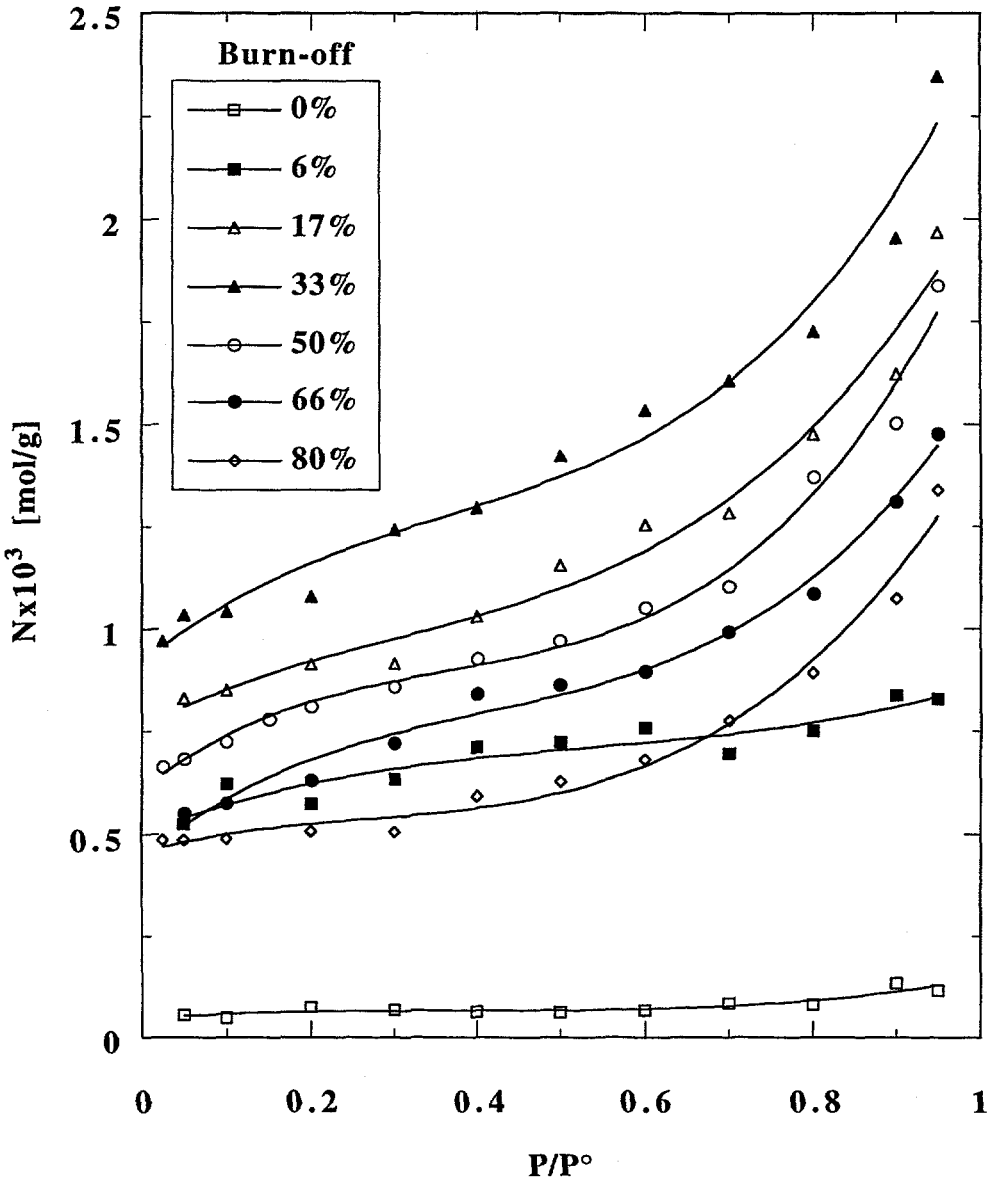

Figure B.2. Nitrogen desorption isotherms for Pittsburgh #8 coal char samples as a function of burn-off in oxygen @ 470°C.

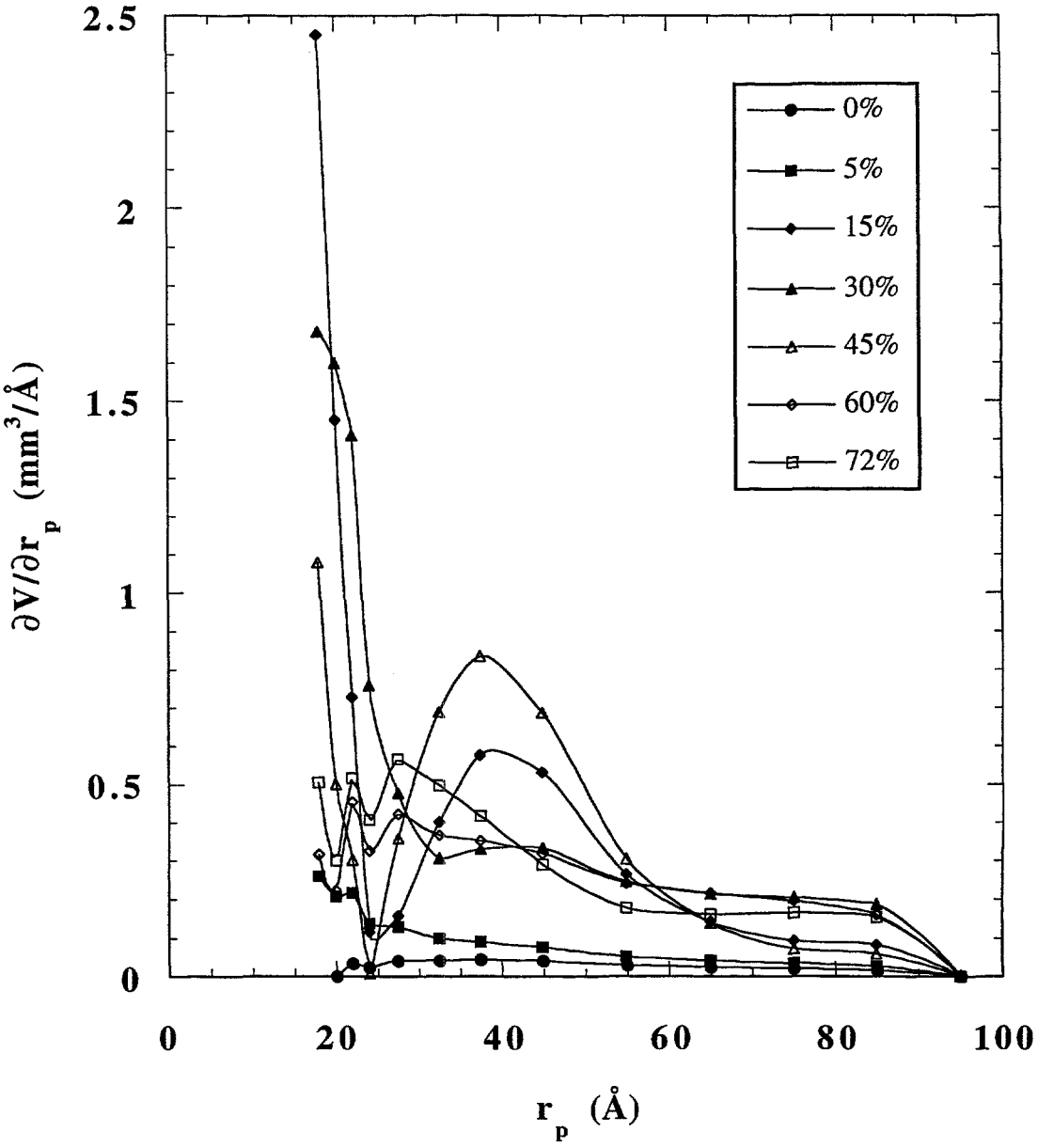

Figure B.3. Mesopore size distributions for Pittsburgh #8 coal char samples as a function of burn-off in oxygen @ 470°C, according to the method of Roberts (Gregg and Sing, 1982), using the nitrogen desorption isotherm data presented in Figure B.2.

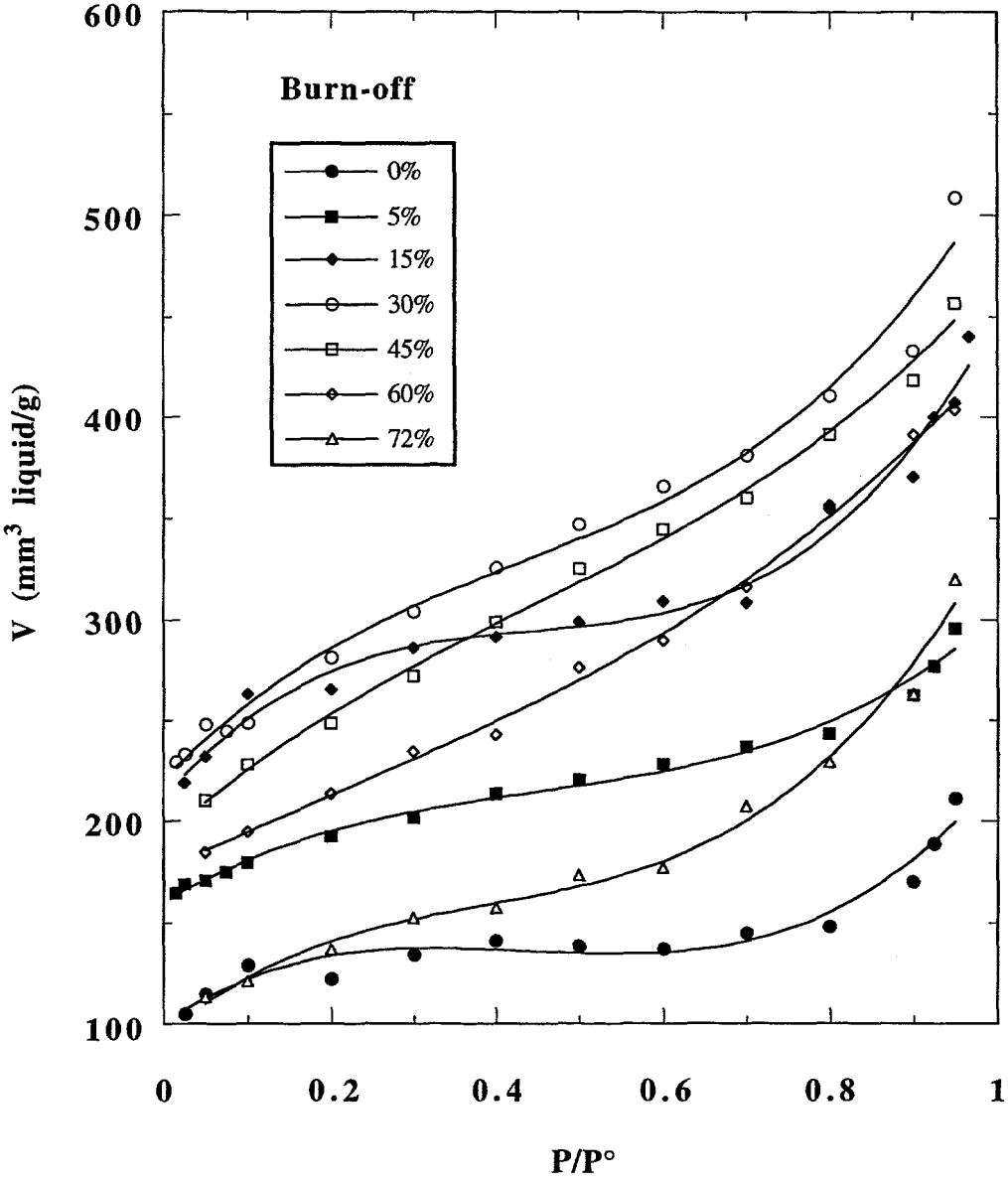

Figure B.4. Nitrogen desorption isotherms for Wyodak coal char samples as a function of burn-off in oxygen @ 420°C.

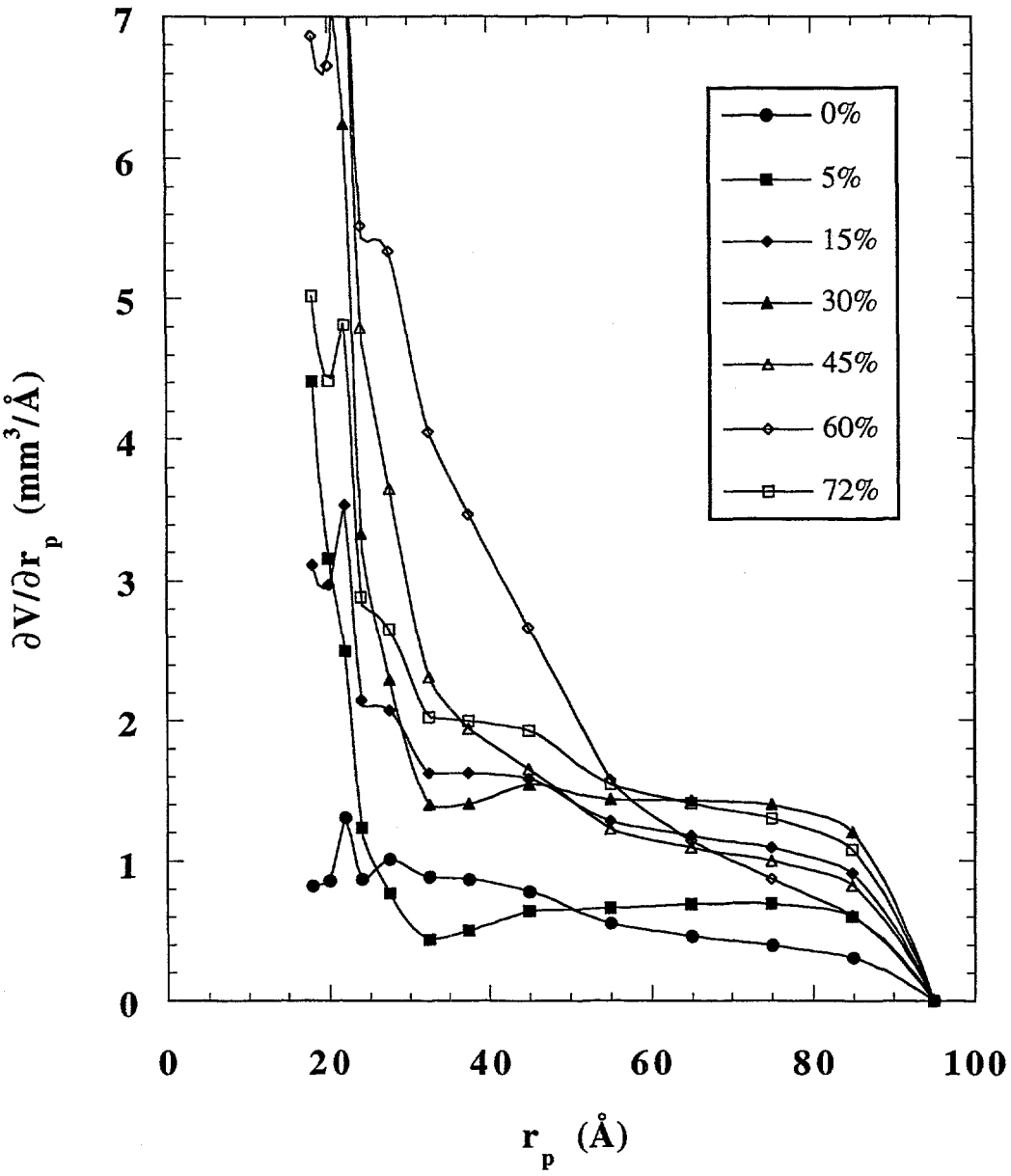

Figure B.5. Mesopore size distributions for Wyodak coal char samples as a function of burn-off in oxygen at 420°C, as determined by the method of Roberts (Gregg and Sing, 1982), using the nitrogen desorption isotherm data presented in Figure B.4.

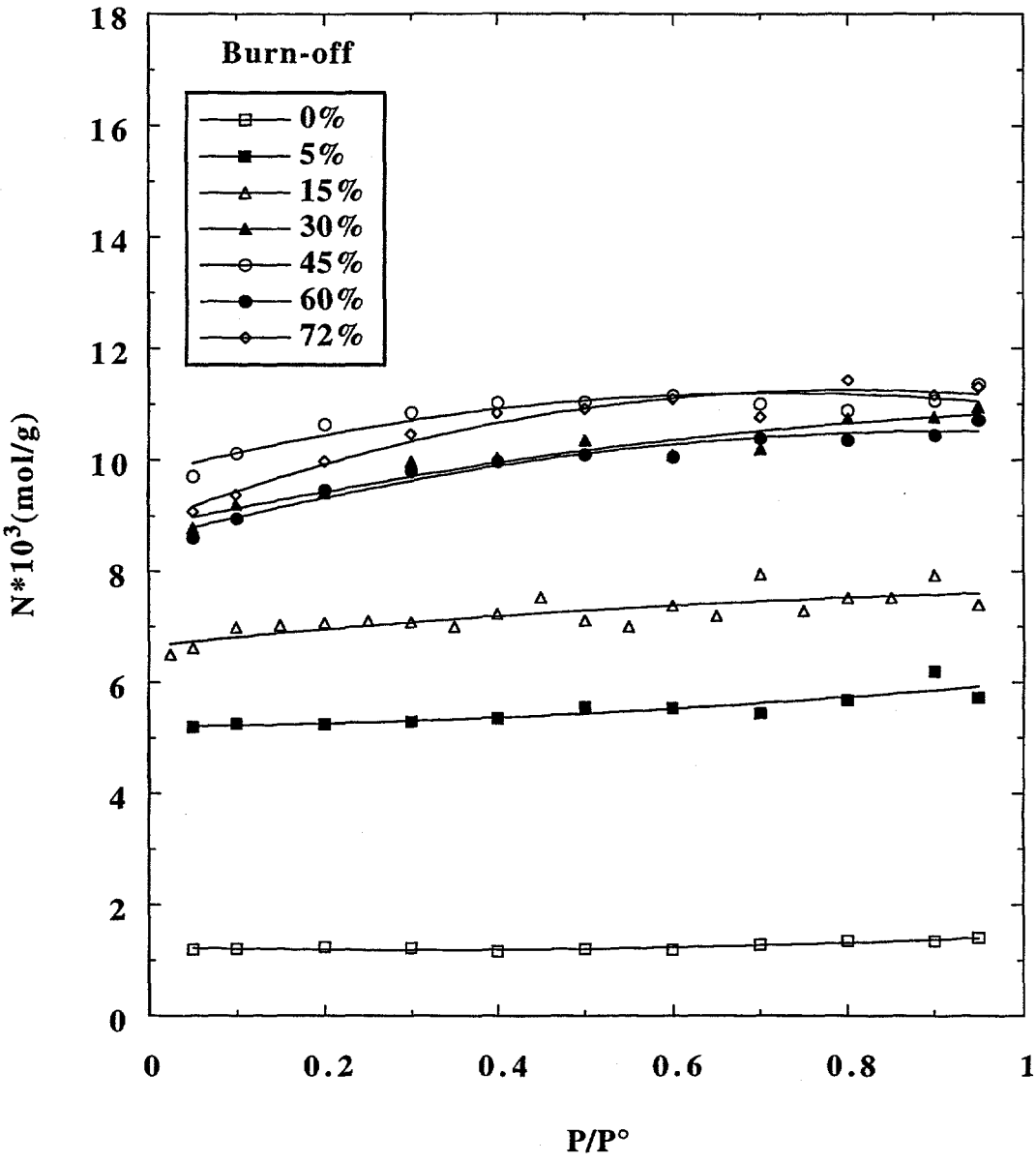

Figure B.6. Nitrogen desorption isotherms for phenol-formaldehyde resin char samples as a function of burn-off in oxygen @ 420°C.

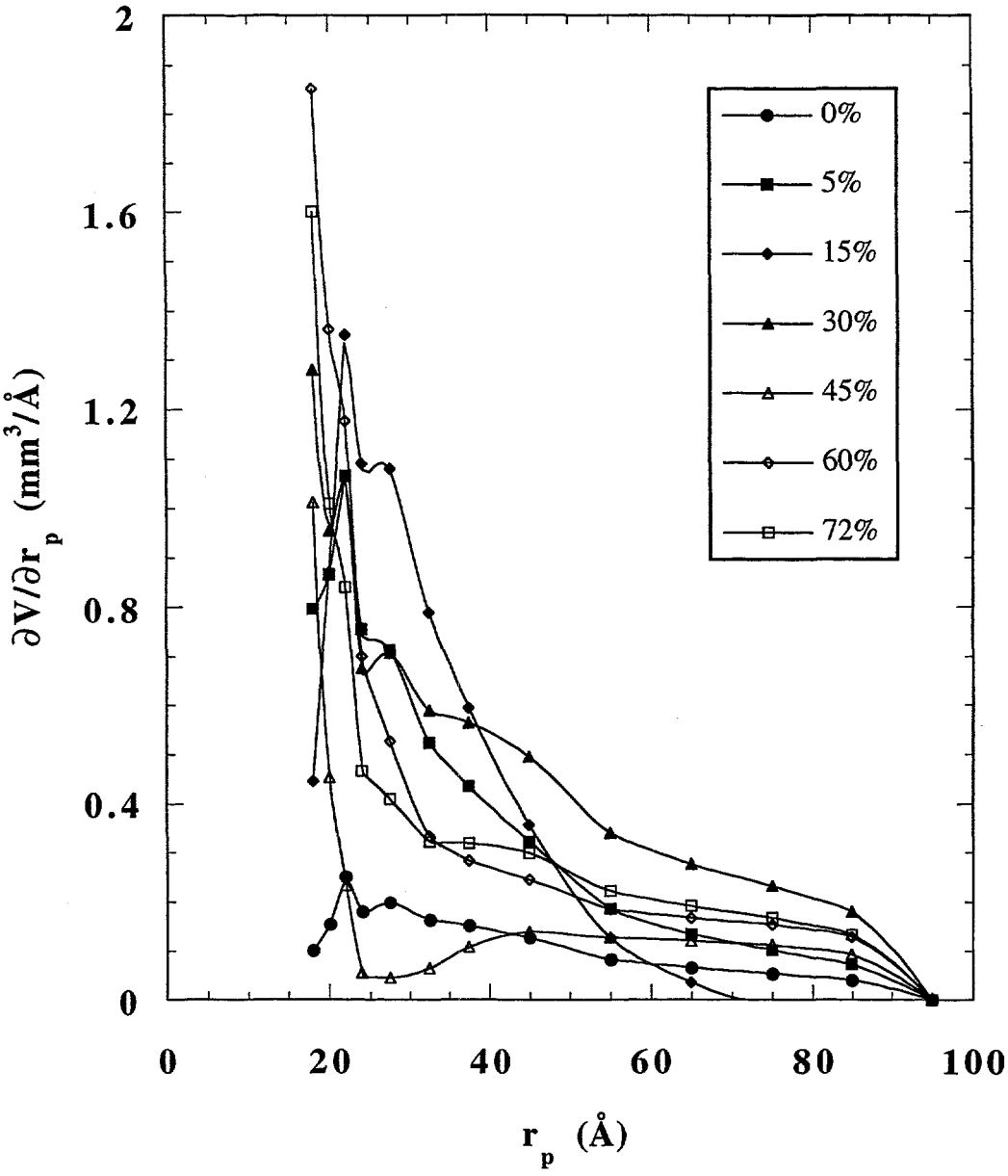

Figure B.7. Mesopore size distributions for phenol-formaldehyde resin char samples as a function of burn-off in oxygen, according to the method of Roberts (Gregg and Sing, 1982).

Appendix C.

Calculation of the CO_2 Mass Spectrometer "Cracking Factor" and Relative Sensitivities of CO and CO_2

C.1. Background.

In the ion source of the mass spectrometer, some of the CO_2 fragments to CO^+ upon electron impact ionization; i.e.,

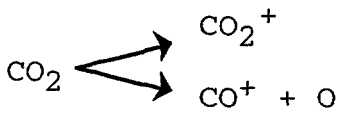

Two types of gases were used for calibration in order to calculate the "cracking factor" and the sensitivities of CO and CO_2. One is a mixture of CO and CO_2, and another is pure CO_2 gas. Here the sensitivity of a specific species is defined as the signal recorded during calibration for per specific amount of that species. The "cracking factor" is defined as the fraction of CO_2 producing CO^+ in the mass spectrometer ion source, which can be calculated from the pure CO_2 calibration. If $(\sum CO_2)_a$ and $(\sum CO)_a$ are the integrals of the CO_2 and CO signals obtained during the calibration run with pure CO_2, then the amount of CO_2 "cracked" into CO^+ is:

$$(\sum CO_2)_{cracked} = (\sum CO)_a \, (S_{CO2}/S_{CO}) \qquad [C.1]$$

where S_{CO_2} and S_{CO} are the sensitivities of CO_2 and CO, respectively, [mv/cm^3], and subscript "a" corresponds to pure CO_2 calibration run. The fraction of CO_2 "cracked" in the pure CO_2 calibration run (i.e. the "cracking factor", C) can be calculated from:

$$C=\frac{(\Sigma CO)_a\left(\frac{S_{CO_2}}{S_{CO}}\right)}{(\Sigma CO_2)_a+(\Sigma CO)_a\left(\frac{S_{CO_2}}{S_{CO}}\right)} \qquad [C.2]$$

From the calibration run using the CO/CO_2 mixture, the total amount of CO_2 "cracked" to CO^+ is then:

$$(\Sigma CO_2)_{b_{cracked}}=(\Sigma CO_2)_b\frac{C}{1-C} \qquad [C.3]$$

where "b" corresponds to the CO/CO_2 mixture calibration run, and $(\sum CO_2)_b$ is the sum of the CO_2^+ signal from the calibration run. Therefore, the sensitivities for CO_2 and CO are given by:

$$S_{CO_2}=\frac{(\Sigma CO_2)_b}{(1-C)(V_{CO_2})_b} \qquad [C.4]$$

$$S_{CO}=\frac{(\Sigma CO)_b-(\Sigma CO_2)_b\frac{C}{(1-C)}\frac{S_{CO}}{S_{CO_2}}}{(V_{CO})_b} \qquad [C.5]$$

where $(V_{CO_2})_b$ and $(V_{CO})_b$ are the volumes of CO_2 and CO, respectively, in the CO/CO_2 mixture calibration run.

Setting X as the relative sensitivity of CO_2 to CO; i.e.,:

$$X=S_{CO_2}/S_{CO} \qquad [C.6]$$

gives:

$$C=\frac{X(\Sigma CO)_a}{(\Sigma CO_2)_a+X(\Sigma CO)_a} \qquad [C.7]$$

Combining Eqns. [C.2] and [C.3] yields:

$$X=\frac{(\Sigma CO_2)_b}{(\Sigma CO)_b(1-C)}\left(\frac{(V_{CO})_b}{(V_{CO_2})_b}+C\right) \qquad [C.8]$$

After the "cracking factor" and relative sensitivities are determined for Eqns.[C.7] and [C.8], the sensitivities of CO and CO_2 can be calculated from Eqns.[C.4] and [C.5].

C.2. Computer Program Listing.

```
c     This program calculates the "cracking factor" of CO2 and the relative sensitivity of CO to CO2 c
      for calibration of the mass spectrometer.
c     Parameters:
c     FCO --- calibration factor for carbon monoxide, mv*min*g/mmol;
c     FCO2 --- calibration factor for carbon dioxide, mv*min*g/mmol;
c     X ----- relative sensitivity,= SCO/SCO2;
c     C --- cracking factor for CO2, =% of CO2 cracked;
c     COA --- integral of CO from pure CO2 calibration data;
c     CO2A --- integral of CO2 from pure CO2 calibration data;
c     COB --- integral of CO from CO/CO2 calibration data;
c     CO2B --- integral of CO from CO/CO2 calibration data;
c     TOTV --- total volume of calibration gas;
c     PCO ---  percentage of CO in CO/CO2 mixture;
c     PCO2 --- percentage of CO2 in CO/CO2 mixture;
c     SW -- sample weight, [G]
c
      IMPLICIT REAL*8 (A-H, O-Z)
      OPEN(UNIT=10,FILE='TPD.DAT',FORM='FORMATTED',STATUS='OLD')
      OPEN(UNIT=11,FILE='TPD.OUT',FORM='FORMATTED',STATUS='NEW')
      READ(10,*) COA,CO2A,COB,CO2B,TOTV,PCO,PCO2,SW
      C1=0.04
      I=0
100   X1=CO2B*(PCO/PCO2+C1)/COB/(1-C)
      I=I+1
      IF (I.GT.2000) GOTO 900
      C=X1*COA/(CO2A+X1*COA)
      IF (ABS(C1-C).LT. 0.0005) GOTO 300
      C1=C1+0.0005
      GOTO 100
```

```
300  C=C1
     X=X1
     CO=COB-C*CO2B/X/(1-C)
     CO2=CO2B/(1-C)    ! CORRECTED SUM FOR CALIBRATION.
     RATE=8.0          ! SEC/SET DATA , RECORDING RATE
     RATE=RATE/60.     ! MIN/SET DATA
     FCO=RATE*22.4./(TOTV*(PCO/100.))      ! 1 MMOL=22.4 CC
     FCO2=RATE*22.4/(TOTV*(PCO2/100.))
     FCO=FCO*CO*SW
     FCO2=FCO2*CO2*SW      ! [MV*MIN*G/MMOL]
     WRITE(11,*) '     A -- FOR PURE CO2 CALIBRATION'
     WRITE(11,*) '     B -- FOR CO/CO2=52/48% CALIBRATION'
     WRITE(11,*) 'COA=',COA,' CO2A=',CO2A,'  COB=',COB,' CO2B=',CO2B
     WRITE(11,*) 'TOTV=',TOTV,'  %CO=',PCO,'  %CO2=',PCO2,'  SW=',SW
     WRITE(11,*) 'C=',C,'  X=',X,'  FCO=',FCO,'  FCO2=',FCO2
     GOTO 1000
900  CONTINUE
     WRITE(11,*) '    NO SOLUTION'
1000 CONTINUE
     STOP
     END
```

Appendix D.

Random Pore Model Program

```
      PROGRAM RANDOM
C     THIS PROGRAM IS TO APPLY THE RANDOM PORE MODEL
C     TO DETERMINE THE POROSITY DEVELOPMENT.
      IMPLICIT REAL*8 (A-H, O-Z)
      PARAMETER (PI=3.14159)
      DIMENSION BOTIME(10), QMICRO(10),SMICRO(10)
      DIMENSION STOTAL(10),QT(10),SNM(10)
      COMMON/M1/VMICRO(10),AN,B0N
      COMMON/M2/BO(10),VS(10)
      COMMON/M3/RM1,SIGMA1,DR,DSIGMA,IRM,ISIGMA
      COMMON/M4/ET0,B0,B1
C     BO ---- BURN-OFF;
C     BOTIME --- BURN-OFF TIME;
C     STOTAL ---- TOTAL SURFACE AREA;
C     QT ----  RADIUS CHANGE FOE ALL PORES;
C     RMICRO ---- MICROPORE RADIUS;
C     QMICRO ---- MICROPORE RADIUS CHANGE;
C     SMICRO ---- SURFACE AREA FOR MICROPORES;
C     VMICRO ---- MICROPOROUS VOLUME;
C     SNM ---- NONMICROPOROUS SURFACE AREA;
C     VS  ----          SPECIFIC VOLUME OF THE CHAR SAMPLE;
C     A0, A1 ---- PARAMETERD DETERMINED FROM EQ.(3.19);
C     RM -----  INITIAL MEAN RADIUS;
C     SIGMA ---- VARIACE FOR GAUSSIAN PORE VOLUME DISTRIBUTION;
      OPEN(UNIT=11,FILE='RANDOM.OUT',FORM='FORMATTED',STATUS='NEW')
      OPEN(UNIT=12,FILE='RANDOM.IN',FORM='FORMATTED',STATUS='OLD')
C     DATA INPUT:
      READ(12,*) A00,A1SQ,S1,VS0,V0,RC,TIME,DTIME,DR,ITOUT
      DO 20 I=1,7
      READ (12,*) BO(I),BOTIME(I),VMICRO(I)
 20   CONTINUE
      READ(12,*) RR0,RMI,DR,SIGMAI,DSIGMA,IRM,ISIGMA
      READ(12,*) AN,VS1,VS2,VM1,VM2,VM3
      DO 25 I=1,7
      VS(I)=(VS1+VS2*BO(I))*1.D-6          !M^3/G
 25   CONTINUE
C     TO CALCULATE PARAMETERS: B0,B1,& V:
```

```
      A1=SQRT(A1SQ)
      A0=A00/60./60.          ![1/MIN^2.]
      A1=A1/60.               ![1/MIN.]
      S1=S1/VS(2)             !(1/M)
      ET0=V0/VS(1)       !INITIAL VOID FRACTION
      A3=S1/(4.*PI)/(1.-BO(2)/100.)/(1-ET0)
      V=(2.*PI*A0*BOTIME(2)+A1)/A3    !REACTION VELOCITY; [M/MIN]
      B1=A1/V
      B0=2.*PI*A0/V/V
C     ++++++++++++++++++++++++++++++++++++++++++++++++++
      CALL RMEAN (RM,SIGMA)
      WRITE(11,*) ' SIGMA= ',SIGMA,'      RM= ',RM
      CALL QMICROPORES (B0,B1,QMICRO,SMICRO)
C     ++++++++++++++++++++++++++++++++++++++++++++++++++
      DO 100 I=1,ITOUT
      TIME=BOTIME(I)
      Q2=V*TIME
      Q=Q2
      QT(I)=Q
      XCONV=BO(I)/100.
      STOTAL(I)=4.*PI*(1-ET0)*(B0*Q2+B1)*(1.-XCONV)
      STOTAL(I)=STOTAL(I)*VS(I)
 100  CONTINUE
      WRITE(11,*)' BQ,  STOTAL,  SMICRO,  SNM,  RMICRO, QMICRO'
      DO 300 I=2,7
      SNM(I)=STOTAL(I)-SMICRO(I)
      RMICRO=RM+QMICRO(I)
      WRITE(11,200)  BO(I),STOTAL(I),SMICRO(I),SNM(I),RMICRO,QMICRO(I)
 200  FORMAT(2X,4(F8.3,','),2(D9.3,','))
 300  CONTINUE
      STOP
      END
C     **********************************************************
      SUBROUTINE RMEAN (RM,SIGMA)
C     **********************************************************
C     THIS SUBROUTINE IS TO DETERMINE THE MEAN PORE RADIUS
C      AT THE INITIAL BY ASSUMING GAUSSIAN DISTRIBUTION
C      FOR PORE VOLUME:
      IMPLICIT  REAL*8  (A-H,  O-Z)
      PARAMETER  (PI=3.14159)
      COMMON/M3/RM1,SIGMA1,DR,DSIGMA,IRM,ISIGMA
      COMMON/M4/ET0,B0,B1
```

```
      RM=RMI
      RM2=5.D-11
      SIGMA2=2.D-11
      ERR1A=1.D20
      ERR2A=1.D10
      DO 40 I=1,IRM
      RM=RM+DR
      SIGMA=SIGMAI
      DO 60 J=1,ISIGMA
      SIGMA=SIGMA+DSIGMA
      CONS=ET0/SIGMA/((2.*PI)**(1.5))    ! DISTRIBUTION CONSTANT
      RR=RR0
      DRR=5.*SIGMA/200.
      E0=0.
      E1=0.
      DO 55 K=1,200
      RR=RR+DRR
      F1=DEXP(-(RR-RM)**2/SIGMA**2/2.)
      F2=F1*CONS/RR
      F1=F1*CONS/RR/RR
      F1=F1*DRR
      F2=F2*DRR
      E0=E0+F1
      E1=E1+F2
55    CONTINUE
      ERR1=ABS(B0-E0)
      ERR2=ABS(B1-E1)
      IF(ERR1.GT.B0/1.5) GOTO 60
      IF(ERR2.GT.B1/1.5) GOTO 60
      IF(ERR1.GT.ERR1A) GOTO 60
      IF(ERR2.GT.ERR2A) GOTO 60
      ERR1A=ERR1
      ERR2A=ERR2
      RM2=RM
      SIGMA2=SIGMA
60    CONTINUE
40    CONTINUE
      RM=RM2
      SIGMA=SIGMA2
      IF (RM.NE.5.D-11) GOTO 100
      WRITE (11,*) 'NO SOLUTION FOR "RMEAN" FOUND'
100   CONTINUE
```

```
      RETURN
      END
C     ****************************************************************
      SUBROUTINE QMICROPORES (B0,B1,QM,S)
C     ****************************************************************
C     THIS SUBROUTINE IS TO DETERMINE THE DISTRIBUTION
C      OF MICROPOROSITY:
      IMPLICIT REAL*8 (A-H, O-Z)
      DIMENSION  X(10),ET(10),S(10),QM(10),VSBO(10)
      COMMON/M1/V(10),AN,B0N
      COMMON/M2/BO(10),VS(10)
C     OPEN(UNIT=11,FILE='RAN2.OUT',FORM='FORMATTED',STATUS='NEW')
C     OPEN(UNIT=12,FILE='VOL1.IN',FORM='FORMATTED',STATUS='OLD')
      ET0=V(1)*1.D-6/VS(1)
      Q=0.1D-9
      DQ=0.01D-9
      DO 50 I=2,7
      ET(I)=V(I)*1.D-6/VS(I)
      A1=-   LOG((1-ET(I))/(1-ET0))/(2.*3.14159)
      N=0
 30   A2=B0*Q*Q+2.*B1*Q
      N=N+1
      IF (N.GT.100) GOTO 200
      IF (ABS(A2-A1).LT.ABS(A1/AN)) GOTO 40
      IF ((A2-A1).LT.0) GOTO 35
      Q=Q-DQ
      GOTO 36
 35   Q=Q+DQ
 36   CONTINUE
      GOTO 30
 40   QM(I)=Q
      S(I)=4.*3.14159*(1-ET(I))
      S(I)=S(I)*(B0*Q+B1)
      S(I)=S(I)*VS(I)
 50   CONTINUE
      GOTO 200
 100  CONTINUE
      WRITE(11,*) 'SUNROUTINE, N>100, NO QMICRO SOLUTION'
 200  CONTINUE
      RETURN
      END
```

Appendix E.

E.1. Program SCATTER - Levenberg-Marquardt parameter estimation code for bimodal Schulz distribution FPPS model.

```
      PROGRAM SCATTER
      DIMENSION HX(200),TENSITY(200),SIG(200),A(6),LISTA(6),
     *  COVAR(6,6),ALPHA(6,6),BETA(6),ATRY(6)
      IMPLICIT REAL*8 (A-H,O-Z)
      CHARACTER*30 filename1
      CHARACTER*30 filename2
      COMMON PP,GB11,GB22,Q

      PRINT *,'Input File Name:'
      READ *,filename1
       PRINT *,'Output File Name:'
       READ *,filename2
      open (UNIT=10,FILE=filename1,ERR=500,
     +STATUS='OLD',ACTION='READ')
11    format(I3)
12    format (F8.5,F15.6)
      READ(10,11) NUM
      PRINT *,NUM

      DO 13 K=1,NUM
        READ(10,12) HX(K),TENSITY(K)
      SIG(K)=1.0D0
        TENSITY(K)=DLOG(TENSITY(K))
13      CONTINUE

      PP=3.141592653589793D0
      goto 501
500   CONTINUE
      PRINT *,'Error Opening File '
501   CONTINUE
      close (10)

      PRINT *,'A01 ='
      READ *,A01
      PRINT *,'B1 ='
      READ *,B1
```

```
      PRINT *,'A02 ='
      READ *,A02
      PRINT *,'B2 ='
      READ *,B2
      PRINT *,'PHI ='
      READ *,PHI
      PRINT *,'EPS1 ='
      READ *,EPS1
      PRINT *,'TEN0 ='
      READ *,Q

  999   CONTINUE

      A(1)=A01
      A(2)=B1
      A(3)=A02
      A(4)=B2
      A(5)=PHI
      A(6)=EPS1
      MA=6

  116    CONTINUE
        DO 15 K=1,6
        DO 16 J=1,6
        COVAR(K,J)=0.0D0
        ALPHA(K,J)=0.0D0
   16   CONTINUE
   15   CONTINUE
      PRINT *,'Number of Fit Parameters: '
      READ *,MFIT
      NCA=6
      DO 888 I=1,6
      PRINT *,'Parameter #',I,' = '
      READ *,LISTA(I)
  888 CONTINUE

      PRINT *,'ALAMDA Initial = '
      READ *,ALAMDA

      GB11=DEXP(GAMMLN(A(2)))
      GB22=DEXP(GAMMLN(A(4)))
      ICOUNT=0
```

```
      PRINT *,A(1),A(2),A(3),A(4),A(5),A(6)
      PRALAMDA=0.0D0
      PRCHISQ=0.1D0
      CRIT=0.01D0
      PRINT *,NUM
      PRINT *,MFIT
      PRINT *,NCA
113   CONTINUE
      CALL MRQMIN(HX,TENSITY,SIG,NUM,A,MA,LISTA,MFIT,
     *     COVAR,ALPHA,BETA,ATRY,NCA,CHISQ,OCHISQ,ALAMDA)
      PRINT *,' '
      PRINT *,'ITERATION NUMBER ',ICOUNT
      PRINT *,'CHISQ = ',CHISQ
      PRINT *,'PREVIOUS CHISQ =',PRCHISQ
      PRINT *,'ALAMDA = ',ALAMDA
      PRINT *,'PREVIOUS ALAMDA =',PRALAMDA
      PRINT *, ATRY
      open (UNIT=10,FILE=filename2,STATUS='UNKNOWN',
     +ERR=700,ACTION='WRITE')
       write(10,34) A01,B1
       write(10,34) A02,B2
       write(10,34) PHI,EPS1
 33   format (E20.8,1H,,E20.8,1H,,E20.8)
 34     format(F10.5,1H,,F10.5,1H,,F10.5)
      goto 701
 700  CONTINUE
      type *,'Error Opening File '
      print *,filename2
 701  CONTINUE
      close (10)
C115  CONTINUE
      IF(ALAMDA.EQ.0.0D0) GO TO 114
      PRALAMDA=ALAMDA
      PRCHISQ=CHISQ
      ICOUNT=ICOUNT+1
      IF(ICOUNT.GT.1000) GO TO 114
      IF(CHISQ.GT.CRIT) GO TO 113
      ALAMDA=0.0D0
      GO TO 113
114   CONTINUE
      PAUSE
      STOP
```

```
      END
C*****************************************************************
      SUBROUTINE MRQMIN(X,Y,SIG,NDATA,A,MA,LISTA,MFIT,
     *    COVAR,ALPHA,BETA,ATRY,NCA,CHISQ,OCHISQ,ALAMDA)
C*****************************************************************
      PARAMETER (MMAX=6)
      DIMENSION X(NDATA),Y(NDATA),SIG(NDATA),A(MA),LISTA(MA),
     *  COVAR(NCA,NCA),ALPHA(NCA,NCA),ATRY(MMAX),BETA(MMAX),DA(MMAX)
      IMPLICIT REAL*8 (A-H,O-Z)
      COMMON PP,GB11,GB22,Q
      IF(ALAMDA.LT.0.0D0)THEN
        KK=MFIT+1
        DO 12 J=1,MA
          IHIT=0
          DO 11 K=1,MFIT
            IF(LISTA(K).EQ.J)IHIT=IHIT+1
11        CONTINUE
          IF (IHIT.EQ.0) THEN
            LISTA(KK)=J
            KK=KK+1
          ELSE IF (IHIT.GT.1) THEN
            PAUSE 'Improper permutation in LISTA'
          ENDIF
12      CONTINUE
        IF (KK.NE.(MA+1)) PAUSE 'Improper permutation in LISTA'
        ALAMDA=1.0D-3
        CALL MRQCOF(X,Y,SIG,NDATA,A,MA,LISTA,MFIT,ALPHA,BETA,NCA,CHISQ)
        OCHISQ=CHISQ
        DO 13 J=1,MA
          ATRY(J)=A(J)
13      CONTINUE
      ENDIF
      DO 15 J=1,MFIT
        DO 14 K=1,MFIT
          COVAR(J,K)=ALPHA(J,K)
14      CONTINUE
        COVAR(J,J)=ALPHA(J,J)*(1.0D0+ALAMDA)
c       PRINT *, BETA(J)
        DA(J)=BETA(J)
15    CONTINUE
      CALL GAUSSJ(COVAR,MFIT,NCA,DA,1,1)
      IF(ALAMDA.EQ.0.0D0)THEN
```

```
        CALL COVSRT(COVAR,NCA,MA,LISTA,MFIT)
        RETURN
      ENDIF
      DO 16 J=1,MFIT
32    CONTINUE
        ATRY(LISTA(J))=A(LISTA(J))+DA(J)
      IF(ATRY(LISTA(J)).LT.0.0D0) GO TO 31
      GO TO 33
31    DA(J)=DA(J)/2.0D0
      GO TO 32
33    PRINT *,'DA(J) = ',DA(J)
16    CONTINUE

C     Check Parameter Values to Keep Them Within Limits

      IF(ATRY(1).GT. 10.0D0) ATRY(1)=10.0D0
      IF(ATRY(3).GT.100.0D0) ATRY(3)=100.0D0
      IF(ATRY(1).LT.1.0D0) ATRY(1)=1.0D0
      IF(ATRY(3).LT.1.0D0) ATRY(3)=1.0D0
      IF(ATRY(3).LT.ATRY(1)) ATRY(3)=1.01D0*ATRY(1)
      IF(ATRY(2).LE.1.0D0) ATRY(2)=1.0D0
      IF(ATRY(4).LE.0.1D0) ATRY(4)=0.1D0
      IF(ATRY(2).GT.65.0D0) ATRY(2)=65.0D0
      IF(ATRY(4).GT.40.0D0) ATRY(4)=40.0D0
      IF(ATRY(5).GT.1.0D0) ATRY(5)=0.99999999D0
      IF(ATRY(5).LT.0.607D0) ATRY(5) = 0.607D0
      IF(ATRY(6).GT.1.0D0) ATRY(6)=0.99999999D0
      IF(ATRY(6).LT.0.1D0) ATRY(6) = 0.1D0

      GB11=DEXP(GAMMLN(ATRY(2)))
      GB22=DEXP(GAMMLN(ATRY(4)))
      WRITE(9,100) ATRY
100     FORMAT(4F8.3,1H ,2E16.8,1H ,F8.3)
C     PRINT *,'MRQMIN: GB11 = ',GB11,'GB22 = ',GB22
      CALL MRQCOF(X,Y,SIG,NDATA,ATRY,MA,LISTA,MFIT,COVAR,DA,NCA,CHISQ)
      IF(CHISQ.LT.OCHISQ)THEN
        ALAMDA=0.1D0*ALAMDA
        OCHISQ=CHISQ
        DO 18 J=1,MFIT
          DO 17 K=1,MFIT
            ALPHA(J,K)=COVAR(J,K)
17        CONTINUE
```

```
          BETA(J)=DA(J)
          A(LISTA(J))=ATRY(LISTA(J))
18      CONTINUE
      ELSE
        ALAMDA=10.0D0*ALAMDA
        OCHISQ=CHISQ
      ENDIF
      RETURN
      END
C*******************************************************************************
      SUBROUTINE MRQCOF(X,Y,SIG,NDATA,A,MA,LISTA,MFIT,ALPHA,BETA,NALP,CH
     *ISQ)
C*******************************************************************************
      PARAMETER (MMAX=6)
      DIMENSION X(NDATA),Y(NDATA),SIG(NDATA),ALPHA(NALP,NALP),BETA(MA),
     *    DYDA(MMAX),LISTA(MA),A(MA)
      IMPLICIT REAL*8 (A-H,O-Z)
      COMMON PP,GB11,GB22,Q
      DO 12 J=1,MFIT
        DO 11 K=1,J
          ALPHA(J,K)=0.0D0
11      CONTINUE
        BETA(J)=0.0D0
12    CONTINUE
      CHISQ=0.0D0
      DO 15 I=1,NDATA
        CALL FUNCS(X(I),A,YMOD,DYDA,MA)
c     PRINT *,' X(I)=',X(I),' Y(I)=',Y(I),' YFIT=',YMOD
        SIG2I=1.0D0/(SIG(I)*SIG(I))
        DY=Y(I)-YMOD
        DO 14 J=1,MFIT
          WT=DYDA(LISTA(J))*SIG2I
c       PRINT *,WT,DYDA(LISTA(J)),SIG2I,DY
          DO 13 K=1,J
            ALPHA(J,K)=ALPHA(J,K)+WT*DYDA(LISTA(K))
13        CONTINUE
          BETA(J)=BETA(J)+DY*WT
C       PRINT *,BETA(J)
14      CONTINUE
        CHISQ=CHISQ+DY*DY*SIG2I
15    CONTINUE
      DO 17 J=2,MFIT
```

```
        DO 16 K=1,J-1
          ALPHA(K,J)=ALPHA(J,K)
16      CONTINUE
17    CONTINUE
      RETURN
      END
C*****************************************************************
      SUBROUTINE FUNCS(H,AP,YFIT,DYDA,MA)
C*****************************************************************
      DIMENSION SUM(7),SST(7),SUMPREV(7),AP(6),DYDA(6)
      IMPLICIT REAL*8 (A-H,O-Z)
      COMMON PP,GB11,GB22,Q
C     H LOOP HERE
C     PRINT *,'Calculating R loop'
      DO 140 I=1,7
      SUM(I) = 0.0D0
      SUMPREV(I)=0.0D0
140   CONTINUE
      DEX=1.0D0
      BEGIN=0.0D0
100   ROOT=DEX*PP/H
      FINISH=ROOT
      CALL QGAUSS(BEGIN,FINISH,H,AP,SST)
      DO 130 I=1,7
      SUM(I) = SUM(I) + SST(I)
130   CONTINUE
      BEGIN = FINISH
      DEX = DEX+1.0D0
C      PRINT *,DEX,SUM(1),SST(1)
C       PRINT *,DEX,SUM(2),SST(2)
C       PRINT *,DEX,SUM(3),SST(3)
C       PRINT *,DEX,SUM(4),SST(4)
C       PRINT *,DEX,SUM(5),SST(5)
      IF(DABS(SST(1)/SUM(1)).GT.1.0D-3) GO TO 100
      IF(DABS(SST(2)/SUM(2)).GT.1.0D-3) GO TO 100
      IF(DABS(SST(3)/SUM(3)).GT.1.0D-3) GO TO 100
      IF(DABS(SST(4)/SUM(4)).GT.1.0D-3) GO TO 100
      IF(DABS(SST(5)/SUM(5)).GT.1.0D-3) GO TO 100
      IF(DABS(SST(6)/SUM(6)).GT.1.0D-3) GO TO 100
      IF(DABS(SST(7)/SUM(7)).GT.1.0D-3) GO TO 100
      IF(SUMPREV(1).EQ.0.0D0) GO TO 102
      SUM(1)=(SUM(1)+SUMPREV(1))/2.0D0
```

```
102   CONTINUE
      YFIT=DLOG(SUM(1))
C      PRINT *,YFIT
      DO 101 I=1,6
      DYDA(I)=(SUMPREV(I+1)+SUM(I+1))/SUM(1)/2.0D0
C      PRINT *,DYDA(I)
101   CONTINUE
      RETURN
      END
C*********************************************************************
      SUBROUTINE QGAUSS(A,B,H,AP,SS)
C*********************************************************************
      DIMENSION X(5),W(5),SS(7),D1(7),D2(7),AP(6)
      IMPLICIT REAL*8 (A-H,O-Z)
      COMMON PP,GB11,GB22,Q
      DATA X/.1488743389,.4333953941,.6794095682,.8650633666,.9739065285
     */
      DATA W/.2955242247,.2692667193,.2190863625,.1494513491,.0666713443
     */
C     1 = GAM
C     2 = DGDA01
C     3 = DGDB1
C     4 = DGDA02
C     5 = DGDB2
C     6 = DGDF
C     7 = DGDEPS1
C     8 = DGDTEN0
      XM=0.5D0*(B+A)
      XR=0.5D0*(B-A)
      DO 12 I=1,7
      SS(I)=0.0D0
 12   CONTINUE
      DO 11 J=1,5
        DX=XR*X(J)
      CALL FUNC(XM+DX,H,AP,D1)
      CALL FUNC(XM-DX,H,AP,D2)
      DO 13 I=1,7
        SS(I)=SS(I)+W(J)*(D1(I)+D2(I))
13    CONTINUE
11    CONTINUE
C     PRINT *,'QGAUSS',H,A,B
      DO 14 I=1,7
```

```
      SS(I)=XR*SS(I)
C      PRINT *,SS(I)
14    CONTINUE
      RETURN
      END
C*******************************************************************************
      SUBROUTINE FUNC(R,H,AP,D)
C*******************************************************************************
      DIMENSION D(7),AP(6)
      IMPLICIT REAL*8 (A-H,O-Z)
      REAL*8 EPS1,EPS2
      COMMON PP,GB11,GB22,Q
C      PRINT *,'SUB FUNC'
      A01=AP(1)
      B1=AP(2)
      A02=AP(3)
      B2=AP(4)
      PHI=AP(5)
      EPS1=AP(6)
      TEN0=Q
      EPS2=1.0D0-EPS1
      CALL S2R(R,A01,B1,PHI,GB11,S1,T31,DIDA1,DIDB1,DT31DA1,DT31DB1)
      CALL S2R(R,A02,B2,PHI,GB22,S2,T32,DIDA2,DIDB2,DT32DA2,DT32DB2)
      IF(R.EQ.0.0D0) GO TO 10
      RFUNC=TEN0*4.0D0*PP*DSIN(H*R)*R**2/H/R
      D1=DEXP(DLOG(PHI)*(EPS1*S1+EPS2*S2))
      D(1)=(D1-PHI**2)*RFUNC
      D(2)=D1*RFUNC*DLOG(PHI)*EPS1*DIDA1
      D(3)=D1*RFUNC*DLOG(PHI)*EPS1*DIDB1
      D(4)=D1*RFUNC*DLOG(PHI)*EPS2*DIDA2
      D(5)=D1*RFUNC*DLOG(PHI)*EPS2*DIDB2
      D(6)=D1*RFUNC*(EPS1*S1+EPS2*S2)/PHI-2.0D0*PHI*RFUNC
C      D(6)=D(6)-(D1-PHI**2)*RFUNC*(1.0D0-2.0D0*PHI)/PHI/(1.0D0-PHI)
      D(7)=D1*RFUNC*DLOG(PHI)*(S1-S2)
      GO TO 20
10    DO 30 J=1,7
      D(J)=0.0D0
30    CONTINUE
20    CONTINUE
      RETURN
      END
```

```
C*****************************************************************************
      SUBROUTINE S2R(R,A0,B,PHI,GB,S,T3,DIDA,DIDB,DT3DA0,DT3DB)
C*****************************************************************************
      IMPLICIT REAL*8 (A-H,O-Z)
      XX = B*R/A0/2.0D0
      T1=DEXP(-XX)
      T3=((A0/B)**3)*(B+2.0D0)*(B+1.0D0)*B
      PAX=GAMMP(B,XX)
      ACTR=(XX**B)*T1/B/GB
      PAX1=PAX-ACTR
      PAX2=PAX1-XX*ACTR/(B+1.0D0)
      PAX3=PAX2-XX**2*ACTR/(B+2.0D0)/(B+1.0D0)
      PAX4=PAX3-XX**3*ACTR/(B+3.0D0)/(B+2.0D0)/(B+1.0D0)
C       PRINT *,T3,PAX,PAX1,PAX2,PAX3,PAX4
      GRAL=(1.0D0+PAX3)+1.5D0*XX*(1.0D0-PAX2)/(B+2.0D0)
     &-XX**3*(1.0D0-PAX)/2.0D0/B/(B+1.0D0)/(B+2.0D0)
      S=GRAL
      DI3DA0=-XX**3*(3.0D0*(1.0D0-PAX)+B*(PAX1-PAX))/
     &2.0D0/B/(B+1.0D0)/(B+2.0D0)/A0
      DI3DB=XX**3*((PAX1-PAX)+(1.0D0-PAX)*(3.0D0*B+4.0D0)/
     &B/(B+1.0D0)/(B+2.0D0))/2.0D0/B/(B+1.0D0)/(B+2.0D0)

      DI2DA0=-1.5D0*XX*((1.0D0-PAX2)+(B+2.0D0)*(PAX3-PAX2))/
     &(B+2.0D0)/A0
C       PRINT *,R,A0,B,XX,T1,GB,PAX,PB
      DI2DB=1.5*XX*(2.0D0*(1.0D0-PAX2)-((B+2.0D0)**2)*(PAX2-PAX3))/
     &((B+2.0D0)**2)/B

      DI1DA0=(B+3.0D0)*(PAX4-PAX3)/A0
      DI1DB=(B+3.0D0)*(PAX3-PAX4)/B
      DIDA=DI1DA0+DI2DA0-DI3DA0
      DIDB=DI1DB+DI2DB-DI3DB
C       PRINT *,DIDA,DT3DA0,DI1DA0,DI2DA0,DI3DA0
C       PRINT *,DIDB,DT3DB,DI1DB,DI2DB,DI3DB
C       PAUSE
      RETURN
      END
C*****************************************************************************
      SUBROUTINE COVSRT(COVAR,NCVM,MA,LISTA,MFIT)
C*****************************************************************************
      DIMENSION COVAR(NCVM,NCVM),LISTA(MFIT)
      IMPLICIT REAL*8 (A-H,O-Z)
      DO 12 J=1,MA-1
```

```
        DO 11 I=J+1,MA
          COVAR(I,J)=0.
11      CONTINUE
12    CONTINUE
      DO 14 I=1,MFIT-1
        DO 13 J=I+1,MFIT
          IF(LISTA(J).GT.LISTA(I)) THEN
            COVAR(LISTA(J),LISTA(I))=COVAR(I,J)
          ELSE
            COVAR(LISTA(I),LISTA(J))=COVAR(I,J)
          ENDIF
13      CONTINUE
14    CONTINUE
      SWAP=COVAR(1,1)
      DO 15 J=1,MA
        COVAR(1,J)=COVAR(J,J)
        COVAR(J,J)=0.
15    CONTINUE
      COVAR(LISTA(1),LISTA(1))=SWAP
      DO 16 J=2,MFIT
        COVAR(LISTA(J),LISTA(J))=COVAR(1,J)
16    CONTINUE
      DO 18 J=2,MA
        DO 17 I=1,J-1
          COVAR(I,J)=COVAR(J,I)
17      CONTINUE
18    CONTINUE
      RETURN
      END
C*****************************************************************
      SUBROUTINE GAUSSJ(A,N,NP,B,M,MP)
C*****************************************************************
      PARAMETER (NMAX=50)
      DIMENSION A(NP,NP),B(NP,MP),IPIV(NMAX),INDXR(NMAX),INDXC(NMAX)
      IMPLICIT REAL*8 (A-H,O-Z)
      DO 11 J=1,N
        IPIV(J)=0
11    CONTINUE
      DO 22 I=1,N
        BIG=0.0D0
        DO 13 J=1,N
          IF(IPIV(J).NE.1)THEN
```

```
          DO 12 K=1,N
            IF (IPIV(K).EQ.0) THEN
              IF (DABS(A(J,K)).GE.BIG)THEN
                BIG=DABS(A(J,K))
                IROW=J
                ICOL=K
              ENDIF
            ELSE IF (IPIV(K).GT.1) THEN
              PAUSE 'Singular matrix'
            ENDIF
12        CONTINUE
          ENDIF
13      CONTINUE
        IPIV(ICOL)=IPIV(ICOL)+1
        IF (IROW.NE.ICOL) THEN
          DO 14 L=1,N
            DUM=A(IROW,L)
            A(IROW,L)=A(ICOL,L)
            A(ICOL,L)=DUM
14        CONTINUE
          DO 15 L=1,M
            DUM=B(IROW,L)
            B(IROW,L)=B(ICOL,L)
            B(ICOL,L)=DUM
15        CONTINUE
        ENDIF
        INDXR(I)=IROW
        INDXC(I)=ICOL
        IF (A(ICOL,ICOL).EQ.0.0D0) PAUSE 'Singular matrix.'
        PIVINV=1.0D0/A(ICOL,ICOL)
        A(ICOL,ICOL)=1.
        DO 16 L=1,N
          A(ICOL,L)=A(ICOL,L)*PIVINV
16      CONTINUE
        DO 17 L=1,M
          B(ICOL,L)=B(ICOL,L)*PIVINV
17      CONTINUE
        DO 21 LL=1,N
          IF(LL.NE.ICOL)THEN
            DUM=A(LL,ICOL)
            A(LL,ICOL)=0.0D0
            DO 18 L=1,N
```

```
            A(LL,L)=A(LL,L)-A(ICOL,L)*DUM
18          CONTINUE
            DO 19 L=1,M
              B(LL,L)=B(LL,L)-B(ICOL,L)*DUM
19          CONTINUE
          ENDIF
21      CONTINUE
22    CONTINUE
      DO 24 L=N,1,-1
        IF(INDXR(L).NE.INDXC(L))THEN
          DO 23 K=1,N
            DUM=A(K,INDXR(L))
            A(K,INDXR(L))=A(K,INDXC(L))
            A(K,INDXC(L))=DUM
23        CONTINUE
        ENDIF
24    CONTINUE
      RETURN
      END
C*******************************************************************************
      SUBROUTINE GCF(GAMMCF,A,X)
C*******************************************************************************
      IMPLICIT REAL*8 (A-H,O-Z)
      PARAMETER (ITMAX=100,EPS=3.D-7)
C      PRINT *,A,X
      GLN=GAMMLN(A)
      GOLD=0.0D0
      A0=1.0D0
      A1=X
      B0=0.0D0
      B1=1.0D0
      FAC=1.0D0
      DO 11 N=1,ITMAX
        AN=DBLE(N)
        ANA=AN-A
        A0=(A1+A0*ANA)*FAC
        B0=(B1+B0*ANA)*FAC
        ANF=AN*FAC
        A1=X*A0+ANF*A1
        B1=X*B0+ANF*B1
        IF(A1.NE.0.0D0)THEN
          FAC=1.0D0/A1
```

```
          G=B1*FAC
          IF(DABS((G-GOLD)/G).LT.EPS)GO TO 1
          GOLD=G
        ENDIF
11    CONTINUE
C      PRINT *,'GCF',A,X
      PAUSE 'A too large, ITMAX too small'
1     GAMMCF=DEXP(-X+A*DLOG(X)-GLN)*G
      RETURN
      END
C*********************************************************************
      SUBROUTINE GSER(GAMSER,A,X)
C*********************************************************************
      IMPLICIT REAL*8 (A-H,O-Z)
      PARAMETER (ITMAX=100,EPS=3.D-7)
      GLN=GAMMLN(A)
      IF(X.LE.0.0D0)THEN
        IF(X.LT.0.0D0)PAUSE
        GAMSER=0.0D0
        RETURN
      ENDIF
      AP=A
      SUM=1.0D0/A
      DEL=SUM
      DO 11 N=1,ITMAX
        AP=AP+1.0D0
        DEL=DEL*X/AP
        SUM=SUM+DEL
        IF(DABS(DEL).LT.DABS(SUM)*EPS)GO TO 1
11    CONTINUE
C      PRINT *,'GSER',A,X
      PAUSE 'A too large, ITMAX too small'
1     GAMSER=SUM*DEXP(-X+A*DLOG(X)-GLN)
      RETURN
      END
C*********************************************************************
      FUNCTION GAMMLN(XX)
C*********************************************************************
      DIMENSION COF(6)
      IMPLICIT REAL*8 (A-H,O-Z)
      REAL*8 COF(6),STP,HALF,ONE,FPF,X,TMP,SER
      DATA COF,STP/76.18009173D0,-86.50532033D0,24.01409822D0,
```

```
     *    -1.231739516D0,.120858003D-2,-.536382D-5,2.50662827465D0/
      DATA HALF,ONE,FPF/0.5D0,1.0D0,5.5D0/
      X=XX-ONE
      TMP=X+FPF
      TMP=(X+HALF)*DLOG(TMP)-TMP
      SER=ONE
      DO 11 J=1,6
        X=X+ONE
        SER=SER+COF(J)/X
11    CONTINUE
      GAMMLN=TMP+DLOG(STP*SER)
      RETURN
      END
C*********************************************************************
      FUNCTION GAMMP(A,X)
C*********************************************************************
      IMPLICIT REAL*8 (A-H,O-Z)
      IF(X.LT.0.0D0.OR.A.LE.0.0D0)PAUSE
      IF(X.LT.A+1.0D0)THEN
        CALL GSER(GAMMP,A,X)
      ELSE
        CALL GCF(GAMMCF,A,X)
        GAMMP=1.0D0-GAMMCF
      ENDIF
      RETURN
      END
C*********************************************************************
      FUNCTION PSI(Z)
C*********************************************************************
      IMPLICIT REAL*8 (A-H,O-Z)
      X=DLOG(Z)-0.5D0/Z-1.0D0/12.0D0/Z**2+1.0D0/120.0D0/Z**4
      PSI=X-1.0D0/252.0D0/Z**6
      RETURN
      END
```

E.2. Program SYNTHESIZE - Calculates Correlation Function and Scattering Intensity for the Bimodal FPPS Schulz Distribution Model.

```
      PROGRAM SYNTHESIZE
c**********************************************************************
c     Compile with:
c     f77 SYNTH.f "{AbsoftLibraries}"MIG.o -o SYNTH ∑∑"{Worksheet}"
c     Calculates Scattering Curve for Bimodal FPPS Schulz Model
c**********************************************************************
      DIMENSION HX(200),TEN(200),TENCAL(200)
      DIMENSION XA(200),YA(200),YACAL(200),A(6)
      IMPLICIT REAL*8 (A-H,O-Z)
      REAL*8 HX,TEN,TENCAL,EPS1
      REAL*4 XA,YA,YACAL
      INTEGER*4 NUM
      CHARACTER*30 filename1
      CHARACTER*30 filename2
      COMMON A01,B1,PC1,A02,B2,PC2,EPS1,PHI,PP,GB11,GB22
      PRINT *,'Data File Name:'
      READ *,filename1
       PRINT *,'Output File Name:'
       READ *,filename2
      open (UNIT=10,FILE=filename1,ERR=500,
     +STATUS='OLD',ACTION='READ')
 11   format(I3)
 12   format (F8.5,F10.6)
      READ(10,11) NUM
      PRINT *,NUM
      DO 13 K=1,NUM
        READ(10,12) HX(K),TEN(K)
c       PRINT *,HX(K),TEN(K)
 13     CONTINUE
      goto 501
 500  CONTINUE
      PRINT *,'Error Opening File '
 501  CONTINUE
      close (10)

      PRINT *,'A01 ='
      READ *,A(1)
      PRINT *,'B1 ='
      READ *,A(2)
```

```
      PRINT *,'A02 ='
      READ *,A(3)
      PRINT *,'B2 ='
      READ *,A(4)
      PRINT *,'PHI ='
      READ *,A(5)
      PRINT *,'EPS1 ='
      READ *,A(6)

 301    CONTINUE
      A01=A(1)
      B1=A(2)
      A02=A(3)
      B2=A(4)
      PHI=A(5)
      EPS1=A(6)
      PP=3.141592653589793D0
      GB11=DEXP(GAMMLN(B1))
      GB22=DEXP(GAMMLN(B2))
      PC1=EPS1
      PC2=(1.0D0-EPS1)
      PRINT *,A01,B1
      PRINT *,A02,B2
      PRINT *,PHI,EPS1
C*************************************************************************
C     INTEGRATION ROUTINE
C     H LOOP HERE
C*************************************************************************
      DO 200 J=1,NUM
      H=HX(J)
      SUM=0.0D0
      DEX=1.0D0
      BEGIN=0.0D0
100   ROOT=DEX*PP/H
      FINISH=ROOT
      CALL QGAUSS(BEGIN,FINISH,H,GRAL)
C      PRINT *,SUM,GRAL
      SUM = SUM + GRAL
      BEGIN = FINISH
      DEX = DEX +1.0D0
      IF(DABS(GRAL/SUM).GT.1.0D-2) GO TO 100
      TENCAL(J)=SUM
```

```
C201    PRINT *,H,TEN(J),TENCAL(J)
200    CONTINUE
       SISUM=0.0D0
       DO J=1,NUM
       SISUM=SISUM+TEN(J)/TENCAL(J)
       REPEAT
       DNUM=NUM
       TEN0=SISUM/DNUM
       PRINT *,TEN0
       PAUSE
       DO J=1,NUM
       TENCAL(J)=TEN0*TENCAL(J)
c      PRINT *,HX(J),TEN(J),TENCAL(J)
       REPEAT
       open (UNIT=10,FILE=filename2,STATUS='UNKNOWN',
      +ERR=700,ACTION='WRITE')
        write(10,34) A01,B1
        write(10,34) A02,B2
        write(10,34) PHI,EPS1
        write(10,33) TEN0,GB11,GB22
        SSUM = 0.0D0
        DO 600 J=1,NUM
       write(10,34) HX(J),TEN(J),TENCAL(J)
       SSUM = SSUM + (DLOG(TENCAL(J))-DLOG(TEN(J)))**2
c      write(10,*) SSUM
  33   format (E20.8,1H,,E20.8,1H,,E20.8)
  34     format(F15.5,1H,,F15.5,1H,,F15.5)
 600     CONTINUE
       goto 701
 700   CONTINUE
       type *,'Error Opening File '
       print *,filename2
 701   CONTINUE
       close (10)
C
C Convert to Single Precision for Plotting
C
       DO 300 I=1,NUM
       XA(I)= REAL(HX(I))
       YA(I)= REAL(TEN(I))
       YACAL(I)= REAL(TENCAL(I))
300    CONTINUE
```

```
      CALL GRAPH(XA,YA,YACAL,NUM)
      PRINT *,A01,B1,PC1
      PRINT *,A02,B2,PC2
      PRINT *,SSUM
      PRINT *,'Another Fit? - Yes = 0, No = Any Number'
      READ *,IGO
      IF(IGO.NE.0) GOTO 400
 302    CONTINUE
      PRINT *,'Change Parameter Number:'
      PRINT *,'A01=1; B1=2; A02=3; B2=4; PHI=5; EPS1=6'
      PRINT *,'Enter 0 (zero) to stop'
      READ *, IPARM
      IF(IPARM.EQ.0) GO TO 303
      READ *,A(IPARM)
      GO TO 302
 303    CONTINUE
      GO TO 301
 400    CONTINUE
      STOP
      END
C*********************************************************************
      SUBROUTINE QGAUSS(A,B,H,SS)
C*********************************************************************
      DIMENSION X(5),W(5)
      IMPLICIT REAL*8 (A-H,O-Z)
C      COMMON TEN0,A01,B1,PC1,A02,B2,PC2,EPS1,PHI,PP,GB11,GB22
      DATA X/.1488743389,.4333953941,.6794095682,.8650633666,.9739065285
     */
      DATA W/.2955242247,.2692667193,.2190863625,.1494513491,.0666713443
     */
      XM=0.5D0*(B+A)
      XR=0.5D0*(B-A)
      SS=0
      DO 11 J=1,5
        DX=XR*X(J)
        SS=SS+W(J)*(FUNC(XM+DX,H)+FUNC(XM-DX,H))
11    CONTINUE
      SS=XR*SS
C      PRINT *,SS
      RETURN
      END
```

```
C*********************************************************************
      FUNCTION FUNC(R,H)
C*********************************************************************
      IMPLICIT REAL*8 (A-H,O-Z)
      COMMON A01,B1,PC1,A02,B2,PC2,EPS1,PHI,PP,GB11,GB22
C      PRINT *,'FUNC',A01
      CALL S2R(R,A01,B1,PHI,GB11,PC1,SR1)
      CALL S2R(R,A02,B2,PHI,GB22,PC2,SR2)
      IF(R.EQ.0.0D0) GO TO 10
      T0=DSIN(H*R)*4.0D0*PP*R**2/H/R
      FUNC=(SR1*SR2-PHI**2)*T0
      GO TO 20
10    FUNC=0.0D0
20    CONTINUE
      RETURN
      END
C*********************************************************************
      SUBROUTINE S2R(R,A0,B,PHI,GB,PC,SR)
C*********************************************************************
      IMPLICIT REAL*8 (A-H,O-Z)
      IF(R.EQ.0.0D0) GOTO 10
      XX = B*R/A0/2.0D0
      T1=DEXP(-XX)
C      PRINT *,'S2R',R,A0,B,XX
      T3=((A0/B)**3)*(B+2.0D0)*(B+1.0D0)*B
      PAX=GAMMP(B,XX)
      ACTR=(XX**B)*T1/B/GB
      PAX1=PAX-ACTR
      PAX2=PAX1-XX*ACTR/(B+1.0D0)
      PAX3=PAX2-XX**2*ACTR/(B+2.0D0)/(B+1.0D0)
C      PRINT *,T3,PAX,PAX1,PAX2,PAX3
      GRAL=(1.0D0+PAX3)+1.5D0*XX*(1.0D0-PAX2)/(B+2.0D0)
     &-XX**3*(1.0D0-PAX)/2.0D0/B/(B+1.0D0)/(B+2.0D0)
      SR=DEXP(DLOG(PHI)*PC*GRAL)
      GO TO 20
10    SR=0.0D0
20    CONTINUE
      RETURN
      END
C*********************************************************************
      SUBROUTINE GCF(GAMMCF,A,X)
C*********************************************************************
```

```
      IMPLICIT REAL*8 (A-H,O-Z)
      PARAMETER (ITMAX=100,EPS=3.D-7)
C      PRINT *,A,X
      GLN=GAMMLN(A)
      GOLD=0.0D0
      A0=1.0D0
      A1=X
      B0=0.0D0
      B1=1.0D0
      FAC=1.0D0
      DO 11 N=1,ITMAX
        AN=DBLE(N)
        ANA=AN-A
        A0=(A1+A0*ANA)*FAC
        B0=(B1+B0*ANA)*FAC
        ANF=AN*FAC
        A1=X*A0+ANF*A1
        B1=X*B0+ANF*B1
        IF(A1.NE.0.0D0)THEN
          FAC=1.0D0/A1
          G=B1*FAC
          IF(DABS((G-GOLD)/G).LT.EPS)GO TO 1
          GOLD=G
        ENDIF
11    CONTINUE
C      PRINT *,'GCF',A,X
      PAUSE 'A too large, ITMAX too small'
1     GAMMCF=DEXP(-X+A*DLOG(X)-GLN)*G
      RETURN
      END
C*********************************************************************
      SUBROUTINE GSER(GAMSER,A,X)
C*********************************************************************
      IMPLICIT REAL*8 (A-H,O-Z)
      PARAMETER (ITMAX=100,EPS=3.D-7)
      GLN=GAMMLN(A)
      IF(X.LE.0.0D0)THEN
        IF(X.LT.0.0D0)PAUSE
        GAMSER=0.0D0
        RETURN
      ENDIF
      AP=A
```

```
      SUM=1.0D0/A
      DEL=SUM
      DO 11 N=1,ITMAX
        AP=AP+1.0D0
        DEL=DEL*X/AP
        SUM=SUM+DEL
        IF(DABS(DEL).LT.DABS(SUM)*EPS)GO TO 1
11    CONTINUE
C      PRINT *,'GSER',A,X
      PAUSE 'A too large, ITMAX too small'
1     GAMSER=SUM*DEXP(-X+A*DLOG(X)-GLN)
      RETURN
      END
C*********************************************************************
      FUNCTION GAMMLN(XX)
C*********************************************************************
      DIMENSION COF(6)
      IMPLICIT REAL*8 (A-H,O-Z)
      REAL*8 COF(6),STP,HALF,ONE,FPF,X,TMP,SER
      DATA COF,STP/76.18009173D0,-86.50532033D0,24.01409822D0,
     *    -1.231739516D0,.120858003D-2,-.536382D-5,2.50662827465D0/
      DATA HALF,ONE,FPF/0.5D0,1.0D0,5.5D0/
      X=XX-ONE
      TMP=X+FPF
      TMP=(X+HALF)*DLOG(TMP)-TMP
      SER=ONE
      DO 11 J=1,6
        X=X+ONE
        SER=SER+COF(J)/X
11    CONTINUE
      GAMMLN=TMP+DLOG(STP*SER)
      RETURN
      END
C*********************************************************************
      FUNCTION GAMMP(A,X)
C*********************************************************************
      IMPLICIT REAL*8 (A-H,O-Z)
      IF(X.LT.0.0D0.OR.A.LE.0.0D0)PAUSE
      IF(X.LT.A+1.0D0)THEN
        CALL GSER(GAMMP,A,X)
      ELSE
        CALL GCF(GAMMCF,A,X)
```

```
        GAMMP=1.0D0-GAMMCF
      ENDIF
      RETURN
      END
C*********************************************************************
       SUBROUTINE GRAPH(X,Y,YCAL,NPP)
C*********************************************************************
C     General Purpose MacGraphics Routine With Absoft FORTRAN
C     MAC GRAPHICS VARIABLES
C
      IMPLICIT NONE
      REAL*4 X(200),Y(200),YCAL(200),X13SCALE,Y13SCALE
      REAL*4 XPIXMAX,XPIXMIN,YPIXMAX,YPIXMIN,XMIN,XMAX,YMIN,YMAX
      REAL*4 XRNG,YRNG
      REAL*4 VX,VY
      INTEGER*4 GCoord,MyCoord
      INTEGER*4 I,NP
      INTEGER*4 NPP

C Character strings
      CHARACTER*80 FONT,STYLE

c Set up some x & y limits
      XMIN=LOG(0.001)
      XMAX=LOG(1.0)
      YMIN=LOG(YCAL(NPP))
      YMAX=LOG(YCAL(1))

C Initialize MIG
      CALL MIGSetup(XPIXMIN,XPIXMAX,YPIXMIN,YPIXMAX,GCoord)

C Scale all the global coordinate numbers to an Apple 13 inch monitor
      X13SCALE=(XPIXMAX-XPIXMIN)/560.0
      Y13SCALE=(YPIXMAX-YPIXMIN)/420.0

C Set the background color
      CALL SetMyColor(1,65535,65535,65535)      ! White

C Set the foreground color
      CALL SetMyColor(0,0,0,65535)        ! Blue

C     SET RANGE OF X AND Y
```

```
      XRNG = XMAX-XMIN
      YRNG = YMAX-YMIN
C Set up the subject units and show border
      CALL DefineCoord(XMIN-0.2*XRNG,YMIN-0.2*YRNG,XMAX+0.2*XRNG,
     &YMAX+0.2*YRNG,1,MyCoord)

C Set up the text characteristics
      FONT='COURIER';STYLE='PLAIN';NP=10
      CALL TextAttributes(FONT,STYLE,NP)

c Box in the plot frame
c      call SetCoord(GCoord)
c      call MovePen(20.*X13SCALE,20.*Y13SCALE)
c      call DrawLine(540.*X13SCALE,20.*Y13SCALE)
c      call DrawLine(540.*X13SCALE,400.*Y13SCALE)
c      call DrawLine(20.*X13SCALE,400.*Y13SCALE)
c      call DrawLine(20.*X13SCALE,20.*Y13SCALE)

C Draw the plot
      call SetCoord(MyCoord)
      VX=LOG(X(1))
      VY=LOG(Y(1))
      CALL MovePen(VX,VY)
      DO I=2,NPP
      VX=LOG(X(I))
      VY=LOG(Y(I))
        CALL DrawLine(VX,VY)
      REPEAT

C Set the foreground color
      CALL SetMyColor(0,65535,0,0)        ! Red

      VX=LOG(X(1))
      VY=LOG(YCAL(1))
      CALL MovePen(VX,VY)
      DO I=2,NPP
      VX=LOG(X(I))
      VY=LOG(YCAL(I))
      CALL DrawLine(VX,VY)
      REPEAT

C Set the foreground color
```

```
      CALL SetMyColor(0,0,0,65535)        ! Blue

c Draw the axis
      call MovePen(XMAX,YMIN)
      call DrawLine(XMIN,YMIN)
      call DrawLine(XMIN,YMAX)

c x-axis tics
      call MovePen(LOG(0.001),YMIN)
      call DrawLine(LOG(0.001),YMIN-YRNG/20.)
      call MovePen(LOG(0.01),YMIN)
      call DrawLine(LOG(0.01),YMIN-YRNG/20.)
      call MovePen(LOG(0.1),YMIN)
      call DrawLine(LOG(0.1),YMIN-YRNG/20.)
      call MovePen(LOG(1.0),YMIN)
      call DrawLine(LOG(1.0),YMIN-YRNG/20.)

c x-axis numbers

      call DrawMyText(LOG(0.001),YMIN-YRNG/15.,'1E-3',4)
      call DrawMyText(LOG(0.01),YMIN-YRNG/15.,'1E-2',4)
      call DrawMyText(LOG(0.1),YMIN-YRNG/15.,'1E-1',4)
      call DrawMyText(LOG(1.0),YMIN-YRNG/15.,'1E0',4)

c title
      call DrawMyText(XMIN+XRNG/2.25,YMAX+YRNG/10.,
     & 'SCATTERING CURVE',16)

c x-axis label
      call DrawMyText(XMIN+XRNG/2.,YMIN-YRNG/10.,'h (1/Å)',7)

c y-axis label
      call DrawMyText(XMIN-XRNG/6.,YMIN+YRNG/2.,'Intensity',9)

C End the plot frame
      CALL EndPlotFrame()

C Close the Grafport , etc., zero-out plot common data
      CALL QuitPlot()

      END
```